UCSF

UC San Francisco Electronic Theses and Dissertations

Title

Dissecting the Mechanisms of Brain Injury for Treatment of Cognitive Dysfunctions

Permalink

https://escholarship.org/uc/item/6wk0v0t6

Author

Frias, Elma Stephanie

Publication Date

2021

Peer reviewed|Thesis/dissertation

Dissecting the Mechanisms of Brain Injury for Treatment of Cognitive Dysfunctions
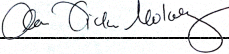
by
Elma Stephanie Frias

DISSERTATION
Submitted in partial satisfaction of the requirements for degree of
DOCTOR OF PHILOSOPHY

in

Biomedical Sciences

in the

GRADUATE DIVISION
of the
UNIVERSITY OF CALIFORNIA, SAN FRANCISCO

Approved:

DocuSigned by:

_____   Anna Molofsky
7148719D502F43A...
                                                                          Chair

DocuSigned by:

Michael Stryker
_____   Michael Stryker
DocuSigned by: ...40C...

Peter Walter
_____   Peter Walter
DocuSigned by: ...40D...

Susanna Rosi
_____   Susanna Rosi
211375A844174DF...

_____
                                                     Committee Members

Dedication

To my parents, for their unconditional support and love. To my family and friends, whom I attribute a significant part of my personal and scientific growth. To my mentor, for her mentorship and resoluteness.

Acknowledgements

I would like to first acknowledge my parents, Elma Frias and Jaime Frias, from whom I have been fortunate to receive all of the support and encouragement to pursue my dreams. I am especially thankful for the stress-relieving chisme chats, Asadas in the park, and knowing that you both will always be my number one fans.

I would like to next acknowledge my family and friends. To my big family, spread across different cities, countries, and worlds of existence, thank you for the words of encouragement and buckets of enthusiasm that motived me along on this journey. To my friends near and afar, thank you for sharing this experience with me (by choice or otherwise) and giving me more laughs, life lessons, and social media comics and videos to last a lifetime (or at least until this dissertation is all said and done).

I would like to acknowledge my dear, Vincent Tolero. Graduate school was a frightening yet thrilling roller coaster, and I could not have found a better person to ride with. Thank you for your love and care and helping me give my best even when I wasn't at my best. A special thanks to the 911.6 miles traveled countless times, messages of encouragement and honesty, and the dragon koala.

I would like to next acknowledge my scientific community, Dr. Krukowski, Katie Grue, Dr. Paladini, Dr. Hoseini, Dr. Stryker, research team and collaborators, committee members, and previous research mentors. I could not have been luckier to be trained by and to work alongside some of the most exceptional scientists, thinkers, and individuals of our time. Thank you for helping me become the scientist and person I am today, *reading* my lengthy emails (drafts included), and showing me the wonders of a good chocolate bar and coffee (1:10000).

Dissecting the Mechanisms of Brain Injury for

Treatment of Cognitive Dysfunctions

Elma Stephanie Frias

Abstract

Between 1.5 – 3.8 million people experience traumatic brain injury each year in the United States and at least 75% of these injuries are a mild TBI (concussive injuries without loss of consciousness). TBI remains a growing health concern, as it's a leading cause of long-term neurological disability in the world, induces accelerated cognitive aging, and is the strongest environmental risk factor for the development of dementia. Even mild TBI (concussive injury) is associated with a >2-fold increase in the risk of dementia diagnosis. The pathophysiology of TBI is very complex, resulting in chronic behavioral and cognitive impairments that affect the quality of life of millions of individuals. Little is known about the cellular mechanisms responsible for the development of cognitive deficits after injury, thus with no identified targetable mechanisms, there are no treatments to prevent or mitigate deficits resulting from TBI. This dissertation investigates mechanisms contributing to brain injury-induced cognitive decline and broadens the scope of TBI research to understand the effect biological sex, aging, and therapeutic whole-brain irradiation.

In Chapter 2, using longitudinal two-photon *in vivo* imaging I investigated the mechanism by which concussive injury induced recognition memory deficits. Concussive injury induced aberrant changes in cortical spine dynamics and density and short-term memory dysfunction. Targeting the integrated stress response (ISR) using the small-molecule inhibitor ISRIB reversed the maladaptive changes in cortical spine

dynamics and the short-term memory dysfunction. Importantly these restorative effects were maintained weeks after treatment ended. In Chapter 3, I investigated the effect of mild repetitive traumatic brain injury, ISR inhibition, and biological sex on cognitive and behavioral function and neuronal function. Mild repetitive injury resulted in increased risk-taking behavior only in male mice and this behavior phenotype was associated with increased activation of the ISR and cell-specific synaptic alterations in type A layer V pyramidal neurons of the medial prefrontal cortex. Importantly, brief pharmacological inhibition of the ISR with ISRIB reversed injury-induced risk-taking behavior and the associated cell-specific deficits in synaptic function. In Chapter 4, I investigated the role of the ISR in healthy age-related cognitive decline. Temporary treatment with ISRIB leads to improvement in spatial, working, and episodic memory. At a cellular level the cognitive enhancement was paralleled by i) improved intrinsic neuron excitability, ii) increased dendritic spine density, iii) reversal of age-induced changes in IFN and T cell responses in the hippocampus and blood, and iv) reversal of ISR activation. In Chapter 5, I investigated the functional role of brain engrafted macrophages (BEMs) in response to a secondary concussive injury. Replacement of microglia with monocyte derived BEMs prevented loss of synapses and consequent memory deficits after therapeutic irradiation and concussive injury. These chapters collectively add to our understanding of the pathophysiology of traumatic brain injury with the aim that we are closer to providing effective treatment for a major health crisis in the future.

Table of Contents

List of Figures

Chapter 2

Chapter 3

Figure 4. Cell-specific vulnerability to mild repetitive traumatic brain injury (rTBI) is observed in the prefrontal cortex with an increase in the frequency of synaptic input in

Chapter 4

Chapter 5

List of Tables

Chapter 3

Chapter 4

List of Abbreviations

Chapter 2

CHI: closed-head injury

ISR: integrated sress response

ISRIB: integrated stress response inhibitor

NORT: novel object recognition task

TBI: traumatic brain injury

Chapter 3

CCI: controlled cortical impact

CHI: closed-head injury

EPM: elevated plus maze

ISR: integrated stress response

ISRIB: integrated stress response inhibitor

mPFC: medial prefrontal cortext

rTBI: mild repetitive traumatic brain injury

TBI: traumatic brain injury

Chapter 4

ISR: integrated stress response

ISRIB: integrated stress response inhibitor

Chapter 5

BEMs: brain-engrafted macrophages

CHI: closed-head injury

CNS: central nervous system

CSF-1R: colony-stimulating factor 1 receptor

CSF-1Ri: colony-stimulating factor 1 receptor inhibitor

DE genes: differentially expressed genes

FACS: fluorescence activated cell sorting

GOBP: gene ontology biological pathway

NOR: novel object recognition

WBRT: whole-brain radiotherapy

Chapter 1: General Introduction

TBI epidemiology

Each year in the United States, an estimated 2.8 million people sustain traumatic brain injury (TBI) [1]. An estimated 3.2 to 5.3 million people live with the long-term, often permanent, physical, cognitive, psychological, and emotional health disabilities resulting from TBI [1]. The increased occurrence of TBI in the United States is estimated to cost over $76 billion annually in direct and indirect expenses [2]. Moreover, TBI remains a leading cause of long-term neurological disability in the world, the strongest environmental risk factor for the development of Alzheimer's and dementia and induces accelerated cognitive aging [3-8]. Even mild TBI (concussive injuries without loss of consciousness) is associated with a >2-fold increase in the risk of dementia diagnosis [9, 10]. TBI is defined as the disruption of normal brain function resulting from an impact (bump, blow, or jolt) to the head [11]. TBI causes both direct damage from mechanical forces (primary injury) imposed on the brain and additive indirect damage from secondary responses such as ischemia, edema, or inflammation (secondary injury) [12]. TBI occurs in a variety of circumstances including traffic accidents, falls, sports, violence, assault, and blasts experienced by active-duty personnel [10, 13]. Injuries are clinically classified as mild, moderate, or severe based on presentation of symptoms [14-16]. Determining patient outcome is complicated: chronic symptoms are dependent upon a multitude of variables, including, but not limited to, location, nature, and extent of injury, pre-existing conditions, psychosocial factors, and possible post-injury treatment [17]. Despite its high prevalence and impact, the diversity of causes and complexity of

injury responses have ultimately hindered the development of effective treatments to prevent or mitigates deficits associated with TBI [18-22]. To adequately model the heterogeneous nature of TBI in humans, pre-clinical studies have been conducted using experimental models that replicate the pathophysiological features of different types of human TBI.

Mouse models of TBI

TBI is biphasic, as evident by a primary and secondary component [23]. The primary injury (phase I) is caused by mechanical disruption to macro- and microscopic structures within the brain at the moment or immediately after impact, resulting in gross tissue deformation, hemorrhaging, sheering of brain cells, and activation of apoptotic pathways in damaged cells [24-26]. Depending on the type of injury this overt tissue damage can come from a penetration injury or from accelerating and rotational forces. The secondary injury (phase II) develops over hours and days and is associated with the activation of various signaling cascades (acting concurrently and often with synergizing effects) that produce inflammation, free radical production, electrolyte imbalances, mitochondrial dysfunction, and excitotoxicity (amongst other sequalae) [25, 27]. Consequently, activation of these mechanisms leads to progressive damage extending long after the initial primary injury [28]. Brain damage at and immediately after impact, as a result from primary injury, is considered irreversible, however, secondary damage results from delayed neurochemical process and intracellular signaling pathways, which can be reversible [29]. Thus, secondary injuries are the focus of most

TBI preclinical studies as they are broader temporal windows for treatment opportunities compared to the primary injury [26].

Numerous preclinical rodent models have been established to study TBI. The method by which TBI is induced is an important consideration given the heterogeneity of the disease. These models developed over the last 80 years replicate different unique features of TBI (i.e. emotional or cognitive symptoms), biomechanical forces (i.e. impact or rotational), as well as levels of severity (i.e. focal-severe or diffuse-moderate) [26, 30, 31]. Mild traumatic brain injuries (mTBI), including concussive injuries, account for 70–90% of all TBI cases [32]; making them a significant health concern. Estimates of these injuries are under-reported attributed to the fact that many individuals who sustain a mTBI never seek medical treatment. Not only are incidences of mTBI on the rise, there is also a growing awareness that these injuries are not benign and that the brain may not fully recover from the injury with time [33, 34]. This has translated to a steadily increasing number of preclinical mTBI studies, although the overall number of them continue to be small. Animal models of mTBI are essential for understanding mechanisms, and pathological outcomes, as well as to identify therapeutic interventions. A variety of closed head models of mTBI in rodents that incorporate different aspects of human mTBI have been reported [30, 35]. Our lab takes advantage of two such models: i) a single closed-head injury without rotational acceleration and ii) a mild repetitive injury model with rotational acceleration.

Concussive brain injury

A concussive brain injury results from an impact to the head and can cause loss of consciousness or not. These injuries are typically diffuse and widespread, wherein damaged structures are scattered among other intact, and in some cases, unaltered structures. Abnormalities resulting from a concussion are difficult to detected on standard structural neuroimaging, such as by CT or MRI [36]. Moreover, brain imaging studies are not performed routinely in the diagnosis of concussions as they typically do not show any significant changes and expose individuals to unnecessary radiation (CT) [37-39].

Following concussion, brain pathophysiology is adversely affected for months in animals and months, sometimes years, in humans [40]. Concussive injuries can lead to an alteration in mental status accompanied by memory dysfunction, all of which may or may not resolve completely over time. Even head-injured patients with normal Glasgow Coma Scores (a common scoring system used to describe level of consciousness in a person following a traumatic brain injury) show significant maladaptive changes in brain pathophysiology [40]. Thus, supporting the need to uncover underlying correlates for altered cognitive function after concussive injuries.

To understand the mechanisms driving the long-term cognitive deficits observed following concussive injury, our lab uses a single closed-head injury (CHI) model [41]. The CHI model is a fixed-skull piston-driven model, where a contusion is induced by placing the piston (a convex tip) on the surface of the fixed-skull (animals are secured to a stereotaxic frame with nontraumatic ear bars) at specified coordinates and then delivering an injury at a specific depth, velocity, or impact force. The piston-driven

model became more commonly used beginning the mid-2000s since it increased the reproducibility of the injury model as compared to other models (weight drop, other/nonconventional) [30].

Repetitive brain injury

Animal and human studies support the concept of post-concussive vulnerability, showing that a second blow before the brain has recovered results in worse outcome [42]. Further, a previous TBI increases the risk for additional TBI [43-45], making it imperative to understand the potential compounding effects of repetitive trauma. Often deficits may not initially be observed after a single TBI, however additional head injuries can have cumulating effects including both increased susceptibility to future injury as well as behavioral and cognitive deficits [42, 46-48]. Highly recurrent concussions such as found in contact sports can be associated with chronic traumatic encephalopathy (CTE), which is defined by the presence of perivascular tau deposits primarily in sulcal depths upon neuropathological examination. A survey of retired professional American football players showed an association between recurrent concussions and clinically diagnosed mild cognitive impairment [49].

To understand the underlying cellular and functional correlates driving maladaptive outcomes to repetitive trauma (rTBI), our lab uses a closed-head impact model of engineered rotational acceleration (CHIMERA) model [35]. The CHIMERA model is a non-surgical impact acceleration model that delivers precise mechanical inputs to reliably induce a combination of linear and rotational movement in a freely moving head.

TBI pathophysiology

Neuronal Dysfunction after TBI

Neurons are the basic building block of the nervous system and specialize in transmitting information, in both chemical and electrical forms. Neuronal dysfunction after TBI can occur due to demyelination and disruption of axonal cytoskeleton, axonal swelling, ionic shifts, altered metabolism, impaired connectivity, and changes in neurotransmission [40]. Synapses, the functional unit responsible for communication between neurons, are microscopic gaps between the terminal buttons of one neuron and dendritic spines (bulbous membrane projections) of another neuron, allowing for electrical signals to be transmitted from one neuron to another via chemical signals (neurotransmission) [50, 51]. Much evidence indicates that cognitive function, such as memory, is supported by synaptic plasticity (ability of synapses to undergo lasting biochemical and morphological changes in response to stimuli and neuromodulators), which in turn depends on structural plasticity (ability of dendritic spines to undergo lasting changes in response to internal and external cues) [52-55].

Structural plasticity of dendritic spines involves modulations to three major arms: dendritic spine dynamics, density, and morphology [56-58]. Spine dynamics describes the structural reorganization of dendritic spines, observed by the formation and elimination of spines [59]. While dendritic spines are stable for months to years, structural plasticity of dendritic spines (observed in the matter of hours or days) is important for the development and function of the CNS [60-63]. Spine density is a calculation of the number of spines per measured length of dendrite. The density of spines can be used as a measure of synaptic strength [52, 57]. Previous studies have

reported an acute loss of spine density followed by an aberrant increase after TBI [64-66]. Spine morphology describes the shape and size of dendritic spines. They are traditionally grouped into four classes according to measurements reflecting spine head and neck properties: mushroom, thin, stubby, and filopodia. However, the classification approach has various limitations and recent data support a continuum of shapes and sizes [58, 67, 68]. Importantly, the size of the spine head has been shown to correlate with the strength of synaptic transmission [55]. The delicate regulation of each arm by internal and external factors is essential for stable synaptic maintenance, connectivity between neurons and thus cognitive and executive function, such as memory [51, 52, 55, 67, 69].

Neuroinflammation after TBI

Although traditionally considered a site of "immunologic privilege", it is now recognized that the CNS does not constitute an immunoprivileged system but rather, that the brain exhibits the classic hallmarks of inflammation following TBI. The inflammatory response of the brain to traumatic insult, referred to as neuroinflammation, is multifactorial, encompassing the activation of resident CNS glia (astrocytes) and immune cells (microglia) and the cerebral infiltration of peripheral immune cells (macrophages, leukocytes), all of which mediate inflammatory processes through a variety of inflammatory cytokines, chemokines, adhesion molecules, reactive oxygen and nitrogen species, complement factors, among others. Analysis of cerebrospinal fluid (CSF) and post-mortem tissue of TBI patients [70-72] and tissue of TBI rodents [73-75] sustained upregulation of various cytokines (complement factors and pro-inflammatory

cytokines such as IL-1β, IL-6 and TNF-α) was found to be associated with altered BBB permeability, formation of edema and neurological deficits [20]. The degree of neuroinflammation depends on the context, duration, and course of the primary insult. Consequently, these responses contribute to unfavorable behavioral and cognitive outcomes following TBI.

Astrocytes execute homeostatic mechanisms important for maintaining neural activity and extracellular composition, including buffering ion concentrations, maintaining the blood brain barrier, facilitating neuronal communication, and engaging in spine dynamics [76-78]. Additionally, astrocytes respond to injury and disease with heterogenous and progressive functional, cellular, and molecular changes, a process collectively termed astrogliosis. TBI is known to induce astrocyte activation (astrogliosis), weighing a lot to the patient outcome [41, 79-82]. It is clear now that astrogliosis is a context-specific response wherein the response to injury, neurodegenerative disease, or normal aging can be deleterious and/or protective to neuronal health and function [83]. Additionally, different signaling molecules have been identified that can induce either a protective or deleterious reactive response [84]. However, suppressing or promoting reactive astrogliosis does not have a satisfying curative effect, whereas selectively stimulating the beneficial astrocyte-derived molecules while attenuating the deleterious ones based on the spatiotemporal-environment represents a promising astrocyte-targeting therapeutic strategy [79].

In human studies, increased microglial activation was observed in the brain up to 18 years after the injury in postmortem analyses [85, 86]. PET scans revealed microglia activation in the brains of TBI patients up to 17 years after the injury [71]. Microglia are

the resident immune cells of the brain that regulate neuronal function through constant surveillance of the milieu. The initial activation of the innate immune response and brain microglia is intended to be protective after brain injury because it is essential for the removal of damaged tissue and the promotion of tissue remodeling [87]. However, following this acute microglial response to injury, several recent studies have shown that microglia can maintain a primed, or proinflammatory profile for weeks to months after the acute effects of injury have dissipated [88]. It is surmised that this primed and possibly hyperreactive microglial phenotype can potentially set the stage for more progressive degenerative change and chronic patient morbidity, along with an increased vulnerability to subsequent insult.

Continuous activation of microglia causes the release of CCL2 with consequent infiltration of peripherally derived macrophages via the CCL2-CCR2 signaling [75, 89]. In mice the chemokine receptor-2 (CCR2) is homogeneously expressed on monocytes and on 2–15% of T cells, closely resembling the expression pattern in humans. Monocytes, which are members of the myeloid cell lineage, infiltrate the brain after TBI, and contribute to the chronic inflammatory reaction that accompanies traumatic brain injury [89]. In human studies, accumulation of macrophages was observed in the brain of TBI survivors years after injury [90, 91]. Brain infiltrated monocytes are also important mediators of innate immune function since they differentiate into tissue macrophages and become microglia-like. Interestingly, CCR2 deletion, which reduces macrophages infiltration to the brain, diminished lesion cavity volume and lessened axonal damage after mild TBI [92]. Notably, preventing infiltration of peripherally derived macrophages

to the brain can significantly modify the acute and chronic inflammatory response to trauma and prevent the development of cognitive deficits [93].

Neuroinflammation is seen in multiple animal models of TBI such as concussive injury, lasting from a month to over a year [94, 95]. In some cases, the degree of the inflammatory response has been found to be predictive of clinical outcome and has been associated with neurodegeneration and cognitive decline. We have shown that neuroinflammation alters the expression of molecules required for synaptic function, which ultimately causes measurable cognitive deficits. Therefore, changes in structural plasticity of dendritic spines may be the missing link between neuroinflammation and cognitive decline following brain injury. Latent and persistent cognitive deficits associated with concussion have been linked to altered synaptic functions. Yet no studies to date have directly linked concussion-induced cognitive changes to structurally based mechanisms.

Behavioral and cognitive outcomes after TBI

Cognitive function refers to the process of acquiring knowledge and understanding through thought, experience, and senses. It encompasses a variety of modalities, including learning, memory and working memory, attention, reasoning, problem solving, decision-making, comprehension, and production of language. Cognitive processes use existing knowledge and generate new knowledge. Cognitive dysfunction is a prominent outcome after TBI, including in planning, problem solving, temporal organization, attention, cognitive-behavioral and psychobehavioral impairment [28, 96, 97]. Persistent deficits in memory and executive function after TBI is also

common [8, 96]. For example, retrograde amnesia persists in patients who survive TBI, similar to cognitive deficits often associated with TBI [97]. Survivors of severe TBI often have cognitive control functions impairments [11, 47].

Integrated stress response in TBI

The ISR is an evolutionary conserved intracellular signaling network that responds to a variable environment to maintain homeostasis [98]. The central regulatory step of the ISR lies on the phosphorylation of a single serine on the α subunit of the eukaryotic translation initiation factor eIF2 [99-101]. Phosphorylation of eIF2 α leads to a reduction in global protein translation but paradoxically also, to the translational up-regulation of a select subset of mRNAs such as activating transcription factor 4 (ATF4) [102]. Phosphorylation of eIF2α is driven upstream by four kinases: HRI (heme-regulated inhibitor), PKR (double-stranded RNA-dependent protein kinase), PERK (PKR-like ER kinase), and GCN2 (General amino acid control nonderepressible 2) [103]. PKR, PERK, and GCN2 are known to be expressed in the mammalian brain. Previously, our group and others have identified that both focal and diffuse head injuries induce phosphorylation of eIF2a in the brain chronically after injury [104, 105]. Brief interference of this pathway using the small-molecule inhibitor ISRIB after insult completely rescued trauma-induced cognitive and behavioral deficits.

Sex differences in TBI

There is growing recognition that an individual's biological sex influences health and disease and consequently the response to treatment. The influence of biological

sex on the outcome of TBI remains poorly understood, with several analyses having contradictory results, possibly due to the relatively small number of women and girls in clinical studies and lack of information on hormonal status and biological sex [43, 106]. Reports show within a given population sample that males do better on some outcome measures (severity in injury, mortality) and females do better on others (fewer complications, better prognosis, suggesting that the role of biological sex in TBI is multifaceted and needs to be further studied [107]. Our group has identified a sex-dimorphic response to mild traumatic brain injury (concussive injury) as measured by lack of cognitive and behavioral impairments [105].

Summary

The following chapters offer different components essential to understanding TBI pathophysiology to inform the development of possible targets of treatment for TBI patients using the CHI and rTBI model in mice. In **Chapter 2**, we investigate the effect of a small-molecule modulator of the ISR (ISRIB) on TBI-induced neuronal structural and cognitive dysfunction following concussive brain injury. Animal studies have demonstrated a cascade of physiological events that adversely affect brain function for a period of days to weeks after a concussive injury. In human studies, clinical signs and symptoms of impaired coordination, attention, memory, and cognition are manifestations of underlying physiological dysfunction. However, little is known about the underlying cellular correlates responsible for these maladaptive changes, particularly at chronic time-points. We find that after concussive injury there is an increase in the ratio of new spines formed and the number of new spines formed per

imaging session. Importantly the newly formed spines are transient, as indicated by the decreased survival ratio, suggestive of a maladaptive response that does not result in functional spines. Targeting the ISR using the small-molecule inhibitor ISRIB reverses the changes in cortical spine dynamics and the short-term memory dysfunction. Importantly these restorative effects are maintained weeks after treatment is ended. This is novel because we identify a structural mechanism for cognitive impairments after traumatic brain injury that are rapidly and persistently reversed by ISR inhibition, representing a key target in maladaptive functions after injury. In **Chapter 3** we investigate the role of ISR activation in behavioral changes and associated neuronal dysfunction after rTBI. A majority of studies report poorer cognitive and behavioral outcomes in individuals following multiple mild head traumas [42]. Despite the increased interest in understanding the long-term consequences of rTBI, little is known about the underlying cellular and functional correlates responsible for these maladaptive behavioral and cognitive changes. We find that rTBI leads to a sex-dependent increase in long-lasting risk-taking behavior in male mice associated with synaptic hyperexcitability. Notably, ISRIB administration post injury completely reversed rTBI-induced deficits. This is novel because for the first time we identified that inhibition of the ISR with ISRIB rescues a behavioral deficit and the associated cell-specific vulnerability, suggesting that this pathway may represent a key target in maladaptive circuit and cognitive functions after injury. In **Chapter 4** we explore the involvement of the ISR in age-related cognitive decline. While often discussed in the context of disease, decreases in executive and cognitive function declines in older, healthy individuals are common [108]. According to the US Department of Commerce the aging

population is estimated to reach 83.7 million individuals above 65 years of age in the US by 2050; this represents a rapidly growing healthcare and economic concern. We find that ISR inhibition by ISRIB modifies age-induced neuronal, immune, and cognitive dysfunction. This is novel given that pharmacological attenuation of the ISR can alleviate age-related neuronal and immune changes potentially resetting age-induced cognitive decline. In **Chapter 5** we investigate the effect of concussive brain injury on the response of whole-brain irradiated mice bearing brain engrafted microglia (repopulated after microglia depletion). In the clinic, cancer patients are likely to experience a secondary insult such as a head trauma after having received whole-brain radiotherapy (WBRT). Therefore, it is important to understand the therapeutic potential of microglia depletion and repopulation. We find that a transcriptional and functional reset of immune cells in the brain to an inactive state spares the brain from irradiation-induced deficits and protects against concussive brain injury induced deficits. This is novel because the replacement of depleted microglia pool by peripheral monocyte-derived BEMs represents a potent treatment for irradiation-induced deficits even after a concussive brain injury.

References

1. Flanagan, S.R., *Invited Commentary on "Centers for Disease Control and Prevention Report to Congress: Traumatic Brain Injury in the United States: Epidemiology and Rehabilitation".* Arch Phys Med Rehabil, 2015. **96**(10): p. 1753-5.

2. Miller, G.F., L. DePadilla, and L. Xu, *Costs of Nonfatal Traumatic Brain Injury in the United States, 2016.* Med Care, 2021. **59**(5): p. 451-455.

3. Fleminger, S., et al., *Head injury as a risk factor for Alzheimer's disease: the evidence 10 years on; a partial replication.* J Neurol Neurosurg Psychiatry, 2003. **74**(7): p. 857-62.

4. Sivanandam, T.M. and M.K. Thakur, *Traumatic brain injury: a risk factor for Alzheimer's disease.* Neurosci Biobehav Rev, 2012. **36**(5): p. 1376-81.

5. Cole, J.H., et al., *Prediction of brain age suggests accelerated atrophy after traumatic brain injury.* Ann Neurol, 2015. **77**(4): p. 571-81.

6. Li, Y., et al., *Head Injury as a Risk Factor for Dementia and Alzheimer's Disease: A Systematic Review and Meta-Analysis of 32 Observational Studies.* PLoS One, 2017. **12**(1): p. e0169650.

7. Masel, B.E. and D.S. DeWitt, *Traumatic brain injury: a disease process, not an event.* J Neurotrauma, 2010. **27**(8): p. 1529-40.

8. Broglio, S.P., et al., *Cognitive decline and aging: the role of concussive and subconcussive impacts.* Exerc Sport Sci Rev, 2012. **40**(3): p. 138-44.

9.   Barnes, D.E., et al., *Association of Mild Traumatic Brain Injury With and Without Loss of Consciousness With Dementia in US Military Veterans.* JAMA Neurol, 2018. **75**(9): p. 1055-1061.

10.   Majdan, M., et al., *Severity and outcome of traumatic brain injuries (TBI) with different causes of injury.* Brain Inj, 2011. **25**(9): p. 797-805.

11.   Faul, M. and V. Coronado, *Epidemiology of traumatic brain injury.* Handb Clin Neurol, 2015. **127**: p. 3-13.

12.   Kaur, P. and S. Sharma, *Recent Advances in Pathophysiology of Traumatic Brain Injury.* Curr Neuropharmacol, 2018. **16**(8): p. 1224-1238.

13.   Butcher, I., et al., *Prognostic value of cause of injury in traumatic brain injury: results from the IMPACT study.* J Neurotrauma, 2007. **24**(2): p. 281-6.

14.   Saatman, K.E., et al., *Classification of traumatic brain injury for targeted therapies.* J Neurotrauma, 2008. **25**(7): p. 719-38.

15.   Andriessen, T.M., B. Jacobs, and P.E. Vos, *Clinical characteristics and pathophysiological mechanisms of focal and diffuse traumatic brain injury.* J Cell Mol Med, 2010. **14**(10): p. 2381-92.

16.   Stocker, R.A., *Intensive Care in Traumatic Brain Injury Including Multi-Modal Monitoring and Neuroprotection.* Med Sci (Basel), 2019. **7**(3).

17.   Riggio, S. and M. Wong, *Neurobehavioral sequelae of traumatic brain injury.* Mt Sinai J Med, 2009. **76**(2): p. 163-72.

18.   Vink, R. and A.J. Nimmo, *Multifunctional drugs for head injury.* Neurotherapeutics, 2009. **6**(1): p. 28-42.

19.   Margulies, S., et al., *Combination Therapies for Traumatic Brain Injury: Retrospective Considerations.* J Neurotrauma, 2016. **33**(1): p. 101-12.

20.   Ng, S.Y. and A.Y.W. Lee, *Traumatic Brain Injuries: Pathophysiology and Potential Therapeutic Targets.* Front Cell Neurosci, 2019. **13**: p. 528.

21.   DeWitt, D.S., et al., *Pre-Clinical Testing of Therapies for Traumatic Brain Injury.* J Neurotrauma, 2018. **35**(23): p. 2737-2754.

22.   Bergold, P.J., *Treatment of traumatic brain injury with anti-inflammatory drugs.* Exp Neurol, 2016. **275 Pt 3**: p. 367-380.

23.   DiSabato, D.J., N. Quan, and J.P. Godbout, *Neuroinflammation: the devil is in the details.* J Neurochem, 2016. **139 Suppl 2**: p. 136-153.

24.   Meaney, D.F., B. Morrison, and C. Dale Bass, *The mechanics of traumatic brain injury: a review of what we know and what we need to know for reducing its societal burden.* J Biomech Eng, 2014. **136**(2): p. 021008.

25.   Loane, D.J., B.A. Stoica, and A.I. Faden, *Neuroprotection for traumatic brain injury.* Handb Clin Neurol, 2015. **127**: p. 343-66.

26.   Xiong, Y., A. Mahmood, and M. Chopp, *Animal models of traumatic brain injury.* Nat Rev Neurosci, 2013. **14**(2): p. 128-42.

27.   Ziebell, J.M. and M.C. Morganti-Kossmann, *Involvement of pro- and anti-inflammatory cytokines and chemokines in the pathophysiology of traumatic brain injury.* Neurotherapeutics, 2010. **7**(1): p. 22-30.

28.   Bramlett, H.M. and W.D. Dietrich, *Long-Term Consequences of Traumatic Brain Injury: Current Status of Potential Mechanisms of Injury and Neurological Outcomes.* J Neurotrauma, 2015. **32**(23): p. 1834-48.

29.   Akamatsu, Y. and K.A. Hanafy, *Cell Death and Recovery in Traumatic Brain Injury.* Neurotherapeutics, 2020. **17**(2): p. 446-456.

30.   Bodnar, C.N., et al., *A Systematic Review of Closed Head Injury Models of Mild Traumatic Brain Injury in Mice and Rats.* J Neurotrauma, 2019. **36**(11): p. 1683-1706.

31.   Nyanzu, M., et al., *Improving on Laboratory Traumatic Brain Injury Models to Achieve Better Results.* Int J Med Sci, 2017. **14**(5): p. 494-505.

32.   Dewan, M.C., et al., *Estimating the global incidence of traumatic brain injury.* J Neurosurg, 2018: p. 1-18.

33.   Prince, C. and M.E. Bruhns, *Evaluation and Treatment of Mild Traumatic Brain Injury: The Role of Neuropsychology.* Brain Sci, 2017. **7**(8).

34.   *StatPearls*. 2021.

35.   McNamara, E.H., et al., *The closed-head impact model of engineered rotational acceleration (CHIMERA) as an application for traumatic brain injury pre-clinical research: A status report.* Exp Neurol, 2020. **333**: p. 113409.

36.   Lee, B. and A. Newberg, *Neuroimaging in traumatic brain imaging.* NeuroRx, 2005. **2**(2): p. 372-83.

37.   Toledo, E., et al., *The young brain and concussion: imaging as a biomarker for diagnosis and prognosis.* Neurosci Biobehav Rev, 2012. **36**(6): p. 1510-31.

38.   Giza, C.C., et al., *Summary of evidence-based guideline update: evaluation and management of concussion in sports: report of the Guideline Development Subcommittee of the American Academy of Neurology.* Neurology, 2013. **80**(24): p. 2250-7.

39.   Belanger, H.G., et al., *Recent neuroimaging techniques in mild traumatic brain injury.* J Neuropsychiatry Clin Neurosci, 2007. **19**(1): p. 5-20.

40.   Giza, C.C. and D.A. Hovda, *The Neurometabolic Cascade of Concussion.* J Athl Train, 2001. **36**(3): p. 228-235.

41.   Bachstetter, A.D., et al., *Attenuation of traumatic brain injury-induced cognitive impairment in mice by targeting increased cytokine levels with a small molecule experimental therapeutic.* J Neuroinflammation, 2015. **12**: p. 69.

42.   McAllister, T. and M. McCrea, *Long-Term Cognitive and Neuropsychiatric Consequences of Repetitive Concussion and Head-Impact Exposure.* J Athl Train, 2017. **52**(3): p. 309-317.

43.   Lasry, O., et al., *Epidemiology of recurrent traumatic brain injury in the general population: A systematic review.* Neurology, 2017. **89**(21): p. 2198-2209.

44.   Belanger, H.G., E. Spiegel, and R.D. Vanderploeg, *Neuropsychological performance following a history of multiple self-reported concussions: a meta-analysis.* J Int Neuropsychol Soc, 2010. **16**(2): p. 262-7.

45.   Geddes, J.F., et al., *Neuronal cytoskeletal changes are an early consequence of repetitive head injury.* Acta Neuropathol, 1999. **98**(2): p. 171-8.

46.   DeKosky, S.T., M.D. Ikonomovic, and S. Gandy, *Traumatic brain injury: football, warfare, and long-term effects.* Minn Med, 2010. **93**(12): p. 46-7.

47.   Engberg, A.W. and T.W. Teasdale, *Psychosocial outcome following traumatic brain injury in adults: a long-term population-based follow-up.* Brain Inj, 2004. **18**(6): p. 533-45.

48. Nelson, L.D., et al., *Recovery After Mild Traumatic Brain Injury in Patients Presenting to US Level I Trauma Centers: A Transforming Research and Clinical Knowledge in Traumatic Brain Injury (TRACK-TBI) Study.* JAMA Neurol, 2019. **76**(9): p. 1049-1059.

49. Guskiewicz, K.M., et al., *Association between recurrent concussion and late-life cognitive impairment in retired professional football players.* Neurosurgery, 2005. **57**(4): p. 719-26; discussion 719-26.

50. Amaral, M.D. and L. Pozzo-Miller, *The dynamics of excitatory synapse formation on dendritic spines.* Cellscience, 2009. **5**(4): p. 19-25.

51. Bailey, C.H., E.R. Kandel, and K.M. Harris, *Structural Components of Synaptic Plasticity and Memory Consolidation.* Cold Spring Harb Perspect Biol, 2015. **7**(7): p. a021758.

52. Citri, A. and R.C. Malenka, *Synaptic plasticity: multiple forms, functions, and mechanisms.* Neuropsychopharmacology, 2008. **33**(1): p. 18-41.

53. Gipson, C.D. and M.F. Olive, *Structural and functional plasticity of dendritic spines - root or result of behavior?* Genes Brain Behav, 2017. **16**(1): p. 101-117.

54. Richter, J.D. and E. Klann, *Making synaptic plasticity and memory last: mechanisms of translational regulation.* Genes Dev, 2009. **23**(1): p. 1-11.

55. Yuste, R. and T. Bonhoeffer, *Morphological changes in dendritic spines associated with long-term synaptic plasticity.* Annu Rev Neurosci, 2001. **24**: p. 1071-89.

56. Nimchinsky, E.A., B.L. Sabatini, and K. Svoboda, *Structure and function of dendritic spines.* Annu Rev Physiol, 2002. **64**: p. 313-53.

57.   Berry, K.P. and E. Nedivi, *Spine Dynamics: Are They All the Same?* Neuron, 2017. **96**(1): p. 43-55.

58.   Bosch, M. and Y. Hayashi, *Structural plasticity of dendritic spines.* Curr Opin Neurobiol, 2012. **22**(3): p. 383-8.

59.   Kasai, H., et al., *Spine dynamics in the brain, mental disorders and artificial neural networks.* Nat Rev Neurosci, 2021. **22**(7): p. 407-422.

60.   Koleske, A.J., *Molecular mechanisms of dendrite stability.* Nat Rev Neurosci, 2013. **14**(8): p. 536-50.

61.   Chen, C.C., J. Lu, and Y. Zuo, *Spatiotemporal dynamics of dendritic spines in the living brain.* Front Neuroanat, 2014. **8**: p. 28.

62.   Grutzendler, J., N. Kasthuri, and W.B. Gan, *Long-term dendritic spine stability in the adult cortex.* Nature, 2002. **420**(6917): p. 812-6.

63.   Holtmaat, A.J., et al., *Transient and persistent dendritic spines in the neocortex in vivo.* Neuron, 2005. **45**(2): p. 279-91.

64.   Winston, C.N., et al., *Dendritic Spine Loss and Chronic White Matter Inflammation in a Mouse Model of Highly Repetitive Head Trauma.* Am J Pathol, 2016. **186**(3): p. 552-67.

65.   Campbell, J.N., D. Register, and S.B. Churn, *Traumatic brain injury causes an FK506-sensitive loss and an overgrowth of dendritic spines in rat forebrain.* J Neurotrauma, 2012. **29**(2): p. 201-17.

66.   Zhao, J., et al., *Mild Traumatic Brain Injury Reduces Spine Density of Projection Neurons in the Medial Prefrontal Cortex and Impairs Extinction of Contextual Fear Memory.* J Neurotrauma, 2018. **35**(1): p. 149-156.

67.   Bourne, J. and K.M. Harris, *Do thin spines learn to be mushroom spines that remember?* Curr Opin Neurobiol, 2007. **17**(3): p. 381-6.

68.   Ghani, M.U., et al., *Dendritic spine classification using shape and appearance features based on two-photon microscopy.* J Neurosci Methods, 2017. **279**: p. 13-21.

69.   Sala, C. and M. Segal, *Dendritic spines: the locus of structural and functional plasticity.* Physiol Rev, 2014. **94**(1): p. 141-88.

70.   Buttram, S.D., et al., *Multiplex assessment of cytokine and chemokine levels in cerebrospinal fluid following severe pediatric traumatic brain injury: effects of moderate hypothermia.* J Neurotrauma, 2007. **24**(11): p. 1707-17.

71.   Frugier, T., et al., *In situ detection of inflammatory mediators in post mortem human brain tissue after traumatic injury.* J Neurotrauma, 2010. **27**(3): p. 497-507.

72.   Goodman, J.C., et al., *Pro-inflammatory and pro-apoptotic elements of the neuroinflammatory response are activated in traumatic brain injury.* Acta Neurochir Suppl, 2008. **102**: p. 437-9.

73.   Ahn, M.J., et al., *The effects of traumatic brain injury on cerebral blood flow and brain tissue nitric oxide levels and cytokine expression.* J Neurotrauma, 2004. **21**(10): p. 1431-42.

74.   Lotocki, G., et al., *Alterations in blood-brain barrier permeability to large and small molecules and leukocyte accumulation after traumatic brain injury: effects of post-traumatic hypothermia.* J Neurotrauma, 2009. **26**(7): p. 1123-34.

75.   Semple, B.D., et al., *Role of CCL2 (MCP-1) in traumatic brain injury (TBI): evidence from severe TBI patients and CCL2-/- mice.* J Cereb Blood Flow Metab, 2010. **30**(4): p. 769-82.

76.   Sofroniew, M.V. and H.V. Vinters, *Astrocytes: biology and pathology.* Acta Neuropathol, 2010. **119**(1): p. 7-35.

77.   Sofroniew, M.V., *Astrocyte Reactivity: Subtypes, States, and Functions in CNS Innate Immunity.* Trends Immunol, 2020. **41**(9): p. 758-770.

78.   Linnerbauer, M., M.A. Wheeler, and F.J. Quintana, *Astrocyte Crosstalk in CNS Inflammation.* Neuron, 2020. **108**(4): p. 608-622.

79.   Burda, J.E., A.M. Bernstein, and M.V. Sofroniew, *Astrocyte roles in traumatic brain injury.* Exp Neurol, 2016. **275 Pt 3**: p. 305-315.

80.   Karve, I.P., J.M. Taylor, and P.J. Crack, *The contribution of astrocytes and microglia to traumatic brain injury.* Br J Pharmacol, 2016. **173**(4): p. 692-702.

81.   Early, A.N., et al., *Effects of advanced age upon astrocyte-specific responses to acute traumatic brain injury in mice.* J Neuroinflammation, 2020. **17**(1): p. 115.

82.   Shandra, O., et al., *Repetitive Diffuse Mild Traumatic Brain Injury Causes an Atypical Astrocyte Response and Spontaneous Recurrent Seizures.* J Neurosci, 2019. **39**(10): p. 1944-1963.

83.   Guttenplan, K.A., et al., *Neurotoxic reactive astrocytes induce cell death via saturated lipids.* Nature, 2021. **599**(7883): p. 102-107.

84.   Liddelow, S.A., et al., *Neurotoxic reactive astrocytes are induced by activated microglia.* Nature, 2017. **541**(7638): p. 481-487.

85.   Donat, C.K., et al., *Microglial Activation in Traumatic Brain Injury.* Front Aging

Neurosci, 2017. **9**: p. 208.

86.   Loane, D.J., et al., *Progressive neurodegeneration after experimental brain

trauma: association with chronic microglial activation.* J Neuropathol Exp Neurol,

2014. **73**(1): p. 14-29.

87.   d'Avila, J.C., et al., *Microglial activation induced by brain trauma is suppressed

by post-injury treatment with a PARP inhibitor.* J Neuroinflammation, 2012. **9**: p.

31.

88.   Witcher, K.G., D.S. Eiferman, and J.P. Godbout, *Priming the inflammatory pump

of the CNS after traumatic brain injury.* Trends Neurosci, 2015. **38**(10): p. 609-

620.

89.   Hsieh, C.L., et al., *Traumatic brain injury induces macrophage subsets in the

brain.* Eur J Immunol, 2013. **43**(8): p. 2010-22.

90.   Johnson, V.E., et al., *Inflammation and white matter degeneration persist for

years after a single traumatic brain injury.* Brain, 2013. **136**(Pt 1): p. 28-42.

91.   Gentleman, S.M., et al., *Long-term intracerebral inflammatory response after

traumatic brain injury.* Forensic Sci Int, 2004. **146**(2-3): p. 97-104.

92.   Hsieh, C.L., et al., *CCR2 deficiency impairs macrophage infiltration and improves

cognitive function after traumatic brain injury.* J Neurotrauma, 2014. **31**(20): p.

1677-88.

93.   Morganti, J.M., et al., *CCR2 antagonism alters brain macrophage polarization

and ameliorates cognitive dysfunction induced by traumatic brain injury.* J

Neurosci, 2015. **35**(2): p. 748-60.

94.   Chiu, C.C., et al., *Neuroinflammation in animal models of traumatic brain injury.* J Neurosci Methods, 2016. **272**: p. 38-49.

95.   Simon, D.W., et al., *The far-reaching scope of neuroinflammation after traumatic brain injury.* Nat Rev Neurol, 2017. **13**(3): p. 171-191.

96.   Rabinowitz, A.R. and H.S. Levin, *Cognitive sequelae of traumatic brain injury.* Psychiatr Clin North Am, 2014. **37**(1): p. 1-11.

97.   Sun, H., et al., *Assessment of cognitive dysfunction in traumatic brain injury patients: a review.* Forensic Sci Res, 2017. **2**(4): p. 174-179.

98.   Costa-Mattioli, M. and P. Walter, *The integrated stress response: From mechanism to disease.* Science, 2020. **368**(6489).

99.   Bond, S., et al., *The Integrated Stress Response and Phosphorylated Eukaryotic Initiation Factor 2α in Neurodegeneration.* J Neuropathol Exp Neurol, 2020. **79**(2): p. 123-143.

100.   Costa-Mattioli, M., et al., *eIF2alpha phosphorylation bidirectionally regulates the switch from short- to long-term synaptic plasticity and memory.* Cell, 2007. **129**(1): p. 195-206.

101.   Pavitt, G.D., *Regulation of translation initiation factor eIF2B at the hub of the integrated stress response.* Wiley Interdiscip Rev RNA, 2018. **9**(6): p. e1491.

102.   Chen, A., et al., *Inducible enhancement of memory storage and synaptic plasticity in transgenic mice expressing an inhibitor of ATF4 (CREB-2) and C/EBP proteins.* Neuron, 2003. **39**(4): p. 655-69.

103.   Donnelly, N., et al., *The eIF2α kinases: their structures and functions.* Cell Mol Life Sci, 2013. **70**(19): p. 3493-511.

104. Chou, A., et al., *Inhibition of the integrated stress response reverses cognitive deficits after traumatic brain injury.* Proc Natl Acad Sci U S A, 2017. **114**(31): p. E6420-E6426.

105. Krukowski, K., et al., *Integrated Stress Response Inhibitor Reverses Sex-Dependent Behavioral and Cell-Specific Deficits after Mild Repetitive Head Trauma.* J Neurotrauma, 2020. **37**(11): p. 1370-1380.

106. Gupte, R., et al., *Sex Differences in Traumatic Brain Injury: What We Know and What We Should Know.* J Neurotrauma, 2019. **36**(22): p. 3063-3091.

107. Biegon, A., *Considering Biological Sex in Traumatic Brain Injury.* Front Neurol, 2021. **12**: p. 576366.

108. Cepeda, N.J., A.F. Kramer, and J.C. Gonzalez de Sather, *Changes in executive control across the life span: examination of task-switching performance.* Dev Psychol, 2001. **37**(5): p. 715-30.

CHAPTER 2: In vivo two-photon imaging after concussive injury reveals aberrant cortical spine dynamics that are reversed by integrated stress response inhibition

Abstract

Traumatic brain injury (TBI) is a leading cause of long-term neurological disability in the world and the strongest environmental risk factor for the development of dementia. Even mild TBI (concussive injury) is associated with a >2-fold increase in the risk of dementia diagnosis. The pathophysiology of TBI is very complex, and little is known about the cellular mechanisms responsible for the development of cognitive deficits after injury. It has been demonstrated that the integrated stress response (ISR), a conserved pathway involved in cellular response to stress, is activated after TBI and inhibition of the ISR weeks after the insult can reverse behavioral and cognitive deficits. However, the cellular mechanisms by which ISR inhibition restores cognition are unknown. Here we used longitudinal two-photon imaging in vivo after concussive injury to study spine dynamics in the parietal cortex, a brain region involved in working memory, specifically short-term memory. Concussive injury altered spine dynamics and density measured up to a month after injury. Strikingly, brief pharmacological treatment with the drug-like small-molecule ISR inhibitor ISRIB reversed the neuronal structural changes measured in the parietal cortex and the associated short-term memory deficits. These findings suggest that both neural and cognitive consequences of concussive injury are mediated in part by activation of the ISR and may be ameliorated by its inhibition.

Introduction

Traumatic brain injury (TBI) is defined as the disruption of normal brain function from an impact (a bump, blow, or jolt) to the head that produces direct damage from mechanical forces and indirect damage from secondary responses. Between 1.5 – 3.8 million people experience a traumatic brain injury each year in the United States and at least 75% of these injuries are a mild TBI (concussive injuries without loss of consciousness) [1]. TBI is a growing health concern due to chronic behavioral and cognitive impairments that affect the quality of life of millions of individuals [2-6]. While pre-clinical experimental studies of TBI are steadily increasing, little is known about the specific changes in brain cells that are associated with and may be responsible for the persistent maladaptive cognitive changes that develop after concussive injury. With no identified mechanisms, there are no treatments to prevent or mitigate deficits resulting from TBI.

The closed head injury (CHI) mouse model for mild TBI produces cognitive deficits similar to those observed after concussive injuries in humans, such as working memory dysfunction [7-9]. A type of working memory, known as short-term memory, is dependent on multiple cortical regions including prefrontal cortex, frontal lobe, and parietal lobe [10-13]. Short-term memory (and all other types of memory) is thought to be encoded in connections among neurons at sites referred to as synapses [14-16]. Most excitatory synapses onto excitatory neurons in the brain are made onto dendritic spines, which are specialized protuberances that contain the receptors for neurotransmitters [17-20]. Different types of cortical neurons have between 100 and a few thousand dendritic spines. Memory function depends on synaptic plasticity, the

capacity of synapses to undergo lasting biochemical and morphological changes in strength in response to neuronal activity and neuromodulators. Moreover, changes in synaptic plasticity are associated with lasting changes in the structure of dendritic spines (structural plasticity) [21-26].

Dendritic spines are composed of a spine head connected to the dendritic shaft by a spine neck [27, 28]. Functional synapses require dendritic spines to have a bulbous spine head, as they harbor neurotransmitter receptors, intracellular signaling molecules, ribosomes that mediate local protein synthesis, and a highly active cytoskeleton meshwork [29-31]. Spine necks are diffusional barriers that are thought to filter the electrical component of synaptic signals and amplify spine head depolarization, as well as to limit the diffusion of intracellular messengers from the spine head into the dendrite [32, 33].

Dendritic spines are part of a dynamic network that has captured the attention of neuroscientists for over 100 years because they are the element of synaptic connectivity that are visible in the light microscope. They are characterized by their dynamics, their density, and their morphology. Spine dynamics describes their structural changes, observed by the formation and elimination of spines. While dendritic spines may be stable for months to years, structural plasticity of dendritic spines (taking place over hours or days) is thought to be important for the development and proper function of the CNS [29, 34]. Spine density is calculated as the number of spines per measured length of dendrite. The density of spines can be used as a measure of the total synaptic strength received by a dendrite [27]. Spine morphology describes the shape and size of dendritic spines [35]. The regulation of each of these factors is thought to be essential

29

for stable synaptic maintenance and transmission and thus cognitive and executive function, such as short-term memory [25].

The pioneering work from Lendvai et al, Gruzendler et al., Trachtenberg et al., and Holtmaat et al in the early 2000s demonstrated the possibility to track the same spine in the living brain over a long period of time using *in vivo* two-photon imaging [36-39]. From such time-lapse imaging studies, a new picture of spines began to emerge. Dendritic spines could be seen *in vivo* changing their shape and size (morphology), forming or disappearing across an animal's life span (dynamics), and being responsive to both the animal's experience and environment. Later studies have shown that spine morphology and dynamics vary among neuronal types and across developmental stages [18]. Moreover, the balance between spines forming or disappearing determines spine density. Currently, changes in spine morphology, dynamics, and density have become accepted markers for changes in synaptic strength or synaptic presence.

The integrated stress response (ISR) is a universal intracellular signaling network that responds to a variable environment to maintain homeostasis [40, 41]. Four specialized kinases (PERK, PRK, GCN2, and HRI) converge on the phosphorylation of a single serine on the α subunit of the translation initiation factor eIF2 [41, 42]. This central regulatory step leads to a reduction in global protein translation but paradoxically also, to the translational up-regulation of a select subset of mRNAs such as activating transcription factor 4 (ATF4) [43, 44]. The ISR maintains or reestablishes physiological homeostasis; however, chronic ISR activation creates maladaptive cellular and functional changes [45].

Previous work from our lab demonstrated that pharmacological inhibition of the ISR using the integrated stress response inhibitor (ISRIB) is sufficient to reverse LTP impairments as well as chronic cognitive and behavioral deficits in different rodent injury models [7, 8]. The cellular mechanisms by which ISR inhibition restores neuronal function, and ultimately cognitive function, remain unknown. In the current study, we used longitudinal *in vivo* two-photon imaging to reveal cortical spine dynamics after a single mild concussive closed head injury (CHI) and measured the effect of ISR inhibition after CHI on both spine dynamics and short-term memory function.

Results

Concussive injury alters cortical spine dynamics

The structural reorganization of dendritic spines (a process termed spine dynamics) is a cellular event essential for neuronal and cognitive function [46]. To determine the effect of concussive injury on spine dynamics and density, we performed longitudinal transcranial two-photon imaging *in vivo* using Thy1-YFP-H transgenic mice. In this transgenic mouse line, YFP is expressed in a small subset of layer V pyramidal neurons that extend their apical dendrites to layer I/II of the cortex [47]. We first subjected mice to a single mild concussive closed head injury (CHI, a reproducible and translational model for concussive injury) over a region including the parietal cortex or to sham surgery (exposing the skull without concussion). Eight days later we implanted a head fixation device and cranial window directly above the parietal cortex (encompassing the impacted region). To collect longitudinal data on dendritic spines, mice were imaged for four sessions over eight days (starting at day 11 post-CHI/sham

surgery) with the final imaging day on day 18 post-CHI or sham surgery (**Figure 1A**).

We used the longitudinal data to quantify spine dynamics, specifically i) spine formation (fraction of new spines), ii) spine elimination (fraction of pre-existing spines eliminated), iii) number of new spines formed per imaging session, iv) survival fraction of dendritic spine populations and spine density.

To perform CHI, animals were secured to a stereotaxic frame with non-traumatic ear bars. We surgically exposed the skull and induced a single bilateral closed-head impact injury with a pneumatic piston over the parietal cortex. Any animals that had a fractured skull after injury were excluded from the study. After impact, the scalp was sutured. Sham controls received the same surgery but without a TBI. This concussive injury produced no changes in neuronal numbers as measured by quantification of NeuN-positive neuronal nuclei in the cortex. There was, as expected, an increase in astrogliosis in the cortex after this injury, as measured by quantification of a glial fibrillary acidic protein (GFAP).

All measurements were made independently on each dendritic segment between 40 and 57 dendritic segments were imaged and measured in each of the 4-5 imaging sessions in all mice studied (**Figure 1B**). Spine formation (fraction of new spines/preexisting spines) was measured as the presence of a new spine in each subsequent imaging session that was not present in the first imaging session. Spine formation was determined by first quantifying the number of spines per dendrite on day 11 (first imaging session) and then identifying new spines present on day 13, 15, and 18 (subsequent imaging sessions) (**Figure 1C**). Spine elimination (fraction of preexisting spines eliminated/preexisting spines) was classified as a spine that was present in the

first imaging session but was not present in subsequent sessions. Spine elimination was determined by first quantifying the number of spines per dendrite on day 11 (first imaging session) and then identifying whether these spines were present on day 13, 15, and 18 (subsequent imaging sessions) (**Figure 1C**). In some cases, in which a spine appeared to be eliminated but reappeared in a subsequent session in the same location, that spine was counted as if it were a reappearance of the same spine. The number of new spines formed per imaging session was quantified by noting the number of new spines formed (first observed) at imaging day 13, 15, and 18. Survival fraction of dendritic spine populations was quantified by the presence or absence of the same dendritic spines over the four imaging sessions. Dendritic spines were classified as T_{11}, T_{13}, T_{15}, or T_{18} depending on which imaging day they were first observed. Spine density was calculated as the number of spines per micron of dendritic length. All protrusions from the dendrites were counted as spines regardless of morphology. We analyzed a total length of at least 3500 μm of dendrites and 200-600 spines per experimental group. For all of these measurements, multiple dendritic segments ranging between 50-100um (+/- 2 um) in length were analyzed per mouse and then averaged (**Figure 1B**). Analysis was done semi-automated and blinded to treatment and surgical condition. A detailed summary of the data sampling is listed in **Table 1**. As a control for our analysis that used the day 11 images as the baseline for comparisons, spine formation and elimination were also analyzed in reverse chronological order, using day 18 as the baseline imaging day.

At 13 days post injury, mice that received CHI showed a significant increase in the fraction of new spines as compared to mice that received sham surgery. This increase in fraction of new spines was sustained at each subsequent imaging session (**Figure 1D-F**). Sham mice maintained a 0.20 fraction of new spines, as expected [48]. There was a significant increase in the fraction of pre-existing spines eliminated observed at 13 days post injury (**Figure 1H-J**). These relationships were also observed in the reverse analysis using day 18 as the baseline imaging day indicating that any measured changes were not due to an analysis artifact or detectable phototoxicity. CHI mice had a significantly higher average number of new spines formed per imaging session compared to sham mice. This increase was present at each imaging session. (**Figure 2A-D**). Sham mice maintained an average of 1 new spine formed per imaging session. $T_{11, 13, 15}$ dendritic spines from CHI mice showed a decrease in survival ratio as compared to sham mice (**Figure 3 A-C**). There were no significant differences in spine density between groups; however, spine density was stable in sham mice, whereas mice that received CHI had more fluctuation over the four imaging sessions. Altogether, these data demonstrate first that concussive injury alters the fraction and number of new spines formed, and second that the new spines formed, independent of when they are first observed, are transient.

Inhibition of the ISR reverses the aberrant cortical spine dynamics measured after concussive injury

We next tested whether pharmacological blockage of the ISR using the drug-like small-molecule ISR inhibitor ISRIB could reset the maladaptive spine dynamics changes measured after concussive injury. We treated a cohort of mice with our established ISRIB treatment protocol of 4 consecutive intraperitoneal injections (2.5mg/kg) starting day 14 post-surgery. Mice that did not receive ISRIB treatment received vehicle injections instead. ISRIB concentration in the brain were consistent with earlier findings (Supplemental Figure). ISRIB treatment reversed the concussive injury-induced increase in fraction of new spines back to sham levels. This effect was observed a day after the first injection and was maintained through the last injection (**Figure 1D-F**). Importantly, there was no effect of ISRIB treatment on mice that received sham surgery and no significant treatment effect on the fraction of pre-existing spines eliminated (**Figure 1H-J**). These relationships were also observed in the reverse analysis using day 18 as the baseline imaging day. ISR inhibition also normalized the average number of new spines formed. The increase caused by CHI in the average number of new spines formed occurred prior to ISRIB treatment and decreased to sham levels during and after treatment (**Figure 2A-D**) in the injured animals. We also measured the effect of ISR inhibition on the survival of T_{11}, T_{13}, T_{15}, and T_{18} dendritic spines. ISRIB treatment altered the survival ratio of the spine populations similarly to untreated injured mice (**Figure 3 A-C**). While there were no significant differences in spine density between groups, the spine density in CHI mice that had increased prior to treatment with ISRIB stabilized over the remainder of the imaging sessions (during

35

treatment). Altogether, these data demonstrate that ISRIB treatment specifically alters the modulation in the fraction and numbers of new spines formed during treatment, returning these measurements to sham levels, while not affecting spine dynamics and density in the absence of injury.

ISRIB effects on cortical spine dynamics are persistent after treatment was terminated

Given the effect of ISRIB treatment on spine dynamics during drug administration, we next sought to determine whether the effect persisted after treatment ended. Using a separate cohort of mice, we imaged for five sessions over 15 days starting at day 11 post-CHI or sham surgery, with the final imaging day on day 25 post-CHI/sham surgery (**Figure 1A**). ISRIB and Vehicle treatment were kept as previously described (**Figure 1A**). CHI mice had significantly increased fraction and number of new spines formed as compared to sham mice (**Figure 1G, Figure 2E**). CHI mice that received ISRIB treatment a week prior had a fraction of new spines comparable to sham levels (**Figure 1G**). There was a significant increase in the fraction of pre-existing spines eliminated observed at 25 days post injury (**Figure 1K**). The average number of new spines formed in the treatment groups remained comparable to sham levels and the survival of T_{11}, T_{13}, T_{15}, or T_{18} dendritic spines remained comparable to that of injured untreated mice (**Figure 2E, Figure 3**). There were no significant differences in spine density between groups however, spine density in CHI mice after ISRIB treatment ended remained unchanged. These results demonstrate that the effects of ISRIB treatment on spine dynamics and density persist after treatment has ended.

Concussive injury impairs short-term memory function

To understand potential functional consequences of the aberrant spine dynamics measured in the parietal cortex after concussive injury, we next carried out behavioral experiments to measure short-term memory, which is known to depend on proper parietal cortex function. We subjected mice to CHI as previously described and on day 18 post injury and measured their performance in the novel object recognition task (NORT) with a 5-minute retention interval. The NORT is a commonly used object recognition task to assay recognition memory, taking advantage of the mouse's innate preference for novelty [49]. The tool can be modified to examine short-term memory by having a retention interval of <1hr. Thus, the 5min NORT can be used to measure parietal cortex-dependent short-term memory function in rodents [49, 50]. Briefly, starting on day 16 post-injury, mice were individually habituated the measurement arena for 10 min per day for 2 days. On the third day, mice were exposed to two identical objects for 5 minutes (learning phase), and then temporarily removed for 5 min, during which time one of the objects was replaced with a novel object. Mice were then returned to the arena for 5 minutes to explore and interact with the objects (testing phase) (**Figure 4A**). We recorded the total interaction time with each object using automated tracking software and calculated a discrimination index (DI) from these times (DI= (Time spent with novel – time spent with familiar)/total time). The DI was used as a metric of short-term memory function, where a high DI score denotes discrimination, and a low DI score is indicative of impaired discrimination. As expected, sham mice distinguished between the novel and familiar object, as indicated by their average DI of 0.4. By contrast, CHI mice did not distinguish between the novel and familiar object

(**Figure 4B**), as indicated by their average DI of 0.1. These data indicate that CHI induces deficits in short-term memory in the brain region where we measured aberrant spine dynamics and density.

Inhibition of the ISR reverses short-term memory deficits measured after concussive injury

We next investigated whether ISRIB treatment could reverse the short-term memory deficit measured 18 days after CHI. A cohort of mice received 4 consecutive intraperitoneal injections (2.5mg/kg) (treatment protocol like that used for mice studied with two-photon imaging) starting at day 14 post injury, two days before the first training day (**Figure 4A**). Strikingly, ISRIB-treated CHI mice distinguished between the novel and familiar object as well as sham mice, while vehicle-treated CHI mice did not distinguish between the objects (**Figure 4B**). It is important to note that ISRIB had no effect on performance of sham animals. These results demonstrate that ISRIB treatment rescues concussive injury-induced short-term memory deficits, furthering a causative role of the ISR on memory dysfunction.

Rescue in short-term memory persists weeks after ISRIB treatment

Given the persistent effects of ISRIB treatment on recovering proper spine dynamics in the parietal cortex after treatment had ended, we next tested whether these structural changes were paralleled by persistent cognitive rescue. On experimental day 49 (32 days post ISRIB treatment and without additional ISRIB treatment), we measured short-term memory using the NORT with a 5-minute retention interval in the

same animal cohort studied above. To control for memory of the objects used previously, we used a different novel object comparable in novelty (**Figure 5A**). Vehicle-treated CHI mice were still unable to distinguish between the novel and familiar object, whereas CHI mice treated with ISRIB 32 days earlier discriminated as well as sham mice treated with vehicle or ISRIB (**Figure 5B**). These data demonstrate the effects of ISRIB administration on short-term memory deficits persist weeks after administration.

Concussive injury increases upstream modifiers of ISR activation

The regulatory step of the ISR lies in the phosphorylation of eIF2α by four kinases: HRI (heme-regulated inhibitor), PKR (double-stranded RNA-dependent protein kinase), PERK (PKR-like ER kinase), and GCN2 (General amino acid control nonderepressible 2). PKR, PERK, and GCN2 are known to be expressed in the mammalian brain. We previously demonstrated that the ISR is activated after CHI (and in other TBI models) [7, 8]. To understand upstream modifiers of ISR activation after concussive injury, we investigated the impact of CHI and ISRIB administration on the expression of the activating kinases. We measured PKR, PERK, and GCN2 protein levels in cortical lysate from a subset of behavior mice at 21 days after injury. There was a significant increase in activated GCN2 (as indicated by its phosphorylated form p-GCN2) after CHI. There was a statistically insignificant downward trend in activated GCN2 in CHI mice with ISRIB administration. A significant injury effect was measured on activated PERK (as indicated by its phosphorylated form p-PERK). There was no effect of injury or ISRIB administration on the phosphorylation status of PKR.

We next explored possible relationships between behavioral performance and ISR activation. Activated GCN2 protein level were negatively correlated with cognitive performance: mice with lower activated GCN2 protein level distinguished between the novel and familiar object. Activated PERK or PRK protein levels were not significantly correlated with cognitive performance.

Discussion

Using longitudinal *in vivo* two-photon imaging we provide the first line of evidence demonstrating that concussive injury induces aberrant spine dynamics in the parietal cortex that are functionally paralleled by impairments in short-term memory. After concussive injury there is an increase in spine formation and the number of new spines formed per imaging session. Importantly, the newly formed spines are transient, as indicated by the decreased survival ratio, suggestive of a maladaptive response that ultimately does not result in functional spines. Targeting the ISR reverses the changes in cortical spine dynamics and the short-term memory dysfunction. Importantly these restorative effects are maintained weeks after treatment is ended. The parallel between the present structural and behavioral findings in the direction and time course of CHI and ISRIB effects suggests that structural changes in dendritic spines may be a mechanism for the cognitive impairments after traumatic brain injury that is rapidly and persistently reversed by ISR inhibition.

Structural plasticity of dendritic spines is tightly coordinated with synaptic function and plasticity; for example, spine enlargement parallels long-term potentiation, whereas

long-term depression is associated with spine shrinkage [51]. Even subtle changes in dendritic spines have marked effects on synaptic function and plasticity and patterns of connectivity in neuronal circuits [20, 28]. Notably, disease-specific disruptions in dendritic spine dynamics, density, or morphology accompany many brain disorders, particularly those that involve deficits in cognitive function (information processing). In an animal model of Huntington's disease spine formation rate increases, but newly formed spines do not persist to be incorporated into the local circuitry [52]. In mice overexpressing MECP2, a Rett Syndrome related gene, it has been found that both spine formation and elimination are elevated, and new spines are more vulnerable to elimination than in wild type mice [53]. Cognitive dysfunction is a prominent outcome after TBI [6, 54]. Therefore, we investigated how trauma, specifically concussive injury, impacted spine dynamics. Here, we identified that concussive injury altered parietal cortex spine dynamics as measured by i) increased spine formation (fraction of new spines formed/preexisting spines), ii) increased number of new spines formed per imaging session, and ii) decreased survival fraction of T_{11}, T_{13}, T_{15}, and T_{18} dendritic spines. Altogether, these data are suggestive of a maladaptive response that results in the formation of transient spines; possibly serving as added noise in the circuit, hindering neuronal communication, or as a compensatory mechanism to maximize communication between neurons. Further investigation is needed to understand the mechanisms underlying the trauma-induced aberrant cortical spine dynamics. Moreover, whether this phenotype extends to other cortical regions responsible for cognitive function given that studies of cortical spine dynamics in healthy adult rodents have shown distinct dynamics and plasticity of apical dendrite spines on pyramidal

neurons in different cortical layers [18]. To our knowledge, this is the first study to use longitudinal *in vivo* two-photon imaging to reveal spine dynamics up to one month after concussive injury.

Spine imaging is typically done in the anesthetized mouse due to the importance of stability when imaging small structures at diffraction limited resolution. In the case of events that happen on the scale of days (average lifetime of newly formed spines being about 2 days), this is not unreasonable, since the time under anesthesia is short (~ 1 hr) as compared to the awake time between imaging sessions, with the changes mostly occurring when the animal is awake. Development of faster structural imaging approaches could facilitate molecular studies of spine dynamics by reducing imaging time so that anesthesia exposure is shortened, or imaging can be performed in the awake state.

Increasing evidence from animal studies demonstrate that TBI-induced functional deficits are closely related to damage to the cellular projections of neurons (including dendritic spines). These studies show an acute reduction in dendritic spine density (observed as early as 1hr and up to 1 week after injury) that is associated with impaired electrophysiological activity of neurons and cognitive function [55-59]. However, a majority of the previous work was done using i) focal brain injury models in rodents, ii) fixed brain tissues, and iii) at acute time-points (hrs to a couple weeks). Less is known about how dendritic spine density is altered acutely and chronically by concussive injuries and whether targeting these modifications opens a new avenue for treatment of concussive injury-induced dysfunctions. One study using a pneumatic piston to deliver a single mild traumatic brain injury in mice found an acute (1-24hrs after injury) steady

reduction in spine density of layer II/III pyramidal neurons within the parietal cortex that was followed by an increase in spine density (at 3 days after injury) [60]. Another study using a fluid percussion in jury in rats found an acute (at 24hrs after injury) reduction in spine density of layer II/III pyramidal neurons within the parietal cortex that returned to sham levels one week after injury [61]. Lastly, another group using a lateral fluid percussion injury in rats found a reduction in dendritic spine density of layer II/III and not layer V/VI pyramidal neurons within the medial prefrontal cortex measured at 1 month after injury that was associated with impairment of contextual fear memory extinction [62]. Here, we did not detect significant differences in spine density after concussive injury, however, spine density was stable in sham mice whereas CHI mice had more fluctuation over the four imaging sessions. Although the injury model, animal, mode of analysis, and time-point of measured spine density are different, the previously shown spontaneous rebound or subtle changes in dendritic spine density is also observed in our concussive injury mouse model. Moreover, our mode of analysis allowed for higher amount of sampling (measured over an 8 to 15 day period), with the goal of providing a better characterization of dendritic spine density after concussive injury.

Persistent deficits in memory and executive function after TBI are measured in both humans and animal models. Unlike moderate and severe TBI (focal injury), mild TBI (concussive or repetitive injuries) does not evoke tissue lesions or cavities in the brain. However, mTBI can lead to long-term cognitive difficulties. Much evidence indicates that synaptic and structural plasticity have been linked to memory function [20, 22, 25, 63]. Therefore, to understand the functional consequences of the aberrant spine dynamics measured in the parietal cortex after concussive injury, we measured short-

term memory function. Here, we found that concussive injury induced short-term memory deficits up to two months after injury.

The ISR is an evolutionary conserved intracellular signaling network that responds to a variable environment to maintain homeostasis [64]. The central regulatory step of the ISR lies on the phosphorylation of a single serine on the α subunit of the eukaryotic translation initiation factor eIF2 [64]. Phosphorylation of eIF2 α leads to a reduction in global protein translation but paradoxically also, to the translational up-regulation of a select subset of mRNAs such as activating transcription factor 4 (ATF4), a memory repressor gene [65, 66]. eIF2α phosphorylation is driven upstream by four kinases: HRI (heme-regulated inhibitor), PKR (double-stranded RNA-dependent protein kinase), PERK (PKR-like ER kinase), and GCN2 (General amino acid control nonderepressible 2) [67]. PKR, PERK, and GCN2 are known to be expressed in the mammalian brain. Our group and others have identified that both focal and diffuse head injuries and various neurodegenerative diseases induce phosphorylation of eIF2a in the brain [7, 8, 68-73]. After trauma, brief interference of this pathway using the small-molecule inhibitor ISRIB completely rescued trauma-induced cognitive and behavioral deficits and neuronal correlates [7, 8]. However, the mechanisms by which ISR inhibition restores cognition are unknown [74]. Here, we identified that targeting the ISR rapidly and persistently reversed the aberrant changes in cortical spine dynamics observed after concussive injury and rescued the short-term memory dysfunction. These findings further strengthen the link between ISR and memory function to the level of neuronal structure. Further investigation is needed to understand the mechanisms

underlying ISR modulation of spine dynamics and whether this phenomenon extends to other neuronal populations.

The influence of biological sex on the outcome of TBI remains poorly understood, despite TBI occurrence being sex-independent [75, 76]. Our group has identified a sex-dimorphic response to mild traumatic brain injury (concussive injury) as measured by lack of cognitive and behavioral impairments [77]. Here, we focused on the impact of concussive injury and the ISR on neuronal and cognitive function in male mice. Further investigation is needed to determine how these relationships are modulated in female mice to improve i) our understanding of TBI pathophysiology, ii) our clinical care and ii) treatment development.

Traumatic brain injury is a silent epidemic, improving our understanding of processes, (such as spine structural plasticity) associated with proper cognitive function can allow for novel approaches to modulate trauma-induced cognitive dysfunction. Here we demonstrate a structural mechanism for cognitive impairments after concussive injury that is rapidly and persistently reversed by ISR inhibition.

Materials and Methods

Animals. All experiments were conducted in accordance with National Institutes of Health (NIH) Guide for the Care and Use of Laboratory Animals and approved by the Institutional Animal Care and Use Committee of the University of California, San Francisco. Male C57B6/J wild-type (WT) mice were received from Jackson Laboratories. Male Thy-1-YFP-H (in C57 background) were bred in house. Animals were 10-16 weeks of age at the time of surgeries. Animal shipments were received at

least one week prior to start of experimentation to allow animals to habituate to the new surroundings. Mice were group housed in environmentally controlled conditions with a reverse light cycle (12:12 h light: dark cycle at 21 ± 1 °C; ~50% humidity) and provided food and water ad libitum. Behavioral analysis was performed during the dark cycle.

Drug Administration. ISRIB solution was made by dissolving 5 mg ISRIB in 1 mL dimethyl sulfoxide (DMSO) (PanReac AppliChem, 191954.1611). The solution was gently heated in a 40 °C waterbath and vortexed every 30 s until the solution became clear. Next 1 mL of Tween 80 (Sigma Aldrich, P8074) was added, solution was gently heated in a 40 °C waterbath and vortexed every 30 s until the solution became clear. Next, 10 mLs of polyethylene glycol 400 (PEG400) (PanReac AppliChem, 142436.1611), solution was added gently heated in a 40 °C waterbath and vortexed every 30 s until the solution became clear. Finally, 36.5 mLs of 5% dextrose (Hospira, RL-3040) was added. The solution was kept at room temperature throughout the experiment. Each solution was used for injections up to 7 d maximum. The vehicle solution consisted of the same chemical composition and concentration (DMSO, Tween 80, PEG400 and 5% dextrose). Stock ISRIB solution was at 0.1 mg/ml, but injections were at 2.5 mg/kg. Each animal received an intraperitoneal injection of 2.5x their body weight.

Novel object recognition task with 5-minute retention interval. For all behavioral assays the experimenter(s) were blinded to therapeutic intervention. Prior to behavioral analysis animals were inspected for gross motor impairments. Animals were inspected

for whisker loss, limb immobility (included grip strength) and eye occlusions. If animals displayed any of these impairments, they were excluded. Behavioral assessment was recorded and scored using a video tracking and analysis setup (Ethovision XT 8.5, Noldus Information Technology).

The novel objective recognition task was modified from a previously described protocol [78]. The task took place during the dark cycle in a room with dim red light. Mice were individually habituated in a 30 cm × 30 cm × 30 cm (L×W×H) opaque plexiglass box (termed 'arena') for 10 min per day for 2 days. On the third day, mice were exposed to two identical objects for 5 minutes (learning phase). The mice were then temporarily removed for 5 min to allow for one of the objects to be replaced by a novel object. Mice were then returned to the arena for 5 minutes to explore and interact with the objects (testing phase). In each experiment, the location of the novel object was randomly selected between the left and right side. Mouse behavior was recorded with an overhead video camera; the video files were exported to Ethovision XT 8.5, Noldus Information Technology for analysis. Data are presented as discrimination Index, calculated using formula DI = (Time spent with novel – time spent with familiar/total time).

Animals were injected (intraperitoneal) with either vehicle or ISRIB (2.5 mg/kg) starting two days before the first training day (day 14 post injury) (Figure 3A) and after each of the final trials of the habituation days (day 1 and 2) for a total of four doses. No injections were given when short-term memory was tested on day 3.

On day 49 (32 days post ISRIB/Vehicle treatment), we measured short-term memory using the NORT with a 5-minute retention interval (as described above) but used a different novel object comparable in novelty. In each experiment, the location of the novel object was randomly selected between the left and right side. Mouse behavior was recorded with an overhead video camera; the video files were exported to Ethovision XT 8.5, Noldus Information Technology for analysis. Data are presented as discrimination Index, calculated using formula DI = (Time spent with novel – time spent with familiar/total time).

Closed head injury and Sham surgery. 10-12 weeks old C57BL/6J or Thy-1-YFP-H (in C57 background) mice were randomly assigned to each TBI or sham surgery group. Animals were anesthetized and maintained at 2-2.5% isoflurane during CHI or sham surgery. Animals were secured to a stereotaxic frame with nontraumatic ear bars, and the head of the animal was supported with foam before injury. Contusion was induced using a 5-mm convex tip attached to an electromagnetic impactor (Leica) at the following coordinates: anteroposterior, −1.50 mm and mediolateral, 0 mm with respect to bregma. The contusion was produced with an impact depth of 1 mm from the surface of the skull with a velocity of 5.0 m/s sustained for 300 ms. Animals that had a fractured skull after injury were excluded from the study. Sham animals were secured to a stereotaxic frame with nontraumatic ear bars and received the midline skin incision but no impact. After CHI or sham surgery, the scalp was sutured, and the animal was allowed to recover in an incubation chamber set to 37 °C. All animals recovered from

the surgical procedures as exhibited by normal behavior and weight maintenance monitored throughout the duration of the experiments.

Headplate and cranial window attachment surgery. 10-12 weeks old Thy-1-YFP-H (in C57 background) mice underwent headplate and cranial window attachment surgery. Animals were anesthetized, maintained at 1.5% isoflurane, and placed over a protected thermal plate (37°C) during surgery. Animals were secured to a stereotaxic frame with nontraumatic ear bars. After anesthesia induction, dexamethasone (intraperitoneal), meloxicam (intraperitoneal), and lidocaine (subcutaneous) drugs were administered. The scalp was cleaned with ethanol 70%, disinfected with Betadine and the skull was exposed with a midline scalp incision. A craniotomy was performed on the right parietal cortex with a high-speed drill equipped with a round bur. To avoid damaging the underlying cortex by friction-induced heat, a cool sterile solution was added to the skull periodically, and drilling was intermittent to permit heat dissipation. The excised skull was replaced by a 3mm coverslip window (Harvard Apparatus, Round Cover Glass) carefully positioned on top of the brain and secured against the skull with tissue adhesive (3M Vetbond tissue adhesive). A custom-made headplate with a central opening was attached with dental cement (Parkell C&B Metbond Quick Adhesive Cement System). After the surgery, the animal was allowed to recover in an incubation chamber set to 37 °C before returning to its home cage. All animals recovered from the surgical procedures as exhibited by normal behavior and weight maintenance monitored throughout the duration of the experiments. Animals were allowed to recover before the start of imaging experiments.

***In vivo* transcranial two-photon imaging.** *In vivo transcranial* two-photon imaging was

performed using a movable objective microscope manufactured by the Sutter

Instrument Company. A mode-locked Ti:Sapphire laser (Chameleon Ultra 2, Coherent,

Inc.) was tuned to 920 nm, and the laser power through the objective was adjusted

within the range of 60 to 80 mW. Emission light was collected by a 40x water-immersion

objective (NA0.8; IR2; Olympus), filtered by emission filters (525/70 and 610/75 nm;

Chroma Technology) and measured by 2 independent photomultiplier tubes

(Hamamatsu R3896). Scanning and image acquisition of apical dendrites in layer I/II of

layer V pyramidal neurons expressing green fluorescent protein was controlled by

ScanImage software (Vidrio Technologies). Z-stacks were collected with a step size of 1

μm in the *z* axis and the pixel size to 0.1513 μm. Each slice of the stack was obtained

by averaging 25 frames. Mice were imaged for 4 or 5 sessions over an 8 or 15 day

period. Care was taken with each imaging session to achieve similar fluorescence

levels. Mice were under isoflurane anesthesia (1.5% in oxygen) for one hour and head

fixed for structural imaging. The body temperature of the mouse was kept at 37°C using

an electric heating pad.

Spine dynamics analysis. For spine remodeling analysis, image stacks collected on

day 13, 15, 18, and 25 were first aligned to their corresponding baseline imaging stack

collected on day 11 using NIH FIJI software (CMTK Registration Gui plugin). Spine

formation and elimination analysis was done semi-automated using the NIH FIJI

software (ROI coordinates) to save the X, Y, Z coordinates of identified dendrites on

traced dendrites from day 11 image stacks. The X, Y, Z coordinates were then applied

to image stacks from subsequent imaging sessions to denote lack of presence,

presence, or presence of a new spine. Spine formation and elimination were graphed as

compared to baseline imaging day 11. Multiple dendrites ranging between 50-100um

(+/- 2um) in length were analyzed per mouse and then averaged. A total length of at

least 3500 μm of dendrites and 200-600 spines were analyzed per experimental group.

To exclude that any measured changes were due to an analysis artifact, spine formation

and elimination were analyzed by reverse analysis comparing days 11, 13, and 15 to

day 18.

The number of new spines formed per imaging session was quantified by

notating the number of new spines formed (first observed) at imaging day 13, 15, and

18. Multiple dendrites ranging were analyzed per mouse and then averaged.

To calculate the survival ratio, we determined the number of spines present at

subsequent imaging sessions divided by number of spines present when first observed.

First, individual spines were first classified as T_{11}, T_{13}, T_{15}, or T_{18} depending on which

imaging day they were first observed. Next, a binary system was used to denote

presence (indicated by a 1) or not (indicated by a 0) across the imaging sessions. In this

scale, a survival ratio closer to 1 denotes "long-lived" and a survival ratio closer to 0

denotes "short-lived." For every dendrite, the survival ratio was calculated per each

dendritic spine population (T_{11}, T_{13}, T_{15}, or T_{18}). The average survival ratio of each

dendritic spine population was graphed per mouse.

Spine density quantification. For spine density analysis (density per um of dendritic length), we determine the total number of spines present at baseline imaging day 11 divided by total number of spines present at each subsequent imaging session per dendrite. All protrusions from a dendrite were counted as spines regardless of morphology. The average spine density at imaging session was graphed per mouse.

Tissue collection. All mice were lethally overdosed using a mixture of ketamine (10 mg/ml) and xylaxine (1 mg/ml). Once animals were completely anesthetized, blood was extracted by cardiac puncture and animals were perfused with 1X phosphate buffer solution, pH 7.4 (Gibco, Big Cabin OK, -70011-044) until the livers were clear (~1–2 min). For drug concentration and western blot analysis following PBS, the whole brain was rapidly removed, and cortical tissue dissected and then snap frozen on dry ice and stored at −80 °C until processing. For immunohistochemistry analysis following PBS, the whole brain was removed and fixed in ice-cold 4% paraformaldehyde, pH 7.5 (PFA, Sigma Aldrich, St. Louis, MO, 441244) for 4 hrs followed by sucrose (Fisher Science Education, Nazareth, PA, S25590A) protection (15% to 30%).

Western Blot Analysis. Animals received all 4 ISRIB injections and were terminated 4 or 51 days after the fourth injection (as described above). Cortical isolates were then homogenized with a T 10 basic ULTRA-TURRAX (IKa) in ice-cold buffer lysis (Cell Signaling 9803) and protease and phosphatase inhibitors (Roche). Lysates were sonicated for 3 min and centrifuged at 13,000 rpm for 20 minutes at 4°C. Protein concentration in supernatants was determined using BCA Protein Assay Kit (Pierce).

Equal amounts of proteins (30 ug) was loaded on SDS-PAGE gels. Proteins were

transferred at 40 mA ON at 4°C onto 0.2 μm PVDF membranes (BioRad) and probed

with primary antibodies diluted in Tris-buffered saline supplemented with 0.1% Tween

20 and 3% bovine serum albumin. Phospho-GCN2 (Abcam ab-75836), phosphor-PERK

(Cell signaling 3179), phosphor-PKR (Invitrogen 44668), phosphor-eIF2α (Cell Signaling

3597), eIF2α (Cell signaling 2103), ATF4 (Abcam ab184909), BACE-1 (Cell signaling

5606) and β-actin (Sigma A5441) antibodies were used as primary antibodies at a

dilution of 1:1000 and incubated ON at 4°C. HRP-conjugated secondary antibodies

(Rockland) were employed to detect immune-reactive bands using enhanced

chemiluminescence (ECL Western Blotting Substrate, Pierce) according to the

manufacturer instructions, using a dilution of 1:5000 and incubated for 1 hour at RT.

Quantification of protein bands was done by densitometry using ImageJ software. Every

blot was normalized to β-actin expression and phospho-eIF2α bands were either

normalized to β-actin or eIF2α.

Immunohistochemistry analysis and quantification. For immunohistochemistry

analysis, following PBS, whole brains were fixed in ice-cold 4% paraformaldehyde, pH

7.5 (PFA, Sigma Aldrich, St. Louis, MO, 441244) for 4 hrs followed by sucrose (Fisher

Science Education, Nazareth, PA, S25590A) protection (15% to 30%). Brains were

embedded with 30% sucrose/ Optimal Cutting Temperature Compound (Tissue Tek,

Radnor, PA, 4583) mixture on dry ice and stored at -80 °C. Brains were sectioned into

20 μm slides using a Leica cryostat (Leica Microsystems, Wetzlar, Germany) and

mounted on slides (ThermoFisher Scientific, South San Francisco, CA). Slides were

brought to room temperature (20 °C) prior to use. Slides were washed in tris buffered

saline tween solution for 10 min. and twice with tris buffered saline (TBS) for 10 min.

each. All slides were blocked in Block Reagent (Perkin Elmer, Waltham, MA, FP1020)

for 30 minutes in the dark. Slides were stained with primary antibodies specific for

GFAP (Rabbit, Dako, Santa Clara, CA Z0334) or NeuN (Rabbit, Abcam, Burlingame,

CA ab128886) overnight, washed three times in TBS, and stained for the secondary

antibody, goat anti-rabbit Alexa-568 (Invitrogen, Carlsbad, CA, A-11011). Tissues were

fixed using ProLong Gold (Invitrogen, Carlsbad, CA, P36930) and a standard slide

cover sealed with nail polish. 3-4 images separated by 60-140 μm in the cortex were

averaged per animal. 9.3 μm z-stack images were acquired on a Zeiss Laser-Scanning

Confocal microscope (Zeiss LSM 780 NLO FLIM) at the HDFCCC Laboratory for Cell

Analysis Shared Resource Facility. 63x magnification water. Quantitative analyses was

performed using NIH FIJI analysis software (v1.52n). Astrocytes were determined using

the glial fibrillary acidic protein (GFAP). Neurons were determined using the neuronal

marker (NeuN). The degree of astrogliosis (GFAP) was determined by the image-

covering staining and expressed as percentage of the total area. The neuronal numbers

were determined by quantification of a neuronal nuclei and by the image-covering

staining and expressed as total numbers or percentage of the total area.

Statistical Analysis. All data were analyzed with GraphPad Prism 9 statistical software.

Unpaired T-test, Two-way analysis of variance (ANOVA), Three-way analysis of

variance (ANOVA), and Pearson R correlations were used (individual statistical tool and

post-hoc analysis denoted in Figure Legends). The p values of < 0.05 were considered

as significant. Individual animal scores represented by dots, lines depict Data mean and

SEM. Group outliers were determined (GraphPad Software Outlier Test-Grubb's test)

and excluded from analysis. At most a single animal was excluded from each

experimental cohort.

Figures
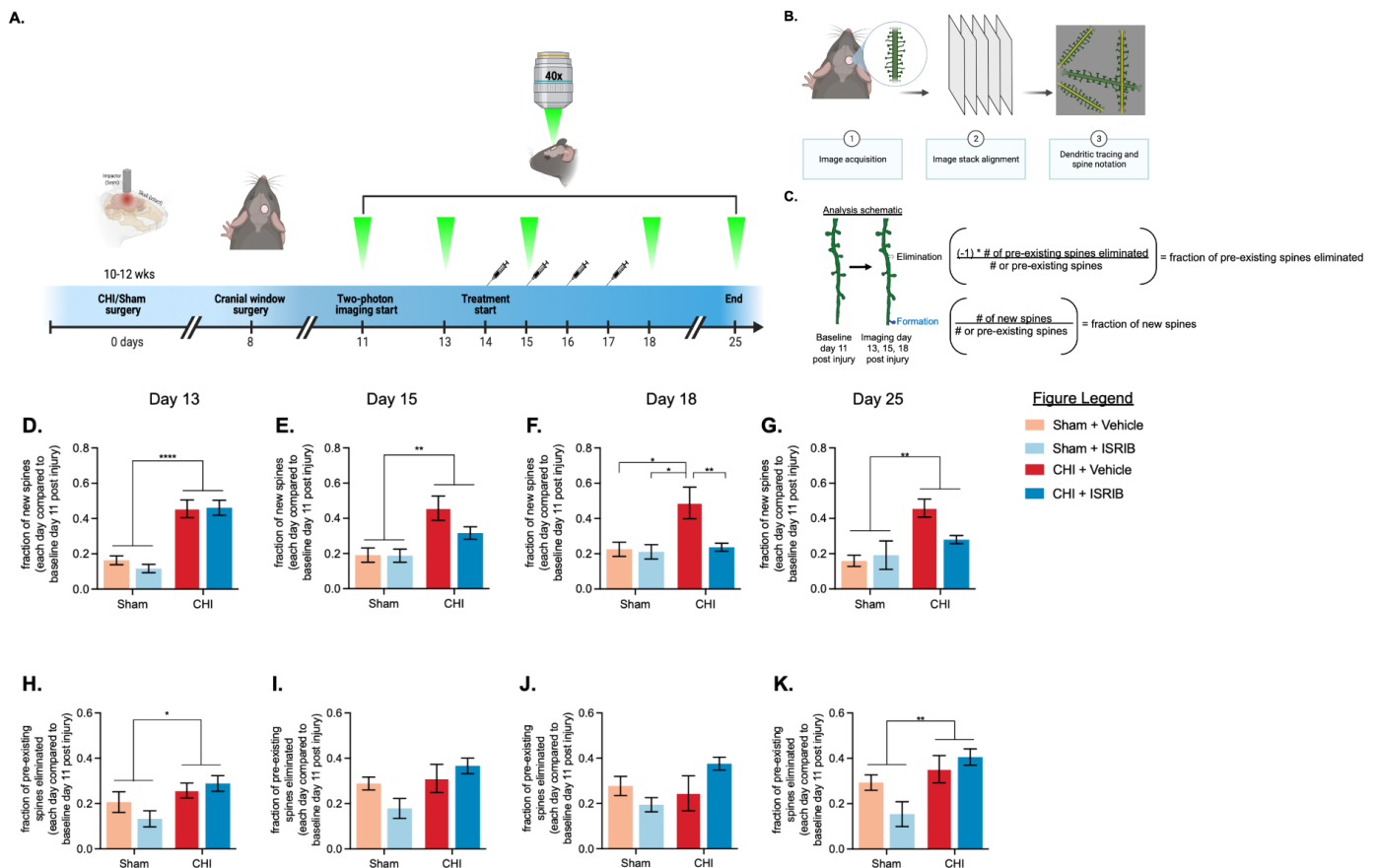
Figure 1. Cortical spine dynamics are altered by concussive injury and restored by ISR inhibition.

(A) Experimental design for surgeries, imaging and ISRIB/Vehicle treatment paradigm. Thy1-YFP-H transgenic male mice (10-12 weeks of age) were subjected to CHI/sham surgery and eight days later a cranial window was implanted directly above the parietal cortex (encompassing the impacted region). Mice were imaged for four to five sessions over 15 days starting at day 11 post-CHI/sham surgery with the final imaging day on day 18 or 25 post-CHI/sham surgery. Mice received four daily intraperitoneal injections of ISRIB or Vehicle (2.5mg/kg) starting day 14 post-CHI. Tissues were collected day 18 or day 25 following the imaging session. (**B**) A schematic illustrating image acquisition,

processing, and analysis. **(C)** An analysis schematic illustrating classification and calculation for spine formation and spine elimination. Fraction of **(D-G)** new spines and **(H-K)** pre-existing spines eliminated after injury and treatment. Mice that received CHI had significantly increased fraction of new spines as compared to mice that received sham surgery. This increase in fraction of new spines was sustained during the imaging sessions. ISRIB treatment on CHI mice reversed the injury-induced increase in fraction of new spines to the level of sham mice. The treatment effect was maintained after treatment ended. As expected, sham mice maintained a 0.20 fraction of new spines. ISRIB treatment had no effect on fraction of new spines of sham mice. At 13 days post injury (dpi) two-way ANOVA revealed a significant injury effect ($p<0.01$). At 25 days post injury (dpi) two-way ANOVA revealed a significant injury effect ($p<0.001$). At 13 days post injury (dpi) two-way ANOVA revealed a significant injury effect ($p<0.0001$). Tukey-post hoc revealed significant differences between groups. At 15 dpi two-way ANOVA revealed significant injury effect ($p= 0.0020$). Tukey-post hoc revealed significant differences between groups. At 18 dpi significant injury effect ($p= 0.0121$), treatment effect ($p= 0.0196$), and interaction ($p= 0.037$). At 25 dpi two-way ANOVA revealed significant injury effect ($p= 0.0044$). Tukey-post hoc revealed significant differences between groups. Data are means ± SEM. Sham + Vehicle n=6; Sham + ISRIB n=7; CHI + Vehicle n=12; CHI + ISRIB n=13.
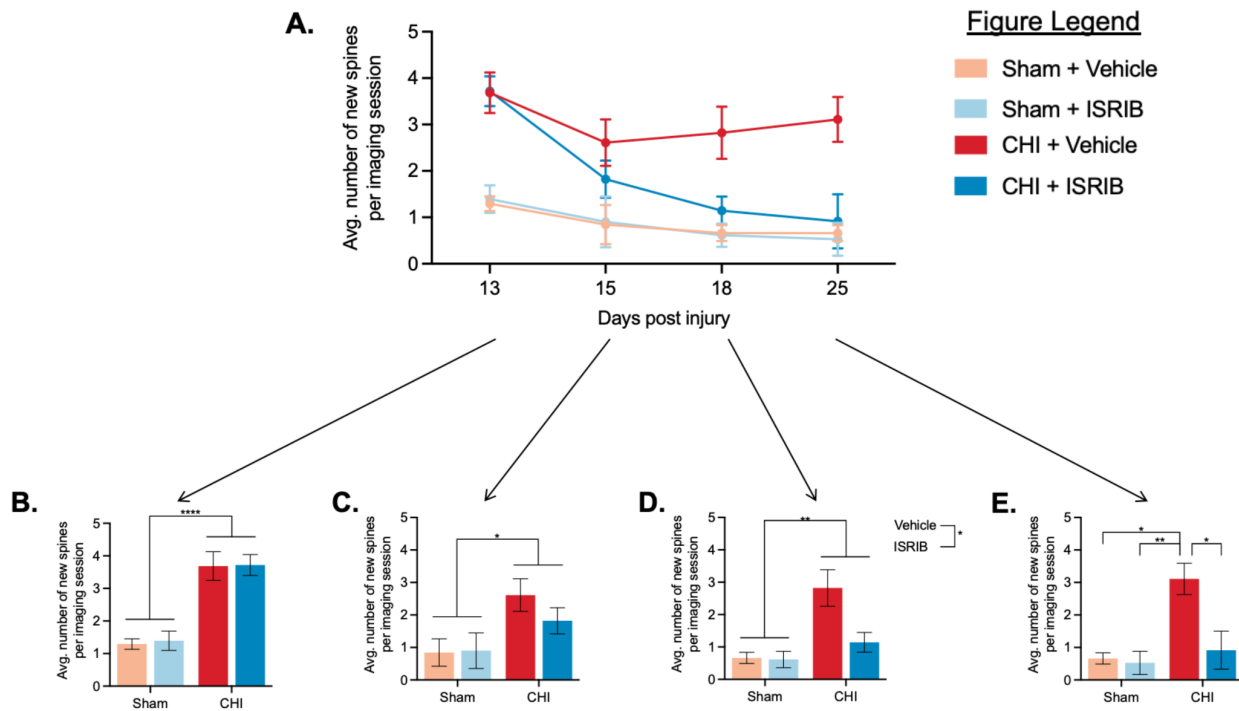
Figure 2. Number of new spines is increased by concussive injury and reversed by ISR inhibition.

(A) Average number of new spines formed per imaging session. (**B**) CHI mice had significantly higher average number of new spines formed per imaging session as compared to sham mice. (**C-E**) This increase was present at each subsequent imaging

session. **(B-E)** CHI mice that received ISRIB treatment had an increase in the average number of new spines formed (prior to treatment) that then decreased to sham levels over the imaging sessions (during and after treatment). At 13 days post injury (dpi) two-way ANOVA revealed a significant injury effect ($p<0.0001$). Tukey-post hoc revealed significant differences between groups. At 18 dpi significant injury effect ($p= 0.0323$). At 25 dpi two-way ANOVA revealed significant injury effect ($p= 0.0084$), treatment effect ($p= 0.0215$), and interaction ($p= 0.0360$). Tukey-post hoc revealed significant differences between groups. Data are means ± SEM. Sham + Vehicle n=6; Sham + ISRIB n=7; CHI + Vehicle n=12; CHI + ISRIB n=13.
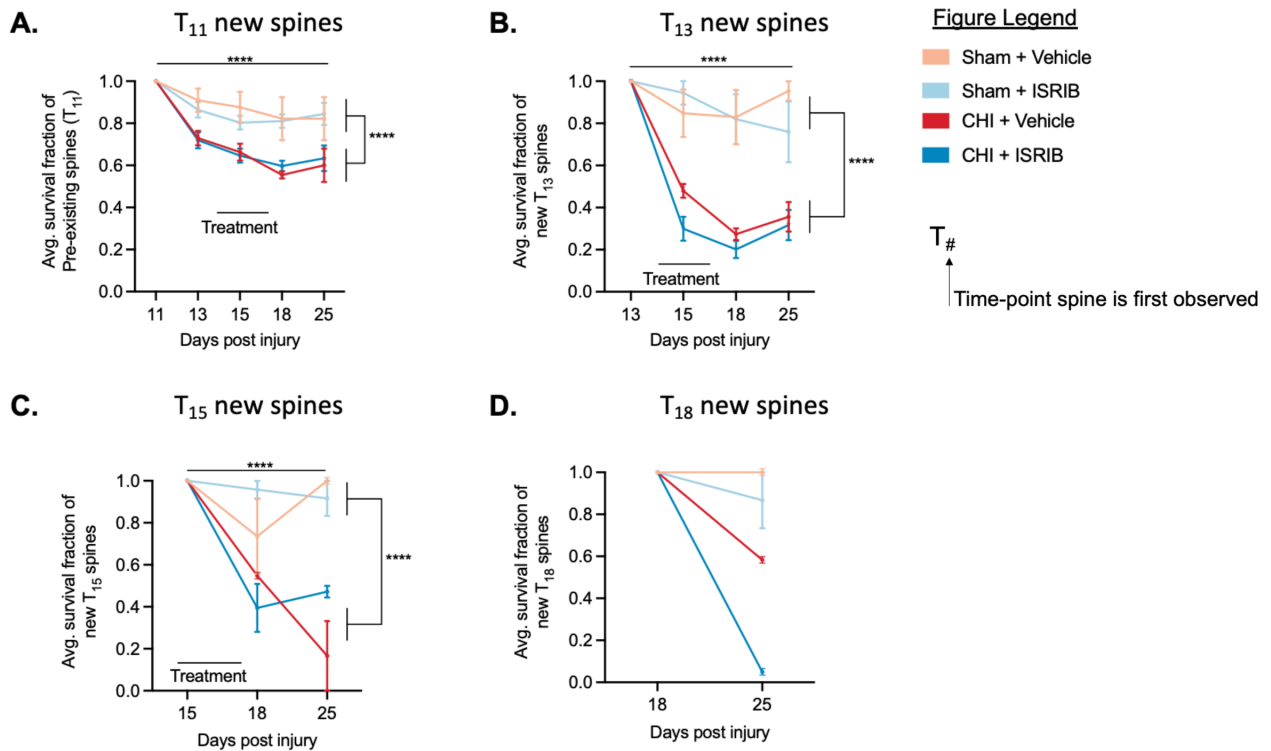
Figure 3. Concussive injury and ISR inhibition decrease survival ratio of T_{11}, T_{13}, T_{15}, and T_{18} spines.

Average survival ratio of **(A)** T_{11} **(B)** T_{13}, **(C)** T_{15}, and **(D)** T_{18} spines after injury and treatment. Mice that received CHI, independent of treatment, consistently had decreased survival ratio for each of the spine populations listed above. Mice that received sham surgery maintained a consistent survival ratio for each of the spine populations. Data are means ± SEM. Sham + Vehicle n=6; Sham + ISRIB n=7; CHI + Vehicle n=12; CHI + ISRIB n=13.
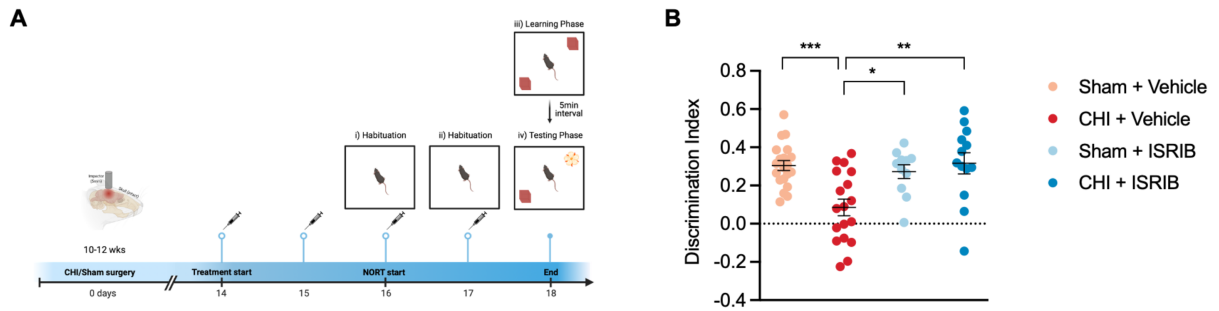
Figure 4. Concussive injury induces short-term memory deficits that are reversed by ISRIB.

(A) Experimental design for surgeries, ISRIB/Vehicle treatment paradigm, and schematic of the novel object recognition task (NORT) with 5-minute retention interval. Male mice (12-16 weeks of age) were subjected to a single mild concussive closed head injury (CHI) or Sham surgery and received four daily intraperitoneal injections of ISRIB (2.5mg/kg) or Vehicle starting day 14 post-CHI. A 3-day NORT with 5-minute retention interval was used to measure short-term memory function, which ended on day 18 post-CHI. A subset of tissues was collected day 21 post-CHI to investigate ISR activation. **(B)** Dot plots showing object discrimination index results. Mice that received CHI did not distinguish between novel and familiar objects in contrast to mice that received sham surgery. ISRIB treatment reversed short-term memory dysfunction in CHI mice. ISRIB treatment had no effect on sham mice. Two-way ANOVA revealed a significant injury effect (p = 0.0389), treatment effect (p= .0198), and interaction (p= .0024). Tukey-post hoc revealed significant differences between groups. Individual animal scores represented in dots, lines depict group mean and SEM. Sham + Vehicle n=20; Sham + ISRIB n=13; CHI + Vehicle n=18; CHI + ISRIB n=13.
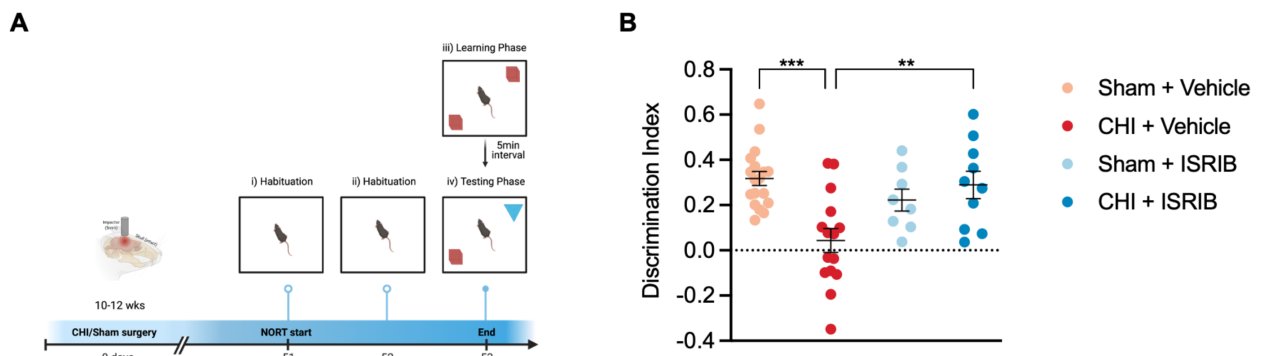
Figure 5. ISR inhibition rescues CHI-induced short-term memory deficits weeks after treatment.

(A) Experimental design for surgeries and schematic of the novel object recognition task (NORT) with 5-minute retention interval. **(B)** Dot plots showing object discrimination results. Male mice that received CHI did not distinguish between novel and familiar objects in contrast to mice that received sham surgery. ISRIB treatment rescue in short-term memory dysfunction in CHI mice persisted weeks after treatment. ISRIB treatment

had no effect on sham mice. Two-way ANOVA revealed significant injury effect (0.0054). Tukey-post hoc revealed significant differences between groups. Individual animal scores represented in dots, lines depict group mean and SEM. Sham + Vehicle n=18; Sham + ISRIB n=8; CHI + Vehicle n=15; CHI + ISRIB n=10.

References

1.   Flanagan, S.R., *Invited Commentary on "Centers for Disease Control and Prevention Report to Congress: Traumatic Brain Injury in the United States: Epidemiology and Rehabilitation".* Arch Phys Med Rehabil, 2015. **96**(10): p. 1753-5.

2.   Fleminger, S., et al., *Head injury as a risk factor for Alzheimer's disease: the evidence 10 years on; a partial replication.* J Neurol Neurosurg Psychiatry, 2003. **74**(7): p. 857-62.

3.   Cole, J.H., et al., *Prediction of brain age suggests accelerated atrophy after traumatic brain injury.* Ann Neurol, 2015. **77**(4): p. 571-81.

4.   Li, Y., et al., *Head Injury as a Risk Factor for Dementia and Alzheimer's Disease: A Systematic Review and Meta-Analysis of 32 Observational Studies.* PLoS One, 2017. **12**(1): p. e0169650.

5.   Masel, B.E. and D.S. DeWitt, *Traumatic brain injury: a disease process, not an event.* J Neurotrauma, 2010. **27**(8): p. 1529-40.

6.   Broglio, S.P., et al., *Cognitive decline and aging: the role of concussive and subconcussive impacts.* Exerc Sport Sci Rev, 2012. **40**(3): p. 138-44.

7.   Chou, A., et al., *Inhibition of the integrated stress response reverses cognitive deficits after traumatic brain injury.* Proc Natl Acad Sci U S A, 2017. **114**(31): p. E6420-E6426.

8.   Krukowski, K., et al., *Integrated Stress Response Inhibitor Reverses Sex-Dependent Behavioral and Cell-Specific Deficits after Mild Repetitive Head Trauma.* J Neurotrauma, 2020. **37**(11): p. 1370-1380.

9. Bachstetter, A.D., et al., *Attenuation of traumatic brain injury-induced cognitive impairment in mice by targeting increased cytokine levels with a small molecule experimental therapeutic.* J Neuroinflammation, 2015. **12**: p. 69.

10. Chai, W.J., A.I. Abd Hamid, and J.M. Abdullah, *Working Memory From the Psychological and Neurosciences Perspectives: A Review.* Front Psychol, 2018. **9**: p. 401.

11. Eriksson, J., et al., *Neurocognitive Architecture of Working Memory.* Neuron, 2015. **88**(1): p. 33-46.

12. Funahashi, S., *Working Memory in the Prefrontal Cortex.* Brain Sci, 2017. **7**(5).

13. Cowan, N., *What are the differences between long-term, short-term, and working memory?* Prog Brain Res, 2008. **169**: p. 323-38.

14. Mayford, M., S.A. Siegelbaum, and E.R. Kandel, *Synapses and memory storage.* Cold Spring Harb Perspect Biol, 2012. **4**(6).

15. Langille, J.J. and R.E. Brown, *The Synaptic Theory of Memory: A Historical Survey and Reconciliation of Recent Opposition.* Front Syst Neurosci, 2018. **12**: p. 52.

16. Citri, A. and R.C. Malenka, *Synaptic plasticity: multiple forms, functions, and mechanisms.* Neuropsychopharmacology, 2008. **33**(1): p. 18-41.

17. Amaral, M.D. and L. Pozzo-Miller, *The dynamics of excitatory synapse formation on dendritic spines.* Cellscience, 2009. **5**(4): p. 19-25.

18. Chen, C.C., J. Lu, and Y. Zuo, *Spatiotemporal dynamics of dendritic spines in the living brain.* Front Neuroanat, 2014. **8**: p. 28.

19. Yang, G., F. Pan, and W.B. Gan, *Stably maintained dendritic spines are associated with lifelong memories.* Nature, 2009. **462**(7275): p. 920-4.

20. Bailey, C.H., E.R. Kandel, and K.M. Harris, *Structural Components of Synaptic Plasticity and Memory Consolidation.* Cold Spring Harb Perspect Biol, 2015. **7**(7): p. a021758.

21. Yap, K., et al., *The actin-modulating protein synaptopodin mediates long-term survival of dendritic spines.* Elife, 2020. **9**.

22. Lai, K.O. and N.Y. Ip, *Structural plasticity of dendritic spines: the underlying mechanisms and its dysregulation in brain disorders.* Biochim Biophys Acta, 2013. **1832**(12): p. 2257-63.

23. Steffens, H., et al., *Stable but not rigid: Chronic in vivo STED nanoscopy reveals extensive remodeling of spines, indicating multiple drivers of plasticity.* Sci Adv, 2021. **7**(24).

24. Hofer, S.B., et al., *Experience leaves a lasting structural trace in cortical circuits.* Nature, 2009. **457**(7227): p. 313-7.

25. Sala, C. and M. Segal, *Dendritic spines: the locus of structural and functional plasticity.* Physiol Rev, 2014. **94**(1): p. 141-88.

26. Holtmaat, A.J., et al., *Transient and persistent dendritic spines in the neocortex in vivo.* Neuron, 2005. **45**(2): p. 279-91.

27. Pchitskaya, E. and I. Bezprozvanny, *Dendritic Spines Shape Analysis-Classification or Clusterization? Perspective.* Front Synaptic Neurosci, 2020. **12**: p. 31.

28.   Nimchinsky, E.A., B.L. Sabatini, and K. Svoboda, *Structure and function of dendritic spines.* Annu Rev Physiol, 2002. **64**: p. 313-53.

29.   Nakahata, Y. and R. Yasuda, *Plasticity of Spine Structure: Local Signaling, Translation and Cytoskeletal Reorganization.* Front Synaptic Neurosci, 2018. **10**: p. 29.

30.   Yasuda, R., *Biophysics of Biochemical Signaling in Dendritic Spines: Implications in Synaptic Plasticity.* Biophys J, 2017. **113**(10): p. 2152-2159.

31.   Bourne, J. and K.M. Harris, *Do thin spines learn to be mushroom spines that remember?* Curr Opin Neurobiol, 2007. **17**(3): p. 381-6.

32.   Adrian, M., et al., *Barriers in the brain: resolving dendritic spine morphology and compartmentalization.* Front Neuroanat, 2014. **8**: p. 142.

33.   Tønnesen, J., et al., *Spine neck plasticity regulates compartmentalization of synapses.* Nat Neurosci, 2014. **17**(5): p. 678-85.

34.   Berry, K.P. and E. Nedivi, *Spine Dynamics: Are They All the Same?* Neuron, 2017. **96**(1): p. 43-55.

35.   Ghani, M.U., et al., *Dendritic spine classification using shape and appearance features based on two-photon microscopy.* J Neurosci Methods, 2017. **279**: p. 13-21.

36.   Holtmaat, A., et al., *Long-term, high-resolution imaging in the mouse neocortex through a chronic cranial window.* Nat Protoc, 2009. **4**(8): p. 1128-44.

37.   Grutzendler, J., N. Kasthuri, and W.B. Gan, *Long-term dendritic spine stability in the adult cortex.* Nature, 2002. **420**(6917): p. 812-6.

38. Lendvai, B., et al., *Experience-dependent plasticity of dendritic spines in the developing rat barrel cortex in vivo.* Nature, 2000. **404**(6780): p. 876-81.

39. Trachtenberg, J.T., et al., *Long-term in vivo imaging of experience-dependent synaptic plasticity in adult cortex.* Nature, 2002. **420**(6917): p. 788-94.

40. Costa-Mattioli, M. and P. Walter, *The integrated stress response: From mechanism to disease.* Science, 2020. **368**(6489).

41. Harding, H.P., et al., *An integrated stress response regulates amino acid metabolism and resistance to oxidative stress.* Mol Cell, 2003. **11**(3): p. 619-33.

42. Donnelly, N., et al., *The eIF2α kinases: their structures and functions.* Cell Mol Life Sci, 2013. **70**(19): p. 3493-511.

43. Hinnebusch, A.G., I.P. Ivanov, and N. Sonenberg, *Translational control by 5'-untranslated regions of eukaryotic mRNAs.* Science, 2016. **352**(6292): p. 1413-6.

44. Sonenberg, N. and A.G. Hinnebusch, *Regulation of translation initiation in eukaryotes: mechanisms and biological targets.* Cell, 2009. **136**(4): p. 731-45.

45. Freeman, O.J. and G.R. Mallucci, *The UPR and synaptic dysfunction in neurodegeneration.* Brain Res, 2016. **1648**(Pt B): p. 530-537.

46. Gipson, C.D. and M.F. Olive, *Structural and functional plasticity of dendritic spines - root or result of behavior?* Genes Brain Behav, 2017. **16**(1): p. 101-117.

47. Feng, G., et al., *Imaging neuronal subsets in transgenic mice expressing multiple spectral variants of GFP.* Neuron, 2000. **28**(1): p. 41-51.

48. Zuo, Y., et al., *Development of long-term dendritic spine stability in diverse regions of cerebral cortex.* Neuron, 2005. **46**(2): p. 181-9.

49.   Lueptow, L.M., *Novel Object Recognition Test for the Investigation of Learning and Memory in Mice.* J Vis Exp, 2017(126).

50.   Antunes, M. and G. Biala, *The novel object recognition memory: neurobiology, test procedure, and its modifications.* Cogn Process, 2012. **13**(2): p. 93-110.

51.   Penzes, P., et al., *Dendritic spine pathology in neuropsychiatric disorders.* Nat Neurosci, 2011. **14**(3): p. 285-93.

52.   Murmu, R.P., et al., *Dendritic spine instability leads to progressive neocortical spine loss in a mouse model of Huntington's disease.* J Neurosci, 2013. **33**(32): p. 12997-3009.

53.   Jiang, M., et al., *Dendritic arborization and spine dynamics are abnormal in the mouse model of MECP2 duplication syndrome.* J Neurosci, 2013. **33**(50): p. 19518-33.

54.   Rabinowitz, A.R. and H.S. Levin, *Cognitive sequelae of traumatic brain injury.* Psychiatr Clin North Am, 2014. **37**(1): p. 1-11.

55.   Winston, C.N., et al., *Controlled cortical impact results in an extensive loss of dendritic spines that is not mediated by injury-induced amyloid-beta accumulation.* J Neurotrauma, 2013. **30**(23): p. 1966-72.

56.   Xiong, Y., A. Mahmood, and M. Chopp, *Remodeling dendritic spines for treatment of traumatic brain injury.* Neural Regen Res, 2019. **14**(9): p. 1477-1480.

57.   Ratliff, W.A., et al., *Dendritic arbor complexity and spine density changes after repetitive mild traumatic brain injury and neuroprotective treatments.* Brain Res, 2020. **1746**: p. 147019.

58. Mulherkar, S., et al., *RhoA-ROCK Inhibition Reverses Synaptic Remodeling and Motor and Cognitive Deficits Caused by Traumatic Brain Injury.* Sci Rep, 2017. **7**(1): p. 10689.

59. Gao, X., et al., *Moderate traumatic brain injury causes acute dendritic and synaptic degeneration in the hippocampal dentate gyrus.* PLoS One, 2011. **6**(9): p. e24566.

60. Winston, C.N., et al., *Dendritic Spine Loss and Chronic White Matter Inflammation in a Mouse Model of Highly Repetitive Head Trauma.* Am J Pathol, 2016. **186**(3): p. 552-67.

61. Campbell, J.N., D. Register, and S.B. Churn, *Traumatic brain injury causes an FK506-sensitive loss and an overgrowth of dendritic spines in rat forebrain.* J Neurotrauma, 2012. **29**(2): p. 201-17.

62. Zhao, J., et al., *Mild Traumatic Brain Injury Reduces Spine Density of Projection Neurons in the Medial Prefrontal Cortex and Impairs Extinction of Contextual Fear Memory.* J Neurotrauma, 2018. **35**(1): p. 149-156.

63. Lamprecht, R. and J. LeDoux, *Structural plasticity and memory.* Nat Rev Neurosci, 2004. **5**(1): p. 45-54.

64. Pavitt, G.D., *Regulation of translation initiation factor eIF2B at the hub of the integrated stress response.* Wiley Interdiscip Rev RNA, 2018. **9**(6): p. e1491.

65. Chen, A., et al., *Inducible enhancement of memory storage and synaptic plasticity in transgenic mice expressing an inhibitor of ATF4 (CREB-2) and C/EBP proteins.* Neuron, 2003. **39**(4): p. 655-69.

66.   Pasini, S., et al., *Specific downregulation of hippocampal ATF4 reveals a necessary role in synaptic plasticity and memory.* Cell Rep, 2015. **11**(2): p. 183-91.

67.   Donnelly, N., et al., *The eIF2alpha kinases: their structures and functions.* Cell Mol Life Sci, 2013. **70**(19): p. 3493-511.

68.   Zhang, G., et al., *The integrated stress response in ischemic diseases.* Cell Death Differ, 2021.

69.   Krukowski, K., et al., *Small molecule cognitive enhancer reverses age-related memory decline in mice.* Elife, 2020. **9**.

70.   Bond, S., et al., *The Integrated Stress Response and Phosphorylated Eukaryotic Initiation Factor 2α in Neurodegeneration.* J Neuropathol Exp Neurol, 2020. **79**(2): p. 123-143.

71.   Wong, Y.L., et al., *eIF2B activator prevents neurological defects caused by a chronic integrated stress response.* Elife, 2019. **8**.

72.   Trinh, M.A., et al., *Brain-specific disruption of the eIF2α kinase PERK decreases ATF4 expression and impairs behavioral flexibility.* Cell Rep, 2012. **1**(6): p. 676-88.

73.   Ma, T., et al., *Suppression of eIF2α kinases alleviates Alzheimer's disease-related plasticity and memory deficits.* Nat Neurosci, 2013. **16**(9): p. 1299-305.

74.   Kelleher, R.J., A. Govindarajan, and S. Tonegawa, *Translational regulatory mechanisms in persistent forms of synaptic plasticity.* Neuron, 2004. **44**(1): p. 59-73.

75.   Biegon, A., *Considering Biological Sex in Traumatic Brain Injury.* Front Neurol, 2021. **12**: p. 576366.

76.   Gupte, R., et al., *Sex Differences in Traumatic Brain Injury: What We Know and What We Should Know.* J Neurotrauma, 2019. **36**(22): p. 3063-3091.

77.   Krukowski, K., et al., *Integrated Stress Response Inhibitor Reverses Sex-Dependent Behavioral and Cell-Specific Deficits after Mild Repetitive Head Trauma.* Journal of Neurotrauma, 2019. **37**(11): p. 1370-1380.

78.   Feng, X., et al., *Colony-stimulating factor 1 receptor blockade prevents fractionated whole-brain irradiation-induced memory deficits.* J Neuroinflammation, 2016. **13**(1): p. 215.

CHAPTER 3: Integrated stress response inhibitor reverses sex-dependent behavioral and cell-specific deficits after mild repetitive head trauma

Abstract

Mild repetitive traumatic brain injury (rTBI) induces chronic behavioral and cognitive alterations and increases the risk for dementia. Currently, there are no therapeutic strategies to prevent or mitigate chronic deficits associated with rTBI. Previously we developed an animal model of rTBI that recapitulates the cognitive and behavioral deficits observed in humans. We now report that rTBI results in an increase in risk-taking behavior in male but not female mice. This behavioral phenotype is associated with chronic activation of the integrated stress response and cell-specific synaptic alterations in the type A subtype of layer V pyramidal neurons in the medial prefrontal cortex. Strikingly, by briefly treating animals weeks after injury with ISRIB, a selective inhibitor of the integrated stress response (ISR), we (1) relieve ISR activation, (2) reverse the increased risk-taking behavioral phenotype and maintain this reversal, and (3) restore cell specific synaptic function in the affected mice. Our results indicate that targeting the ISR even at late time points after injury can permanently reverse behavioral changes. As such, pharmacological inhibition of the ISR emerges as a promising avenue to combat rTBI-induced behavioral dysfunction.

Introduction

Traumatic brain injury (TBI) is a growing health problem. Approximately 5 million Americans are living with a TBI related disability [1-4], and even mild TBI can elicit chronic cognitive dysfunction and functional limitation [2, 3, 5]. Furthermore, a prior TBI

increases the risk for additional TBI [6-8], making it imperative to understand the potential compounding effects of repetitive trauma. Rising concern for repetitive head trauma has led to an increase in studies of concussive and sub-concussive injuries (reviewed in [9, 10]). While there is still debate as to the severity of symptoms, the majority of studies report poorer cognitive and behavioral outcomes in individuals following multiple mild head traumas [9-11]. Specifically, increased risk-taking behavior and disinhibited symptoms are often reported by individuals who have suffered from mild single or repetitive traumatic brain injury (rTBI) [12-17]. Despite the increased interest in understanding the long-term consequences of rTBI, little is known about the underlying cellular and functional correlates responsible for these maladaptive behavioral and cognitive changes. With no identified mechanisms, there are no pharmacological treatment options for individuals suffering from rTBI-induced deficits.

The integrated stress response (ISR) is a universal cellular pathway that serves to cope with different cellular stressors [18] and it is induced after a single TBI [19-21]. In mammals, activation of the ISR modulates protein translation through the phosphorylation of a single serine on the α subunit of the translation initiation factor eIF2, which leads to a reduction in global protein translation [22, 23]. A select number of proteins are up-regulated with ISR activation including the β-site APP-cleaving enzyme 1 (BACE1) [24-27] and activating transcription factor 4 (ATF4), a memory repressor gene [28, 29]. Chronic ISR activation creates maladaptive cellular and functional changes including cognitive decline [19, 30-32].

It is not known whether mild rTBI induces ISR activation and whether it plays a role in behavioral changes and the associated neuronal dysfunction in the prefrontal

cortex. Recently, we discovered a potent and surprisingly non-toxic ISR inhibitor (ISRIB) [33-35] that completely reverses memory deficits resulting from single impact TBI. When administered weeks after injury, ISRIB treatment reversed memory. deficits in two distinct focal and diffuse TBI rodent models [19]. Further, ISRIB reversed trauma-induced suppression in hippocampal long-term potentiation. These findings lay the foundation for targeting the ISR for reversal of trauma-induced behavioral changes in the prefrontal cortex.

Recently we developed a pre-clinical rodent model to investigate cognitive and behavioral outcomes associated with rTBI [36]. In this model, animals receive a mild impact to the head daily for five days. When we investigated behavioral (risk-taking and social behaviors) and cognitive performance (episodic and working memory), we found behavioral impairments in animals that received five mild impacts. This is in line with other studies of rTBI in rodent models [38, 39] and corresponds with patient reported outcomes after rTBI [12–15]. Our previous studies did not measure significant changes in the intrinsic excitability of layer V (L5) pyramidal neurons in the medial prefrontal cortex (mPFC), a brain region vital for integration of these complex behaviors [41, 43].

In the current study, we evaluate excitatory synaptic input in L5 pyramidal neurons and explicitly assess function by neuronal subtype, because divergent patterns of synaptic input have been reported in L5 pyramidal neuron subtypes [41]. Specifically, we analyze the two subtypes of L5 pyramidal neurons that project subcortically ("type A") or callosally to other cortical locations ("type B") [41]. Finally, we investigate whether ISR activation plays a role in these deficits and whether ISRIB treatment can reverse behavioral and cellular changes associated with rTBI.

Result

Repetitive mild traumatic brain injury increases risk-taking behaviors in males but not female cohorts.

We reported previously that five mild rTBI resulted in increased risk-taking behaviors in male rodents [36]. Here we wanted to determine whether the changes in risk-taking behavior measured after rTBI are also observed after other commonly used single injury models and whether female mice are impaired equally. We compared trauma- induced behavioral deficits between: (1) five rTBIs [36], (2) a single mild concussive closed head injury (CHI) [19], (3) a moderate, focal injury model—CCI [19, 37, 40] and (4) sham surgery in male and female mice.

We evaluated changes in risk-taking behavior approximately one-month post-injury with the EPM testing paradigm (**Figure 1A**). In the EPM, animals are positioned in the center of a four-arm arena and allowed to freely explore the maze composed of two dark arms and two brightly illuminated arms for 5 min. Healthy rodents ex- plore all the arms but spend the majority of time in the closed arms [42.] Increased time spent exploring the open arms denotes increased risk-taking behavior. When comparing different trauma models, we found that only male mice that received rTBI spent significantly more time in the open arms compared with sham control animals (**Figure 1B**).

None of the injury models evaluated impacted risk-taking behavior in the female cohorts (**Figure 1C**). When comparing male and female rTBI mice, we measured a significant sex-dependent injury effect; further, we did not observe differences in the time spent in the open arms when comparing male and female sham animals. These

results demonstrate that rTBI results in increased risk-taking behavior in male but not in female mice. Because no deficits were observed in female mice, we focused on rTBI-induced cellular changes in male mice.

The integrated stress response is activated at one-month after rTBI.

Aberrant activation of the ISR has been measured acutely and chronically in different models of TBI [19–21]. We investigated whether mild rTBI induces chronic activation of the ISR by quantifying p- eIF2a, ATF4, and BACE-1 levels in hemibrain lysates ~one month post-injury (**Supplementary Figure 1**). When investigating the impact of rTBI and ISRIB on p-eIF2a protein expression, we measured a significant injury ($p < 0.001$) and ISRIB effect ($p < 0.01$) (**Figure 2A**). Downstream modulators of ISR activation, ATF4 and BACE-1, were significantly increased when comparing sham and rTBI male mice (**Figure 2B, C**). Importantly, ISRIB administration reversed rTBI-induced ISR activation and downstream modulators to levels com- parable to sham animals (**Figure 2**). These data indicate that rTBI triggers a persistent activation of the ISR and that ISRIB can relieve this activation.

The small-molecule Integrated Stress Response Inhibitor, ISRIB, reverses rTBI mediated increased risk-taking behavior.

We demonstrated previously that ISR inhibition with the small molecule ISRIB can fully reverse trauma-induced hippocampal-dependent learning and memory deficits [19]. Here, we investigated whether ISR inhibition can reverse the increased risk-taking behavior. Male mice received five mild head injuries or sham surgery. We then

assessed risk-taking behavior one-month post-injury with the EPM (**Figure 3A**). The evening before EPM (day 30), animals received intraperitoneal injections of ISRIB (2.5 mg/kg) or vehicle (**Figure 3A**). Quantification of the time spent in the open arms was indistinguishable when comparing rTBI + ISRIB and sham groups (**Figure 3B**). Notably, a single injection of ISRIB was sufficient to reverse the rTBI-induced risk-taking phenotype.

Next, we investigated whether ISRIB could permanently reverse rTBI-induced risk-taking behavior. Animals received two additional doses of ISRIB, one immediately after EPM (day 31) and one the next day (day 32, **Figure 3A**—three doses in total) [19]. At ~three months (100 days) post-injury, we measured risk-taking behavior. No additional doses of ISRIB were administered after the initial three injections (**Figure 3A**). Once again, rTBI + vehicle animals displayed significant increases in time spent in the open arms of the EPM (**Figure 3C**). Importantly, the three ISRIB injections administered ~70 days prior reversed long-term rTBI-induced risk-taking behavior (**Figure 3C**). The ISRIB administration also reduced time spent in the open arms in sham animals. These data demonstrate that a pulse administration of ISRIB, one month after injury, can completely reverse the long-lasting risk-taking behavior phenotype after rTBI.

ISRIB treatment restores cell-specific vulnerability in type A layer V pyramidal neurons of the medial prefrontal cortex after rTBI.

The mPFC is a brain region implicated in complex behaviors, including contextual response and risk-taking behavior [43]. To investigate the neurophysiological

correlates of risk-taking behavior after rTBI and ISRIB treatment, we evaluated the intrinsic and synaptic properties of layer V pyramidal neurons in the mPFC, the primary output of the microcircuit. Layer V pyramidal neurons include at least two subtypes, denoted type A and type B, characterized by their morphology, intrinsic ion channel composition, and axonal projections to primarily subcortical or other cortical regions, respectively [41] (**Figure 4A, 5A**).

We distinguished these layer V neuronal subtypes by their electrophysiological properties (with prominence of the I_h-induced parameters in type A neurons including the sag and rebound in response to hyperpolarization, as well as the afterhyperpolarization after depolarization), as reported previously [41]. We detected no effect of trauma on the intrinsic excitability of either type A or type B neurons, similar to our previous results that grouped layer V neurons together [36] (**Supplementary Figure 2 and 3, Supplementary Tables 5 and 6**).

Conversely, we found a cell-specific change in synaptic input after rTBI. Specifically, type A neurons demonstrated a significant increase in the frequency of spontaneous excitatory synaptic currents (sEPSC) after rTBI (**Figure 4B, C**) without changes in the amplitude of sEPSCs (**Figure 4B, D**). Strikingly, a single treatment with ISRIB ~one month after rTBI reversed this synaptic hyperexcitability, decreasing the frequency of synaptic input to sham levels (**Figure 4B, C**). Excitatory synaptic frequency and amplitude did not change after rTBI or with ISRIB treatment in type B neurons (**Figure 5**).

Discussion

An estimated three million TBIs are reported annually in the United States. Of the reported cases, 70-90% are considered mild [44] and in anywhere from 10-40% of these individuals. long-term behavioral and cognitive impairments will develop [45–47]. Often deficits may not initially be observed after a single TBI; however, additional head injuries can have cumulating effects including both increased susceptibility to future injury as well as behavioral and cognitive deficits [6–8]. There are no clinically available therapeutics to treat or even ameliorate the devastating effects of mild rTBI. In this study, we found that male mice that received a mild TBI daily for five days (five total) displayed increased risk- taking behavior measured one and three months later. This behavior was specific to both type of trauma and sex of the animal. We detected no increase in risk-taking behavior in male mice exposed to other trauma models including a single focal injury and a single concussive injury without rotational acceleration. Further, female mice exposed to an identical rTBI paradigm did not display increased risk-taking behavior. This persistent behavioral phenotype corroborates the long-term maladaptive behavioral effects of rTBI also observed in humans. At the cellular and functional level, we found that the risk-taking behavior was associated with increased activation of the ISR and cell-specific synaptic alterations in the type A subtype of layer V pyramidal neurons of the mPFC. Importantly, targeting the ISR using the small molecule inhibitor ISRIB reversed rTBI-induced risk-taking behavior and the associated cell-specific deficits in synaptic function. Thus, we have identified for the first time the effectivity of ISRIB in reversing chronic behavioral deficits after rTBI along with cell-specific synaptic dysfunction in the mPFC.

In the general population, men are 40% more likely to have a TBI [48, 49]. Studies of female athletes, however, have found that women have more concussions than men when playing the same sport [50], making understanding of sex-dimorphic injury responses critical for a comprehensive appreciation of rTBI pathology. Further, a recent review suggested that in ~93% of pre-clinical TBI studies, biological sex as a variable was ignored [51]. Here we identified a different behavioral response to rTBI (five midline impacts) in male and female mice. Whereas multiple mild traumas resulted in significant increased risk-taking behavior in male mice, this maladaptive behavioral response did not develop in female rodents. To our knowledge, this is the first study to investigate sex- dimorphic responses at a chronic time point after repetitive TBI. Only one other group has investigated sex differences acutely after a unilateral rTBI (three total impacts)—in adolescent rats and measured increased anxiety-like behavior in both male and female rats [52, 53]. The behavioral end-point, number of impacts, or placement of the impact could account for the differences in our read-outs. Other studies of repetitive head injury replicated this increase in risk-taking phenotype in male mice [54-57]; however, sex differences were not evaluated in these previous reports.

Young female athletes are reported to have increased rates of concussion and more neurological symptoms that last longer compared with male counterparts [58, 59]. The frequency of global disability measured in females after work-related concussion, however, was lower when compared with male cohorts [58]. Importantly, superior executive function measured with the Wisconsin Card Sorting Test was identified in females compared with males with TBI after con- trolling for education, ethnicity, and

injury severity [61]. These studies suggest that much more research is needed to identify factors affecting vulnerability or resilience to TBI, especially rTBI, in women.

Likewise, the physiology underlying the sex-dimorphic response to rTBI that we have identified here is unclear. The biophysics of injury to the mPFC might be different in female mice given their smaller head size [62]. Notably, the volume of the mPFC exhibits sexual dimorphism in humans [63] and inhibitory neuronal subtypes show striking differences in composition by sex in some brain regions [64]. These differences might contribute to increased vulnerability to repetitive brain injury in male mice; however, the exact mechanism remains to be determined.

The ISR is a universal pathway that responds to a wide array of cellular stressors. The central regulatory step of the ISR is the phosphorylation of the a-subunit of eIF2 [18, 65–67]. Phosphorylation of eIF2a leads to inhibition of general protein synthesis [22, 23], with translation of a few select proteins including ATF4 [28, 29] and BACE-1 [24–27]. Previously, our group and others have identified that both focal and diffuse head injuries induce phosphorylation of eIF2a in the brain chronically after injury [19–21]. Brief interference with this pathway using the small-molecule inhibitor ISRIB at chronic time points completely rescued trauma-induced hippocampal-dependent learning and memory deficits [19]. In this study, we demonstrated that rTBI results in chronic activation of the ISR, and ISRIB administration at ~one month post-injury significantly reduced ATF4 and BACE-1 protein levels to those comparable to sham. Further, ISRIB treatment completely reversed rTBI-induced risk-taking behavior, and this rescue was long-lasting. Interestingly, while ISRIB treatment had no effect in sham animals acutely after treatment, we measured a long-term effect in the elevated plus

maze assay at the three month time point, similar to our previous reports that ISRIB treatment can improve performance in naïve and sham rodents [19, 33–35]. Our previous studies have focused on hippocampal-dependent memory, but risk-taking behavior has been associated with PFC function [43, 68]. Taken together, these studies suggest that ISR intervention strategies can restore and modify not only cognitive, but also behavioral changes controlled by diverse brain regions.

The mPFC integrates complex sensory information and modulates behavioral response [69]; as such, deficits in mPFC function have been linked to cognitive and behavioral dysfunction, including risk- taking behavior [43, 68]. Here, we demonstrated that an increase in the frequency of excitatory synaptic input specifically occurs in the type A layer V pyramidal neuron subtype at chronic time points after mild rTBI, associated with risk-taking behavior. This is the first study to examine mPFC function after rTBI, and only one other study has evaluated synaptic input in the mPFC after a single moderate TBI. Smith and associates [70] identified a prominent increase in the frequency of spontaneous and miniature excitatory post-synaptic currents and a decrease in the amplitude of inhibitory input in layer 2/3 pyramidal neurons ~one week after a single lateral fluid percussion injury that was associated with deficits in working memory. In contrast, layer V neurons did not show changes in synaptic input, and risk-taking behavior was not evaluated. The discrepancy between our studies could be because of several factors, including a different (and not repetitive) model of injury, the more subacute rather than chronic timing of their studies, and/or in particular, the fact that they did not specifically evaluate layer V neuronal subtypes.

Subtype-specific vulnerability of type A or subcortically projecting L5 pyramidal neurons has been identified in other animal models with behavioral deficits, including models of autism [71], suggesting that changes in synaptic input to these neurons might also directly affect mPFC-mediated behaviors after TBI. Properties of synaptic input to type A neurons in the mPFC have been hypothesized to be specifically responsive to focal strong input in the dendritic tree, ultimately providing a salient signal to subcortical structures [41]. Thus, altered synaptic properties in type A neurons after repetitive injury might be responsible for lack of appreciation of danger or risk in the animal.

Not only did we identify subtype-specific vulnerability in layer V after TBI, we notably found that this synaptic hyperexcitability could be rescued by a single injection of ISRIB at one month after injury. ISRIB has been found to exert activity-dependent changes in synaptic function including blocking metabotropic glutamate receptor-mediated long-term depression in the ventral tegmental area (VTA) in vitro [72] and enhancing cocaine-induced long-term potentiation in the VTA after in vivo injection [73]. In addition, ISRIB application in vitro has rescued TBI-induced deficits in LTP in the hippocampus [19]. Here, we expand the range of ISRIB treatment effects to include not only activity-dependent synaptic regulation, but also a rescue of cell-specific vulnerability in synaptic hyper-excitability. These intriguing findings suggest that cell-specific vulnerability, a common feature in neurodegenerative disease and now identified in rTBI, might be specifically addressed with inhibiting cellular stress.

We demonstrated that rTBI leads to a sex-dependent increase in long-lasting risk-taking behavior in male mice associated with synaptic hyperexcitability specifically in type A L5 pyramidal neurons of the mPFC. For the first time, we identified that

inhibition of the integrated stress response with ISRIB rescues a mPFC- dependent behavioral deficit and the associated cell-specific vulnerability. Overall, these results suggest that the ISR pathway may represent a key target in maladaptive circuit and cognitive functions after injury.

Materials and Methods

Animals. All experiments were conducted in accordance with National Institutes of Health (NIH) Guide for the Care and Use of Laboratory Animals and approved by the Institutional Animal Care and Use Committee of the University of California, San Francisco (AN170302). Male and female C57B6/J wild-type mice were received from Jackson Laboratories. Male animals were 8–10 weeks of age at the time of surgeries. Female animals were 10 weeks of age at the time of surgery to ensure full sexual maturity. Animal shipments were received at least one week before the start of experimentation to allow animals to habituate to the new surroundings. Mice were group housed in environmentally controlled conditions with a reverse light cycle (12:12 h light: dark cycle at 21 – 1°C; *50% humidity) and provided food and water ad libitum.

Surgical Procedure. All animals were randomly assigned to each TBI or sham surgery groups. Animals were anesthetized and maintained at 2-2.5% isoflurane.

Sham with sutures. Sham with sutures was performed as previously described [37]. Briefly, animals were secured to a stereotaxic frame with non- traumatic ear bars. A midline incision was made to expose the skull and the scalp was sutured.

Sham with no sutures. Sham without sutures was performed as described previously [36].

Repetitive mild TBI. The rTBI animals underwent multiple mild closed head injuries using the CHIMERA (Closed-Head Impact Model of Engineered Rotational Acceleration) device as reported previously [36, 38, 39]. Briefly, mice were placed supine into an angled holding platform to ensure the head was level with the piston target hole and that the impact was centered at the midline dorsal convexity of the skull, targeting bregma. A nose cone delivering isoflurane was removed just before impact. The impact was administered with a velocity range of ~3.9–4.5m/sec, resulting in an impact energy of 0.5J from the 5 mm, 50 g piston. The rTBI animals received an injury once per day for five days with ~24h interval in between impacts.

Focal TBI. Controlled cortical impact (CCI) surgery was performed as de- scribed previously [19, 37, 40]. Briefly, animals were secured to a stereotaxic frame with non-traumatic ear bars. A midline incision was made to expose the skull followed by a ~3.5-mm diameter craniectomy, a removal of part of the skull, using an electric micro- drill. The coordinates of the craniectomy were: anteroposterior, -2.00 mm and mediolateral, +2.00 mm with respect to bregma. Any animal that experienced excessive bleeding because of disruption of the dura was removed from the study.

After the craniectomy, the contusion was induced using a 3-mm convex tip attached to an electromagnetic impactor (Leica). The contusion depth was set to 0.95 mm from dura with a velocity of 4.0 m/sec sustained for 300 msec. After impact, the scalp was

sutured. These injury parameters were chosen to target, but not penetrate, the hippocampus.

Concussive TBI. Closed head injury (CHI) surgery was performed as described previously [19]. Briefly, animals were secured to a stereotaxic frame with non-traumatic ear bars, and the head of the animal was sup- ported with foam before injury. Contusion was induced using a 5- mm convex tip attached to an electromagnetic impactor (Leica) at the following coordinates: anteroposterior, -1.50 mm and medio- lateral, 0 mm with respect to bregma. The contusion was produced with an impact depth of 1 mm from the surface of the skull with a velocity of 5.0 m/sec sustained for 300 msec. Any animals that had a fractured skull after injury were excluded from the study. After impact, the scalp was sutured.

The approximate isoflurane exposure for each procedure is as follows: ~20–25 min for CCI and CHI, ~15–25 min for rTBI (3–5 min per exposure and five exposures total), ~20 min for sham with sutures, ~15–25 min for sham without sutures (3–5 min per exposure and five exposures total). After all surgeries, the animal recovered in an incubation chamber set to 37°C. Animals were returned to their home cage after showing normal walking and grooming behavior. All animals fully recovered from the surgical procedures as exhibited by normal behavior and weight maintenance monitored throughout the duration of the experiments.

Drug Administration. The ISRIB solution was made by dissolving 5 mg ISRIB in 1 mL dimethyl sulfoxide (DMSO) (PanReac AppliChem, 191954.1611). The solution was

heated gently in a 40°C water bath and vortexed every 30 sec until the solution became clear. Next, 1 mL of Tween 80 (Sigma Aldrich, P8074) was added, solution was heated gently in a 40°C water bath and vortexed every 30 sec until the solution became clear. Next, 10 mL of polyethylene glycol 400 (PEG400) (PanReac AppliChem, 142436.1611) solution was added, heated gently in a 40°C water bath and vortexed every 30 sec until the solution became clear. Finally, 36.5 mL of 5% dextrose (Hospira, RL-3040) was added. The solution was kept at room temperature throughout the experiment. Each solution was used for injec- tions up to 7 days maximum. The vehicle solution consisted of the same chemical composition and concentration (DMSO, Tween 80, PEG400, and 5% dextrose).

Stock ISRIB solution was at 0.1 mg/mL, but injections were at 2.5 mg/kg. We reported previously that a dose of 2.5 mg/kg reversed trauma-induced cognitive decline [19] and improved memory function in healthy animals [33]. In addition, we identified that a minimal dosing paradigm (3–4 treatments) was sufficient for learning and memory rescue [19].

Risk-taking Behavioral test. For all behavioral assays, the experimenters were blinded to surgery and drug intervention. Before behavioral analysis, animals were inspected for gross motor impairments. Animals were inspected for suture healing, whisker loss, limb immobility (including grip strength), and eye occlusions. If animals displayed any of these impairments, they were eliminated from the study. Behavioral tests were recorded and scored using a video tracking and analysis setup (Ethovision XT 8.5, Noldus

Information Technology). If tracking was unsuccessful, videos were scored by two individuals blinded to surgery and treatment group.

Risk-taking behavioral phenotype was evaluated using the Elevated Plus Maze (EPM) between 21–31 days (~one month) post-injury (counted from the day of the first injury) as described previously [36]. The EPM consists of two exposed, open arms (35 cm) opposite each other and two enclosed arms (30.5 cm) also across from each other. The four arms are attached to a center platform (4.5 cm square), and the entire maze is elevated 40 cm off the floor. Bright white lights illuminated both ends of the open arm. Mice were placed individually onto the center of the maze and allowed to explore the maze for 5 min, and their activity was recorded. The maze was cleaned with 70% ethanol between animals. Risk-taking behavior was measured by changes in time spent in the open arms + center.

No difference in time spent exploring the open arms was observed when comparing the sham animals – sutures and animals – vehicle injections (**Supplementary Table 1**); therefore, sham groups were combined for analysis. No differences in time spent exploring the open arms were observed when comparing the rTBI – vehicle injections (**Supplementary Table 2**); thus, rTBI groups were combined for analysis. Finally, no differences were observed when comparing animals that were exposed to the EPM once or twice (with three months in between exposures, **Supplementary Table 3**).

Western Blot Analysis. At the end of the behavioral test, animals were sacrificed, and the hemibrains were extracted and snap frozen on dry ice and then stored at -80°C.

Hemibrains were used for protein analysis because preliminary analysis found insufficient protein amounts (ATF4, BACE-1) in isolated brain regions. The frozen samples were then homogenized with a T 10 basic ULTRA-TURRAX (IKa) in ice- cold buffer lysis (Cell Signaling 9803) and protease and phosphatase inhibitors (Roche). Lysates were sonicated for 3min and centrifuged at 13,000 rpm for 20 min at 4°C.

Protein concentration in supernatants was determined using BCA Protein Assay Kit (Pierce). Equal amount of proteins (30 lg) was loaded on SDS-PAGE gels. Proteins were transferred onto 0.2 lm PVDF membranes (BioRad) and probed with primary antibodies diluted in Tris-buffered saline supplemented with 0.1% Tween 20 and 3% bovine serum albumin.

Phospho-eIF2a (Cell Signaling), eIF2a (Cell Signaling, Danvers, MA), BACE-1 (Cell Signaling), ATF4 (Abcam), and b-actin (Sigma-Aldrich) antibodies were used as primary antibodies. The horseradish peroxidase (HRP)-conjugated secondary antibodies (Rockland) were employed to detect immune-reactive bands using enhanced chemiluminescence (ECL Western Blotting Substrate, Pierce) according to the manufacturer's instructions. Quantification of protein bands was performed by densitometry using ImageJ software.

Phospho-eIF2a was normalized to total eIF2 protein levels. The ATF4 and BACE-1 levels were normalized to b-actin expression, and fold change is calculated as the levels relative to the expression in sham + vehicle-treated derived samples.

Electrophysiology. Coronal brain slices (250 lm) including the mPFC were pre- pared from mice that underwent rTBI or a sham procedure, 35–60 days prior, as well as mice

that underwent rTBI and received an ISRIB injection at *30 days post-injury. To conserve mice, a sham group that received an ISRIB injection was not included, because there was no difference in EPM behavior at 1 month after injury between sham mice alone compared with sham + ISRIB mice.

Mice were anesthetized with Euthasol (0.1 mL/25 g, Virbac, Fort Worth, TX, NDC-051311-050-01), and transcardially perfused with an ice-cold sucrose solution containing (in mM): 210 sucrose, 1.25 NaH_2PO_4, 25 $NaHCO_3$, 2.5 KCl, 0.5 $CaCl_2$, 7 $MgCl_2$, 7 dextrose, 1.3 ascorbic acid, 3 sodium pyruvate (bubbled with 95% O_2-5% CO_2, pH ~7.4) (see **Supplementary Table 4** for reagent information). Mice were then decapitated, and the brain was isolated in the same sucrose solution and cut on a slicing vibratome (Leica, VT1200S, Leica Microsystems, Wetzlar, Germany). Slices were incubated in a holding solution (composed of (in mM) 125 NaCl, 2.5 KCl, 1.25 NaH_2PO_4, 25 $NaHCO_3$, 2 $CaCl_2$, 2 $MgCl_2$, 10 dextrose, 1.3 ascorbic acid, 3 sodium pyruvate, bubbled with 95% O_2-5% CO_2, pH *7.4) at 36°C for 30 min and then at room temperature for at least 30 min until recording.

Whole cell recordings were obtained from these slices in a submersion chamber with a heated (32–34°C) artificial cerebrospinal fluid (aCSF) containing (in mM): 125 NaCl, 3 KCl, 1.25 NaH_2PO_4, 25 $NaHCO_3$, 2 $CaCl_2$, 1 $MgCl_2$, 10 dextrose (bubbled with 95% O_2/5% CO_2, pH *7.4). Patch pipettes (3–6MO) were manufactured from filamented borosilicate glass capillaries (Sutter Instruments, Novato, CA, BF100-58-10) and filled with an intra- cellular solution containing (in mM): 135 KGluconate, 5 KCl, 10 HEPES, 4 NaCl, 4 MgATP, 0.3 Na3GTP, 7 2K-phosphcreatine, and 1–2% biocytin.

Layer V pyramidal neurons were identified using infrared microscopy with a 40 · water-immersion objective (Olympus, Burlingame, CA).

Recordings were made using a Multiclamp 700B (Molecular Devices, San Jose, CA) amplifier, which was connected to the computer with a Digidata 1440A ADC (Molecular Devices, San Jose, CA), and recorded at a sampling rate of 20 kHz with pClamp software (Molecular Devices). We did not correct for the junction potential, but access resistance and pipette capacitance were appropriately compensated before each recording.

The passive membrane and active action potential (AP) spiking characteristics were assessed by injection of a series of hyperpolarizing and depolarizing current steps with a duration of 250 msec from -250 pA to 700 pA (in increments of 50 pA). The resting membrane potential was the measured voltage of the cell 5min after obtaining whole cell configuration without current injection; this value thus represents the resting potential of the cell after internal dialysis with the intracellular solution reported above. A holding current was then applied to maintain the neuron at ~-67 mV before/after current injections. The membrane resistance was determined from the steady-state voltage reached during the -50 pA current injection. The time constant was the time required to reach 63% of the maximum change in voltage for the -50 pA current injection.

The AP parameters including the half width, threshold, amplitude, and spike afterhyperpolarization (AHP) were measured from the current injection that was 100 pA above the first current injection that elicited spiking. The AP times were detected by re-cording the time at which the positive slope of the membrane potential crossed 0mV. From the AP times, the instantaneous frequency for each AP was determined (1/inter

spike interval). The AP rate as a function of current injection was examined by plot- ting the first instantaneous AP frequency versus current injection

amplitude. The F/I slope was then determined from the best linear fit of the positive values of this plot.

The AP or spike threshold was defined as the voltage at which the third derivative of V (d3V/dt) was maximal just before the AP peak. The AP amplitude was calculated by measuring the voltage difference between the peak voltage of the AP and the spike threshold. The half width of the AP was determined as the duration of the AP at half the amplitude. The spike AHP was the voltage difference between the AP threshold and the minimum voltage before the next AP. The rising and falling slopes of the AP were the maximum of the first derivative of V between the threshold to the peak amplitude, and the peak amplitude to the minimum voltage before the next AP, respectively. The adaptation index of each cell was the ratio of the last over the first instantaneous firing frequency, calculated at 250 pA above the current step that first elicited spiking.

Subthreshold properties indicative of the degree of IH current were assessed with two parameters: (1) the voltage sag—defined as the change in voltage between the maximum hyperpolarization and the steady state potential for the -200 pA current injection; (2) the rebound afterdepolarization (ADP)—defined as the change in voltage between the maximum depolarization and the steady state potential achieved immediately after ending the -200 pA current injection. Finally, the rebound AHP was measured as the change in voltage between the maximum hyperpolarization and the steady state potential achieved immediately after ending the +250 pA current injection.

The sum of these three variables was used as described previously to categorize pyramidal neurons as type A (> 6,5 mv) or type B (<6.5 mV) [41].

To measure the spontaneous excitatory post-synaptic currents (sEPSCs), cells were recorded in voltage clamp at a holding potential of -75 mV for 4 min, a holding potential that should have little inhibitory component given the reversal potential of chloride with these solutions. Analysis of sEPSCs was performed using a template matching algorithm in ClampFit 10.7 (Molecular De- vices, San Jose, CA). The template was created using recordings from multiple pyramidal cells and included several hundred synaptic events.

Access resistance (Ra) was monitored during recordings, and recordings were terminated if Ra exceeded 30 megaohms. Only stable recordings (< 50 pA baseline change) with a low baseline noise (< 8 pA root mean square) were included. The first 250 synaptic events or all the events measured in the 4 min interval from each cell were included for analysis. The median frequency and amplitude for these events was calculated for each cell to compare between groups.

Statistical Analysis. All data were analyzed with GraphPad Prism 8 statistical software. Statistical significance between groups for most variables was determined using a two-tailed t test, one-way analysis of variance (ANOVA), or two-way ANOVA. If data were outside of the normal distribution as indicated by an alpha <0.01 for both D'Agostino-Pearson omnibus and Shapiro-Wilk tests, a non- parametric test was used—specifically, a Kruskal-Wallis test was used for the electrophysiology parameters.

The firing responses to increasing current injections were analyzed as a repeated measures two-way ANOVA. The p values below 0.05 were considered significant.
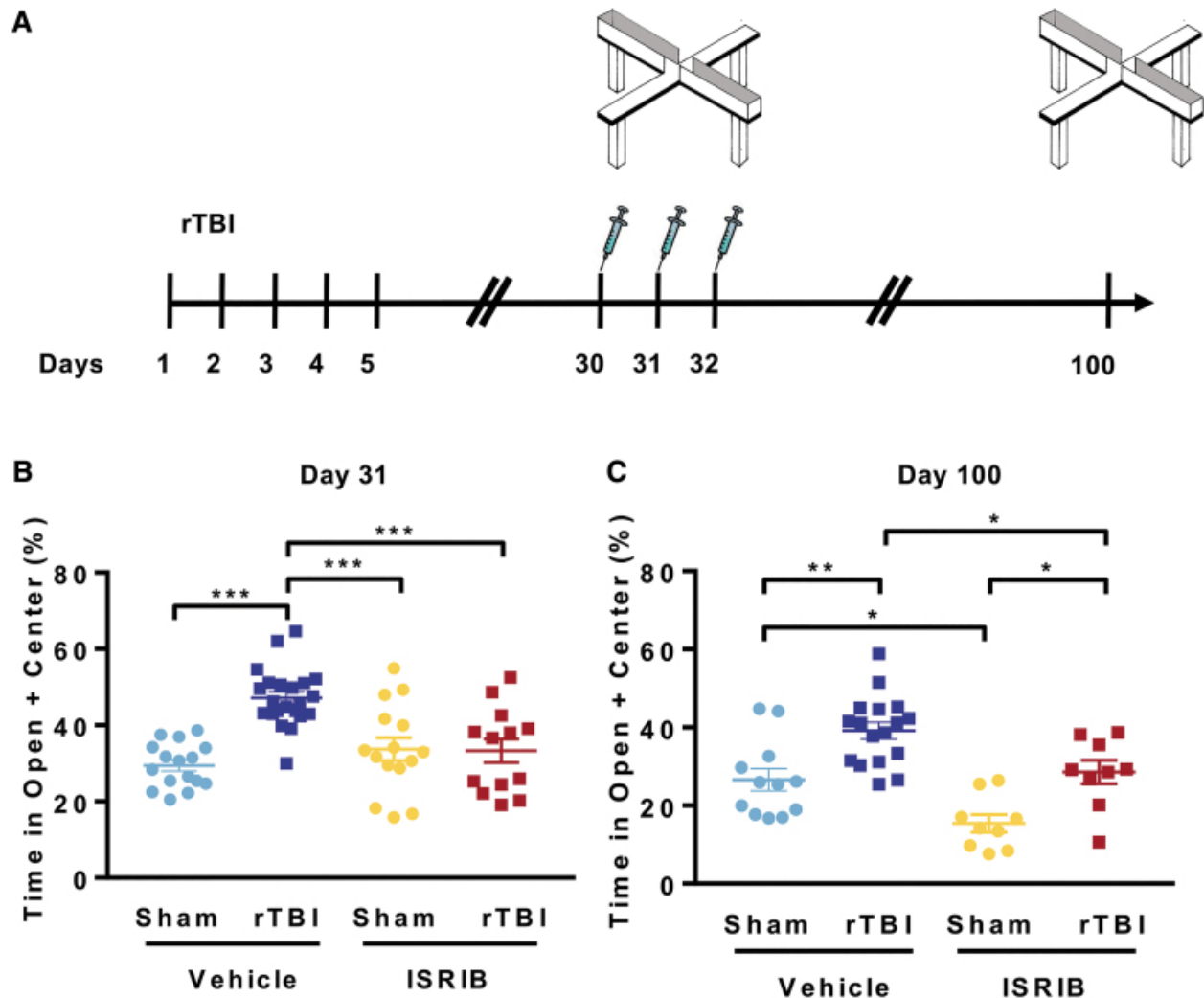
Figures
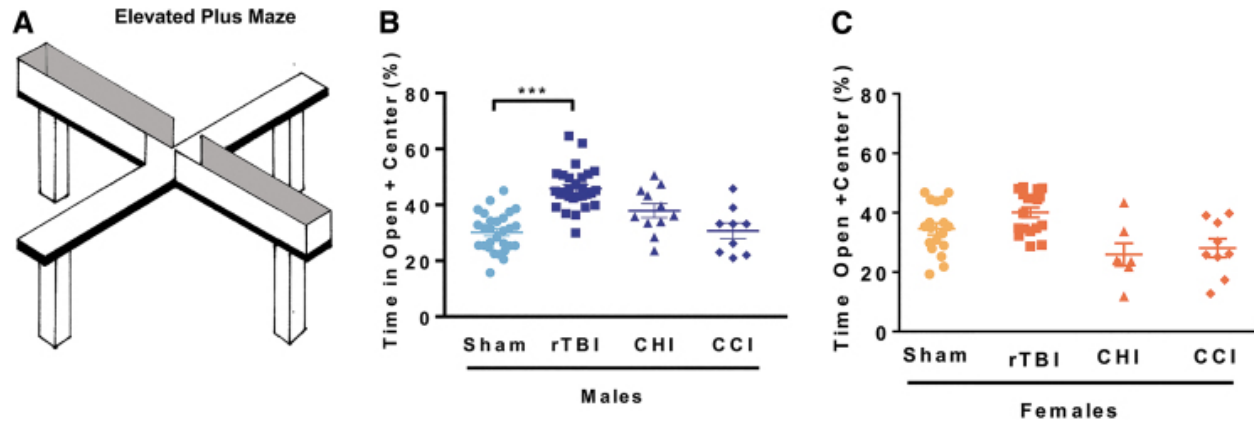
Figure 1. Repetitive mild traumatic brain injury increases risk-taking behaviors in males but not female cohorts.

Risk-taking behavior was measured in the elevated plus maze by increased time spent in the open arms (including center space). Comparison of three rodent trauma models found that risk-taking behavior was only measured after mild repetitive trauma in male cohorts. (**A**) Schematic of the elevated plus maze. (**B**) Male mice were exposed to either (1) mild rTBI, (2) mild concussive injury-closed head injury (CHI), (3) moderate focal injury-controlled cortical impact (CCI), or (4) sham surgery; risk-taking behavior was measured 30 days post-injury. Significant increases in time spent in the open arm were measured after rTBI. (**C**) Female mice were exposed to either (1) rTBI, (2) CHI, (3) CCI, or (4) sham surgery; risk-taking behavior was measured one month post-injury. No differences in risk- taking behavior were measured between groups. Two-way analysis of variance measured significant injury (p<0.001), sex effects (p < 0.001), and interaction (p < 0.001). Tukey post hoc analysis revealed group differences. Individual animal scores represented in dots; lines depict group mean and standard error of the mean.
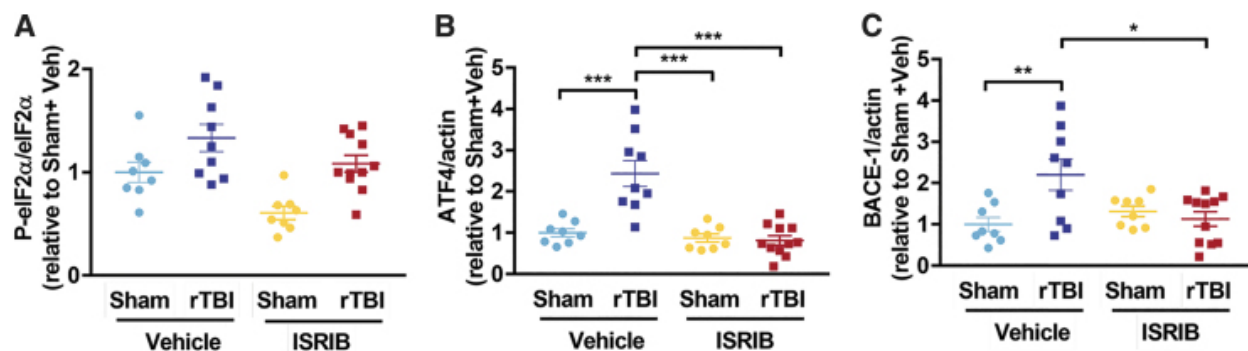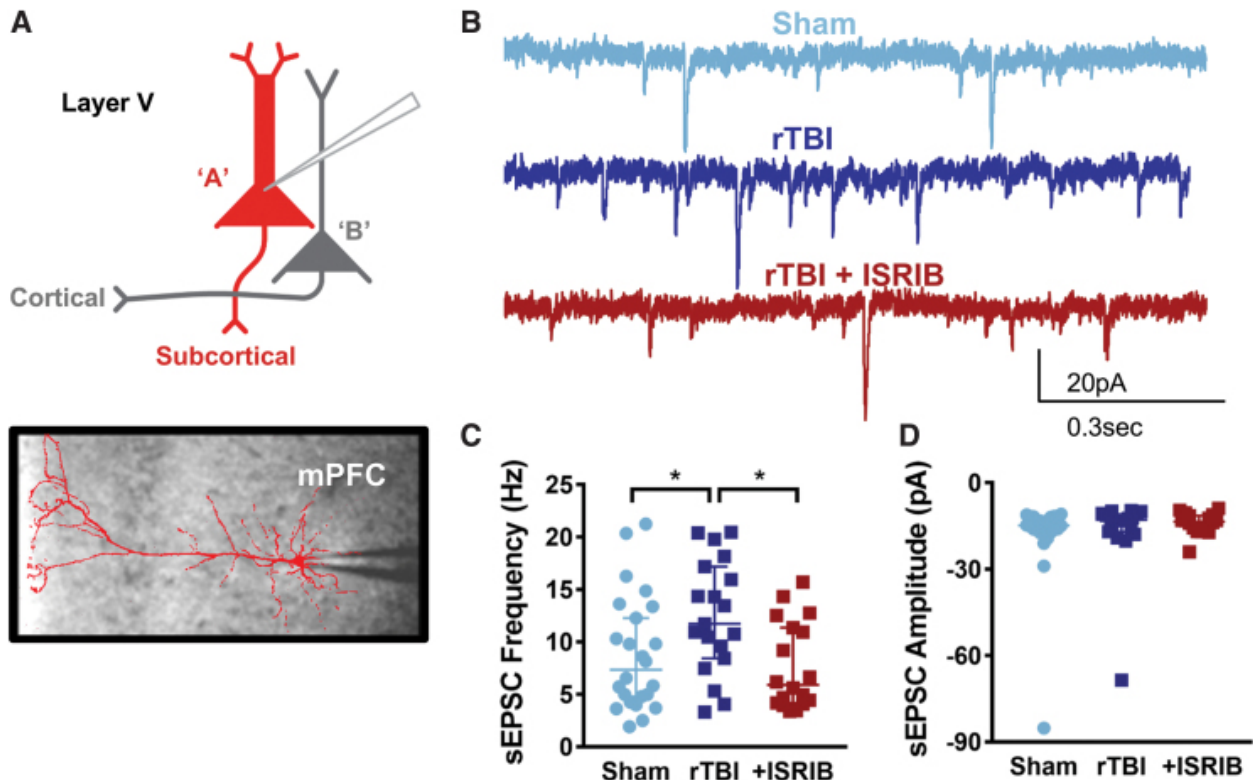
Figure 2. Integrated stress response (ISR) activation one month after repetitive mild traumatic brain injury (rTBI).

The impact of rTBI on ISR activation was investigated by Western blot analysis of hemibrain lysates. (**A**) Mild rTBI induced increases in p-eIF2a protein levels one-month post-injury. The p-eIF2a protein levels normalized to total eIF2a and standardized to sham vehicle group. Two-way analysis of variance (ANOVA) revealed a significant injury ($p < 0.001$), and ISR inhibitor (ISRIB) effect ($p < 0.01$). The rTBI significantly increased (**B**) ATF4 and (**C**) BACE-1 protein levels. The ISRIB treatment reversed rTBI-induced increases. (**B**) Two-way ANOVA revealed a significant injury ($p < 0.001$), ISRIB ($p < 0.001$) and ISRIB x injury effect ($p < 0.001$). Tukey post hoc analysis revealed differences between groups. (**C**) Two-way ANOVA revealed a significant injury ($p < 0.05$) and ISRIB x injury effect ($p < 0.01$). Tukey post hoc analysis revealed differences between groups. Individual animal scores represented in dots; lines depict group mean and standard error of the mean.

Figure 3. Small molecule inhibitor, ISRIB, reverses repetitive traumatic brain injury (rTBI) mediated risk- taking behavior.

(**A**) Experimental Design. Elevated Plus maze was performed at *31 and 100 days post-injury (dpi). The ISRIB (2.5 mg/kg intraperitoneal) was administered on days 30, 31, and 32 dpi. (**B**) A single ISRIB dose (2.5 mg/kg intraperitoneal) reversed trauma-induced risk-taking behavior at one-month post-surgery. Two-way analysis of variance (ANOVA) measures significant injury ($p<0.001$), ISRIB ($p<0.05$), and ISRIB x injury effect ($p<0.001$). Tukey post hoc analysis revealed differences between groups. (**C**) Permanent changes in risk-taking behavior were observed at ~3 months (100 days) post-injury. Three injections of ISRIB (70 days prior) completely reversed trauma-induced behavioral changes. Two-way ANOVA measures significant injury ($p < 0.001$) and ISRIB ($p < 0.001$) effect. Tukey post hoc analysis revealed differences between groups. Individual animal scores represented in dots; lines depict group mean and standard error of the mean.

Figure 4. Cell-specific vulnerability to mild repetitive TBI is observed in the prefrontal cortex with an increase in the frequency of synaptic input in type A layer V pyramidal neurons that is restored after integrated stress response inhibitor (ISRIB) treatment.

(**A**) Depiction of layer V pyramidal neurons indicating type A being recorded along with representative image of a filled type A pyramidal neuron overlaying image of patch pipette in the medial prefrontal cortex (mPFC). (**B**) Representative whole cell voltage-clamp recordings showing spontaneous excitatory post-synaptic currents (sEPSC) from layer V type A pyramidal neurons from sham mice (light blue), rTBI mice (dark blue), and rTBI mice treated with ISRIB (red). (**C**) The sEPSC frequency is increased in the rTBI neurons compared with both sham and rTBI+ISRIB groups (p = 0.028 for group effect; Kruskal-Wallis test, *p < 0.05 for post hoc tests controlling for false discovery rate). (**D**) The sEPSC amplitude is not significantly different between groups (p = 0.469 for group effect; Kruskal-Wallis test). The median frequency or amplitude for each neuron is represented with a symbol; solid lines indicate the median –95% confidence interval (n = 24, 19, 18 sham, rTBI, rTBI+ISRIB neurons, respectively, from 11 (sham), 7 (rTBI), and 9 (rTBI+ISRIB) animals/group with 1–4 neurons recorded per animal).
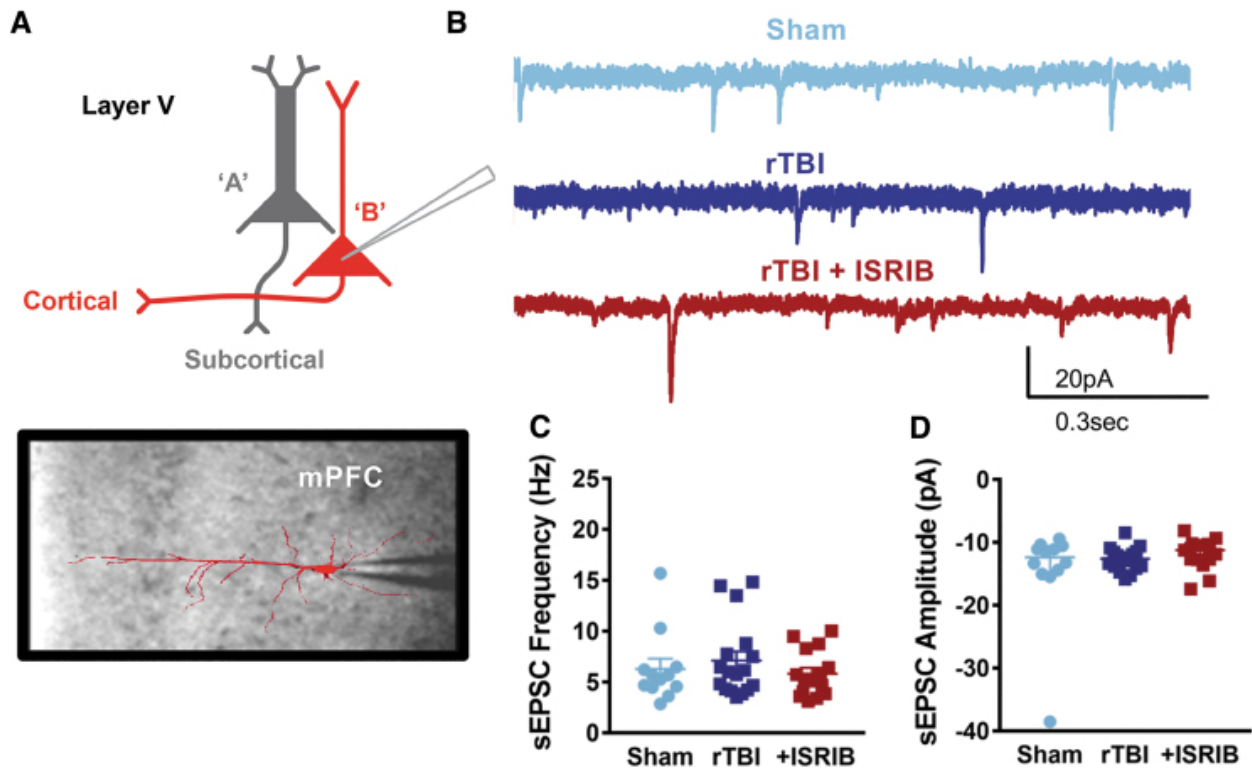
Figure 5. Synaptic input in type B layer V pyramidal neurons in the prefrontal cortex is not affected by mild repetitive traumatic brain injury (rTBI) or integrated stress response inhibitor (ISRIB) treatment.
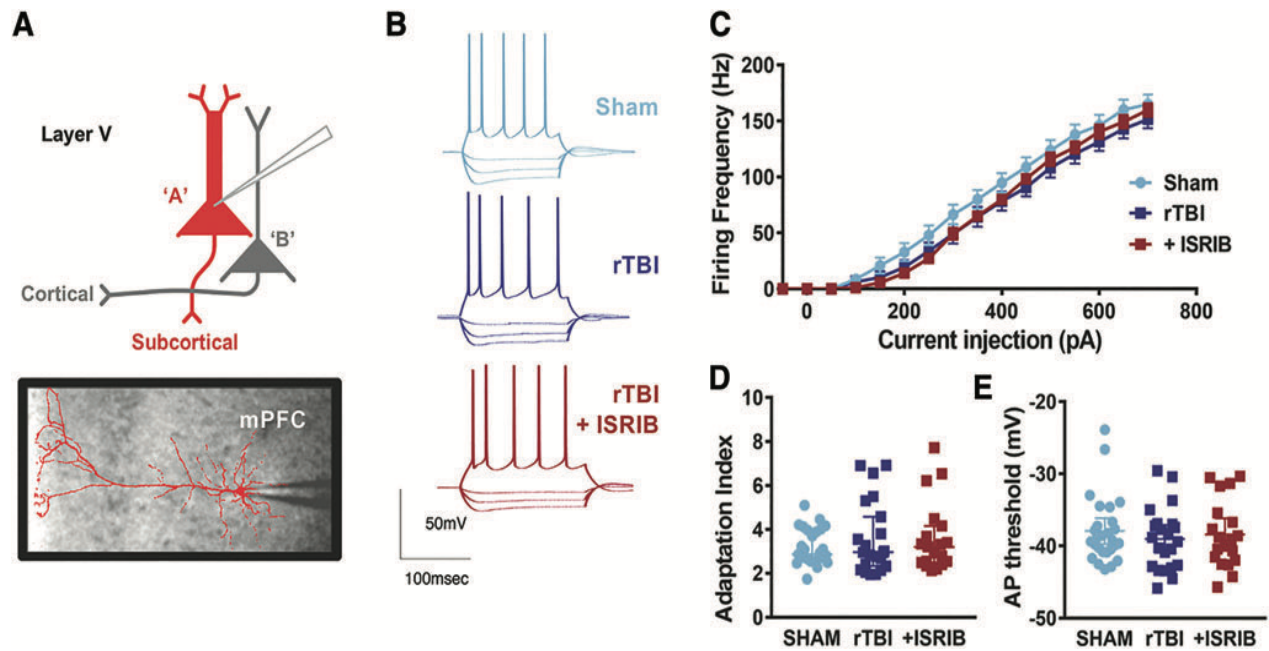
(**A**) Depiction of layer V pyramidal neurons indicating type B being recorded along with representative image of a filled type B pyramidal neuron overlaying image of patch pipette in the medial prefrontal cortex (mPFC). (**B**) Representative whole cell voltage-clamp recordings showing spontaneous excitatory post-synaptic currents (sEPSC) from layer V type B pyramidal neurons from sham mice (light blue), rTBI mice (dark blue), and rTBI mice treated with ISRIB (red). (**C**) The sEPSC frequency is not significantly different between groups (p = 0.664 for group effect; Kruskal-Wallis test). (**D**) The sEPSC amplitude is not significantly different between groups (p = 0.401 for group effect; Kruskal-Wallis test). The median frequency or amplitude for each neuron is represented with a symbol; solid lines indicate the median –95% confidence interval (n = 12, 17, 15 sham, rTBI, rTBI+ISRIB neurons, respectively, from 7 (sham), 5 (rTBI), and 8 (rTBI+ISRIB) animals/group with 1–4 neurons recorded per animal).
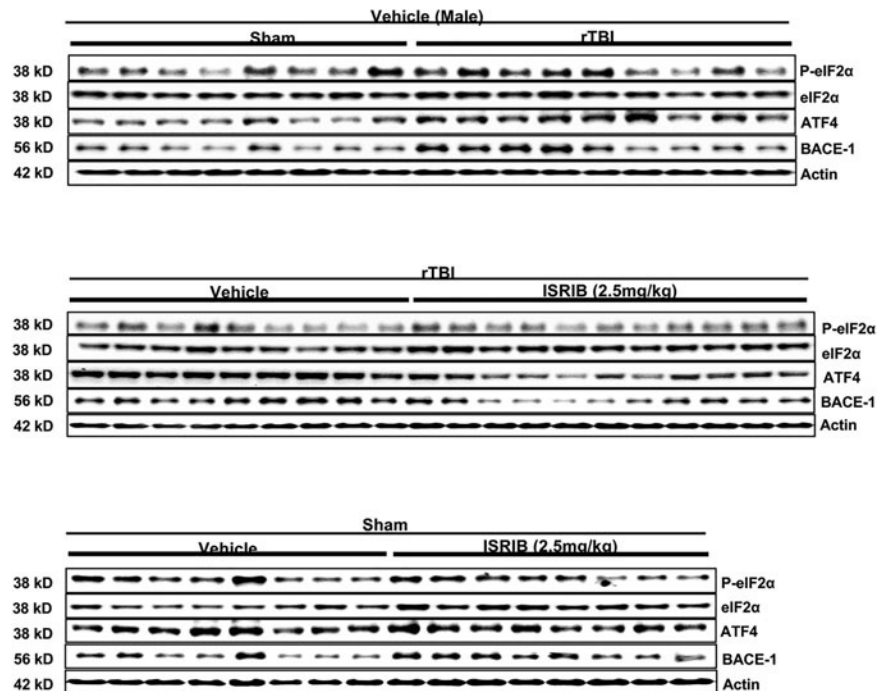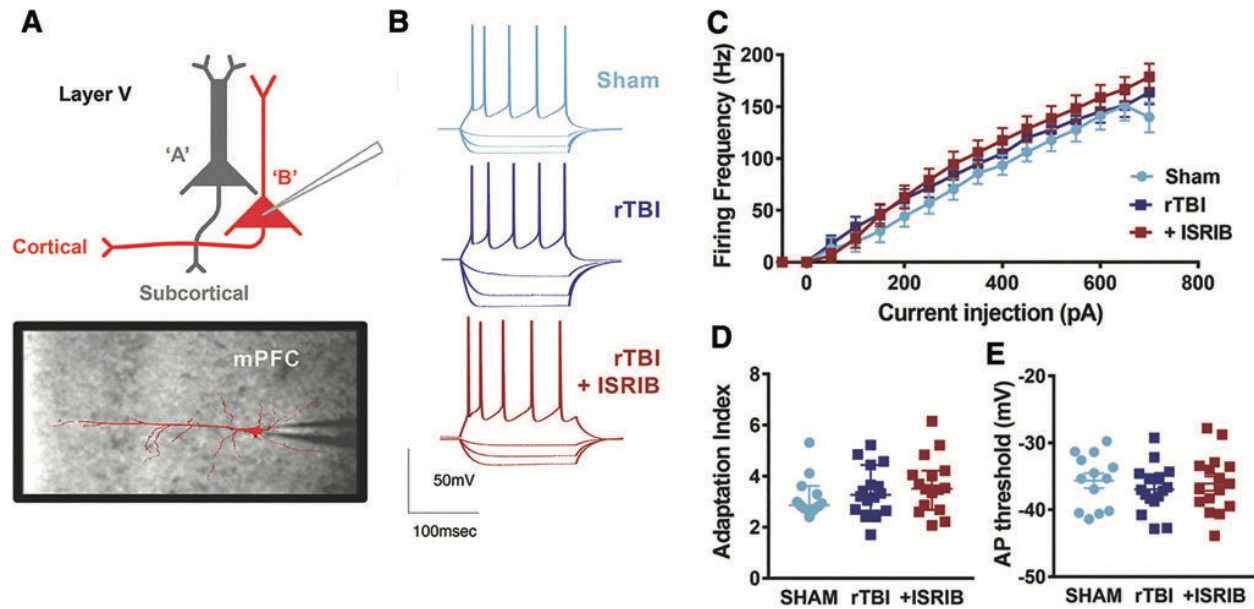
Supplemental Figure 1. Integrated stress response (ISR) pathway activation marker raw data.

Western blot analysis of hemibrains for ISR activation: p-eIF2a, total eIF2a, ATF4, BACE-1, and actin protein. Analysis was performed on multiple blots; raw data shown here. Protein levels were quantified to total eIF2a (p-eIF2a) or actin (ATF4, BACE-1) levels and standardized to sham + vehicle group. rTBI, repetitive traumatic brain injury; ISRIB, integrated stress response inhibitor.

Supplemental Figure 2. Intrinsic excitability in type A layer V pyramidal neurons is not modified by mild repetitive TBI (rTBI) or integrated stress response inhibitor (ISRIB) treatment.

(**A**) Depiction of layer V pyramidal neurons indicating type A being recorded along with representative image of a filled type A pyramidal neuron overlaying image of patch pipette in the medial prefrontal cortex. (**B**) Representative traces from type A layer V pyramidal neurons showing the membrane potential response to current injection (-250, -150, -50, 200pA) from sham mice (light blue), rTBI mice (dark blue), and rTBI mice treated with ISRIB (red). (**C**) No difference in the relationship of the first firing frequency versus amplitude of current injection was observed between groups (p = 0.252; repeated measures two-way analysis of variance). Likewise, other measures of intrinsic excitability including the adaptation index (**D**), p = 0.961; Kruskal- Wallis test) and the action potential threshold (**E**), p = 0.759; Kruskal-Wallis test) were similar between neurons from sham, rTBI, and rTBI+ISRIB mice. Each neuron is represented with a symbol; solid lines indicate the mean – standard error of the mean in C, and median – 95% confidence interval in D and E (n = 2 7, 22, 19 sham, rTBI, rTBI+ISRIB neurons, respectively, from 14 (sham), 11 (rTBI) and 9 (rTBI+ISRIB) animals/group with 1–4 neurons recorded per animal).

Supplemental Figure 3. Intrinsic excitability in type B layer V pyramidal neurons is not modified by mild repetitive TBI (rTBI) or integrated stress response inhibitor (ISRIB) treatment.

(**A**) Depiction of layer V pyramidal neurons indicating type B being recorded along with representative image of a filled type B pyramidal neuron overlaying image of patch pipette in the medial prefrontal cortex. (**B**) Representative traces from type B layer V pyramidal neurons showing the membrane potential response to current injection (-250, -150, -50, 200pA) from sham mice (light blue), rTBI mice (dark blue), and rTBI mice treated with ISRIB (red). (**C**) No difference in the relationship of the first firing frequency versus amplitude of current injection was observed between groups ($p = 0.423$; repeated measures two-way analysis of variance [ANOVA]). Likewise, other measures of intrinsic excitability including the adaptation index (**D**), $p = 0.425$; Kruskal- Wallis test) and the action potential threshold (**E**), $p = 0.675$; one-way ANOVA) were similar between neurons from sham, rTBI, and rTBI+ISRIB mice. Each neuron is represented with a symbol; solid lines indicate the mean – standard error of the mean in C and E, and median –95% confidence interval in D (n = 13, 16, 16 sham, rTBI, rTBI+ISRIB neurons, respectively, from 9 (sham), 8 (rTBI), and 8 (rTBI+ISRIB) animals/group with 1–4 neurons recorded per animal).

Supplemental Table 1. Elevated plus maze scores – Sham.

Elevated Plus Maze scores were compared between different types of sham surgeries. Specifics of different sham surgeries performed denoted in table but included number of isoflurane exposure, sutures, and vehicle injections. No differences between groups were observed; therefore, sham groups were combined for analysis.

Surgery	No. of isoflurane exposure	Sutures	No of vehicle Injections	Time in open + center (%)
Sham	1	Yes	0	31.1±2.4
Sham	5	No	0	31.5±1.7
Sham	5	No	1	26.7±2.2

Supplemental Table 2. Elevated plus maze scores – Vehicle.

Elevated Plus Maze scoreswere compared between rTBI +/- vehicle injection. No differences between groups were observed; therefore, repetitive traumatic brain injury (rTBI) groups were combined for analysis.

Surgery	No of vehicle Injections	Time in open + center (%)
rTBI	0	46.2±1.9
rTBI	1	45.2±1.9

Supplemental Table 3. Elevated plus maze scores – Performance.

Elevated Plus Maze (EPM) scores were compared between mice that performed EPM at both 31 days and 100 days versus mice that only performed EPM at 100 days. No differences between groups were observed; therefore, repetitive traumatic brain injury (rTBI) groups were combined for analysis.

Surgery	No of EPM	Time in open + center (%)
rTBI	1	40.0±3.2
rTBI	2	37.8±2.5

Supplemental Table 4. List of electrophysiology reagents.

Reagents for Patching	Company	Product #
Sucrose	Sigma-Aldrich, St. Louis, MO	S5016
NaH2PO4	Sigma-Aldrich, St. Louis, MO	S9638
NaHCO3	Sigma-Aldrich, St. Louis, MO	S6014
KCl	Sigma-Aldrich, St. Louis, MO	P9333
NaCl	Sigma-Aldrich, St. Louis, MO	S9888
CaCl2	Sigma-Aldrich, St. Louis, MO	223506
MgCl2	Sigma-Aldrich, St. Louis, MO	M9272
Dextrose	Sigma-Aldrich, St. Louis, MO	G5767
Ascorbic acid	Sigma-Aldrich, St. Louis, MO	A5960
Sodium pyruvate	Sigma-Aldrich, St. Louis, MO	P5280
K-gluconate	Sigma-Aldrich, St. Louis, MO	P1847
HEPES	Sigma-Aldrich, St. Louis, MO	H3375
MgATP	Sigma-Aldrich, St. Louis, MO	A9187
Na3GTP	Sigma-Aldrich, St. Louis, MO	G8877
2K-phosphcreatine	Millipore, Burlington, MA	237911
Biocytin	Tocris, Bristol, UK	3349

Supplemental Table 5. Intrinsic properties of Type A layer V pyramidal neurons.

rTBI, repetitive traumatic brain injury; ISRIB, integrated stress response inhibitor; ANOVA, analysis of variance; AHP, afterhyperpolarization. Values are mean (standard error of the mean) or *median (95% confidence interval). Statistical test is indicated with associated p-value.

Variables	Type A sham	Type A rTBI	Type A rTBI + ISRIB	p
Action potential properties				
Half width (msec)	*0.917 (0.859–1.008)	*0.858 (0.823–0.966)	*0.850 (0.792–0.916)	0.2430 (Kruskal-Wallis)
Amplitude (mV)	78.77 (1.87)	78.23 (1.90)	78.20 (1.90)	0.9704 (one-way ANOVA)
Threshold (mV)	*-39.25 (-39.76- -36.15)	*-39.14 (-40.97- - 37.14)	*-39.33 (-40.69- -36.19)	0.7586 (Kruskal-Wallis)
Rising slope (mv/s)	331.3 (16.8)	324.8 (16.4)	333.4 (16.3)	0.9353 (one-way ANOVA)
Falling slope (mv/s)	-79.86 (3.33)	-86.89 (4.14)	-89.83 (4.22)	0.1666 (one-way ANOVA)
Spike AHP (mV)	*10.80 (9.61–12.44)	*10.41 (7.97–12.74)	*11.46 (9.54–12.73)	0.3549 (Kruskal-Wallis)
Adaptation index	*2.86 (2.86–3.50)	*2.95 (2.84–4.30)	*3.20 (2.83– 4.37)	0.9614 (Kruskal-Wallis)
F/I slope (Hz/pA)	*0.287 (0.242–0.311)	*0.268 (0.212–0.305	*0.278 (0.246–0.291)	0.6500 (Kruskal-Wallis)
Subthreshold responses				
Sag+rebound+AHP (mV)	*8.81 (7.61-11.81)	*8.12 (7.53-8.71)	*8.893 (7.16- 10.16)	0.2097 (Kruskal-Wallis)
Rebound AHP	3.06 (0.23)	3.13 (0.13)	3.24 (0.25)	0.8362 (one-way ANOVA)
Passive properties				
Resting potential (mV)	*-62 (-65- -60)	*-63 (-66- -60)	*-65 (-66- -64)	0.2066 (Kruskal-Wallis)
Membrane resistance (MW)	*108.2 (88.6–125.7)	*82.81 (73.6–111.1)	*79.97 (65.3–105.7)	0.2015 (Kruskal-Wallis)

Supplemental Table 6. Intrinsic properties of Type B layer V pyramidal neurons.

rTBI, repetitive traumatic brain injury; ISRIB, integrated stress response inhibitor; ANOVA, analysis of variance; AHP, afterhyperpolarization. Values are mean (standard error of the mean) or *median (95% confidence interval). Statistical test is indicated with associated p-value.

Variables	Type B sham	Type B rTBI	Type B rTBI + ISRIB	p
Action potential properties				
Half width (msec)	*0.988 (0.906-1.262)	*1.050 (0.941-1.184)	*1.131 (1.033-1.213)	0.3524 (Kruskal-Wallis)
Amplitude (mV)	71.01(2.27)	73.66 (1.50)	70.44 (1.72)	0.3951 (one- way ANOVA)
Threshold (mV)	-35.65 (1.11)	-36.93 (0.89)	-36.09 (1.08)	0.6753 (one- way ANOVA)
Rising slope (mv/s)	266.8 (21.8)	279.3 (13.1)	251.7 (12.6)	0.4400 (one- way ANOVA)
Falling slope (mv/s)	-64.46 (5.44)	-65.44 (4.17)	-60.53 (3.04)	0.6688 (one- way ANOVA)
Spike AHP (mV)	13.16 (0.63)	11.76 (0.77)	11.65 (0.62)	0.2648 (one- way ANOVA)
Adaptation index	*2.86 (2.69–3.64)	*3.26 (2.88–3.91)	*3.51 (3.06–4.23)	0.4252 (Kruskal-Wallis)
F/I slope (Hz/pA)	0.236 (0.15)	0.221 (0.021)	0.244 (0.018)	0.6597 (one- way ANOVA)
Subthreshold responses				
Sag+rebound +AHP (mV)	4.47 (0.48)	3.60 (0.40)	3.86 (0.42)	0.3794 (one-way ANOVA)
Rebound AHP	1.24 (0.21)	1.48 (0.20)	1.42 (0.26)	0.7607 (one-way ANOVA)
Passive properties				
Resting potential (mV)	-64 (2)	-67 (1)	-64 (2)	0.3267 (one-way ANOVA)
Membrane resistance (MW)	175.0 (21.2)	199.9 (23.5)	177.9 (18.4)	0.6588 (one-way ANOVA)
Time constant	24.47 (1.56)	26.18 (2.03)	23.98 (1.91)	0.6771 (one-way ANOVA)

References

1. Smith, D.H., Johnson, V.E., Stewart, W., *Chronic neuropathologies of single and repetitive TBI: substrates of dementia?* Nat Rev Neurol, 2013. **9**: p. 211-221.

2. DeKosky, S.T., Ikonomovic, M.D., Gandy, S., *Traumatic brain injury--football, warfare, and long-term effects.* N Engl J Med, 2010. **363**: p. 1293-1296.

3. Engberg, A.W., Teasdale, T.W., *Psychosocial outcome following traumatic brain injury in adults: a long-term population-based follow-up.* Brain Inj, 2004. **18**: p. 533-545.

4. Sullivan, P., Petitti, D., Barbaccia, J., *Head trauma and age of onset of dementia of the Alzheimer type.* JAMA, 1987. **257**: p. 2289-2290.

5. Nelson, L.D et al., *Recovery After Mild Traumatic Brain Injury in Patients Presenting to US Level I Trauma Centers: A Transforming Research and Clinical Knowledge in Traumatic Brain Injury (TRACK-TBI) Study.* JAMA Neurol, 2019.

6. Lasry, O. et al., *Epidemiology of recurrent traumatic brain injury in the general population: A systematic review.* Neurology, 2017. **89**: p. 2198-2209.

7. Belanger, H.G., Spiegel, E., Vanderploeg, R.D., *Neuropsychological performance following a history of multiple self-reported concussions: a meta-analysis.* J Int Neuropsychol Soc, 2010. **16**: p. 262-267.

8. Geddes, J.F. et al., *Neuronal cytoskeletal changes are an early consequence of repetitive head injury.* Acta Neuropathol, 1999, **98**: p. 171-178.

9. Manley, G et al., *A systematic review of potential long-term effects of sport-related concussion.* Br J Sports Med, 2017. **51**: p. 969-977.

10. McAllister, T. and McCrea, M., *Long-Term Cognitive and Neuropsychiatric Consequences of Repetitive Concussion and Head-Impact Exposure.* J Athl Train, 2017 **52**: p. 309-317.

11. Castile, L et al., *The epidemiology of new versus recurrent sports concussions among high school athletes, 2005-2010.* Br J Sports Med, 2012. **46**: p. 603-610.

12. McKee, A.C. et al., *Chronic traumatic encephalopathy in athletes: progressive tauopathy after repetitive head injury.* J Neuropathol Exp Neurol, 2009. **68**: p. 709-735.

13. Stern, R.A. et al., *Clinical presentation of chronic traumatic encephalopathy.* Neurology, 2013. **81**: p. 1122-1129.

14. Mez, J. et al., *Clinicopathological Evaluation of Chronic Traumatic Encephalopathy in Players of American Football.* JAMA, 2017. **318**: p. 360-370.

15. Juengst, S.B. et al., *Exploratory associations with tumor necrosis factor-alpha, disinhibition and suicidal endorsement after traumatic brain injury.* Brain Behav Immun, 2014. **41**: p. 134-143.

16. Polinder, S. et al., *A Multidimensional Approach to Post-concussion Symptoms in Mild Traumatic Brain Injury.* Front Neurol 9, 2018. **1113**.

17. Tellier, A. et al., *The heterogeneity of mild traumatic brain injury: Where do we stand?* Brain Inj, 2009. **23**: p. 879-887.

18. Donnelly, N. et al., *The eIF2alpha kinases: their structures and functions.* Cell Mol Life Sci, 2013. **70**: p. 3493-3511.

19. Chou, A., Krukowski, K. et al., *Inhibition of the integrated stress response reverses cognitive deficits after traumatic brain injury.* Proc Natl Acad Sci U S A, 2017. **114**: p. E6420-E6426.

20. Dash, P.K. et al., *Inhibition of Eukaryotic Initiation Factor 2 Alpha Phosphatase Reduces Tissue Damage and Improves Learning and Memory after Experimental Traumatic Brain Injury.* J Neurotrauma, 2015. **32**: p. 1608-1620.

21. Rubovitch, V. et al., *The neuroprotective effect of salubrinal in a mouse model of traumatic brain injury.* Neuromolecular Med, 2015. **17**: p. 58-70.

22. Hinnebusch, A.G., Ivanov, I.P., Sonenberg, N., *Translational control by 5'-untranslated regions of eukaryotic mRNAs.* Science, 2016. **352**: p. 413-1416.

23. Sonenberg, N. and Hinnebusch, A.G., *Regulation of translation initiation in eukaryotes: mechanisms and biological targets.* Cell, 2009. **136**: p. 731-745.

24. De Pietri Tonelli, D. et al., *Translational regulation of BACE-1 expression in neuronal and non-neuronal cells.* Nucleic Acids Res, 2004. **32**: p. 1808-1817.

25. Lammich, S. et al., *Expression of the Alzheimer protease BACE1 is suppressed via its 5'-untranslated region.* EMBO Rep, 2004. **5**: p. 620-625.

26. Mihailovich, M. et al., *Complex translational regulation of BACE1 involves upstream AUGs and stimulatory elements within the 5' untranslated region.* Nucleic Acids Res, 2007. **35**: p. 2975-2985.

27. O'Connor, T. et al., *Phosphorylation of the translation initiation factor eIF2alpha increases BACE1 levels and promotes amyloidogenesis.* Neuron, 2008. **60**: p. 988-1009.

28. Chen, A. et al., *Inducible enhancement of memory storage and synaptic plasticity in transgenic mice expressing an inhibitor of ATF4 (CREB-2) and C/EBP proteins.* Neuron, 2003. **39**: p. 655-669.

29. Pasini, S. et al., *Specific downregulation of hippocampal ATF4 reveals a necessary role in synaptic plasticity and memory.* Cell Rep, 2015. **11**: p. 183-191.

30. Costa-Mattioli, M. et al., *eIF2alpha phosphorylation bidirectionally regulates the switch from short- to long-term synaptic plasticity and memory.* Cell, 2017. **129**: p. 195-206.

31. Batista, G. et al., *Translational control of auditory imprinting and structural plasticity by eIF2alpha.* Elife, 2016. **5**.

32. Jiang, Z. et al., *eIF2alpha Phosphorylation-dependent translation in CA1 pyramidal cells impairs hippocampal memory consolidation without affecting general translation.* J Neurosci, 2010. **30**: p. 2582-2594.

33. Sidrauski, C. et al., *Pharmacological brake-release of mRNA translation enhances cognitive memory.* Elife, 2013. **2**: p. e00498.

34. Sidrauski, C. et al., *The small molecule ISRIB reverses the effects of eIF2alpha phosphorylation on translation and stress granule assembly.* Elife, 2015. **4**.

35. Sidrauski, C. et al., *Pharmacological dimerization and activation of the exchange factor eIF2B antagonizes the integrated stress response.* Elife, 2015. **4**: p. e07314.

36. Nolan, A. et al., *Repeated Mild Head Injury Leads to Wide-Ranging Deficits in Higher-Order Cognitive Functions Associated with the Prefrontal Cortex.* J Neurotrauma, 2018. **35**: p. 2425-2434.

37. Krukowski, K., Chou, A. et al., *Traumatic brain injury in aged mice induces chronic microglia activation, synapse loss, and complement-dependent memory deficits.* Int J Mol Sci, 2018. **19**.

38. Namjoshi, D.R. et al., *Merging pathology with biomechanics using CHIMERA (Closed-Head Impact Model of Engineered Rotational Acceleration): a novel, surgery-free model of traumatic brain injury.* Mol Neurodegener, 2014. **9**: p. 55.

39. Namjoshi, D.R. et al., *Defining the biomechanical and biological threshold of murine mild traumatic brain injury using CHIMERA (Closed Head Impact Model of Engineered Rotational Acceleration).* Exp Neurol, 2017. **292**: p. 80-91.

40. Chou, A., Krukowski, K. et al., *Persistent Infiltration and Impaired Response of Peripherally-Derived Monocytes after Traumatic Brain Injury in the Aged Brain.* Int J Mol Sci, 2018. **19**.

41. Lee, A.T. et al., *Pyramidal neurons in prefrontal cortex receive subtype-specific forms of excitation and inhibition.* Neuron, 2014. **81**: p. 61-68.

42. Lister, R.G., *The use of a plus-maze to measure anxiety in the mouse.* Psychopharmacology (Berl), 1987. **92**: p. 180-185.

43. Bogg, T. et al., *Cognitive control links alcohol use, trait disinhibition, and reduced cognitive capacity: Evidence for medial prefrontal cortex dysregulation during reward-seeking behavior.* Drug Alcohol Depend , 2012. **122**: p. 112-118.

44. Cassidy, J.D. et al., *Incidence, risk factors and prevention of mild traumatic brain injury: results of the WHO Collaborating Centre Task Force on Mild Traumatic Brain Injury.* J Rehabil Med, 2004. p 28-60.

45. Binder, L.M., Rohling, M.L., Larrabee, G.J., *A review of mild head trauma. Part I: Meta-analytic review of neuropsychological studies.* J Clin Exp Neuropsychol, 1997. **19**: p. 421-431.

46. Willer, B. and Leddy, J.J., *Management of concussion and post-concussion syndrome.* Curr Treat Options Neurol, 2006. **8**: p. 415-426.

47. Mittenberg, W. et al., *Treatment of post-concussion syndrome following mild head injury.* J Clin Exp Neuropsychol, 2001. **23**: p. 829-836.

48. Faul, M. and Coronado, V., *Epidemiology of traumatic brain injury.* Handb Clin Neurol, 2015. **127**: p. 3-13.

49. Coronado, V.G. et al., *Trends in Traumatic Brain Injury in the U.S. and the public health response: 1995-2009.* J Safety Res, 2012. **43**: p. 299-307.

50. Covassin, T., Moran, R., Elbin, R.J., *Sex Differences in Reported Concussion Injury Rates and Time Loss From Participation: An Update of the National Collegiate Athletic Association Injury Surveillance Program From 2004-2005 Through 2008-2009.* J Athl Train, 2016. **51**: p. 189-194.

51. Spani, C.B., Braun, D.J., Van Eldik, L.J., *Sex-related responses after traumatic brain injury: Considerations for preclinical modeling.* Front Neuroendocrinol, 2018. **50**: p. 52-66.

52. Yamakawa, G.R. et al., *Behavioral and pathophysiological outcomes associated with caffeine consumption and repetitive mild traumatic brain injury (RmTBI) in adolescent rats.* PLoS One, 2017. **12**: p. e0187218.

53. Wright, D.K. et al., *Sex matters: repetitive mild traumatic brain injury in adolescent rats.* Ann Clin Transl Neurol, 2017. **4**: p. 640-654.

54. Mouzon, B.C. et al., *Chronic neuropathological and neurobehavioral changes in a repetitive mild traumatic brain injury model.* Ann Neurol, 2014. **75**: p. 241-254.

55. Petraglia, A.L. et al., *The spectrum of neurobehavioral sequelae after repetitive mild traumatic brain injury: a novel mouse model of chronic traumatic encephalopathy.* J Neurotrauma, 2014. **31**: p. 1211-1224.

56. Kondo, A. et al., *Antibody against early driver of neurodegeneration cis P-tau blocks brain injury and tauopathy.* Nature, 2015. **523**: p. 431-436.

57. Mouzon, B.C. et al., *Lifelong behavioral and neuropathological consequences of repetitive mild traumatic brain injury.* Ann Clin Transl Neurol, 2018. **5**: p. 64-80.

58. Mollayeva, T., El-Khechen-Richandi, G., Colantonio, A., *Sex & gender considerations in concussion research.* Concussion, 2018. **3**: p. CNC51.

59. Covassin, T., Schatz, P., Swanik, C.B., *Sex differences in neuropsychological function and post-concussion symptoms of concussed collegiate athletes.* Neurosurgery, 2007. **61**: p. 341-350.

60. Hatskevich, C.W., Itkis, M.L., Maloletnev, V.I. *Off-line methods for detection and correction of EEG artefacts of various origin.* Int J Psychophysiol, 1992. **12**: p. 179-185.

61. Niemeier, J.P. et al., *Gender differences in executive functions following trau- matic brain injury.* Neuropsychol Rehabil, 2007. **17**: p. 293–313.

62. Caccese, J.B. et al., *Head and neck size and neck strength predict linear and rotational acceleration during purposeful soccer heading.* Sports Biomech, 2018. **17**: p. 462-476.

63. Ruigrok, A.N. et al., *A meta-analysis of sex differences in human brain structure.* Neurosci Biobehav Rev, 2014. **39**: p. 34-50.

64. Kim, Y. et al., *Brain-wide Maps Reveal Stereotyped Cell-Type-Based Cortical Architecture and Subcortical Sexual Dimorphism.* Cell, 2017. **171**: p. 456-469 e422.

65. Ron, D. and Harding, H.P., *Protein-folding homeostasis in the endoplasmic reticulum and nutritional regulation.* Cold Spring Harb Perspect Biol, 2012. **4**.

66. Tsai, J.C. et al., *Structure of the nucleotide exchange factor eIF2B reveals mechanism of memory-enhancing molecule.* Science, 2018. **359**.

67. Zyryanova, A.F. et al., *Binding of ISRIB reveals a regulatory site in the nucleotide exchange factor eIF2B.* Science, 2018. **359**: p. 533-1536.

68. St Onge, J.R. and Floresco, S.B., *Prefrontal cortical contribution to risk-based decision making.* Cereb Cortex, 2010. **20**: p. 1816-1828.

69. Riga, D. et al, *Optogenetic dissection of medial prefrontal cortex circuitry.* Front Syst Neurosci, 2014. **8**: p. 230.

70. Smith, C.J. et al., *Brain Injury Impairs Working Memory and Prefrontal Circuit Function.* Front Neurol, 2015. **6**: p. 240.

71. Brumback, A.C. et al., *Identifying specific prefrontal neurons that contribute to autism-associated abnormalities in physiology and social behavior.* Mol Psychiatry, 2018. **23**: p. 2078-2089.

72. Di Prisco, G.V. et al., *Translational control of mGluR-dependent long-term depression and object-place learning by eIF2alpha.* Nat Neurosci, 2014. **17**: p. 1073-1082.

73. Placzek, A.N. et al., *eIF2alpha-mediated translational control regulates the persistence of cocaine-induced LTP in midbrain dopamine neurons.* Elife, 2016. **5**.

CHAPTER 4: Small molecule cognitive enhancer reverses age-related memory decline

Abstract

With increased life expectancy age-associated cognitive decline becomes a growing concern, even in the absence of recognizable neurodegenerative disease. The integrated stress response (ISR) is activated during aging and contributes to age-related brain phenotypes. We demonstrate that treatment with the drug-like small-molecule ISR inhibitor ISRIB reverses ISR activation in the brain, as indicated by decreased levels of activating transcription factor 4 (ATF4) and phosphorylated eukaryotic translation initiation factor eIF2. Furthermore, ISRIB treatment reverses spatial memory deficits and ameliorates working memory in old mice. At the cellular level in the hippocampus, ISR inhibition i) rescues intrinsic neuronal electrophysiological properties, ii) restores spine density and iii) reduces immune profiles, specifically interferon and T cell-mediated responses. Thus, pharmacological interference with the ISR emerges as a promising intervention strategy for combating–age-related cognitive decline in otherwise healthy individuals.

Introduction

The impact of age on cognitive performance represents an important quality-of-life and societal concern, especially given our prolonged life expectancy. While often discussed in the context of disease, decreases in executive function as well as learning and memory decrements in older, healthy individuals are common [1, 2, 3 , 4]. According to the US Department of Commerce the aging population is estimated by

2050 to reach 83.7 million individuals above 65 years of age in the US; this represents a rapidly growing healthcare and economic concern [5].

Age-related decline in memory has been recapitulated in preclinical studies with old rodents [6-9]. Specifically, prior studies have identified deficits in spatial memory [8, 10], working and episodic memory [7, 9] and recognition memory [11], when comparing young, adult mice with older sex-matched animals. The hippocampus is the brain region associated with learning and memory formation and is particularly vulnerable to age-related changes in humans and rodents [12-15]. Deficits in a number of cellular processes have been suggested as underlying causes based on correlative evidence, including protein synthesis [16], metabolism [17], inflammation [18], and immune responses [8, 10, 19, 20]. While providing a wealth of parameters to assess, by and large the causal molecular underpinnings of age-related memory decline have remained unclear.

The principle that blocking protein synthesis prevents long-term memory storage was discovered many years ago [21]. With age there is a marked decline of protein synthesis in the brain that correlates with defects in proper protein folding [11, 22-24]. Accumulation of misfolded proteins can activate the integrated stress response (ISR) [25], an evolutionary conserved pathway that decreases protein synthesis. In this way, the ISR may have a causative role in age-related cognitive decline. We previously discovered that interference with the drug-like small-molecule inhibitor (integrated stress response inhibitor, or ISRIB) rescued traumatic brain injury-induced behavioral and cognitive deficits [26-28], suggesting that this pharmacological tool may be useful in testing this notion.

Increasing age leads to structural and functional changes in hippocampal neurons. Specifically, in old animals there is an increase in neuronal hyperpolarization after spiking activity ("afterhyperpolarization", or AHP) that decreases intrinsic neuronal excitability and correlates with memory deficits [12-15, 29]. Aging also manifests itself with synaptic excitability changes in the hippocampus that correlate with a reduction in the bulbous membrane projections that form the postsynaptic specializations of excitatory synapses, termed dendritic spines [30, 31]. Morphological changes in dendritic spine density are critical for spatial learning and memory [32, 33]. Whether these age-related neuronal changes can be modified or are linked with ISR activation has yet to be determined.

In addition to neuronal changes, ISR activation can modify immune responses via alterations in cytokine production [34]. Indeed, maladaptive immune responses have been linked with cognitive decline in the old brain [7, 8, 10, 19]. Initial studies focused on age-associated cytokine responses, including interferon (IFN)-mediated cognitive changes [19, 35]. Type-I IFN responses can induce age-related phenotypes in rodents. Furthermore, the adaptive immune system (T cell infiltration into the old brain) can regulate neuronal function via IFN-γ production [20], suggesting the possibility that age-induced maladaptive immune responses and the ISR are linked. Here we explore the possibility of ISR inhibition by ISRIB as a potential strategy for modifying age-induced neuronal, immune, and cognitive dysfunction.

Results

ISRIB resets the ISR in the brain of old mice.

ISR activation leads to global reduction in protein synthesis but also to translational up-regulation of a select subset of mRNAs whose translation is controlled by small upstream open-reading frames in their 5'-UTRs [36, 37]. One well-studied ISR-upregulated target protein is ATF4 (activating transcription factor 4) [38, 39]. We recently showed ISRIB administration reversed mild head trauma-induced elevation in ATF4 protein [27]. Using the same ISRIB treatment paradigm of daily injections on 3 consecutive days [26, 27], we found decreased age-associated ATF4 protein levels in mouse brain lysates when compared to vehicle-treated controls during ISRIB administration (**Supplemental Figure 1**). ATF4 levels 18 days after cessation of ISRIB treatment showed persistent reduction in age-induced ATF4 protein levels that were indistinguishable from young mice (**Figure 1A, B, Supplemental Figure 2A**).

The key regulatory step in the ISR lies in the phosphorylation of eukaryotic translation initiation factor eIF2 [25]. Four known kinases can phosphorylate Ser51 in its α-subunit of (eIF2α) to activate the ISR [40]: HRI (heme-regulated inhibitor), PKR (double-stranded RNA-dependent protein kinase), PERK (PKR-like ER kinase) and GCN2 (General amino acid control nonderepressible 2). Only three of these kinases are known to be expressed in the mammalian brain (PKR, PERK, GCN2). To understand upstream modifiers of age-related ISR activation, we investigated the impact of age and ISRIB administration on the expression of these kinases. We found a modest, but significant increase in activated GCN2 (as indicated by its phosphorylated form p-GCN2) when comparing young and old brain lysates (**Figure 1C**, **Supplemental Figure**

113

2B). Moreover, when ISRIB was administered weeks prior (**Figure 1A**), GCN2 activation returned to levels comparable to young brains (**Figure 1C**, **Supplemental Figure 2B**). Age and ISRIB did not impact phosphorylation status of PERK and PKR in total brain lysates (**Figure 1D**, **E**, **Supplemental Figure 2B**). Thus, brief ISRIB administration in the old brain has long-lasting effects on ISR activation.

Inhibition of the ISR reverses age-induced decline in spatial learning and memory.

To assess whether the reduction in ISR activation affects age-related cognitive defects, we tested the capacity for spatial learning and memory in young and old mice in a radial arm water maze [26, 41]. This particular forced-swim behavior tool measures hippocampal-dependent spatial memory functions in rodents and has been previously used to assess age-related cognitive deficits [6, 42]. Animals were trained for two days (two learning blocks/day) to locate a platform hidden under opaque water in one of the eight arms using navigational cues set in the room (**Figure 2A**). We recorded the total number of entries into the non-target arm (errors) before the animal found the escape platform with automated tracking software and used it as a metric of learning. After two days of training, young animals averaged one error prior to successfully locating the escape platform, while old animals averaged three errors, indicating their reduced learning capacity (**Supplemental Figure 3A**).

We next tested whether pharmacological inhibition of the ISR could modify the age-related spatial learning deficits. ISRIB treatment started the day before the first training day and continued with daily injections throughout the duration of the training (3

114

injections in total; see **Figure 2A**, left). By the end of two days of training, ISRIB-treated old animals averaged two errors prior to finding the escape platform, while vehicle-treated old animals averaged three, denoting significant learning improvement in the mice that received ISRIB (**Supplemental Figure 3B**). No difference in learning performance was measured in young mice that received the identical treatment paradigm (**Supplemental Figure 3C**), suggesting that ISRIB-induced learning improvement measured in this training regime is age-dependent. These results were confirmed in an independent old animal cohort, in which we tested an additional ISR inhibitor (Cmp-003, a small molecule with improved solubility and pharmacological properties (PCT/US18/65555)), using an identical training/injection paradigm (**Supplemental Figure 3D**). Old animals that received Cmp-003 made significantly fewer errors prior to locating the escape platform than old animals that received vehicle injections, again indicating significant learning improvement.

Spatial memory of the escape location was measured one week later by reintroducing the animals into the pool and measuring the number of errors before they located the hidden platform. The animals did not receive any additional treatment during this task. Old mice treated with ISRIB one week before made significantly fewer errors compared to matched, vehicle-treated old male (**Figure 2B**) and female (**Supplemental Figure 4**) mice. Remarkably, the memory performance of old animals treated with ISRIB a week before was comparable to that of young mice (**Figure 2B**). These results demonstrate that brief treatment with ISRIB rescues age-induced spatial learning and memory deficits, cementing a causative role of the ISR on long-term memory dysfunction.

ISRIB administration improves age-induced deficits in working and episodic memory weeks after treatment.

Given the long-lasting effect of brief ISRIB treatment on ATF4 protein levels in the brain and on memory function one week after drug administration, we next tested the duration of ISRIB effects on age-related cognitive function. On experimental day 20 (18 days post ISRIB treatment, **Figure 2A**, right), we measured working and episodic memory using a delayed-matching-to-place paradigm (DMP) [26, 43] in the same animal cohort without additional ISRIB treatment. Previous work has demonstrated that old mice display significant impairments when compared to young mice [7, 9]. During DMP animals learned to locate an escape tunnel attached to one of 40 holes in a circular table using visual cues. The escape location was changed daily, forcing the animal to relearn its location. To quantify performance, we used analysis tracking software to measure "escape latency", reporting the time taken by the mouse to enter the escape tunnel. Old mice that received ISRIB treatment 18 days earlier displayed significant improvement over the four-day testing period (**Figure 2C**; Day 20 vs. Day 23). By Day 23 post-treatment animals were locating the escape tunnel on average 20 seconds faster than the matched-vehicle group (**Figure 2C**). This behavior is indicative of improved working and episodic memory. By contrast, old animals that received vehicle injections did not learn the task (**Figure 2C**; Day 20 vs. Day 23), as previously observed [7, 9]. These results demonstrate that ISRIB administration increases cognitive performance in a behavioral paradigm measured weeks after administration.

ISRIB treatment reverses age-associated changes in hippocampal neuron function.

To determine the neurophysiological correlates of ISRIB treatment on cognition, we investigated its effects on hippocampal neuronal function. Utilizing whole cell patch clamping, we recorded intrinsic electrophysiological firing properties and synaptic input in CA1 pyramidal neurons of young and old mice and compared them to those of old mice treated with a single injection of ISRIB the day prior to recording (**Figure 3A**).

We evaluated alterations in intrinsic excitability by measuring action potential shape and frequency properties and passive membrane response properties produced by a series of hyperpolarizing and depolarizing current steps (20 steps from -250 to 700 pA, 250 ms duration). We also assessed the hyperpolarization of the membrane potential following high frequency firing, specifically the AHP following ~50 Hz spiking activity induced with a current step (**Figure 3A**). In agreement with previous reports [12-15, 29], old mice displayed a significantly increased AHP amplitude when compared to young mice (**Figure 3B**). ISRIB treatment reversed the age-induced increase in AHP amplitude, rendering the CA1 neuronal response in ISRIB-treated old mice indistinguishable from young mice (**Figure 3B**). We did not find significant differences in other action potential or passive membrane properties between groups (**Supplemental Figure 5**).

We also measured spontaneous excitatory postsynaptic currents (sEPSC), while holding the cell at -75 mV in a voltage clamp. Both the frequency and amplitude of sEPSCs were indistinguishable between groups (**Supplemental Figure 6**). These data support that ISRIB treatment in old animals restores neuronal function to levels

comparable to young neurons by affecting intrinsic excitability and specifically reducing the AHP following high frequency firing.

ISRIB treatment reduces dendritic spine loss.

To determine if ISRIB might affect age-induced synaptic structural changes, we quantified dendritic spine density after ISRIB treatment in old mice with fluorescently labeled excitatory neurons (marked by a genomically encoded Thy1-YFP fusion protein). The hippocampus of old mice is characterized by a reduction in dendritic spine density that correlates with diminished cognitive output [30, 31]. Old Thy1-YFP expressing mice received ISRIB treatment and two days of behavioral training as described in **Figure 2A**. At the end of Day 2, we terminated the animals and harvested the brains for quantification of dendritic spine density in the hippocampus (stratum radiatum of CA1) (**Figure 3C**) using confocal microscopy imaging and unbiased analysis (**Figure 3D**). Similar to previous reports, we measured a significant reduction in dendritic spine density in old when compared to young Thy1-YFP mice (**Figure 3E**) [30, 31]. ISRIB treatment significantly increased spine numbers when compared with age-matched vehicle-treated mice (**Figure 3E**). Taken together these data demonstrate that ISRIB administration improves both neuron structure and function in old mice.

Age-induced inflammatory tone is reduced following ISRIB treatment.

Because it is known that immune dysregulation in the brain increases with age [44] and correlates with reduced cognitive performance in old animals [7, 8, 10, 19], we next investigated immune parameters impacted by ISRIB administration in the old brain. To this end, we first investigated glial cell activation (microglia and astrocytes) in

118

hippocampal sections from of old mice and ISRIB-treated old mice by fluorescent microscopic imaging (during ISRIB administration, **Supplemental Figure 7**). We measured, astrocyte and microglia reactivity as the percent area covered by GFAP and Iba-1. In these analyses, we observed no differences between the old and ISRIB-treated old animals (**Supplemental Figure 7B-G**).

Next, we performed quantitative PCR (qPCR) analyses on hippocampi from young, old, and ISRIB-treated animals on samples taken at the same time point as in the microscopic analysis (**Supplemental Figure 7A**). We measured a panel of inflammatory markers, many of which are known to increase with age [44], with a particular focus on IFN-related genes as this pathway is implicated in age-related cognitive decline [19, 35]. Indeed, we found that age increased expression of a number of IFN response pathway genes, *Rtp4, Ifit1, and Gbp10* (**Figure 4A-C**). Importantly, ISRIB administration reduced expression of *Rtp4, Ifit1, and Gbp10* to levels that became indistinguishable from young animals **(Figure 4A-C)**. Other inflammatory makers were also increased with age (*Ccl2, Il6*) but not affected by ISRIB treatment, whereas *Cd11b* was increased upon ISRIB administration alone (**Table 1**).

Using these same hippocampal extracts, we next measured T cell responses. Similar to other reports [20, 45], we observed a significant increase in T cell marker mRNA expression (*Cd3*) in the hippocampus of old compared to young mice (**Figure 4D**). ISRIB treatment in the old mice reduced the expression of the T cell marker to a level comparable to that observed in young mice (**Figure 4D**). The ISRIB-induced reduction in T cell marker levels was not limited to the brain but extended to the peripheral blood of old animals, with CD8$^+$ T cell percentages reduced following ISRIB

administration (**Figure 4E**). By contrast, we observed no changes in CD4$^+$ T cell levels (**Figure 4F**).

Given the broad and varied response of immune parameters in response to ISRIB treatment, we next explored possible relationships between behavioral performance and age-related inflammatory tone. T cell marker mRNA expression in the brain positively correlated with cognitive performance: mice with lower T cell marker expression made fewer errors prior to locating the escape platform during memory testing on Day 2 (**Figure 4G**). We also observed significant positive correlations when comparing memory performance on day 2 (errors) with the mRNA levels of multiple IFN response pathway genes (*Ifit1, Rtp4, Gbp10, Gbp5, Oasl1*) and additional inflammatory markers (*Ccl2, Il6*) (**Figure 4G**). These data demonstrate that increased inflammatory marker expression correspond with poorer cognitive performance, even when we did not observed differences between the groups. These studies revealed that ISRIB treatment impacts a broad number of immune parameters both in the periphery and in the brain reducing the age-related inflammatory tone which strongly correlates with improved cognition.

ISRIB treatment resets age-related ISR activation

Finally, we investigated the transcriptional expression of ISR mediators and neuronal health markers in the hippocampal lysates used above. We did not detect differences in *Gadd34, Pkr, Bdnf1,* and *Ophn1* mRNA levels with age or ISRIB treatment (**Table 1**). Interestingly however, when analyzed as individual animals, we found a negative correlation between *Gadd34* mRNA and cognitive performance:

animals with less *Gadd34* mRNA made more errors prior to locating the escape platform during memory testing (**Figure 5A**). GADD34, the regulatory subunit of one of the two eIF2α phosphatases, acts in a feedback loop as a downstream target of ATF4 [46-48]. Induction of GADD34 leads to decreased phosphorylation of eIF2 which counteracts ISR activation. Indeed, ISRIB treatment reduced p-eIF2 levels in total brain lysates (**Figure 5B; Supplemental Figure 8**), suggesting that ISRIB may break a feedback loop thereby resetting age-related ISR activation.

Discussion

Here we provide evidence for a direct involvement of the ISR in age-related cognitive decline. Temporary treatment with ISRIB causes a long lasting down-regulation of ATF4 (measured up to 20 days post treatment). The "ISR reset" leads to improvement in spatial, working, and episodic memory. At a cellular level the cognitive enhancement is paralleled by i) improved intrinsic neuron excitability, ii) increased dendritic spine density, iii) reversal of age-induced changes in IFN and T cell responses in the hippocampus and blood, and iv) reversal of ISR activation. Thus, we identify broad-spectrum anatomical, cellular, and functional changes caused by ISR activation in old animals. If these findings in mice translate into human physiology, they offer hope and a tangible strategy to sustain cognitive ability as we age.

Alterations in proteostasis, the process of protein synthesis, folding and degradation, is a hallmark of aging [22]. Accumulation of protein aggregate in the brain is a contributing factor to disease development and progression in several age-related neurodegenerative diseases including Alzheimer's and Parkinson's disease [49, 50].

The rate of protein synthesis reportedly also declines with age in various regions of the brain [16]. Protein synthesis is critical for memory consolidation and the ISR pathway is one of the major nodes for protein synthesis control. Therefore, we investigated how interference with the ISR impacted healthy age-related cognitive decline. ISRIB rapidly enters the brain of old animals and interferes with ISR activation as measured by decreased phosphorylation of eIF2α and ATF4 levels. ISRIB acts downstream of phosphorylation of eIF2α [51]; therefore, the decrease in phosphorylation of eIF2α suggests a possible block in the feedback loop that keeps the ISR activated in the old brain; further investigation is needed to understand the exact mechanism. Initial findings suggest this could be through modulation of the kinase GCN2. Here we found that age increased activation of GCN2 (denoted by increased phosphorylation) was attenuated by ISRIB administration. These data indicate that even brief inhibition of the ISR allows the system to 'reset' and dampen the stress response in the old brain.

Along with the ISR, the mammalian target of rapamycin (mTOR), is the other important pathway that cells employ to respond to environmental stress and balance between survival and death. Rapamycin, arguably the most studied and validated small molecule for lifespan expansion, targets mTOR and therefore inhibits mTOR-controlled mRNA translation. However, increased protein production due to mTOR (over)activation can in turn induce the ISR [52-54], which serves as a governor keeping protein synthesis in check. Interestingly, despite these two pathways regulating distinct stress responses to translational regulation, it was recently reported that both the ISR and mTOR converge at the level of mRNA translation and both inhibit the translation of the same set of proteins [55]. This complex interplay between mTOR signaling and the ISR

could potentially explain how pharmacological treatment with seemingly opposing strategies could both be beneficial.

The reduction in ISR activation corresponded with improved memory performance in old mice weeks after treatment was stopped. Importantly, brief ISRIB treatment improved performance in two different behavioral paradigms (radial arm water maze and the delayed matching to place) previously shown to capture age-related cognitive decline [7, 9, 10, 35, 42, 56]. These behavioral paradigms model different aspects of cognitive loss observed during aging in rodents: spatial, working and episodic memory [41, 43]. Therefore, our results suggest that ISR inhibition can reverse a broad spectrum of cognitive decline. Notably, spatial learning reversal occurred during ISRIB treatment while the effects on memory were measured weeks after administration and demonstrate the long-lasting effects of ISRIB even in the aging brain. Most of the previous studies were performed exclusively in male rodents [10, 35, 42, 56]. Sex-dimorphic cognitive decline has been reported with age in humans [57-59] and rodents [60, 61]. In the current study we identified cognitive reversal with ISRIB administration in both male and female mice; taking the critical first steps towards studying sex-dimorphic age responses in the ISR. However, we only validated ISRIB-mediated neuronal and immune correlates in male mice. Further work is required to investigate the restorative effects in females.

The neuronal correlates of improved memory function were identified in measures of i) intrinsic excitability and ii) dendritic spine number. In CA1 pyramidal neurons, we found that ISRIB treatment reversed the age-associated increase in the afterhyperpolarization (AHP) amplitude following high frequency (50 Hz) spiking activity

123

to levels found in young mice. AHP is the hyperpolarization of the neuron after an action potential or series of action potentials. The hyperpolarization affects the amount of depolarization needed for subsequent firing thereby influencing intrinsic excitability. An increase of AHP is associated with aging [29, 62] and impaired learning in young rodents [63]. We recapitulated these cellular deficits and we demonstrated that inhibition of the ISR can revert the age-induced increase in intrinsic excitability back to young levels.

Changes in dendritic spine density or structural reorganization of spines are thought to be important for synaptic function [64] and cognitive processes such as learning and memory [32, 33, 65, 66]. In the aging brain there is a reduction in hippocampal spine density that has been suggested to be responsible for the poor memory functions [11, 30, 31]. A number of age-related molecular processes have been linked to spine loss including disruption in local protein synthesis [67]. We demonstrated that ISRIB administration alleviated the age-related reductions in hippocampal spine density.

ISRIB down-regulated several immune response pathways in the hippocampus of old animals, including IFN response genes. The importance of this molecule in age-related decline has been demonstrated: Type I IFN responses are increased with age [19, 35], IFN-β expression in the brain is associated with cognitive decline, and injection of IFN-β expressing viral vectors into an adult mouse can induce an old phenotype [19, 35]. Here we found that ISRIB administration reversed age-induced type I IFN responses in the hippocampus suggesting that ISR activation plays a role in this pathway. However, it is still unclear if this is via a direct or indirect effect on

inflammatory cells. Several recent publications have identified deleterious roles for T cells in neuronal health or cognitive decline [20, 68, 69]. Two recent reports found that persistent T cell infiltration in the brain following viral infection leads to synapse loss [68, 69]. Investigators identified that IFN-γ produced by T cells mediated synapse loss [68, 69]. Here we find that ISRIB treatment impacted T cell levels both in the brain and periphery. The changes in T cells and IFN responses directly correlated with cognitive performance and, again, were restored by ISRIB to the levels observed in young animals. Whether ISRIB reverses cognitive decline by directly modulating one of the measured processes (neuronal intrinsic excitability, dendritic spine number, IFN response, or T cell numbers) or by impacting a number of them remains to be determined.

Aging is an inevitable process for all living creatures, improving our understanding of cellular and molecular processes associated with healthy aging can allow for intervention strategies to modulate cognitive decline. Here we demonstrate that pharmacological attenuation of the ISR can alleviate age-related neuronal and immune changes potentially resetting age-induced cognitive decline.

Materials and Methods

Animals. All experiments were conducted in accordance with National Institutes of Health (NIH) Guide for the Care and Use of Laboratory Animals and approved by the Institutional Animal Care and Use Committee of the University of California, San Francisco (Protocol 170302). Male and female C57B6/J wild-type (WT) mice were received from the National Institute of Aging. Thy-1-YFP-H (in C57 background) males

125

were bred and aged in house. Old animals started experimentation at ~19 months of age and young animals 3-6 months of age. Animal shipments were received at least one week prior to start of experimentation to allow animals to habituation the new surroundings. Mice were group housed in environmentally controlled conditions with reverse light cycle (12:12 h light:dark cycle at 21 ± 1 °C; ~50% humidity) and provided food and water ad libitum. Behavioral analysis was performed during the dark cycle.

Drug Administration. ISRIB solution was made by dissolving 5 mg ISRIB in 2.5 mLs dimethyl sulfoxide (DMSO) (PanReac AppliChem, 191954.1611). The solution was gently heated in a 40 °C water bath and vortexed every 30 s until the solution became clear. Next 1 mL of Tween 80 (Sigma Aldrich, P8074) was added, the solution was gently heated in a 40 °C water bath and vortexed every 30 s until the solution became clear. Next, 10 mL of polyethylene glycol 400 (PEG400) (PanReac AppliChem, 142436.1611) solution was added gently heated in a 40 °C water bath and vortexed every 30 s until the solution became clear. Finally, 36.5 mL of 5% dextrose (Hospira, RL-3040) was added. The solution was kept at room temperature throughout the experiment. Each solution was used for injections up to 7 day maximum. The vehicle solution consisted of the same chemical composition and concentration (DMSO, Tween 80, PEG400 and 5% dextrose). Stock ISRIB solution was at 0.1 mg/ml and injections were at 2.5 mg/kg. Each animal received an intraperitoneal injection of 2.5x their body weight.

Cmp-003 solution was made by dissolving Cmp-003 (donated by Praxis Biotech) in 50% PEG400 (PanReac AppliChem, 142436.1611) and 50% sterile water. The

solution was gently heated in a 40 °C water bath and vortexed every 30 s until the solution became clear. Stock Cmp-003 solution was at 0.5 mg/ml and animal injections were at 5.0 mg/kg. Solution was used immediately and made fresh daily.

Behavioral assessment of cognitive functions. For all assays the experimenter(s) were blinded to therapeutic intervention. Prior to behavioral analysis animals were inspected for gross motor impairments. Animals were inspected for whisker loss, limb immobility (included grip strength) and eye occlusions. If animals displayed *any* of these impairments, they were excluded. Behavioral assessment was recorded and scored using a video tracking and analysis setup (Ethovision XT 8.5, Noldus Information Technology).

Radial Arm Water Maze. The radial arm water maze (RAWM) was used to test spatial learning and memory in rodents [26, 41]. The pool is 118.5 cm in diameter with 8 arms, each 41 cm in length, and an escape platform. The escape platform is slightly submerged below the water level, so it is not visible to the animals. The pool was filled with water that was rendered opaque by adding white paint (Crayola, 54–2128-053). Visual cues are placed around the room such that they were visible to animals exploring the maze. Animals ran 6 trials a day during learning and 3 trials during each memory probe. On both learning and memory days there is a 10-minute inter-trial interval. Animals were trained for 2 days and then tested on memory tests 24 hours and 8 days after training. During a trial, animals were placed in a random arm that did not include the escape platform. Animals were allowed 1 min to locate the escape platform. On successfully finding the platform, animals remained there for 10 s before being returned

to their warmed, holding cage. On a failed trial, animals were guided to the escape platform and then returned to their holding cage 10 s later. The escape platform location was the same, whereas the start arm varied between trials.

Animals were injected (intraperitoneal) with either vehicle or ISRIB (2.5 mg/kg) starting the day prior to behavior (**Figure 2A**) and after each of the final trials of the learning days (day 1 and 2) for a total of three doses. No injections were given when memory was tested on days 3 and 10. RAWM data were collected through a video tracking and analysis setup (Ethovision XT 8.5, Noldus Information Technology). The program automatically analyzed the number of entries into non-target arms made per trial. Every three trials were averaged into a block to account for large variability in performance; each learning day thus consisted of 2 blocks, whereas each memory test was one block each. Importantly, in all animal cohorts tested (regardless of age or drug treatment) learning was measured (Significant time effect observed in all Two-way repeated measure ANOVA analysis when groups are analyzed independently).

Delayed Matching to Place Barnes Maze. Beginning at day 20 animals were tested on DMP using a modified Barnes maze [26, 43]. The maze consisted of a round table 112 cm in diameter with 40 escape holes arranged in three concentric rings consisting of 8, 16, and 16 holes at 20, 35, and 50 cm from the center of the maze, respectively. An escape tunnel was connected to one of the outer holes. Visual cues were placed around the room such that they were visible to animals on the table. Bright overhead lighting and a loud tone (2 KHz, 85 db) were used as aversive stimuli to motivate animals to locate the escape tunnel. The assay was performed for 4 days (days 20-23). The

escape tunnel location was moved for each day and animals ran four trials on the first two days and 3 trials on the last two days. During a trial, animals were placed onto the center of the table covered by an opaque plastic box so they were not exposed to the environment. After they had been placed on the table for 10 s, the plastic box was removed and the tone started playing, marking the start of the trial. Animals were given 90 s to explore the maze and locate the escape tunnel. When the animals successfully located and entered the escape tunnel, the tone was stopped. If the animals failed to find the escape tunnel after 90 s, they were guided to the escape tunnel before the tone was stopped. Animals remained in the escape tunnel for 10 s before being returned to their home cage. The maze was cleaned with ethanol between each trial. A new escape tunnel was used for each trial. The experimenter was blind to the treatment groups during the behavioral assay. Each trial was recorded using a video tracking and analysis setup (Ethovision XT 8.5, Noldus Information Technology) and the program automatically analyzed the amount of time required to locate the escape tunnel. Animal improvement was calculated by Day 20 escape latency – Day 23 escape latency.

Tissue collection. All mice were lethally overdosed using a mixture of ketamine (10 mg/ml) and xylaxine (1 mg/ml). Once animals were completely anesthetized, blood was extracted by cardiac puncture and animals were perfused with 1X phosphate buffer solution, pH 7.4 (Gibco, Big Cabin, OK, -70011-044) until the livers were clear (~1–2 min). For Western blot analysis following phosphate buffered solution (PBS), the whole brain (regions dissected discussed below) was rapidly removed and snap frozen on dry ice and stored at −80 °C until processing.

Western Blot Analysis. Animals received all 3 ISRIB injections and were terminated 20 h after the third injection (as described above). Frozen brain lysates or hippocampi isolates were then homogenized with a T 10 basic ULTRA-TURRAX (IKa) in ice-cold buffer lysis (Cell Signaling 9803) and protease and phosphatase inhibitors (Roche). Lysates were sonicated for 3 min and centrifuged at 13,000 rpm for 20 min at 4°C. Protein concentration in supernatants was determined using BCA Protein Assay Kit (Pierce). Equal amount of proteins was loaded on SDS-PAGE gels. Proteins were transferred onto 0.2 μm PVDF membranes (BioRad) and probed with primary antibodies diluted in Tris-buffered saline supplemented with 0.1% Tween 20 and 3% bovine serum albumin. ATF4 (11815) (Cell Signaling), p-GCN2 (Abcam Cat No ab-75836), p-PERK (Cell Signaling Cat No 3179), p-PKR (Abcam Cat No ab-32036), and p-eIF2 (Cell Signaling, Cat No 3597) and β-actin (Sigma-Aldrich) antibodies were used as primary antibodies. HRP-conjugated secondary antibodies (Rockland) were employed to detect immune-reactive bands using enhanced chemiluminescence (ECL Western Blotting Substrate, Pierce) according to the manufacturer instructions. Quantification of protein bands was done by densitometry using ImageJ software. ATF4, p-GCN2, p-PERK, p-PKR and p-eIF2 levels were normalized to β-actin expression and fold-change was calculated as the levels relative to the expression in vehicle-treated derived samples, which corresponds to 1.

Electrophysiology. Sagittal brain slices (250 μm) including the hippocampus were prepared from old mice (~19 mo) treated with either vehicle or ISRIB or young mice (~3 mo), treated with vehicle, 12-18 hours prior (n = 5, 7, and 5 per group respectively).

Mice were anesthetized with Euthasol (0.1 ml / 25 g, Virbac, Fort Worth, TX, NDC-051311-050-01), and transcardially perfused with an ice-cold sucrose cutting solution containing (in mM): 210 sucrose, 1.25 NaH_2PO_4, 25 $NaHCO_3$, 2.5 KCl, 0.5 $CaCl_2$, 7 $MgCl_2$, 7 dextrose, 1.3 ascorbic acid, 3 sodium pyruvate (bubbled with 95% O_2 − 5% CO_2, pH 7.4) (see Supplemental Table 1 for reagent information). Mice were then decapitated and the brain was isolated in the same sucrose solution and cut on a slicing vibratome (Leica, VT1200S, Leica Microsystems, Wetzlar, Germany). Slices were incubated in a holding solution (composed of (in mM): 125 NaCl, 2.5 KCl, 1.25 NaH_2PO_4, 25 $NaHCO_3$, 2 $CaCl_2$, 2 $MgCl_2$, 10 dextrose, 1.3 ascorbic acid, 3 sodium pyruvate, bubbled with 95% O_2 − 5% CO_2, pH 7.4) at 36 °C for 30 min and then at room temperature for at least 30 min until recording.

Whole cell recordings were obtained from these slices in a submersion chamber with a heated (32 – 34 °C) artificial cerebrospinal fluid (aCSF) containing (in mM): 125 NaCl, 3 KCl, 1.25 NaH_2PO_4, 25 $NaHCO_3$, 2 $CaCl_2$, 1 $MgCl_2$, 10 dextrose (bubbled with 95% O_2 - 5% CO_2, pH 7.4). Patch pipettes (3–6 MΩ) were manufactured from filamented borosilicate glass capillaries (Sutter Instruments, Novato, CA, BF100-58-10) and filled with an intracellular solution containing (in mM): 135 KGluconate, 5 KCl, 10 HEPES, 4 NaCl, 4 MgATP, 0.3 Na_3GTP, 7 2K-phosphcreatine, and 1-2% biocytin. CA1 pyramidal neurons were identified using infrared microscopy with a 40x water-immersion objective (Olympus, Burlingame, CA). Recordings were made using a Multiclamp 700B (Molecular Devices, San Jose, CA) amplifier, which was connected to the computer with a Digidata 1440A ADC (Molecular Devices, San Jose, CA), and recorded at a sampling rate of 20 kHz with pClamp software (Molecular Devices, San

131

Jose, CA). We did not correct for the junction potential, but access resistance and pipette capacitance were appropriately compensated before each recording.

The passive membrane and active action potential spiking characteristics were assessed by injection of a series of hyperpolarizing and depolarizing current steps with a duration of 250 ms from −250 pA to 700 nA (in increments of 50 pA). The resting membrane potential was the measured voltage of the cell 5 min after obtaining whole cell configuration without current injection. A holding current was then applied to maintain the neuron at -67 +/- 2 mV before/after current injections. The input resistance was determined from the steady-state voltage reached during the -50 pA current injection. The membrane time constant was the time required to reach 63% of the maximum change in voltage for the -50 pA current injection. Action potential parameters including the half width, threshold, and amplitude were quantified from the first action potential elicited. Action potential times were detected by recording the time at which the positive slope of the membrane potential crossed 0 mV. From the action potential times, the instantaneous frequency for each action potential was determined (1 / inter spike interval). The maximum firing frequency was the highest frequency of firing identified throughout all current injections. Action potential rate as a function of current injection was examined by plotting the first instantaneous action potential frequency versus current injection amplitude. The F/I slope was then determined from the best linear fit of the positive values of this plot. The action potential or spike threshold was defined as the voltage at which the third derivative of V (d3V/dt) was maximal just prior to the action potential peak. The action potential (AP) amplitude was calculated by measuring the voltage difference between the peak voltage of the action potential and

the spike threshold. The half-width of the action potential was determined as the duration of the action potential at half the amplitude. The adaptation index of each cell was the ratio of the last over the first instantaneous firing frequency, calculated at 250 pA above the current step that first elicited spiking. The afterhyperpolarization (AHP) was calculated as the change in voltage from baseline (measured as the mean voltage over a 100 ms interval 600 ms after termination of a current injection that first elicited at least 12 spikes corresponding to a firing frequency of ~50 Hz) compared to immediately after cessation of current injection (the minimum voltage reached in the first 175 ms immediately after cessation of current injection). Cells were excluded from analysis if excessive synaptic input was noted during recording of the mAHP or if the cell did not fire at least 12 spikes during current injections.

To measure the spontaneous excitatory postsynaptic currents (sEPSCs), cells were recorded in voltage clamp at a holding potential of -75 mV for 4 min, a holding potential that should have little inhibitory components given the reversal potential of chloride with these solutions. Analysis of sEPSCs was performed using a template matching algorithm in ClampFit 10.7 (Molecular Devices, San Jose, CA). The template was created using recordings from multiple pyramidal cells and included several hundred synaptic events. Access resistance (Ra) was monitored during recordings, and recordings were terminated if Ra exceeded 30 megaohms. Only stable recordings (< 50 pA baseline change) with a low baseline noise (< 8 pA root mean square) were included. The first 250 synaptic events or all the events measured in the 4 min interval from each cell were included for analysis.

Fluorescent spine imaging preparation. For fluorescent spine analysis, following PBS animals were perfused with ice-cold 4% paraformaldehyde, pH 7.5 (PFA, Sigma Aldrich, St. Louis, MO, 441244) and fixed for 4 - 24 h followed by sucrose (Fisher Science Education, Nazareth, PA, S25590A) protection (15% to 30%). Brains were embedded with 30% sucrose/ Optimal Cutting Temperature Compound (Tissue Tek, Radnor, PA, 4583) mixture on dry ice and stored at -80 °C. Brains were sectioned into 20 µm slides using a Leica cryostat (Leica Microsystems, Wetzlar, Germany) and mounted on slides (ThermoFisher Scientific, South San Francisco, CA). Slides were brought to room temperature (20 °C) prior to use. Tissues were fixed using ProLong Gold (Invitrogen, Carlsbad, CA, P36930) and a standard slide cover sealed with nail polish.

Spine density quantification. For spine density quantification, whole brains from young and old male Thy1-YFP-H transgenic line were used. 3-6 images separated by 60-140 µm in the dorsal hippocampus were imaged per animal and used for dendritic spine density analysis. 9.3 µm z-stack images were acquired on a Zeiss Laser-Scanning Confocal microscope (Zeiss LSM 780 NLO FLIM) at the HDFCCC Laboratory for Cell Analysis Shared Resource Facility. 63x magnification with a water immersion objective. All protrusions from the dendrites were manually counted as spines regardless of morphology. Two individuals (blinded to age and treatment) analyzed a total length of at least 3200 µm of dendrites from each animal using NIH FIJI analysis software (v1.52n). Individual dendritic spine was calculated as density per micron and graphed relative to old mice.

qPCR Analysis. Hippocampus samples, of approximately the same size per animal were process as previously described [70, 71]. Relative gene expression was determined using the $2^{-\Delta\Delta Ct}$ method and normalized using GAPDH. Primers used were the following:

Cd3: Fw 5' TGACCTCATCGCAACTCTGCTC-3'

Rev 5' TCAGCAGTGCTTGAACCTCAGC-3'

Ifit1: Fw 5' CTGAGATGTCACTTCACATGGAA-3'

Rev 5' GTGCATCCCCAATGGGTTCT-3'

Rtp4: Fw 5' TGGGAGCAGACATTTCAAGAAC-3'

Rev 5'ACCTGAGCAGAGGTCCAACTT-3'

Gbp10: Fw 5' GGAGGCTCAAGAGAAAAGTCACA-3',

Rev 5' AAGGAAAGCCTTTTGATCCTTCAGC-3'

Ccl2: Fw 5' GCTGACCCCAAGAAGGAATG-3'

Rev 5' GTGCTTGAGGTGGTTGTGGA-3'

Il1β: Fw 5' TGTAATGAAAGACGGCACACC-3'

Rev 5' TCTTCTTTGGGTATTGCTTGG-3'

Tnfα: Fw 5' TGCCTATGTCTCAGCCTCTTC-3'

Rev 5' GAGGCCATTTGGGAACTTCT-3'

Il-6: Fw 5' TACCACTTCACAAGTCGGAGGC-3'

Rev 5' CTGCAAGTGCATCATCGTTGTTC-3'

Irf7: Fw 5'- GAGACTGGCTATTGGGGGAG-3'

Rev 5'- GACCGAAATGCTTCCAGGG-3'

Ifitm3: Fw 5'- CCCCCAAACTACGAAAGAATCA-3'

Rev 5'- ACCATCTTCCGATCCCTAGAC-3'

Isg15: Fw 5'- GGTGTCCGTGACTAACTCCAT-3'

Rev 5'- TGGAAAGGGTAAGACCGTCCT-3'

Ifi204: Fw 5'- AGCTGATTCTGGATTGGGCA-3'

Rev 5'- GTGATGTTTCTCCTGTTACTTCTGA-3'

Eif2ak2 (Pkr): Fw 5'- CTGGTTCAGGTGTCACCAAAC-3'

Rev 5'- ACAACGCTAGAGGATGTTCCG-3'

Cd11b: Fw 5'- CTGAGACTGGAGGCAACCAT- 3'

Rev 5' GATATCTCCTTCGCGCAGAC-3'

Il-10: Fw 5'- GCCAAGCCTTATCGGAAATG- 3'

Rev 5' CACCCAGGGAATTCAAATGC -3'

Bdnf: Fw 5'- GGCTGACACTTTTGAGCACGT - 3'

Rev 5' CTCCAAAGGCACTTGACTGCTG -3'

Ophn1: Fw 5'- CTTCCAGGACAGCCAACCATTG - 3'

Rev 5' CTTAGCACCTGGCTTCTGTTCC -3'

Gbs5: Fw 5'- CTGAACTCAGATTTTGTGCAGGA - 3'

Rev 5' CATCGACATAAGTCAGCACCAG -3'

Oasl1: Fw 5'- CAGGAGCTGTACGGCTTCC - 3'

Rev 5' CCTACCTTGAGTACCTTGAGCAC -3'

Gadd34: Fw 5'- GGCGGCTCAGATTGTTCAAAGC - 3'

Rev 5' CCAGACAGCAAGGAAATGGACTG -3'

Gapdh: Fw 5' AAATGGTGAAGGTCGGTGTG-3'

Rev 5' TGAAGGGGTCGTTGATGG-3'

Flow Cytometric Analysis. To assess circulating cell populations peripheral blood was collected by cardiac puncture and transferred into an EDTA collection tube. Blood was aliquoted into flow cytometry staining tubes and stained with surface antibodies for 30-60 min at room temperature [72]. Surface antibodies included anti-CD45 (FITC-conjugated; BD Biosciences), Ly-6G (PE-conjugated; BD Biosciences), CD8 (PE-Cy7-conjugated; BD Biosciences), CD4 (APC-conjugated; BD B), and CD11b (APC-Cy7; BD Biosciences). Leukocyte subpopulations were identified as follows: Forward and side scatter was used to exclude debris and doublet populations. Specific T- cell populations were identified as follows: CD4 T-cell subsets were $CD4^+$, $CD45^+$, $Ly-6G^-$, $CD8^-$, $CD11b^-$. CD8 T-cell subsets were $CD8^+$, $CD45^+$, $Ly-6G^-$, $CD4^-$, $CD11b^-$. After surface antibody staining, red blood cells were lysed with RBC lysis (BD Biosciences). Cell population gating occurred as previously described [72]. (Data were collected on an LSRII (BD) and analyzed with Flowjo™ software (v10, Tree Star Inc.).

Statistical Analysis. Results were analyzed using Prism software or IBM SPSS Statistics. Individual animals. Individual animal scores represented by dots, lines depict group mean and SEM. Student t-test, one-way ANOVA, two-way repeated measures ANOVA and Pearson R correlations were used (individual statistical tool and post-hoc analysis denoted in Figure Legends). p values of < 0.05 considered as significant. Group outliers were determined (GraphPad Software Outlier Test-Grubb's test) and excluded from analysis. At most a single animal was excluded from each experimental cohort.

The numbers of mice used was sufficient to result in statistically significant differences using standard power calculations with alpha = 0.05 and a power of 0.8. We used an online tool (http://www.bu.edu/orccommittees/iacuc/policies-and-guidelines/sample-size-calculations/) to calculate power and samples size based on experience with the respective tests, variability of the assays and inter-individual differences within groups. All experiments were randomized and blinded by an independent researcher prior to treatment.

Biological replicates are measurements of biologically distinct animals/tissues/cells used to measure biological differences. Technical replicates are repeated measurements of the same animals/tissues/cells.
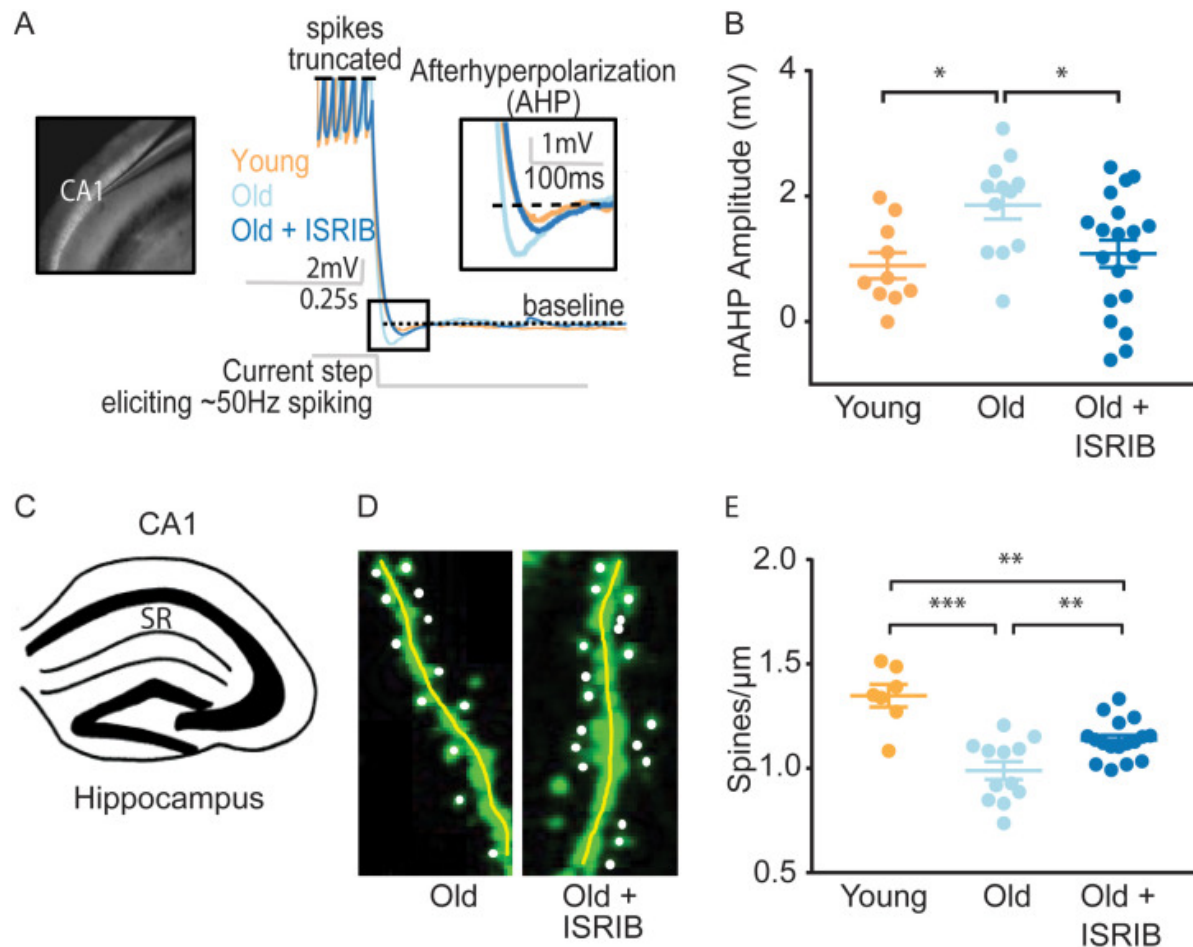
Figures
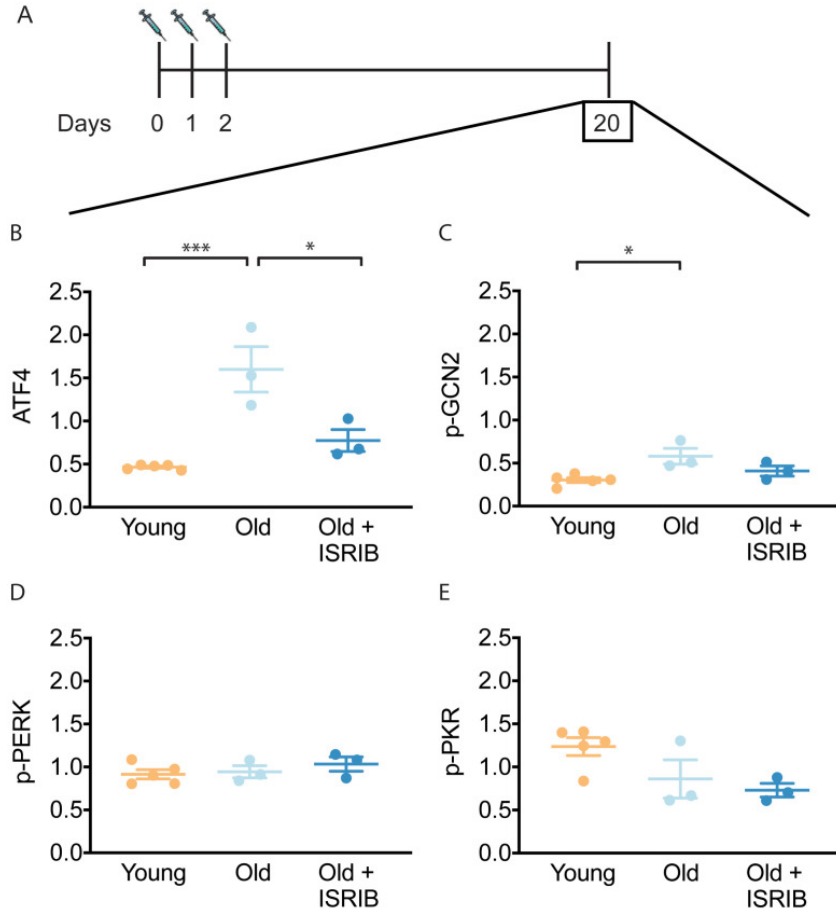
Figure 1. ISRIB resets the ISR in the brain of old mice.

(**A**) Experimental dosing scheme: ISRIB treatment denoted by syringes (3 injections). (**B**) ISRIB treatment reduced ATF4 protein levels chronically 18 days after ISRIB treatment was complete. One-way ANOVA (F = 18.8, p < 0.001); with Tukey post-hoc analysis. (**C**) Modest age-induced increases in p-GCN2 when comparing young and old male mice. One-way ANOVA (F = 6.6, p < 0.05); with Tukey post-hoc analysis. (**D, E**) Age and ISRIB administration did not impact p-PERK or p-PKR protein levels. Brain lysates of specific protein levels listed normalized to actin. Young n = 5, Old = 3, Old + ISRIB = 3. Individual animal values represented by dots; lines depict group mean ± SEM. *p < 0.05; ***p < 0.001
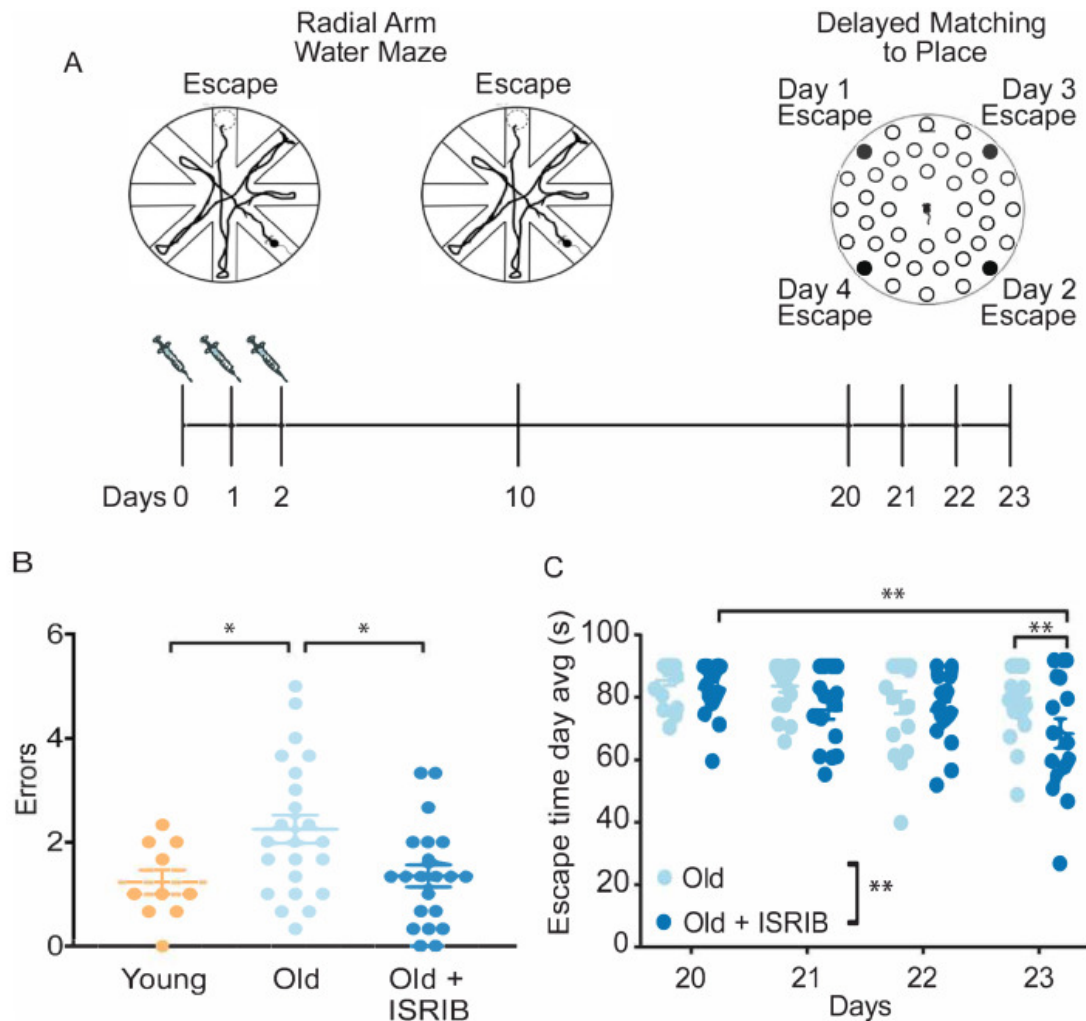
**Figure 2. Inhibition of the ISR reverses age-induced decline in spatial, working and episodic memory.**

(**A**) Experimental Design: Old (~19 months) animals underwent behavioral analysis in a radial arm water maze (RAWM) and a delayed matching to place paradigm (DMP). ISRIB or vehicle administration (2.5 mg/kg intraperitoneal) occurred daily during the learning phase of RAWM denoted by syringes (days 0-2). (**B**) ISRIB treatment improved memory one week after administration in male rodents. One-way ANOVA (F = 4.8, p < 0.05); with Tukey post-hoc analysis. Young n = 10; Old n = 23; Old + ISRIB n = 21. (**C**) Age-induced deficits in working and episodic learning and memory restored weeks after ISRIB administration. Animals performed the DMP from day 20 – 23. Average of all trials per group for each day. Day 20, 21 = 4 trials/day. Day 22,23 = 3 trials/day. Two-way repeated measures ANOVA reveals a significant difference between groups p < 0.01 (denoted in figure legend) and time effect p < 0.01. *p < 0.05, **p < 0.01. Old n = 18; Old + ISRIB n = 16. Individual animal scores represented by dots; lines depict group mean ± SEM.

Figure 3. ISRIB treatment alleviates age-associated changes in CA1 pyramidal neuron function and structure.

(**A**) Left: Image of pipette patched onto CA1 neuron in sagittal slice of hippocampus. Right: Representative traces from hippocampal CA1 pyramidal neurons from old animals treated with either vehicle (light blue) or ISRIB (dark blue) or young animals treated with vehicle (orange) showing the response to a current injection eliciting ~50Hz spiking activity. Spikes are truncated (dashed line), and the AHP is visualized immediately following cessation of current injection (yellow square) and quantified as the change in voltage from baseline (dotted line). (**B**) Age-induced increases in AHP were measured when comparing young and old animals. ISRIB treatment reversed increased AHP to levels indistinguishable from young animals. Animals were injected with ISRIB (2.5 mg/kg) or vehicle intraperitoneal one day prior to recordings. One-way ANOVA (F = 4.461, $p < 0.05$); with Tukey post-hoc analysis. *$p < 0.05$. Each neuron is represented with a symbol; lines indicate the mean ± SEM (Neurons: Young males n = 10 (5 animals); Old males n = 12 (5 animals), Old + ISRIB males n = 19 (7 animals) with 1-5 neurons recorded per animal. (**C-E**) Spine density was quantified in the CA1 region of the dorsal hippocampus from young and old Thy1-YFP-H mice. (**C**) Diagram of hippocampal region analyzed. SR = stratum radiatum. (**D**) Representative images from Old and Old + ISRIB mice. (**E**) A decrease in dendritic spine density was measured when comparing old mice to young mice. ISRIB treatment significantly increased spine

density levels of old mice when compared to vehicle treated old mice. 63x magnification with a water immersion objective. Young males n = 7 slides (2 animals); Old males + Vehicle n = 12 slides (3 mice); Old males + ISRIB n = 17 slides (4 mice). Individual slide scores (relative to old mice) represented in dots, lines depict group mean ± SEM. One-way ANOVA (F = 18.57, $p < 0.001$) with Tukey post-hoc analysis. **$p < 0.01$; ***$p < 0.001$.
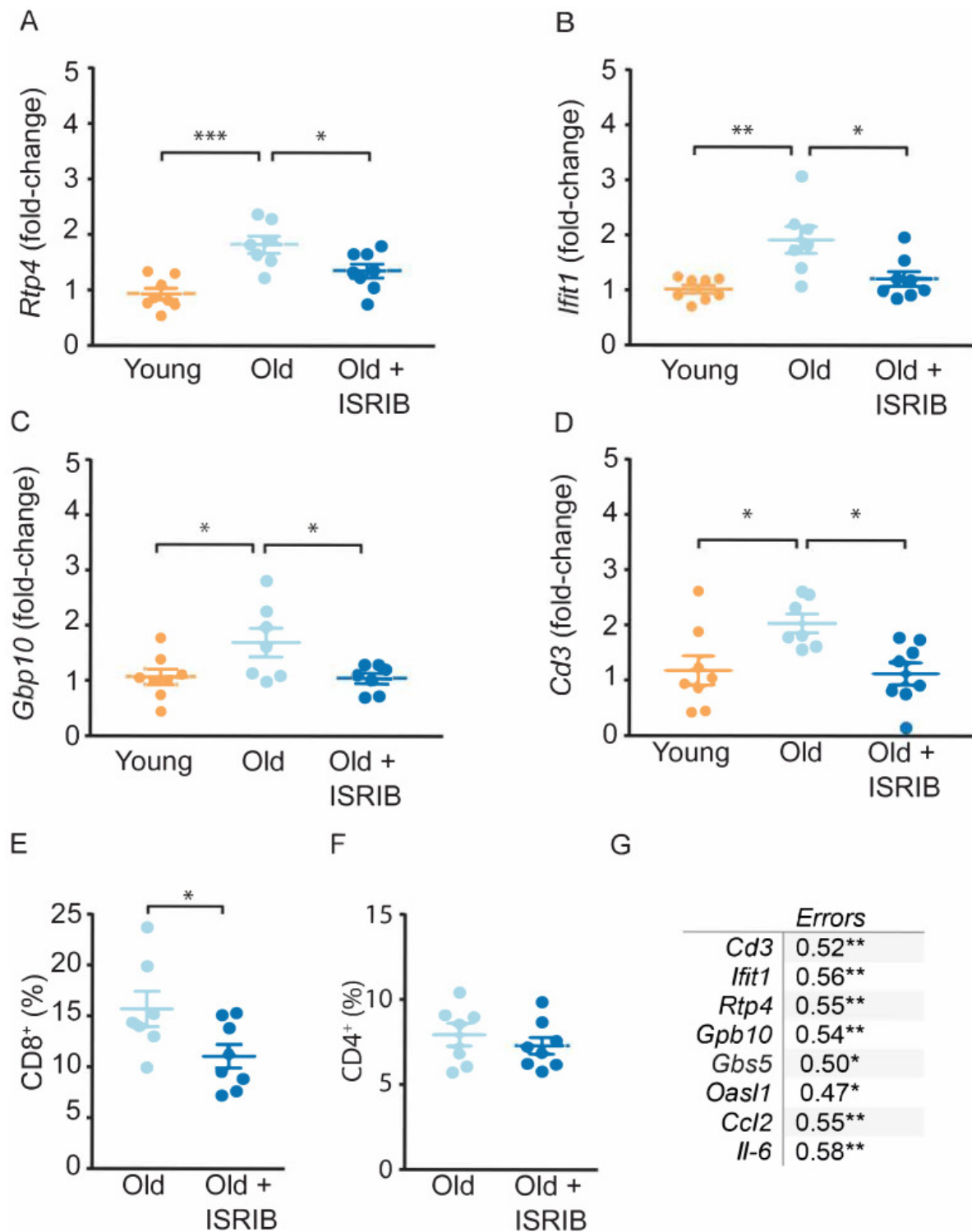
Figure 4. Age-induced inflammatory tone is reduced following ISRIB treatment.

Inflammatory genes were investigated in the hippocampus of young and old mice by qPCR analysis. (**A-C**) ISRIB administration reversed age-induced increases in *Rtp4, Ifit1,* and *Gbp10*. (A) *Rtp4*, One-way ANOVA (F = 12.23, p < 0.001) with a Tukey-post analysis. Young males n = 8; Old males n = 7; Old + ISRIB males n = 8. (**B**) *Ifit1*, One-

way ANOVA (F = 8.8; $p < 0.01$) with a Tukey-post analysis. Young males n = 8; Old males n = 7; Old + ISRIB males n = 8. (**C**) *Gbp10*, One-way ANOVA (F = F4.2, $p < 0.05$) with a Tukey-post analysis. Young males n = 8; Old males n = 7; Old + ISRIB males n = 7. (**D**) *Cd3* gene-expression (a marker for T cells) changes in the hippocampus of young and old animals were measured by qPCR analysis. *Cd3* was significantly increased with age. ISRIB administration returned *Cd3* expression levels to those comparable to young animals. One-way ANOVA (F = 5.2; $p < 0.05$). Tukey-post hoc analysis. Young males n = 8; Old males n = 7; Old + ISRIB males n = 8. (**E, F**) Peripheral T cell levels were measured by flow cytometric analysis of whole blood. (**E**) ISRIB treatment reduced CD8$^+$ T cell percentages (of CD45$^+$ cells) in the peripheral blood. Student t-test. Old males n = 7; Old + ISRIB males n = 8. (**F**) CD4$^+$ T cell percentages (of CD45$^+$ cells) were not impacted. Individual animal scores represented by dots; lines depict group mean ± SEM. (**G**) A significant positive correlation was measured between cognitive performance on day 2 of the RAWM (errors) and multiple inflammatory markers (*Cd3*, *Ifit1*, *Rtp4*, *Gbp10*, *Gbp5*, *Oasl1*, *Ccl2*, *Il-6*). Linear regression was measured by Pearson R correlation, R value denoted with significance. *$p < 0.05$; **$p < 0.01$; ***$p < 0.001$.
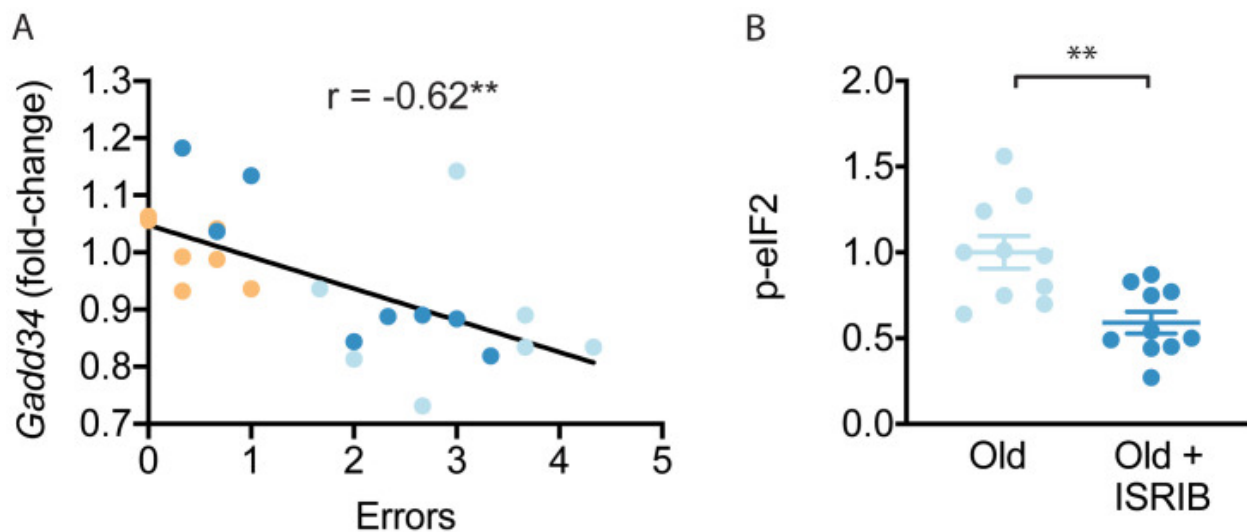

Figure 5. ISRIB treatment resets age-related ISR activation.

(**A**) A significant negative correlation was measured between cognitive performance on day 2 of the RAWM (errors) and *Gadd34* mRNA expression. Linear regression was measured by Pearson R correlation, R value denoted with significance. (**B**) ISRIB treatment reduced p-eIF2α protein levels. Brain lysates of p-eIF2α protein levels normalized to actin. Old males n = 10; ISRIB males n = 10. Student's t-test. **$p < 0.01$. Data are means ± SEM.

**Table 1. Impact of age and ISRIB on mRNA expression in the hippocampus.**

Inflammatory, ISR mediators and neuronal health targets were investigated by qPCR analysis of hippocampal lysates after two ISRIB injections. Columns: (i) mRNA targets (ii) Young group mean ± SEM (iii) Old group mean ± SEM (iv) Old + ISRIB group mean ± SEM (v) ANOVA F value (vi) Significant denotation between groups (vii) n/group.

TARGET	Young	Old	Old + ISRIB	ANOVA	Btw Groups	n: Yg/Old/Old + ISRIB
Ccl2	1.0 ± 0.1	2.3 ± 0.4	1.6 ± 0.1	F = 5.6*	Yg v Old**	8/7/7
Cd11b	1.0 ± 0.0	1.0 ± 0.0	1.2 ± 0.0	F = 6.6**	Yg v Old + ISRIB** Old v Old + ISRIB*	8/7/8
Il1-β	1.1 ± 0.1	1.4 ± 0.1	1.7 ± 0.1	F = 3.6*	Yg v Old + ISRIB*	8/7/8
Tnfα	1.0 ± 0.1	1.6 ± 0.3	2.1 ± 0.4	F = 2.7		7/7/8
Il-6	1.1 ± 0.2	1.8 ± 0.1	1.8 ± 0.2	F = 4.1*	Yg v Old*	8/7/8
Il-10	1.0 ± 0.1	1.4 ± 0.2	1.5 ± 0.2	F = 1.1		7/7/7
Irf7	1.0 ± 0.1	1.4 ± 0.1	1.2 ± 0.1	F = 1.5		8/7/8
Ifitm3	1.0 ± 0.0	1.2 ± 0.1	1.0 ± 0.0	F = 0.8		8/7/8
Isg15	1.0 ± 0.0	1.3 ± 0.1	1.2 ± 0.0	F = 2.0		8/7/7
Ifi204	1.1 ± 0.2	1.4 ± 0.2	1.5 ± 0.1	F = 1.2		6/7/7
Gbp5	1.0 ± 0.0	1.2 ± 0.1	1.1 ± 0.0	F = 2.6		8/7/8
Oasl1	1.0 ± 0.0	1.8 ± 0.3	0.9 ± 0.1	F = 4.9*	Yg v Old*; Old v Old + ISRIB*	8/7/8
Ophn1	1.0 ± 0.0	0.9 ± 0.0	1.1 ± 0.0	F = 1.8		8/7/8
Bdnf	1.0 ± 0.0	0.9 ± 0.0	1.0 ± 0.0	F = 2.7		8/7/8
Gadd34	1.0 ± 0.0	0.8 ± 0.0	0.9 ± 0.0	F = 1.8		7/7/8
Pkr	1.0 ± 0.0	1.0 ± 0.0	1.1 ± 0.0	F = 1.0		8/7/8
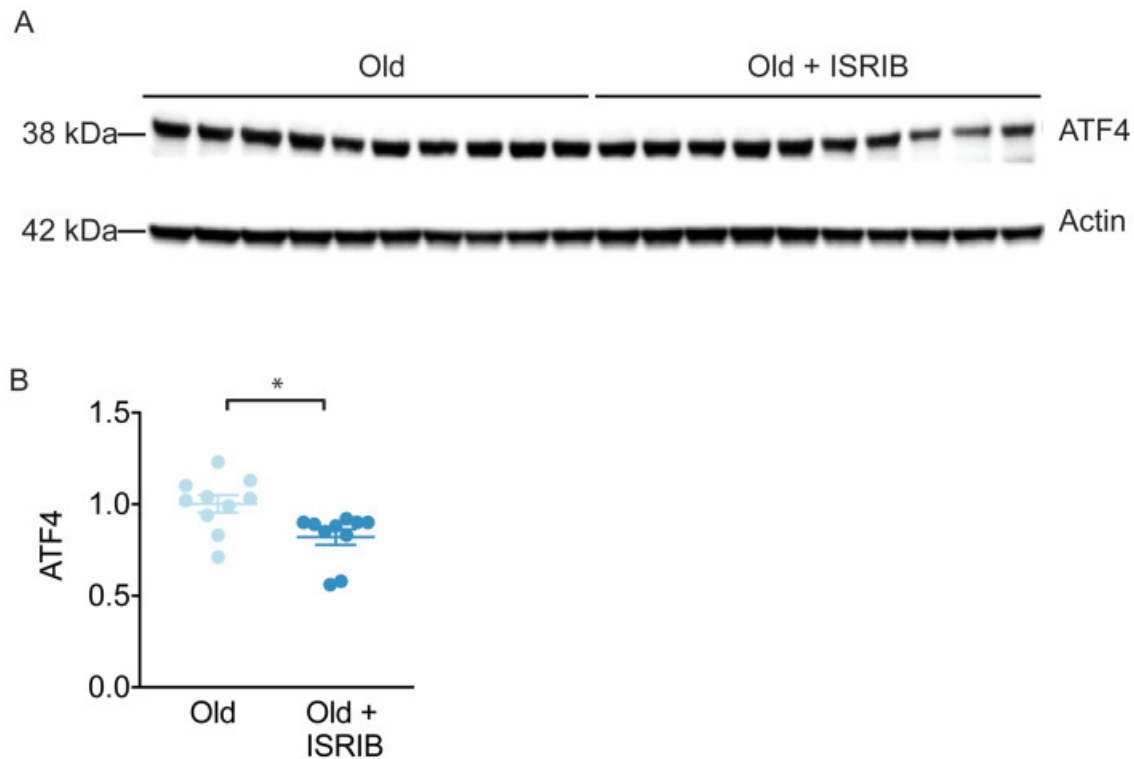
Supplemental Figure 1. ISRIB downregulates ATF4 during administration.

The impact of ISRIB on known ISR activation pathways was investigated by western blot analysis of brain lysates after 3 ISRIB injections. (**A**) Raw western blot data. Each lane represents an individual animal brain extract. (**B**) ISRIB treatment reduced ATF4 protein levels during drug administration. Old males (Chou et al., 2018) and females (Anderson et al., 1998): Old n = 10; Old + ISRIB n = 10. Student's t-test. *p<0.05. Individual animal values represented by dots; lines depict group mean ± SEM.
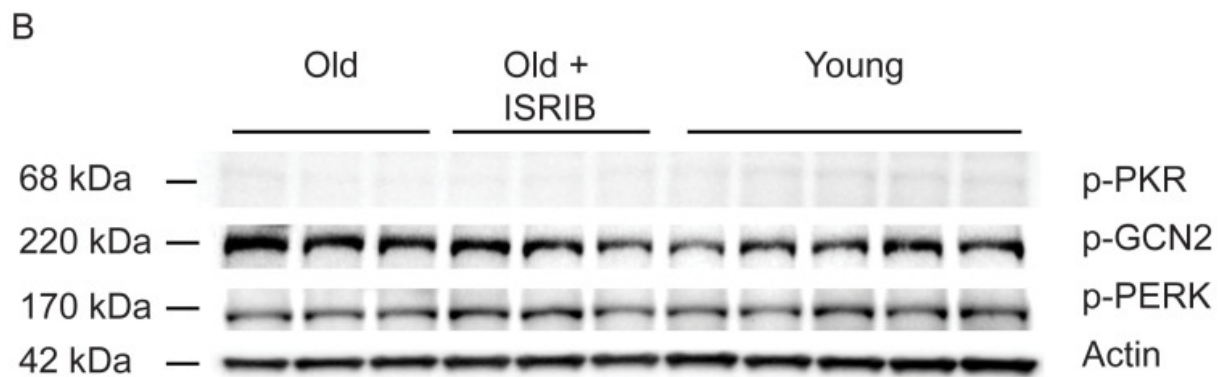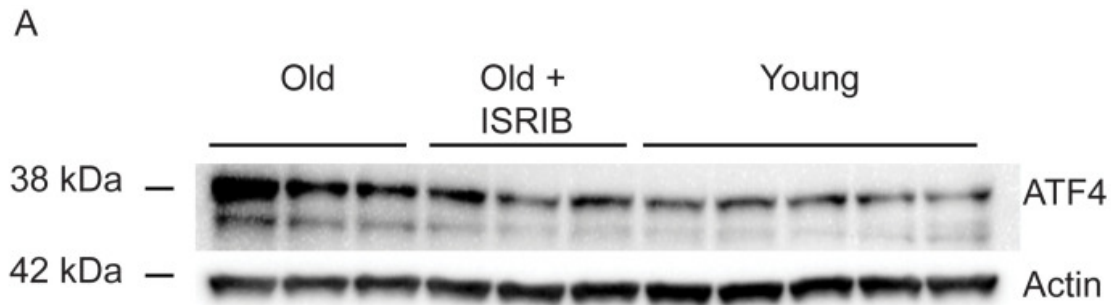
Supplemental Figure 2. ISRIB down-regulates the ISR in the brain of old mice.

The impact of ISRIB on known ISR kinases and activation pathways was investigated by western blot analysis of brain lysates (raw western blot data) at day 20. (**A**) ATF4 (**B**) p-GCN2, p-PKR, p-PERK. Each lane represents an individual animal brain extract.
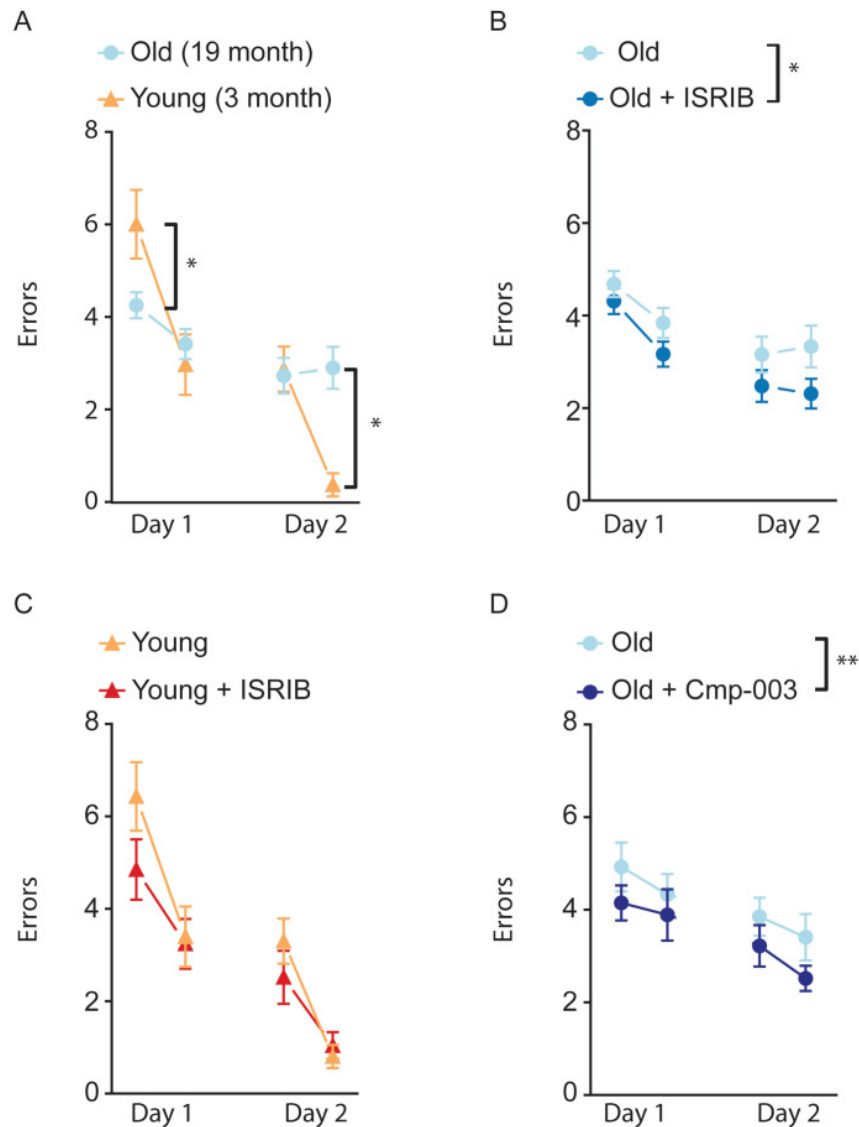
Supplemental Figure 3. ISR inhibitors relieve age-induced deficits in spatial learning.

RAWM was used to measure age-induced deficits in spatial learning. Animals ran two blocks (three trials/block) on each learning day. (**A**) Old animals performed significantly worse that young animals. Two-way repeated measures ANOVA revealed a significant interaction ($p<0.001$). Bonferroni post-hoc to determine differences at various blocks. Old males n = 19, Young males n = 10. *$p<0.05$. (**B**) ISRIB or vehicle administration (2.5 mg/kg intraperitoneal) occurred days 0–2. Compared with the old group, ISRIB treated animals made significantly fewer errors over the course of learning. Two-way repeated measures ANOVA reveals a significant difference between groups $p<0.05$. Old males n = 19; Old + ISRIB males n = 15. (**C**) No differences were measured between young +/- ISRIB administration. Two-way repeated measures ANOVA revealed no significant differences. Young males n = 10; Young males + ISRIB n = 10 (**D**) Cmp-003 (5 mg/kg intraperitoneal) administration occurred days 0–2. Old mice that received Cmp-003 performed significantly better than old mice that received vehicle. Two-way repeated

measures ANOVA revealed a significant group ($p<0.01$) and time effect ($p<0.05$). Old males n = 9, Old males + Cmp-003 n = 9. **$p<0.01$. Data are means ± SEM.
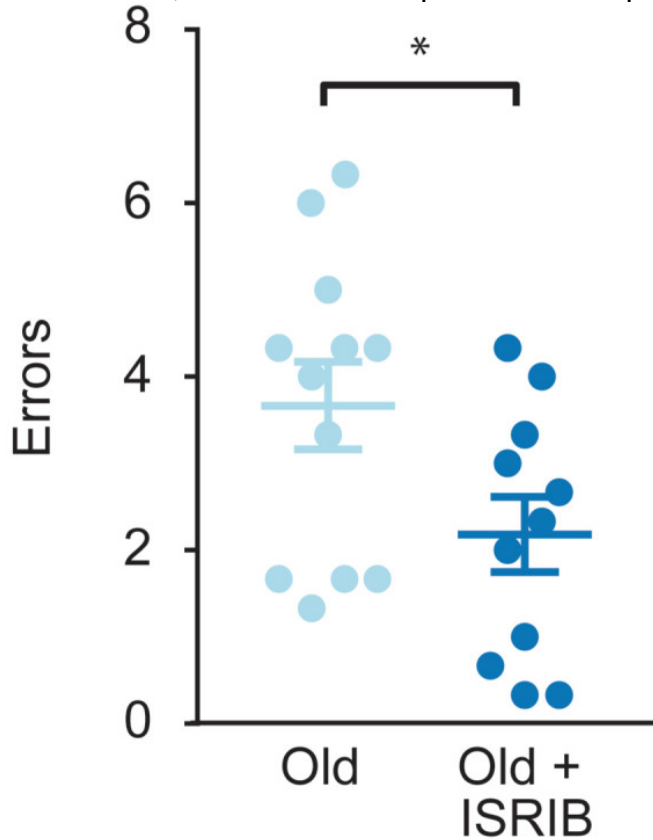
Supplemental Figure 4. ISRIB reduces age-induced memory deficits in female mice.

RAWM was used to measure age-induced deficits in learning and memory. ISRIB treatment improved memory 1 week after administration in female rodents. Student t-test. Old female n = 12; Old female + ISRIB n = 11. *$p<0.05$. Individual animal scores represented by dots, lines depict group mean and SEM.
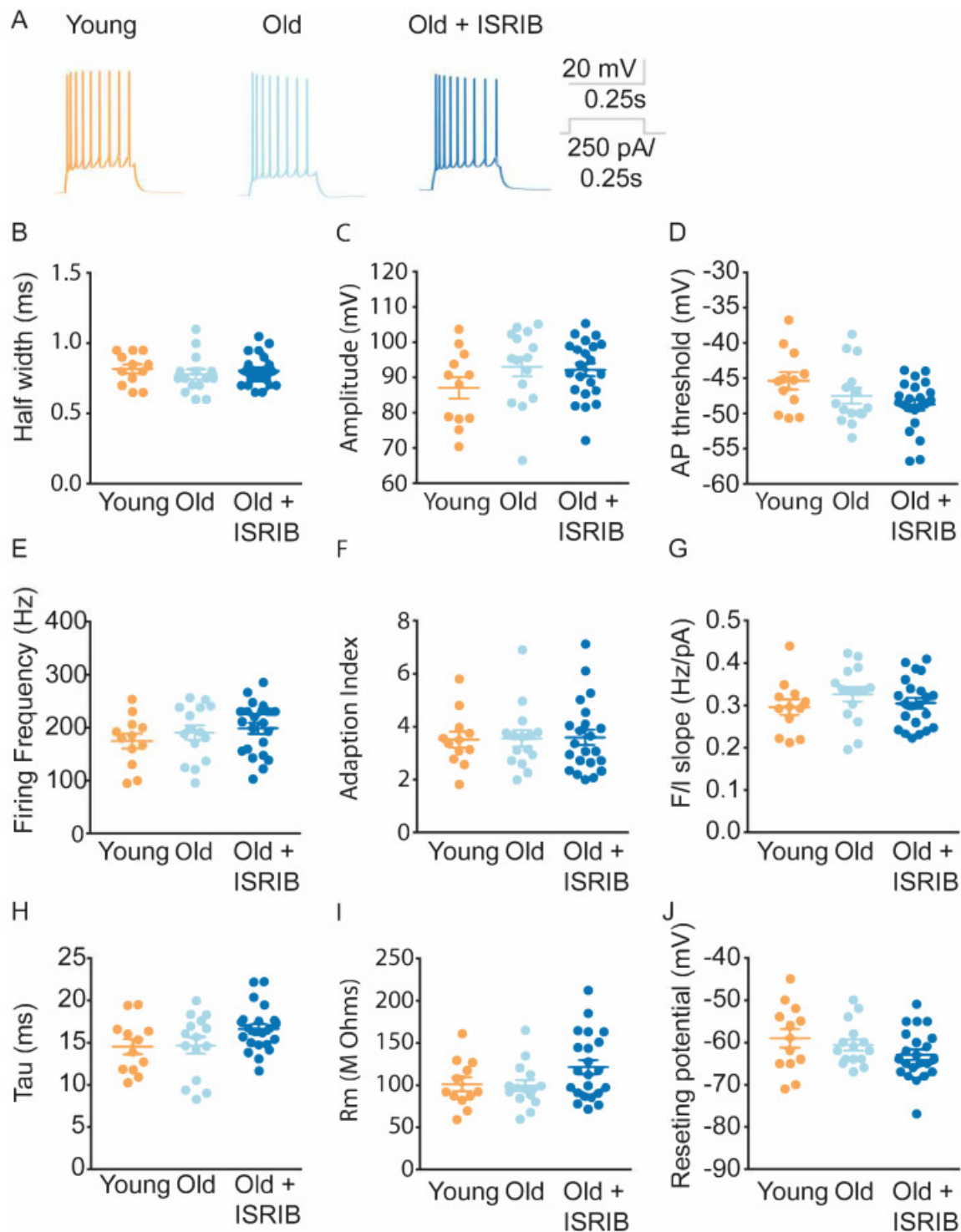
Supplemental Figure 5. Age and ISRIB treatment do not modify other passive or active intrinsic membrane properties in CA1 pyramidal neurons.

 (**A**) Representative traces from CA1 pyramidal neurons showing the membrane potential response to a 250 pA current injection in neurons from old animals treated with either vehicle (light blue) or ISRIB (dark blue) or young animals treated with vehicle (orange). Quantification of the action potential (AP) including the half width (**B**),

amplitude (**C**), and threshold (**D**) did not show significant differences between CA1 pyramidal recordings from old, old + ISRIB-treated, or young mice. Likewise, evaluation of the maximum firing frequency (**E**) or how the frequency of spiking changes over time, quantified by the adaptation index (**F**) or with current injection, quantified by the slope of the relationship of firing frequency versus amplitude of current injection (F/I slope) (**G**) was also not significantly different between groups. Finally, passive membrane properties including the membrane time constant (tau) (**H**), membrane resistance (Rm) (**I**), and the resting membrane potential (**J**) were not significantly altered by age or ISRIB treatment. Each neuron is represented with a symbol; solid lines indicate the mean ± SEM. (One-way ANOVA for all comparisons; Neurons: and Young males n = 12 (5 animals); Old males n = 15 (5 animals), Old + ISRIB males n = 22 (7 animals)) with 1–5 neurons recorded per animal.
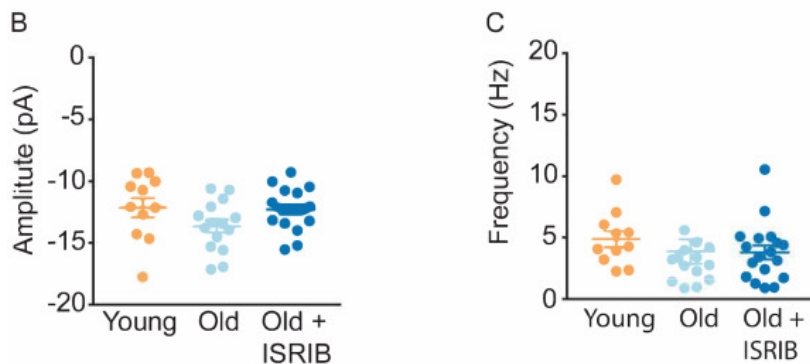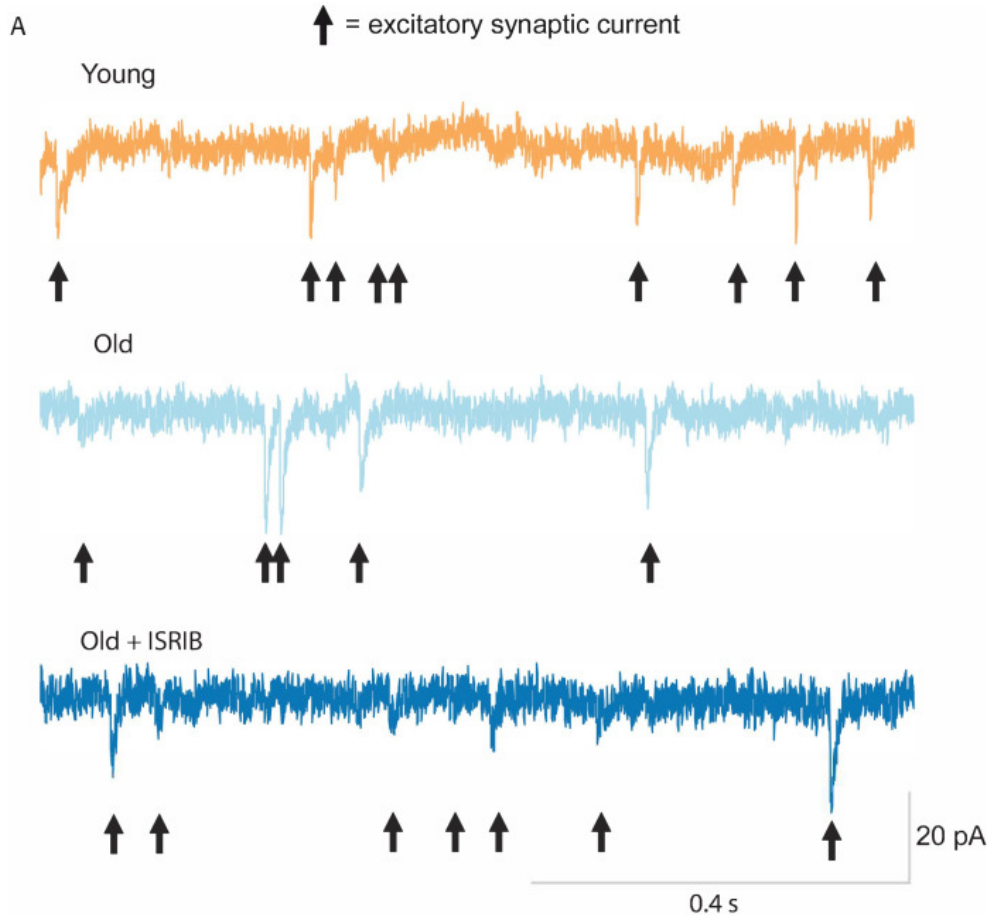
Supplemental Figure 6. Age and ISRIB treatment do not affect spontaneous excitatory post-synaptic currents (sEPSC) in CA1 pyramidal neurons.

(**A**) Representative whole cell voltage-clamp recordings showing sEPSCs from CA1 pyramidal neurons from old animals treated with either vehicle (light blue) or ISRIB (dark blue) or young animals treated with vehicle (orange). Arrows denote synaptic currents. (**B**) The sEPSC amplitude was not significantly different between groups (one-way ANOVA). (**C**) The sEPSC frequency was unchanged after ISRIB treatment or compared to young mice (Kruskal-Wallis test). The median amplitude or frequency for each neuron is represented with a symbol; solid lines indicate the mean ± SEM. (Neurons: Young males n = 11 (5 animals); Old males n = 15 (5 animals), Old + ISRIB males n = 18 (7 animals) with 1–5 neurons recorded per animal).

152
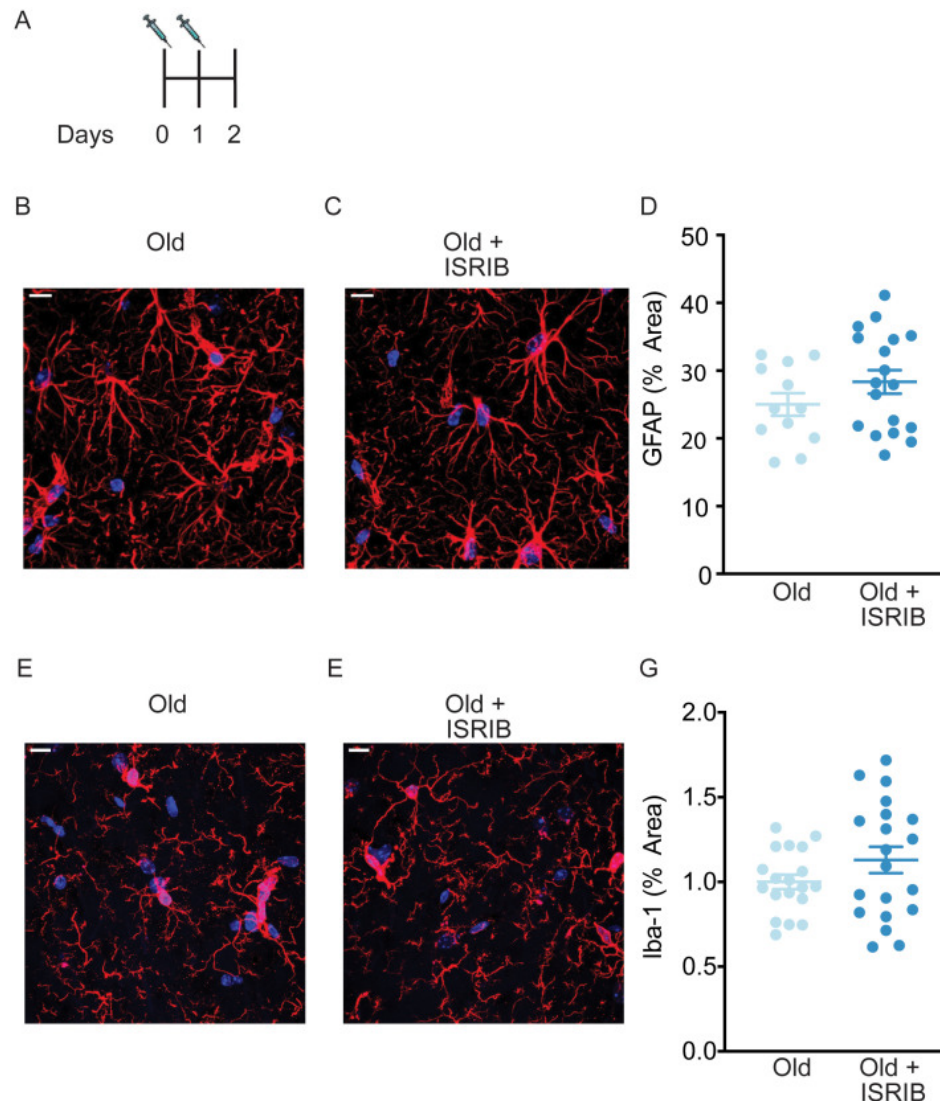
Supplemental Figure 7. ISRIB administration does not impact glial cell activation.

(**A**) ISRIB administration scheme. (**B–G**) Glial cell was quantified in the stratum radiatum of the CA1 region of the dorsal hippocampus from old Thy1-YFP-H mice. GFAP was used to measure astrocyte activity. Representative images for GFAP staining of (**B**) old and (**C**) old + ISRIB mouse. (**D**) No differences in GFAP percent area were measured when comparing old and old + ISRIB animals. Iba-1 was used to measure microglia activity. Representative images for Iba-1 staining of (**E**) old and (**F**) old + ISRIB mouse. (**G**) No differences in Iba-1 percent area were measured when comparing old and old + ISRIB animals. 63x magnification with a water immersion objective. Old males n = 12–19 slides (three mice); Old males + ISRIB n = 18–20 slides (four mice). Individual slide scores (relative to old mice) represented in dots, lines depict group mean ± SEM.
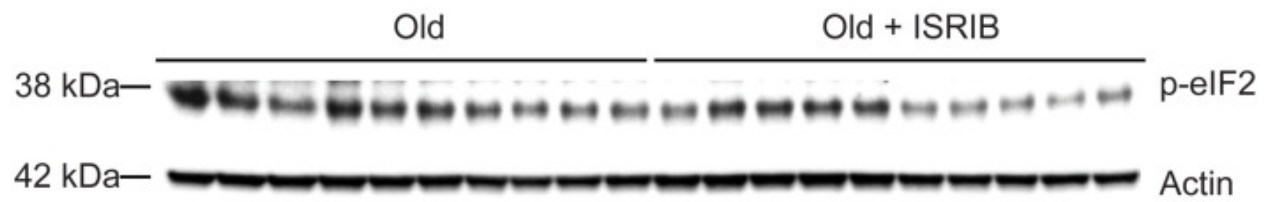
Supplemental Figure 8. ISRIB treatment breaks age-related ISR activation.

The impact of ISRIB on p-eIF2 was investigated by western blot analysis of brain lysates after three ISRIB injections. Raw western blot data. Each lane represents an individual animal brain extract.

References

1. Connelly, S.L., L. Hasher, and R.T. Zacks, *Age and reading: the impact of distraction.* Psychol Aging, 1991. **6**(4): p. 533-41.

2. Anderson, N.D., F.I. Craik, and M. Naveh-Benjamin, *The attentional demands of encoding and retrieval in younger and older adults: 1. Evidence from divided attention costs.* Psychol Aging, 1998. **13**(3): p. 405-23.

3. Kramer, A.F., S. Hahn, and D. Gopher, *Task coordination and aging: explorations of executive control processes in the task switching paradigm.* Acta Psychol (Amst), 1999. **101**(2-3): p. 339-78.

4. Cepeda, N.J., A.F. Kramer, and J.C. Gonzalez de Sather, *Changes in executive control across the life span: examination of task-switching performance.* Dev Psychol, 2001. **37**(5): p. 715-30.

5. Ortman JM, V.V.H.H., *An Aging Nation: The Older Population in the United States*, U.D.o. Commerce, Editor. 2014.

6. Chou, A., et al., *Persistent Infiltration and Impaired Response of Peripherally-Derived Monocytes after Traumatic Brain Injury in the Aged Brain.* Int J Mol Sci, 2018. **19**(6).

7. Yousef, H., et al., *Aged blood impairs hippocampal neural precursor activity and activates microglia via brain endothelial cell VCAM1.* Nat Med, 2019. **25**(6): p. 988-1000.

8. Villeda, S.A., et al., *The ageing systemic milieu negatively regulates neurogenesis and cognitive function.* Nature, 2011. **477**(7362): p. 90-4.

9.   Castellano, J.M., et al., *Human umbilical cord plasma proteins revitalize hippocampal function in aged mice.* Nature, 2017. **544**(7651): p. 488-492.

10.   Villeda, S.A., et al., *Young blood reverses age-related impairments in cognitive function and synaptic plasticity in mice.* Nat Med, 2014. **20**(6): p. 659-63.

11.   Cabral-Miranda, F.T., G. Martinez, G. Medinas, D. Gerakis, Y. Miedema, T. Duran-Aniotz, C. Ardiles, AO. Gonzalez, C. Sabusap, C. Bermedo-Garcia, F. Adamson, S. Vitangcol, K. Huerta, H. Zhang, X. Nakamura, T. Pablo Sardi, S. Lipton, SA. Kenedy, BK. Cárdenas, JC. Palacios, AG. Plate, L. Henriquez, JP. Hetz, C., *Control of mammalian brain aging by the unfolded protein response (UPR).* Biorxiv, 2020.

12.   Disterhoft, J.F. and M.M. Oh, *Alterations in intrinsic neuronal excitability during normal aging.* Aging Cell, 2007. **6**(3): p. 327-36.

13.   McKiernan, E.C. and D.F. Marrone, *CA1 pyramidal cells have diverse biophysical properties, affected by development, experience, and aging.* PeerJ, 2017. **5**: p. e3836.

14.   Oh, M.M., F.A. Oliveira, and J.F. Disterhoft, *Learning and aging related changes in intrinsic neuronal excitability.* Front Aging Neurosci, 2010. **2**: p. 2.

15.   Rizzo, V., J. Richman, and S.V. Puthanveettil, *Dissecting mechanisms of brain aging by studying the intrinsic excitability of neurons.* Front Aging Neurosci, 2014. **6**: p. 337.

16.   Schimanski, L.A. and C.A. Barnes, *Neural Protein Synthesis during Aging: Effects on Plasticity and Memory.* Front Aging Neurosci, 2010. **2**.

17. Azzu, V. and T.G. Valencak, *Energy Metabolism and Ageing in the Mouse: A Mini-Review.* Gerontology, 2017. **63**(4): p. 327-336.

18. Franceschi, C., et al., *Inflamm-aging. An evolutionary perspective on immunosenescence.* Ann N Y Acad Sci, 2000. **908**: p. 244-54.

19. Baruch, K., et al., *Aging. Aging-induced type I interferon response at the choroid plexus negatively affects brain function.* Science, 2014. **346**(6205): p. 89-93.

20. Dulken, B.W., et al., *Single-cell analysis reveals T cell infiltration in old neurogenic niches.* Nature, 2019. **571**(7764): p. 205-210.

21. Flexner, J.B., et al., *Inhibition of protein synthesis in brain and learning and memory following puromycin.* J Neurochem, 1962. **9**: p. 595-605.

22. Lopez-Otin, C., et al., *The hallmarks of aging.* Cell, 2013. **153**(6): p. 1194-217.

23. Ingvar, M.C., et al., *Effects of ageing on local rates of cerebral protein synthesis in Sprague-Dawley rats.* Brain, 1985. **108 (Pt 1)**: p. 155-70.

24. Smith, C.B., Y. Sun, and L. Sokoloff, *Effects of aging on regional rates of cerebral protein synthesis in the Sprague-Dawley rat: examination of the influence of recycling of amino acids derived from protein degradation into the precursor pool.* Neurochem Int, 1995. **27**(4-5): p. 407-16.

25. Harding, H.P., et al., *An integrated stress response regulates amino acid metabolism and resistance to oxidative stress.* Mol Cell, 2003. **11**(3): p. 619-33.

26. Chou, A., et al., *Inhibition of the integrated stress response reverses cognitive deficits after traumatic brain injury.* Proc Natl Acad Sci U S A, 2017. **114**(31): p. E6420-E6426.

27.   Krukowski, K., et al., *Integrated Stress Response Inhibitor Reverses Sex-Dependent Behavioral and Cell-Specific Deficits after Mild Repetitive Head Trauma.* J Neurotrauma, 2020.

28.   Costa-Mattioli, M. and P. Walter, *The integrated stress response: From mechanism to disease.* Science, 2020. **368**(6489).

29.   Kaczorowski, C.C. and J.F. Disterhoft, *Memory deficits are associated with impaired ability to modulate neuronal excitability in middle-aged mice.* Learn Mem, 2009. **16**(6): p. 362-6.

30.   von Bohlen und Halbach, O., et al., *Age-related alterations in hippocampal spines and deficiencies in spatial memory in mice.* J Neurosci Res, 2006. **83**(4): p. 525-31.

31.   Xu, B., et al., *Loss of thin spines and small synapses contributes to defective hippocampal function in aged mice.* Neurobiol Aging, 2018. **71**: p. 91-104.

32.   Bloss, E.B., et al., *Evidence for reduced experience-dependent dendritic spine plasticity in the aging prefrontal cortex.* J Neurosci, 2011. **31**(21): p. 7831-9.

33.   Yasumatsu, N., et al., *Principles of long-term dynamics of dendritic spines.* J Neurosci, 2008. **28**(50): p. 13592-608.

34.   Onat, U.I., et al., *Intercepting the Lipid-Induced Integrated Stress Response Reduces Atherosclerosis.* J Am Coll Cardiol, 2019. **73**(10): p. 1149-1169.

35.   Deczkowska, A., et al., *Mef2C restrains microglial inflammatory response and is lost in brain ageing in an IFN-I-dependent manner.* Nat Commun, 2017. **8**(1): p. 717.

36.   Hinnebusch, A.G., I.P. Ivanov, and N. Sonenberg, *Translational control by 5'-untranslated regions of eukaryotic mRNAs.* Science, 2016. **352**(6292): p. 1413-6.

37.   Sonenberg, N. and A.G. Hinnebusch, *Regulation of translation initiation in eukaryotes: mechanisms and biological targets.* Cell, 2009. **136**(4): p. 731-45.

38.   Chen, A., et al., *Inducible enhancement of memory storage and synaptic plasticity in transgenic mice expressing an inhibitor of ATF4 (CREB-2) and C/EBP proteins.* Neuron, 2003. **39**(4): p. 655-69.

39.   Pasini, S., et al., *Specific downregulation of hippocampal ATF4 reveals a necessary role in synaptic plasticity and memory.* Cell Rep, 2015. **11**(2): p. 183-91.

40.   Wek, R.C., *Role of eIF2alpha Kinases in Translational Control and Adaptation to Cellular Stress.* Cold Spring Harb Perspect Biol, 2018. **10**(7).

41.   Alamed, J., et al., *Two-day radial-arm water maze learning and memory task; robust resolution of amyloid-related memory deficits in transgenic mice.* Nat Protoc, 2006. **1**(4): p. 1671-9.

42.   Horowitz, A.M., et al., *Blood factors transfer beneficial effects of exercise on neurogenesis and cognition to the aged brain.* Science, 2020. **369**(6500): p. 167-173.

43.   Feng, X., et al., *Delayed-matching-to-place Task in a Dry Maze to Measure Spatial Working Memory in Mice.* Bio Protoc, 2017. **7**(13).

44.   Oliveira Pisco A, M.A., Schaum N, Karkanias J, Neff NF, Darmanis S, Wyss-Coray T, Quake SR, *A Single Cell Transcriptomic Atlas Characterizes Aging Tissues in the Mouse.* bioRxiv, 2020.

45.   Mrdjen, D., et al., *High-Dimensional Single-Cell Mapping of Central Nervous System Immune Cells Reveals Distinct Myeloid Subsets in Health, Aging, and Disease.* Immunity, 2018. **48**(3): p. 599.

46.   Brush, M.H., D.C. Weiser, and S. Shenolikar, *Growth arrest and DNA damage-inducible protein GADD34 targets protein phosphatase 1 alpha to the endoplasmic reticulum and promotes dephosphorylation of the alpha subunit of eukaryotic translation initiation factor 2.* Mol Cell Biol, 2003. **23**(4): p. 1292-303.

47.   Connor, J.H., et al., *Growth arrest and DNA damage-inducible protein GADD34 assembles a novel signaling complex containing protein phosphatase 1 and inhibitor 1.* Mol Cell Biol, 2001. **21**(20): p. 6841-50.

48.   Novoa, I., et al., *Feedback inhibition of the unfolded protein response by GADD34-mediated dephosphorylation of eIF2alpha.* J Cell Biol, 2001. **153**(5): p. 1011-22.

49.   Powers, E.T., et al., *Biological and chemical approaches to diseases of proteostasis deficiency.* Annu Rev Biochem, 2009. **78**: p. 959-91.

50.   Hetz, C., J.M. Axten, and J.B. Patterson, *Pharmacological targeting of the unfolded protein response for disease intervention.* Nat Chem Biol, 2019. **15**(8): p. 764-775.

51.   Sidrauski, C., et al., *Pharmacological brake-release of mRNA translation enhances cognitive memory.* Elife, 2013. **2**: p. e00498.

52.   Tenkerian, C., et al., *mTORC2 Balances AKT Activation and eIF2alpha Serine 51 Phosphorylation to Promote Survival under Stress.* Mol Cancer Res, 2015. **13**(10): p. 1377-88.

53.   Cagnetta, R., et al., *Noncanonical Modulation of the eIF2 Pathway Controls an Increase in Local Translation during Neural Wiring.* Mol Cell, 2019. **73**(3): p. 474-489 e5.

54.   Koromilas, A.E., *M(en)TORship lessons on life and death by the integrated stress response.* Biochim Biophys Acta Gen Subj, 2019. **1863**(3): p. 644-649.

55.   Klann, K., G. Tascher, and C. Munch, *Functional Translatome Proteomics Reveal Converging and Dose-Dependent Regulation by mTORC1 and eIF2alpha.* Mol Cell, 2020. **77**(4): p. 913-925 e4.

56.   Smith, L.K., et al., *beta2-microglobulin is a systemic pro-aging factor that impairs cognitive function and neurogenesis.* Nat Med, 2015. **21**(8): p. 932-7.

57.   Casaletto, K.B., et al., *Cognitive aging is not created equally: differentiating unique cognitive phenotypes in "normal" adults.* Neurobiol Aging, 2019. **77**: p. 13-19.

58.   Casaletto, K.B., et al., *Sexual dimorphism of physical activity on cognitive aging: Role of immune functioning.* Brain Behav Immun, 2020. **88**: p. 699-710.

59.   Jack, C.R., Jr., et al., *Age, Sex, and APOE epsilon4 Effects on Memory, Brain Structure, and beta-Amyloid Across the Adult Life Span.* JAMA Neurol, 2015. **72**(5): p. 511-9.

60.   Davis, E.J., I. Lobach, and D.B. Dubal, *Female XX sex chromosomes increase survival and extend lifespan in aging mice.* Aging Cell, 2019. **18**(1): p. e12871.

61.   Davis, E.J., et al., *A second X chromosome contributes to resilience in a mouse model of Alzheimer's disease.* Sci Transl Med, 2020. **12**(558).

62. Gant, J.C., et al., *Early and simultaneous emergence of multiple hippocampal biomarkers of aging is mediated by Ca2+-induced Ca2+ release.* J Neurosci, 2006. **26**(13): p. 3482-90.

63. Oh, M.M., et al., *Learning-related postburst afterhyperpolarization reduction in CA1 pyramidal neurons is mediated by protein kinase A.* Proc Natl Acad Sci U S A, 2009. **106**(5): p. 1620-5.

64. Ultanir, S.K., et al., *Regulation of spine morphology and spine density by NMDA receptor signaling in vivo.* Proc Natl Acad Sci U S A, 2007. **104**(49): p. 19553-8.

65. Frank, A.C., et al., *Hotspots of dendritic spine turnover facilitate clustered spine addition and learning and memory.* Nat Commun, 2018. **9**(1): p. 422.

66. Lu, J. and Y. Zuo, *Clustered structural and functional plasticity of dendritic spines.* Brain Res Bull, 2017. **129**: p. 18-22.

67. Tolino, M., M. Kohrmann, and M.A. Kiebler, *RNA-binding proteins involved in RNA localization and their implications in neuronal diseases.* Eur J Neurosci, 2012. **35**(12): p. 1818-36.

68. Garber, C., et al., *T cells promote microglia-mediated synaptic elimination and cognitive dysfunction during recovery from neuropathogenic flaviviruses.* Nat Neurosci, 2019. **22**(8): p. 1276-1288.

69. Di Liberto, G., et al., *Neurons under T Cell Attack Coordinate Phagocyte-Mediated Synaptic Stripping.* Cell, 2018. **175**(2): p. 458-471 e19.

70. Krukowski, K., et al., *Traumatic Brain Injury in Aged Mice Induces Chronic Microglia Activation, Synapse Loss, and Complement-Dependent Memory Deficits.* Int J Mol Sci, 2018. **19**(12).

71.   Krukowski, K., et al., *Female mice are protected from space radiation-induced maladaptive responses.* Brain Behav Immun, 2018. **74**: p. 106-120.

72.   Krukowski, K., et al., *Peripheral T Cells as a Biomarker for Oxygen-Ion-Radiation-Induced Social Impairments.* Radiat Res, 2018. **190**(2): p. 186-193.

Chapter 5: Functional role of brain engrafted macrophages against brain injuries

Abstract

Brain resident microglia have a distinct origin compared to macrophages in other organs. Under physiological conditions, microglia are maintained by self-renewal from the local pool, independent of hematopoietic progenitors. Pharmacological depletion of microglia during whole-brain radiotherapy prevents synaptic loss and long-term recognition memory deficits. However, the origin or repopulated cells and the mechanisms behind these protective effects are unknown. CD45$^{low/int}$/CD11b$^+$ cells from naïve brains, irradiated brains, PLX5622 treated brains and PLX5622 + whole-brain radiotherapy treated brains were FACS sorted and sequenced for transcriptomic comparisons. Bone marrow chimeras were used to trace the origin and long-term morphology of repopulated cells after PLX5622 and whole-brain radiotherapy. FACS analyses of intrinsic and exotic synaptic compartments were used to measure phagocytic activities of microglia and repopulated cells. In addition, concussive brain injuries were given to PLX5622 and brain-irradiated mice to study the potential protective functions of repopulated cells after PLX5622 + whole-brain radiotherapy. After a combination of whole-brain radiotherapy and microglia depletion, repopulated cells are brain-engrafted macrophages that originate from circulating monocytes. Comparisons of transcriptomes reveal that brain-engrafted macrophages have an intermediate phenotype that resembles both monocytes and embryonic microglia. In addition, brain-engrafted macrophages display reduced phagocytic activity for synaptic compartments compared to microglia from normal brains in response to a secondary concussive brain injury. Importantly, replacement of microglia by brain-engrafted

macrophages spare mice from whole-brain radiotherapy-induced long-term cognitive deficits and prevent concussive injury-induced memory loss. Brain-engrafted macrophages prevent radiation- and concussion-induced brain injuries and cognitive deficits.

Introduction

Brain resident microglia are the innate immune cells of the central nervous system (CNS). Arisen from the yolk sac during embryonic development, microglia actively survey the environment to maintain normal brain functions [1, 2]. Under physiological conditions, microglia are maintained solely by self-renewal from the local pool [3]. Following brain injury and other pathological conditions, microglia become activated and play a central role in the clearance of cellular debris, but if not controlled this process can result in aberrant synaptic engulfment [4-7]. Temporary depletion of microglia can be achieved by using pharmacologic inhibitors of the colony-stimulating factor 1 receptor (CSF-1R) [8]. In the normal brain, treatment with CSF-1R inhibitors (CSF-1Ri) can deplete up to 99% of microglia without causing detectable changes to cognitive functions [8, 9]. Full repopulation occurs within 14 days of inhibitor withdrawal and the repopulated microglia are morphologically and functionally identical to the microglia in naïve brains [9]. Microglia depletion and repopulation by local progenitors has been shown to be beneficial for disease-, injury-, and age-associated neuropathological and behavioral conditions [10-15]. However, the mechanisms for these protective effects are unknown.

Whole-brain radiotherapy (WBRT), delivered in multiple fractions, is routinely used to treat patients with brain tumors. It is estimated that more than 200,000 patients receive WBRT yearly in the US alone [16]. While it is effective in improving intracranial tumor control, WBRT leads to deterioration of patients' cognitive functions and quality of life [17-19]. Currently, there is no treatment available to prevent or mitigate these adverse effects. Previous studies demonstrated that WBRT causes deleterious effects to the CNS microenvironment by a number of mechanisms including apoptosis of neural progenitor cells, disruption of the blood-brain barrier, activation of microglia and accumulation of peripherally derived macrophages [20-25]. We and others have reported that depletion of microglia during or shortly after brain irradiation in animal models can prevent loss of dendritic spines in hippocampal neurons and cognitive impairments that develop at later time points [12-14]. These reports suggest that microglial plays a critical role in inducing synaptic abnormalities and consequently, cognitive deficits after brain irradiation. The underlying molecular pathways responsible for the protective effects of repopulated microglia against radiotherapy-induced neuronal alterations remain unknown.

In the current study, 1) we first defined signature of repopulating cells and analyzed the transcriptional profile of repopulated brain macrophages from irradiated mouse brains after CSF-1R inhibitor-mediated depletion. 2) We next sought to establish the origin of repopulated cells coming from the peripheral monocytic lineage. 3) We identified the functionality of repopulated macrophages by measuring the ability to engulf synaptic compartments compared to brain resident microglia. Lastly, 4) we determined the protective properties of brain-engrafted macrophages (BEMs) against a

secondary concussive brain injury. Together, these results uncover the mechanism by which brain-engrafted macrophages preserve hippocampal synapses and memory functions after radiation injury and in response to an additional brain injury.

Results

Microglia depletion and repopulation prevents radiation-induced hippocampal-dependent memory deficits.

Temporary microglia depletion during or shortly after exposure to brain irradiation prevents cognitive deficits, suggesting microglia's key role in modifying neuronal and cognitive functions [12-14]. Changes in expression levels of pro-inflammatory cytokine/chemokines have been shown to correlate with cognitive performance in mice [12, 15, 20], however, the exact change in the transcriptional profile of repopulated microglia after brain irradiation is unknown and is an important tool to dissect the roles that repopulated microglia play in preventing of radiation-induced memory deficits. In this study we used a previously reported WBRT and microglia depletion paradigm [13] and performed RNA sequencing using repopulated microglia with and without WBRT, and compared with transcriptomes of microglia obtained from mice without CSF-1R inhibitor-mediated depletion (**Figure 1A, B**). A CSF-1R inhibitor was used to fully deplete microglia in 8-weeks old male mice, for a duration of 21 days. Three fractions of therapeutic whole-brain irradiation were given to each mouse every other day over five days starting from day 7 of CSF-1R inhibitor treatment. Novel Object Recognition (NOR) test was used to measure recognition memory 4 weeks after the last fraction of WBRT. Consistent with our previous report, fractionated WBRT resulted in impairment in

recognition memory, which was prevented by CSF-1R inhibitor treatment (**Figure 1A,** lower panel). No deficits in motor functions or changes of anxiety levels were found in the open field test (scored from day 1 of NOR test, data not shown). One day after the NOR test, mice were euthanized and whole brains were used to sort microglia (Control Sham and Control + WBRT, CD45$^{low/int}$CD11b$^+$) and repopulated cells (CSF-1R inhibitor Sham and CSF-1R +WBRT, CD45$^{low/int}$CD11b$^+$) for RNA extraction and RNA sequencing (**Figure 1A**).

Microglia depletion and repopulation eliminates radiation-induced transcriptome signatures.

To identify biological pathways involved in radiation-induced memory deficits, we listed genes differentially expressed in microglia after WBRT with and without microglia depletion and repopulation for Gene Ontology Biological Process (GOBP) enrichment analysis. 204 genes were found to be differentially expressed (DE genes) only in microglia isolated from irradiated brains (**Figure 1B, Supplementary Table 1**). No enriched GOBP terms were found from the 87 WBRT down-regulated genes (**Supplementary Table 1**). There were 193 enriched GOBP terms from the 117 WBRT up-regulated genes, the top 20 enriched GOBP terms are listed in **Figure 1C.** Almost half (96) of these enriched GOBP terms were associated with increased response to cell cycle regulation, radiation, DNA repair and stress; the rest enriched GOBP terms were associated with increased metabolism (21), development (12), regulation of protein kinase activity (8), cellular adhesion (4) and other functions (**Figure 1D, Supplementary Table 1**). Notably, regardless of WBRT, the expression of these

WBRT-induced DE genes did not change in cells isolated from brains treated with CSF-1Ri. These results demonstrate that the transcriptomic changes in microglia induced by WBRT can be completely eliminated after microglia depletion and repopulation.

To validate the RNAseq results, we next performed qPCR analyses using sorted microglia from animals in the same cohort (**Figure 1B,** and **Supplementary Table 1**). The expression of the toll-like receptor 3 (TLR3) family gene *Lgals9* was significantly increased by irradiation (WBRT + Control diet versus Sham + Control diet) and was at levels comparable to the shams (Sham + Control diet) when treated with CSF-1Ri despite of irradiation (**Supplementary Figure 1A**). *TNFα*, another TLR3 family member which also belongs to GOBP "regulation of response to reactive oxygen species (ROS)", was significantly upregulated by irradiation (WBRT + Control diet versus Sham + Control diet); its expression levels are comparable between the Sham + Control diet and the WBRT + CSF1Ri treated groups. However, *TNFα* remained elevated in microglia from mice treated only by CSF-1Ri (**Supplementary Figure 1B**). Another gene from the GOBP "regulation of response to ROS", *Sesn2*, was also significantly upregulated by WBRT (**Supplementary Figure 1C**). *Sesn2* remained at the control sham levels in CSF-1Ri only group and was significantly down-regulated in the WBRT + CSF-1Ri group. *Mdm2*, a gene that belongs to GOBP "cellular response to ionizing radiation", was increased after WBRT, and significantly downregulated in in CSF-1Ri treated groups (**Supplementary Figure 1D**). Other WBRT-induced expression of radiation induced genes, *Ddias*, *Rad51, FoxM1* and *Check 1*, were all at the control sham levels in repopulated microglia regardless of the exposure to WBRT (**Supplementary Figure 1E – H**). In conclusion, the qPCR validation confirmed that the

transcriptomic changes seen in our RNAseq dataset were reliable. These results suggest that CSF-1Ri mediated microglia depletion during WBRT followed by repopulation eliminated radiation-induced signatures in the microglia transcriptome.

Microglia depletion and repopulation prevents radiation-induced loss of hippocampal PSD-95.

We previously demonstrated that brain irradiation resulted in reduced density of dendritic spines in hippocampal neurons [13]. To accurately determine the effect of WBRT in the intrinsic synaptic protein levels we measured pre- (Syn1) and post-synaptic (PSD-95) markers in the hippocampus by flow-synaptometry [26, 27]. Fractionated hippocampal cell membranes containing synaptosomes were enriched and particles between 1 – 3 μm were analyzed to measure synaptic protein levels using mean fluorescent intensities by FACS (**Figure 1E**). We observed no changes in pre-synaptic Synapsin-1 protein levels in the hippocampi across all groups (**Figure 1F**). However, we measured a significant reduction in post-synaptic protein PSD-95 after WBRT, which was completely prevented by CSF-1R inhibitor mediated microglia depletion (**Figure 1G**). These results cement the role of microglia in the radiation-induced loss of post-synaptic components after WBRT.

Repopulated microglia after WBRT originate from peripheral monocytes.

The fractalkine receptor CX3CR1 is expressed in both microglia and peripheral monocytes [28], while chemokine receptor CCR2 is mainly expressed in monocytes [29]. In the Cx3cr1$^{GFP/+}$Ccr2$^{RFP/+}$ reporter mice, the different expression patterns of GFP

and RFP can be used to distinguish microglia (GFP+RFP-) from monocytes (GFP+RFP+) [29]. To investigate the cell-of-origin of repopulated microglia in our experimental paradigm we generated bone marrow chimeras with head-protected irradiation using fluorescent labeled bone marrow from Cx3cr1$^{GFP/+}$Ccr2$^{RFP/+}$ donor mice (**Figure 2A**). This allowed partial replacement of bone marrow cells without changing the permeability of the blood-brain-barrier [2, 30, 31]. At 6 weeks after bone marrow transplantation about two thirds of peripheral monocytes were replaced by transplanted cells with fluorescent labels (**Figure 2B**). Bone marrow chimera animals were then treated with WBRT and CSF-1R inhibitor following the same experimental timeline used for RNA sequencing (**Figure 2A**). Next, we compared the compositions of myeloid cells in the brain after CSF-1R inhibitor-mediated depletion and repopulation. Flow cytometry analyses performed 33 days after WBRT revealed that microglia depletion and repopulation alone (Sham + CSF-1Ri) only resulted in limited accumulation of transplanted cells in the brain (**Figure 2C**, BMT only). However, in mice that received WBRT and CSF-1R inhibitor two thirds of the microglia were replaced by Cx3cr1-GFP labeled cells, close to the chimera efficiency (**Figure 2B, C,** BMT +fWBI). These results suggest that microglia depletion during WBRT resulted in significant contribution of the CNS microglia pool by peripheral monocyte-derived BEMs.

Brain-engrafted macrophages retain monocyte signatures.

We next assessed the transcriptomic profile of the BEMs after microglia depletion and WBRT by comparing our RNAseq dataset with a previous report by Lavin and Winter *et al* [32]. To minimize false discovery and noise signals, we examined 1201

genes from this published dataset with a fold change greater than 1.50 or smaller than 0.667 for down-regulated genes (FDR <0.01, monocyte compared to naïve microglia), and found that 1066 genes were expressed in our samples (**Supplementary Table 2**). Strikingly, the hierarchical clustering of 525 monocyte- and 541 microglia-signature genes revealed that the expression profile of monocyte-derived BEMs (WBRT + CSF-1Ri) does not cluster with naïve (Sham + Control diet), irradiated (WBRT + Control diet) or repopulated (Sham + CSF-1Ri) microglia (**Figure 2D**). Similarity matrix analysis using this microglia/monocyte signature gene list revealed that the expression pattern in BEMs is different from naïve, irradiated and repopulated microglia (**Figure 2E**). Next, we counted genes in each group that expressed in the same trends as microglia or monocyte signature genes from the Lavin data set to determine the similarity scores to these two cell populations. We found that naïve, irradiated and repopulated microglia had 60%, 57% and 51% (718, 685 and 612) genes expressed in the same trends as microglia signature genes, respectively, with minimum similarity (2-3%) to monocyte signature genes; while BEMs expressed both microglia (28%, 331 genes) and monocyte signature genes (32%, 386 genes) (**Figure 2F**).

To validate microglia and monocyte signature genes that were differentially expressed in our RNAseq results we performed qPCR analyses (**Supplementary Figure 2, Supplementary Table 2**). Microglia signature genes *Sall1*, *P2ry12*, *Tmem119* and *Trem2* were expressed at comparable levels in naïve, irradiated and repopulated microglia, while at significantly lower level in BEMs (**Supplementary Figure 2A – D**). On the other hand, expression of monocyte signature gene *Runx3*, was significantly higher in BEMs than other groups (**Supplementary Figure 2E**). Notably, previously

172

reported brain-engrafted macrophage specific genes *Lpar6* and *Pmepa1 [33]* have significantly higher expression levels in BEMs after CSF-1Ri and WBRT treatments compared to other groups (**Supplementary Figure 2 F, G**). In addition, the expression of *Ccr2*, a monocyte signature gene that was not differentially expressed in our RNAseq dataset, was also not differentially expressed among the four experimental groups by qPCR, suggesting that monocyte derived BEMs had lost their Ccr2 expression at this time point (**Supplementary Figure 2H**). Taken together, these results confirm that after WBRT and CSF-1R inhibitor-mediated microglia depletion BEMs originate from peripheral monocytes.

Monocyte-derived brain-engrafted macrophages resemble embryonic microglia signatures.

Because monocyte-derived BEMs were exposed to the brain microenvironment for a short period of time, we hypothesized that they were functionally immature. To test this hypothesis, we first examined genes that were highly expressed at different developmental stages in microglia, and used yolk sac/embryonic and adult-specific genes as references (called embryonic and adult signature genes hereon) [34]. Hierarchical clustering of 1617 embryonic and 785 adult microglia signature genes revealed that transcriptomes of BEMs were highly similar to embryonic microglia, while the transcriptomes of microglia from other groups were similar to adult microglia and did not resemble the embryonic microglia (**Supplementary Figure 3A, Supplementary Table 3**). In addition, a similarity matrix analysis using all 2402 overlapped genes between two datasets showed that BEMs had the lowest similarity with microglia from

other groups (**Supplementary Figure 3B**). In addition, 54% of the listed genes (n=1306) in BEMs expressed in the same trends as *yolk sac*/embryonic microglia compared to adult microglia (**Supplementary Figure 3C**). In contrast, naïve (Sham), irradiated (WBRT only) and repopulated microglia (CSF-1Ri only) had much lower embryonic signature similarity scores (16%, 19% and 17%, n=381, 445 and 405, respectively, Supplementary Figure S3c). Notably, naïve, irradiated and repopulated microglia transcriptomes had high adult signature similarity scores (69%, 59% and 63%, n=1649, 1409 and 1507, respectively), while BEMs had the lowest adult similarity score (32%, n=759). These data suggest that the monocyte-derived BEMs start to resemble microglia by expressing more embryonic than adult microglia transcriptomic signature genes.

Radiation-induced phagocytosis activity is abrogated in brain-engrafted macrophages.

Aberrant loss of synapses during neuroinflammatory conditions has been linked with increased engulfment of synaptic compartments by microglia [35]. To determine if WBRT affects the phagocytosis potency of microglia, we injected pre-labeled synaptosomes from a naïve donor mouse into the hippocampi of mice after WBRT and CSF-1R inhibitor treatment and measured engulfment by microglia using flow cytometry (**Figure 3A**). After WBRT there was a significant increase in the number of microglia engulfing synaptosomes in the hippocampus compared to naïve non-irradiated animals (**Figure 3B**). Strikingly, synapse engulfment activity was unchanged compared to naïve animals in animals treated with CSF-1R inhibitor during WBRT (**Figure 3B**).

Immunofluorescent imaging at the injection sites confirmed that the injected synaptosomes were indeed engulfed by microglia, and the increased trend of engulfment by irradiated microglia remained unchanged (**Figures 3C and D, Supplementary Figure 4A).** Notably, after hippocampal injection of fluorescent labeled latex beads into the hippocampus, we found that WBRT resulted in increased engulfment of latex beads was also inhibited by CSF-1R inhibitor treatment, suggesting that the WBRT-induced increase of engulfment was not specific to synaptosomes, but rather a general increase of phagocytosis potency (**Supplementary Figure 4B**). These data are the first to demonstrate that WBRT results in an increase in microglial phagocytosis activity in the hippocampus that can be prevented by transient microglia depletion and full repopulation.

Irradiation-induced complement and phagocytic receptors expression in microglia are absent in BEM after WBRT.

Microglial complement receptors play essential roles in physiologic synaptic elimination during development and aberrant elimination during neuroinflammatory conditions [35, 36]. To understand the mechanisms of increased microglia phagocytic activity after WBRT, we measured expression levels of a list of complement receptors, phagocytic markers and lysosome proteins in microglia by flow cytometry. The expression of complement receptor C5aR was significantly elevated in microglia at one month after WBRT. However, in animals treated with CSF-1Ri C5aR expression was unchanged from naïve animals (**Figure 3E**). The same trend was observed in the expression levels of CD68 and lysosomal-associated membrane protein 1 (LAMP-1)

(**Figure 3 F and G**). These results were consistent with our data demonstrating decreased PSD95 levels (Figure 3b) and increased microglial phagocytosis activity in the hippocampus after WBRT (**Figure 3 B and D**). In addition, complement receptor CR3 (CD11b) was significantly elevated in microglia after WBRT or CSF-1Ri treatments alone, and remained unchanged in BEMs with combined WBRT and CSF-1Ri treatments (**Supplementary Figure 5A**). No changes in the complement receptor C3ar1 were measured after WBRT or CSF-1R inhibitor treatment (**Supplementary Figure 5B**). These results demonstrate that the increased microglia phagocytosis of synaptosomes after WBRT was associated with increased phagocytic and lysosome proteins, and was likely through the complement pathways.

Brain-engrafted macrophages after microglia depletion persist in the brain.

To determine whether BEMs are present long-term in the brain, we monitored this cellular population for 6 months after WBRT. To eliminate the limitation of using bone marrow obtained from the Cx3cr1$^{+/GFP}$Ccr2$^{+/RFP}$ knock-in reporter mouse strain, we used an actin-GFP transgenic line as bone marrow donors and generated chimeras using the same body-only irradiation protocol (**Figure 4A**). Six weeks later, mice were treated with CSF-1R inhibitor and WBRT and then used to trace BEMs at varies time points (**Figure 4A**). Whole coronal sections at the level of the dorsal hippocampus were stained with Iba1 and imaged to quantify total Iba1+ and GFP+ cells (**Supplementary Figure 6A**). We found that all GFP+ cells in the brain were also Iba1+, suggesting that BEMs were indeed derived from the periphery. In addition, the morphology of Iba1+GFP+ BEMs were analyzed and compared to Iba1+GFP- microglia (**Figure 4B**

176

and D). We found that round-shaped Iba1+GFP+ BEM cells entered the brain starting from 7 days after WBRT, and started to obtain more processes that resembled microglia morphology (**Figure 4B**). However, Sholl analysis demonstrated that the morphology of BEMs remained stable from 33 days after WBRT and never reached the structural complexity of microglia (**Figure 4C, Supplementary Figure 7**). We found that 40 – 90% of Iba1+ cells are also GFP+ at 14 days after WBRT. This ratio remained at high levels at 1, 3 and 6 months after WBRT (**Figure 4E**). Interestingly, although the Iba1+ and Iba1+GFP+ cell numbers are not fully recovered at 14 days after WBRT, the microglia replacement ratio was similar to the level of later time points (**Figure 5E, Supplementary Figure 6B and C**), suggesting a non-competitive manner of brain parenchyma occupancy by microglia and BEMs. These data demonstrate that BEMs enter the brain shortly after WBRT, adapt to a microglia-like morphology and maintain a stable population.

BEMs provide long-term protection against WBRT-induced memory deficits and hippocampal dendritic spine loss.

To measure the long-term cognitive outcomes, we treated a batch of wildtype animals, and tested their recognition memory at 3 and 6 months after WBRT (**Figure 5A**). We found that WBRT resulted in persistent loss of recognition memory also at 3 and 6 months, while CSF-1Ri treatment alone did not alter recognition memory performance (**Figure 5B and C**). Strikingly, mice that received WBRT along with temporary microglia depletion did not show any memory deficits and performed undistinguishable from control animals at 3 and 6 months (**Figure 5B and C**). Our

previous report demonstrated that WBRT-induced dendritic spine loss in hippocampal neurons was fully prevented by temporary microglia depletion during irradiation [13]. In this study, we sought to understand if the protective effects persisted up to 6 months after WBRT. Our results clearly show that radiation-induced loss of dendritic spines in hippocampal neurons persists to this time point, and that the protective effect of microglia depletion and subsequent replacement by BEMs is long lasting (**Figure 5D**). Taken together, brief depletion of microglia during WBRT induces sustainable BEMs in the brain and provides long-term protection against irradiation-induced deficits in recognition memory.

Replacement of microglia by BEMs protects against concussive injury-induced memory loss.

To investigate the function of BEMs after they replaced microglia, a single mild concussive Closed Head Injury (CHI) was given to mice 30 days after CSF-1R inhibitor treatment and WBRT; microglia/BEMs morphology and phagocytic activities were measured following recognition memory test by NOR (**Fig 6A**). By FACS analysis at 24 days post injury, we found that phagocytosis activity increased (p=0.0419) after CHI in microglia but not in BEMs (**Figure 6B**). Quantification of immunofluorescent staining of Iba-1/PSD-95 co-localization also revealed a trend of increased engulfment towards pre-stained synaptosomes by microglia but not by BEMs (**Fig 6C and D**). In addition, the structural complexity of microglia decreased in Sholl analysis, while the morphology of BEMs remained unchanged after CHI (**Figure 6E**). Furthermore, at 20 days after injury, CHI-induced recognition memory deficits were spared in mice whose microglia

178

were replaced by BEMs (**Figure 6F**). These results demonstrate that unlike resident microglia which transition to a less ramified morphology and exhibit increased phagocytic activity towards injected synaptosomes, BEMs remain unchanged in both morphology and phagocytic activity in response to CHI. More importantly, our data suggest that replacement of microglia by BEMs can protect against CHI-induced memory loss.

Discussion

Here we provide evidence for the direct involvement of microglia phagocytic activity towards synaptic compartments as a mechanistic cause for loss of dendritic spines with consequent impairments in memory functions after WBRT. Replacement of microglia with monocyte derived BEMs prevents loss of synapses and consequent memory deficits. Importantly, BEMs replacing microglia are also protective against a second injury to the brain. Together our results unravel novel immediate and long lasting therapeutic benefits of microglia depletion and repopulation during WBRT.

Microglia play pivotal roles in reshaping synaptic networks during neonatal brain development [37, 38]. They engulf synaptic elements by active synaptic pruning in an activity- and complement-dependent manner [38]. Microglia-driven aberrant loss of synapses and consequent impairment of cognitive functions have also been reported in animal models of AD [35], infection [39], injury [40, 41], and aging [42]. Using RNA sequencing, we compared the transcriptomes of microglia from irradiated and non-irradiated brains after CSF-1Ri-mediated microglia depletion and repopulation. WBRT induces increased expression of genes that mainly belong to cell cycle regulation, DNA

damage repair and stress-induced biological processes (**Figure 1D**). As a result, activated microglia have higher engulfing potential towards both intrinsic and extrinsic synaptic compartments (**Figures 1G, Figure 3B - D**). This view is further supported by the increased expression of endosome/lysosome proteins CD68 and CD107a with the complement receptors CR3 and C5ar1 measured in microglia chronically after WBRT (**Figure 3E – G, and Supplementary Figure 5**). Notably, both endosome/lysosome proteins and complement receptor expressions were comparable to naïve microglia (sham + control diet) in BEMs (WBRT + CSF-1Ri) and repopulated microglia (CSF-1Ri only). These results suggest that the loss of hippocampal synapses after WBRT may be dependent on the activation of the alternative complement pathway. Interestingly, although BEMs are morphologically similar to adult microglia, they retain a transcriptomic signature similar to both circulating monocytes and embryonic microglia (**Figure 2 and Supplementary Figure 3**).

The decrease in post-synaptic protein PSD95 level in hippocampal synaptosomes is also paralleled with reductions in hippocampal dendritic spines (**Figures 5D** and Feng et al [13]). However, pre-synaptic Synapsin 1 protein levels are not affected by WBRT or microglia depletion, suggesting that WBRT mainly induces loss of post-synaptic compartments. Interestingly, although the phagocytosis potency of repopulated microglia and BEMs are both low (**Figures 3B and D**), microglia depletion and repopulation alone does not affect dendritic spine density (**Figures 5D and E**). On the other hand, microglia replacement by BEMs results in increased dendritic spine density compared to those with radiation alone, and microglia depletion alone [13]. Strikingly, the protective effect of microglia depletion during WBRT results in protected

memory functions and extends to 3- and 6-months following irradiation (**Figure 5B and C**). The dendritic spine density in mice that received WBRT and CSF-1Ri remained higher than those who only received CSF-1Ri (**Figure 5E**) suggesting that in an non-reactivate state (evidenced by no changes in genes involved in cell cycle and radiation response, in microglial phagocytosis and lysosome proteins, and in phagocytosis activity towards injected synaptosomes and latex beads) of repopulated microglia and BEMs may have intrinsic differences in maintaining the homeostasis of dendritic spines, which appears to diminish over time.

In the CNS, microglia maintain a stable population by self-renewal in either a random manner or through clonal expansion [3, 43]. CSF-1R inhibitor treatment alone results in acute depletion of up to 99% of CNS resident microglia, with repopulated microglia arising solely from the residual microglia and their progenitor cells that remain after treatment [8] [44]. The repopulated microglia have transcriptional and functional profiles similar to naïve microglia [9]. Peripheral macrophages can engraft into the brain but remain morphologically, transcriptionally and functionally different from CNS resident microglia [45, 46]. Under specific circumstances, monocytes entering the CNS can become microglia-like cells. This is most clearly demonstrated in experiments where lethal whole-body irradiation was followed by bone marrow transplantation with labeled monocytes (Ccr2$^+$Ly6C^{high}), resulting in accumulation of these cells in the brain [30]. In neonatal mouse brains monocytes can enter the brain parenchyma without head irradiation and become microglia-like cells at a low frequency [47]. In addition, chronic depletion of microglia without irradiation also results in myeloid cells entering the CNS and becoming BEMs [33]. However, the roles of BEMs in cognitive functions are largely

unknown. Here we report that concurrent microglia depletion and therapeutic brain irradiation causes peripheral monocytes to enter the brain parenchyma and become microglia-like BEMs. BEMs enter the brain at 14 days after the completion of brain irradiation, or 4 days after the CSF-1Ri withdrawal (**Figure 4E, and Supplementary Figure 6**). Notably, although the ratio of BEMs was high at this time point the total number of Iba1 positive cells is not fully recovered (**Supplementary Figure 6B**). This ratio remains at high levels in head-irradiated mice throughout the current study (**Figure 5E**), suggesting that microglia depletion during WBRT results in sustainable replacement of microglia by BEMs. Importantly, this observation correlates with long-term protection against WBRT-induced loss of recognition memory and dendritic spines in hippocampal granule neurons (**Figure 6B – E**).

In the clinic, cancer patients are unlikely to receive a second round of radiotherapy to the brain. Therefore, instead of introducing a second round of WBRT, after they occupied the brain we gave BEM-bearing mice CHI that causes memory deficits [48, 49], and further examined BEMs' response to a single head trauma. Our data show that microglia had increased phagocytic potential to exogenous synaptosomes after CHI, while phagocytic activity of BEMs did not change and remained at a similar level as naïve microglia (**Figure 6B and C**). This is further demonstrated by Sholl analysis of BEMs showing no change in morphology after CHI (**Figure 6E**). Most importantly, CHI-induced memory deficit was prevented in BEM-bearing mice (**Figure 7F**). These data are the first to demonstrate that BEMs can prevent brain injury-induced cognitive dysfunction.

A limitation of the current study is that we didn't investigate transcriptomic profiles and phagocytic functions of BEMs at chronic time points after they replaced microglia. Therefore, it is unknown whether BEMs can obtain transcriptomic profiles and functions closer to adult microglia at later time points. In addition, microglia have been shown to mediate forgetting through complement-dependent synaptic elimination [50]. We did observe increased dendritic spines in hippocampal granule neurons at both 1 and 6 months after WBRT compare to sham animals, suggesting that BEMs may have lower activity in eliminating synapses than naïve microglia. Therefore, the consequences of microglia replacement by BEMs in normal forgetting need further investigation. Furthermore, in the current study we rely solely on the NOR test to measure memory functions. It is possible that the behavioral changes we saw are results from differences in motivation of exploratory behavior or curiosity rather than recognition memory. Additional behavior assays such as Morris Water Maze could be used to detect changes in memory more stringently. Finally, transcriptomic and functional studies at chronic time points with other microglia depletion models will provide insights into the transcriptomic and functional dynamics of BEMs in the brain.

Although the CSF-1Ri used in the current study (PLX5622) was only tested in phase I clinical trials, other formats of CSF-1Ri are approved for use in patients. Pexidartinib (PLX3397), which has been shown to deplete microglia with high efficiency [8, 9, 11], is approved for use in the treatment of symptomatic tenosynovial giant cell tumor [51]. Other CSF-1R Inhibitors including Imatinib, dasatinib and bosutinib are approved for use in patients with leukemia and other types of cancer [52]. In addition, a

few small molecule CSF-1R inhibitors are currently under clinical trials. Therefore, the proposed treatment have the potential for quick assessment in clinical phases.

We report evidence for the mechanism by which microglia depletion and repopulation after WRBT prevents memory loss. Our data demonstrate that replacement of CNS resident microglia by peripheral monocyte-derived BEMs results in a transcriptional and functional reset of immune cells in the brain to an inactive state, which spares the brain from WBRT-induced dendritic spine loss in hippocampal neurons and recognition memory deficits. Most importantly, replacement of microglia by BEMs protects against concussive brain injury-induced cognitive deficits. These results suggest that replacement of depleted microglia pool by peripheral monocyte-derived BEMs represents a potent treatment for irradiation-induced memory deficits.

Materials and methods

Animals. All experiments were conducted in compliance with protocols approved by the Institutional Animal Care and Use Committee at the University of California, San Francisco (UCSF), following the National Institutes of Health Guidelines for Animal Care. 7 weeks old C57BL/6J male mice were purchased from the Jackson Laboratory and housed at UCSF animal facilities and were provided with food and water ad libitum. All mice were habituated for one week before any treatments or procedures. 8–10 weeks old $Cx3cr1^{GFP/+}Ccr2^{RFP/+}$ mice were breed by crossing the $Cx3cr1^{GFP/GFP}Ccr2^{RFP/RFP}$ line with wildtype C57BL/6J mice, and used as donors for the bone marrow chimeras.

CSF-1Ri treatment. CSF-1Ri (PLX5622 formulated in AIN-76A standard chow at 1200 ppm, Research Diets, Inc) were provided by Plexxikon, Inc (Berkeley, CA). Mice were given free access to either CSF-1Ri chow or control diet (AIN-76A without PLX5622) for 21 days. Approximately 4.8 mg of PLX5622 was ingested by each mouse per day in the treated group (calculation based on 4 g/mouse daily consumption).

Fractionated whole-brain radiotherapy (WBRT). 8 weeks old mice were injected with ketamine (90mg/kg) /Xylazine (10 mg/kg) mix. When fully immobilized mice were placed in irradiator with cesium-137 source at the dose rate of 2.58 Gy/min. The body was shielded with a lead collimator that limited the radiation beam to a width of 1 cm to cover the brain. Three radiation fractions (3.3 Gy) were delivered every other day over 5 days. Sham animals received ketamine/xylazine without irradiation.

Bone marrow chimeras. 8 weeks old C57BL/6J mice were used as bone marrow recipients. 8 weeks old males received two doses of 6 Gy cersium-137 irradiation at the dose rate of 2.58 Gy/min with head protected by lead plates 6 hours apart. Bone marrow cells from 6–10 weeks old donors $Cx3cr1^{+/GFP}Ccr2^{+/RFP}$ or B6-EGFP (The Jackson Laboratory, stock No 003291) were isolated and resuspended in sterile saline at a concentration of 100 million cells/ml. 0.1 ml of bone marrow cells were injected into recipients via retro-orbital injection immediately after the second head protected irradiation. Bone marrow chimeras were housed with 1.1 mg/ml neomycin as drinking water for 4 weeks and allowed an additional 2 weeks to recover before any treatments.

Concussive TBI – Closed head injury. 12 weeks old C57BL/6J mice were randomly assigned to each TBI or sham surgery group. Animals were anesthetized and maintained at 2-2.5% isoflurane during CHI or sham surgery. Animals were secured to a stereotaxic frame with nontraumatic ear bars and the head of the animal was supported with foam. Contusion was induced using a 5-mm tip attached to an electromagnetic impactor (Leica) at the following coordinates: anteroposterior, −1.50 mm and mediolateral, 0 mm with respect to bregma. The contusion was produced with an impact depth of 1 mm from the surface of the skull with a velocity of 5.0 m/s sustained for 300 ms. Animals that had a fractured skull after injury were excluded from the study. Sham animals were secured to a stereotaxic frame with nontraumatic ear bars and received the midline skin incision but no impact. After CHI or sham surgery, the scalp was sutured and the animal was allowed to recover in an incubation chamber set to 37 °C. All animals recovered from the surgical procedures as exhibited by normal behavior and weight maintenance monitored throughout the duration of the experiments.

Synaptosome isolation staining and injection. Fresh hippocampi from a naïve mouse was homogenized and spun down in 0.32M sucrose solution (dissolved in 50 mM HEPES buffer). Supernatant was centrifuged in 0.65M sucrose solution at 12,000 rpm for 30 minutes at 4°C. The synaptosome containing pellet was resuspended in 1 x ice-cold PBS, diluted to 100 µg/ml, and stained with PSD-95 antibody (Millipore) on ice for 30 minutes followed by a secondary antibody staining (Invitrogen, goat anti-mouse AF488). Stained synaptosomes were washed and diluted 20 times in PBS and stored at -80°C. 2 µl of pre-stained synaptosomes were injected into the right hippocampus of

each recipient mouse at the coordinate relative to the bregma: AP + 1.6 mm, ML + 1.6 mm and DV -2.0 mm. Mice were euthanized 3 days later. The left hemispheres (uninjected) were used for phagocytosis markers staining and the right hemispheres (injected) were used to assess synaptosome phagocytosis levels by flow cytometry or immunofluorescent staining.

Immunofluorescent Staining. hemi-brains with synaptosome injection were fixed in 4% PFA overnight, cryo-protected in 30% sucrose solution in 1 x PBS and sliced in 20 μm sections. Sliced tissues were stained with Iba1 (Fujifilm Wako Pure Chemical Corporation, 019-19741) followed by a secondary antibody staining (goat anti-rabbit AF568, Invitrogen, A-11011). DAPI was used for nuclear staining. Images close to the injection site (Supplementary Figure 1a) were taken using a Zeiss Imager Z1 microscope under a 20x objective lens. Tissues from bone marrow chimeras were processed and stained as described above. Images were taken using a CSU-W1 Nikon Spinning Disk Confocal microscope under 10x air, 20x air or 100x immerse oil lenses. All images were analyzed using the Fiji/ImageJ software by experimenters blinded to sample information.

Behavior test. Novel Object Recognition (NOR) task was used to test hippocampal dependent recognition memory at one, three and six months after the last dose of irradiation. All tests took place during the dark cycle in a room with dim red light as previously described [13, 14]. Briefly, mice were habituated in an open arena (30 cm x 30 cm x 30 cm, L x W x H) for 10 minutes on day one and day two. On day three, two

identical objects were put into the arena at a distance of 21 cm and mice were allowed to explore for 5 minutes. On day four, one object was replaced by a novel object and mice were allowed to explore for 5 minutes. All trials were recorded by an overhead camera and analyzed using Ethovision software. Data are presented as discrimination Index, calculated using fomular $DI = (T_{Novel} - T_{Familiar})/(T_{Novel} + T_{Familiar})$.

Flow cytometry. mice were perfused with cold PBS after euthanasia. Brains were immediately removed and dissociated using a Neural Tissue Dissociation kit (P) (Miltenyi Biotec). Brain cells were resuspended in 30% Percoll solution diluted in RPMI medium, and centrifuged at 800 g for 30 minutes at 4°C. Cell pellets were washed with FACS buffer (1 x DPBS with 0.5% BSA fraction V and 2% FBS), blocked with mouse CD16/32 Fc block (BD Biosciences #553141) and stained with fluorophore conjugated antibodies (CD11b-AF700, CD45-FITC, BD Pharmingen 557690 and 553080, C5aR-PE, CD68-PE and CD107a-PE, Miltenyi Biotec 130-106-174, 130-102-923 and 130-102-219), washed with FACS buffer and used for sort or analyses of bone marrow chimera efficiency. Data were collected on an Aria III sorter using the FACSDIVA software (BD Biosciences, V8.0.1), and analyzed with Flowjo software (FlowJo, LLC, V10.4.2).

Flow synaptometry. after isolation (described above) synaptosomes were stained with PSD-95 (Abcam ab13552) or Synapsin-1 (Millipore #1543) antibodies on ice for 30 minutes, washed and followed by a secondary antibody staining (Invitrogen, goat anti-mouse AF488, A-11001). Stained synaptosomes were used immediately for analysis of

mean fluorescent intensity measurement. Fluorescent latex beads of 1 μm, 2 μm, 3 μm and 6 μm were used as references of particle sizes in the FSC-A vs SSC-A dot plot. Events between 1 μm and 3 μm were used to measure mean fluorescent intensities of isolated synaptosomes under the FITC channel. Data were collected on an Aria III sorter using the FACSDIVA software, and analyzed with Flowjo software. At least 100,000 events were collected from each sample for the analyses.

RNA sequencing. mRNA was isolated from 100,000 to 400,000 sorted microglia or BEMs (CD45$^{low/int}$/CD11b^{+} cells) using the Dynabeads mRNA DIRECT Purification Kit (Invitrogen #61011) following the manufacturer's instructions. RNA sequencing libraries were generated using the Ovation RNA-seq system V2 and Ultralow Library Construction System sample prep kits (NuGEN). Libraries were sequenced on the HiSeq 2500 to generate single end 50bp reads according to the manufacturer's instructions. Normalized per-gene read counts were used to compare relative gene expression levels across samples. Only genes with average read counts greater than 10 were included for analyses. Heatmaps were drawn using the online analysis software Morpheus (Broad Institute, https://software.broadinstitute.org/morpheus), followed by hierarchical clustering using the One minus pearson correlation method. Gene Ontology analysis was performed using the Statistical overrepresentation test (GO biological process complete, PANTHER version 14) [53]. Bar graphs to visualize fold enrichment and p values of enriched GO biological pathways were drawn using the GraphPad Prism software (V 7.01, GraphPad Software, Inc). For analysis of monocyte/microglia signature genes, dataset from Lavin and Winter et al was used as

reference (GSE63340) [32]. Genes significantly up or down regulated (p<0.05, fold-change > 1.5 or <0.667) in monocytes vs microglia comparisons are defined as monocyte or microglia signature genes, respectively. Heatmaps were drawn as described above, and similarity matrix were drawn using the Morpheus online tool with Pearson correlation. Monocyte/microglia similarity scores were calculated based on the numbers of genes in each treatment group from this study that expressed in the same trend as monocyte/microglia signature genes (genes with fold-change between 0.6667 and 1.500 or with FDR>0.01 were defined as unspecified). For juvenile/embryonic signature analysis, dataset from Matcovitch-Natan and Winter et al was used as reference (GSE79819) [34]. Gene listed to be highly expressed in Yolk Sac and embryonic day 10.5–12.5 were defined as embryonic/juvenile microglia signatures, genes highly expressed in adult cortex/hippocampus/spinal cord were defined as adult microglia signatures. Heatmaps, similarity matrix and similarity scores were drawn or calculated as described above.

qPCR. mRNAs were extracted from sorted microglia using the Dynabeads mRNA DIRECT Purification Kit (Invitrogen #61011), and reverse transcribed into cDNAs using reverse transcription kit (info). qPCR reactions were set up in duplicate reactions using the PowerUp SYBR Green Master Mix kit (Applied Biosystems #A25777) using an Mx3000P qPCR System (Agilent, Santa Clara, CA) following the manufacturer's instructions. Data were analyzed using the standard curve method. Standard cDNAs were generated with total RNAs from mixed naïve and irradiated mouse brains. qPCR primers sequences are listed in Supplementary Table 4.

Sholl analysis. Images of GFP+ (BEMs from bone marrow chimeras) or Iba1+ (AF555, all microglia cells, and BEMs from non-bone marrow chimeras) cells were acquired from stained frozen sections (20um) using a confocal microscope under 100x objectives (CSU-W1 Spinning Disk/High Speed Widefield, Nikon). Max Z-projections from Z-stack images (0.26um step size) were used for Sholl analysis [54] in Fiji [55] software using the following settings: manually defined cell center at the cell body, the numbers of intersections between cellular processes and circles with incremental radius (2um step size, up to 60um) were recorded, plotted and compared across samples.

Statistical analyses. Two-way ANOVA was used to determine radiation and CSF-1Ri treatment effects for NOR, qPCR, flowsynaptometry, flow cytometry, immunofluorescent staining counts and dendritic spine count results, with Tukey's post hoc multiple comparisons. One-way ANOVA with Sidak's post hoc multiple comparisons was used to determine effect of developmental stages for dataset published by Matcovitch-Natan and Winter et al. Unpaired t-test was used to determine differentially expressed microglia/monocyte signature genes from dataset published by Lavin and Winter et al. Unpaired t-test was used calculate the p value of the comparison of BEMs contributions between the BMT and BMT + WBRT groups. Exact p values and numbers of animals used in each experiment were listed in each related figure legend. All error bars represent mean ± SEM.

191
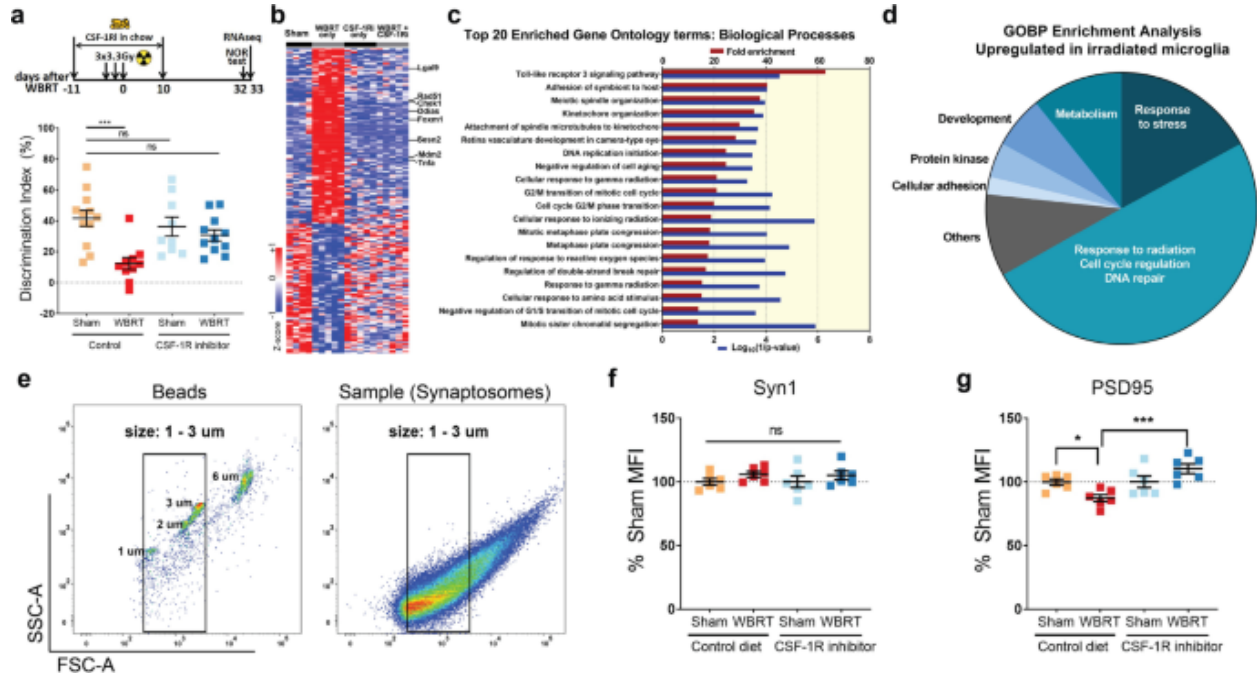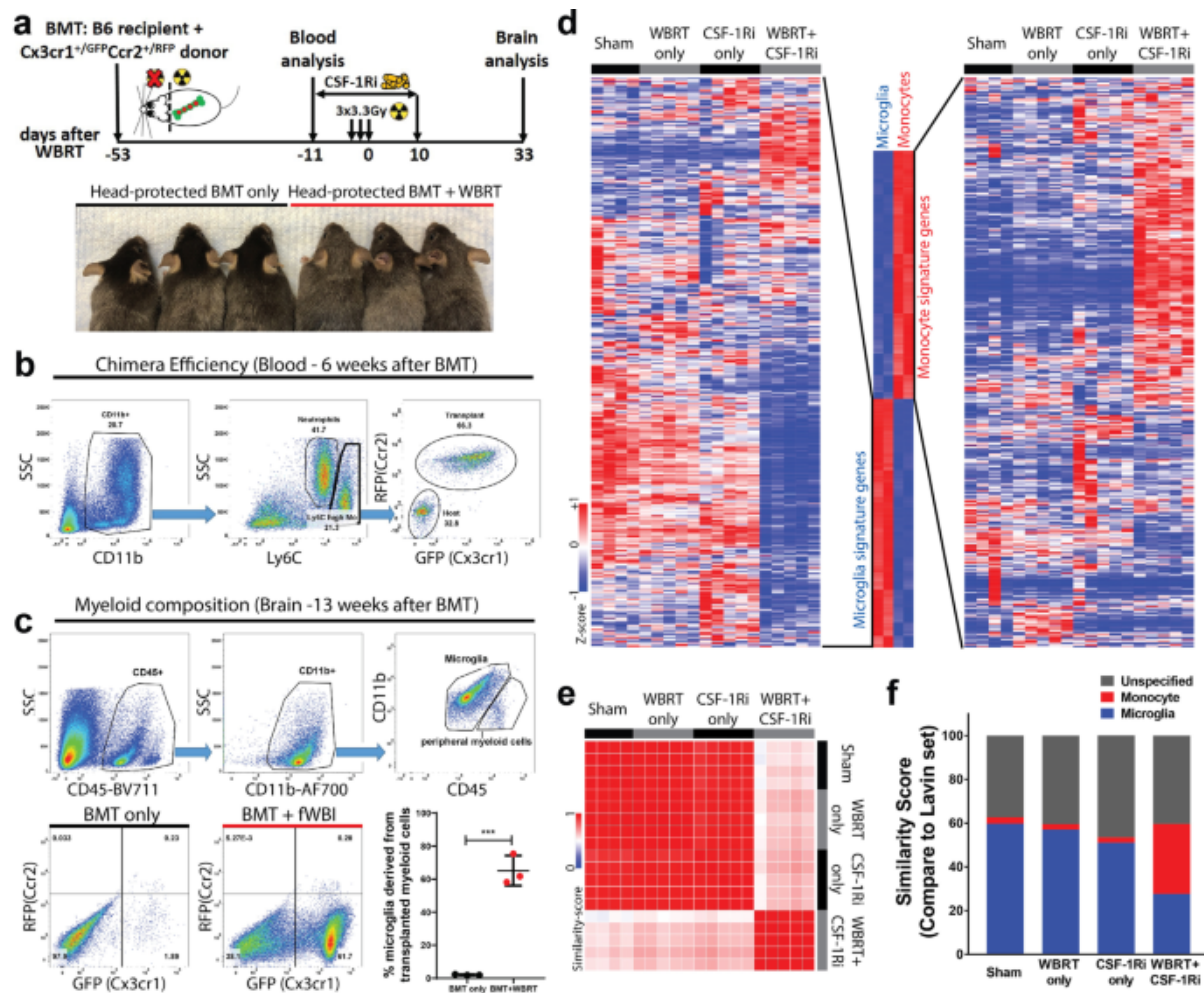
Figure 1. Microglia depletion and repopulation prevents long-term radiation-induced memory deficits and loss of hippocampal PSD95.

A) Experimental design and Novel Object Recognition (NOR) test result. CSF-1R inhibitor was used to deplete microglia during 3 doses of 3.3 Gy of whole-brain radiotherapy (WBRT). A 4-day NOR protocol was used to measure recognition memory, which ended on day 32 post WBRT. Microglia were isolated using fluorescent activated cell sorting (FACS) on day 33 and dot plots showing NOR results. Statistical analysis was performed using two-way ANOVA with Dunnett's multiple comparisons test. There is no CSF-1Ri treatment effect (F (1, 38) = 1.787, p = 0.1893), but significant WBRT effect (F (1, 38) = 13.23, p = 0.0008) and interaction between CSF-1Ri treatment and WBRT (F (1,38) = 6.07, p = 0.0184), N = 9–12, animals with insufficient exploration time on NOR test day were excluded. **B)** Hierarchically clustered heatmap showing significantly altered microglial genes by WBRT, but not changed with CSF-1Ri treatment. **C)** Bar graphs summarizing fold enrichment and p values of the top 20 enriched Biological Processes by Gene Ontology analysis from up-regulated microglial genes after WBRT (full list in Additional file 2: Table S1). No significantly enriched terms were identified by GO analysis from down-regulated genes by WBRT. **D)** A pie chart summarizing all enriched GOBP terms. ns = not significant, ***p < 0.0001. **E)** Scatter plots showing gating strategy in flow synaptometry analyses. Fluorescent beads at various sizes were used as standard to gate isolated hippocampal cell membrane fractions. Particles between 1 μm and 3 μm were considered synaptosomes and used to determine Synapsin 1 and PSD95 protein levels by mean fluorescent intensities (MFIs). **F)** Dot plots to compare Synapsin 1 and PSD95 MFI levels in hippocampal cell fractions. Statistical analyses were performed using two-way ANOVA with Tukey's multiple comparisons test. ns = not significant, *p < 0.05, ***p < 0.001. N = 6.

Figure 2. Repopulated microglia-like cells after depletion and WBRT originate from peripheral monocytes and retain monocytic signatures.

(**A**) Experimental design of head-protected bone marrow transplantation (BMT) followed by CSF-1Ri-mediated microglia depletion and WBRT. Lower panel shows fur colors before euthanasia for brain analysis. (**B**) Representative FACS analysis gating strategy to analyze bone marrow chimera efficiency 6 weeks after BMT, about two-thirds of the CD11b$^+$Ly6C^{high} monocytes are replaced by GFP$^+$RFP$^+$ cells derived from donor bone marrow cells. (**C**) Representative FACS analysis gating strategy and brain myeloid composition results. Upper panel shows FACS gating using CD45 and CD11b staining; microglia and microglia-like cells are defined by positive CD11b staining and low or intermediate CD45 levels. Lower panel shows scatter plots of GFP/RFP fluorescent levels of the CD11b$^+$CD45$^{low/intermediate}$ population in the brain, and a dot plot comparing percentages of peripheral myeloid cell derived microglia-like cells. Statistical analysis was performed using unpaired t-test, ***$p < 0.001$. (**D**) Hierarchically clustered heatmaps to compare microglia and monocyte signatures. A signature gene list was defined using a dataset published by Lavin and Winter et al., GSE63340. Defined list and expression details are in Additional file 3: Table S2. (**E**) Similarity matrix comparisons using defined monocyte and microglia signature genes. (**F**) Bar graph showing similarity scores to

compare relative numbers of genes (in percentage of the defined list) that express in the same trends as monocytes or microglia based on the Lavin and Winter et al. dataset.
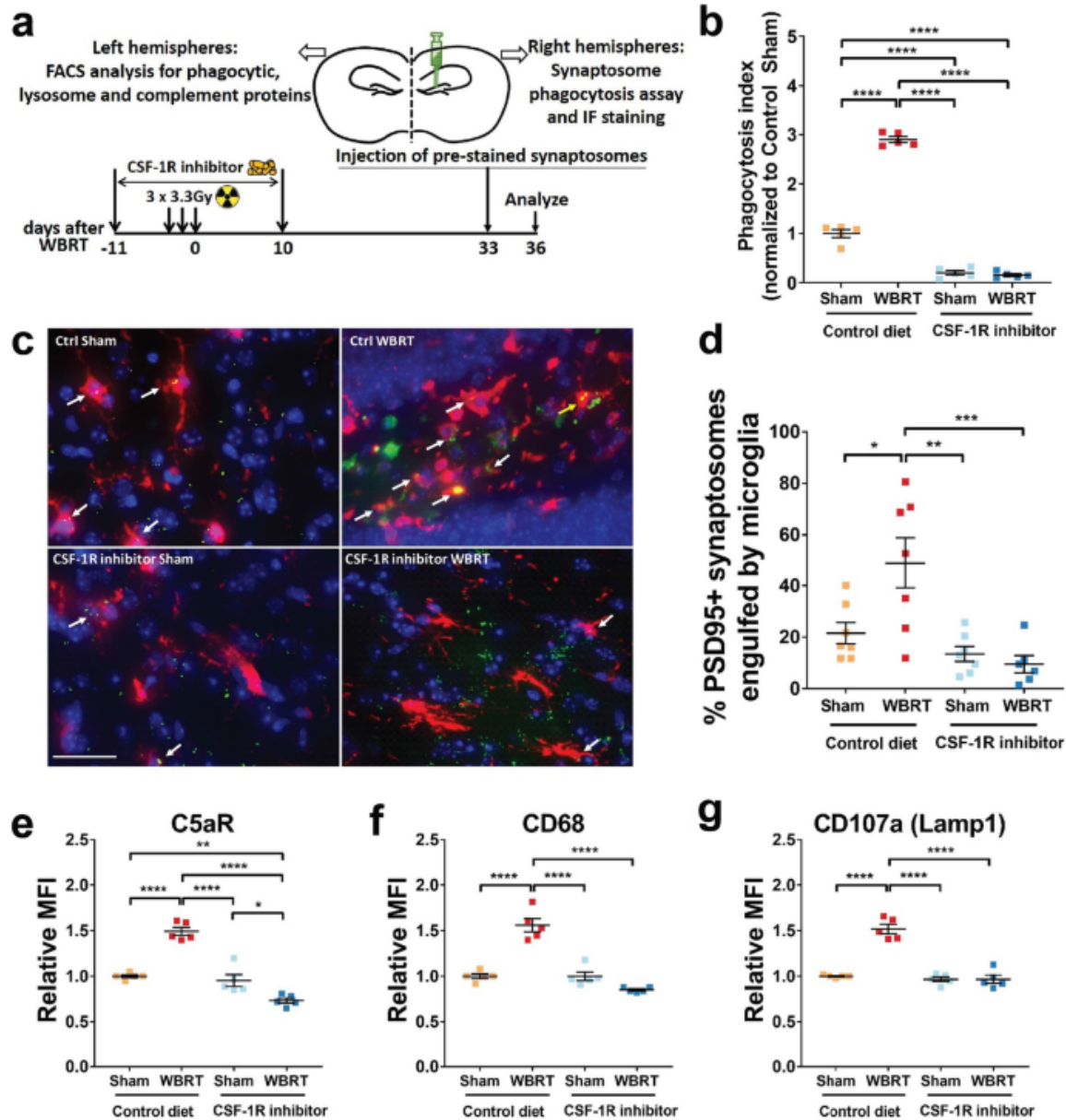
Figure 3. Repopulated microglia and brain-engrafted macrophages are not activated and phagocyte less synaptic compartments.

(**A**) Experimental design for in vivo synaptosome phagocytosis assays. Injection of pre-stained synaptosomes was timed to be the same as previous experiments. Three days later, on day 36 after WBRT, ipsilateral hemispheres were harvested and used for engulfment measurement using FACS or Immunofluorescent staining. (**B**) FACS analysis result showing levels of microglia that engulfed pre-stained PSD-95 signals. (**C**) Representative images showing engulfment of pre-stained synaptosomes by microglia near injection site. White arrows point at microglia that have engulfed pre-stained synaptosomes. scale bar = 20 μm. (**D**) Dot plot to show quantification result of

synaptosome engulfment by immunofluorescent staining. (**E-G**) Dot plots showing cell surface C5aR, and intracellular CD68 and CD107a protein levels in microglia and BEMs. Statistical analyses were performed using two-way ANOVA with Tukey's multiple comparisons test. $*p < 0.05$, $**p < 0.01$, $***p < 0.001$, $****p < 0.0001$. $N = 5–6$.
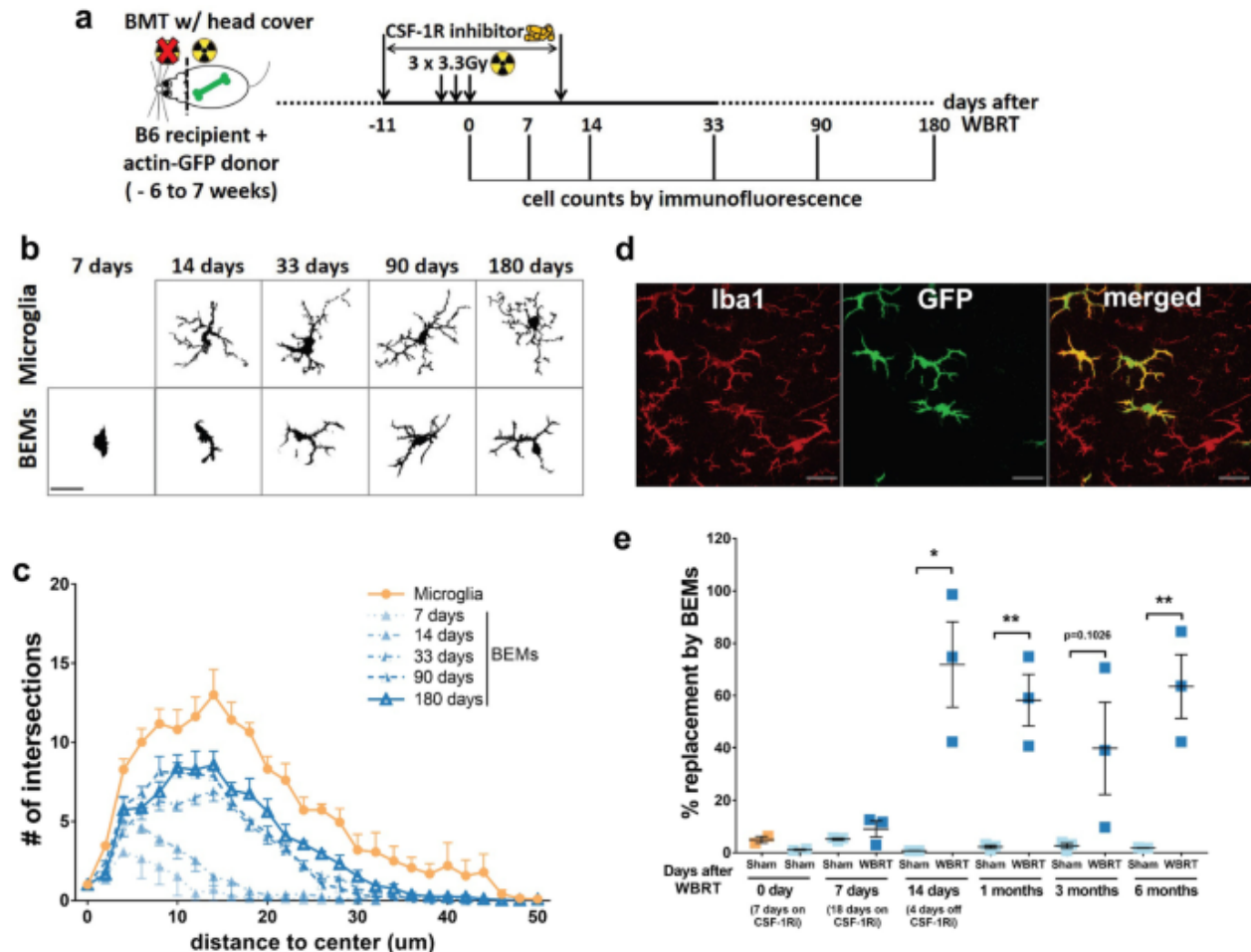

Figure 4. BEMs gradually adapt to microglia-like morphology and persist in the brain.

(**A**) Schematic of experimental design for long-term assessment of BEMs. (**B**) Representative images of microglia/BEMs counting, scale bar = 20 μm. (**C**) Sholl analysis results showing numbers of intersections at different distances to cell center, BEMs at 7, 14, 33, 90 and 180 days after WBRT were compared to naïve microglia age-matched to 90 days after WBRT. (**D**) Representative images showing differential Iba1 and GFP-expressing profiles of microglia (Iba1 + GFP−) and BEMs (Iba1 + GFP +) in a BEM-bearing brain at 33 days after WBRT. (**E**) Dot plot to show percentage of replacement of microglia by BEMs, each dot represent an individual mouse. $n = 2–3$. Statistical analyses were performed using unpaired t-test at each distance point (**C**) or time point (**E**). See Additional file 1: Fig. S7 for detailed comparisons between microglia and BEMs at each time point.
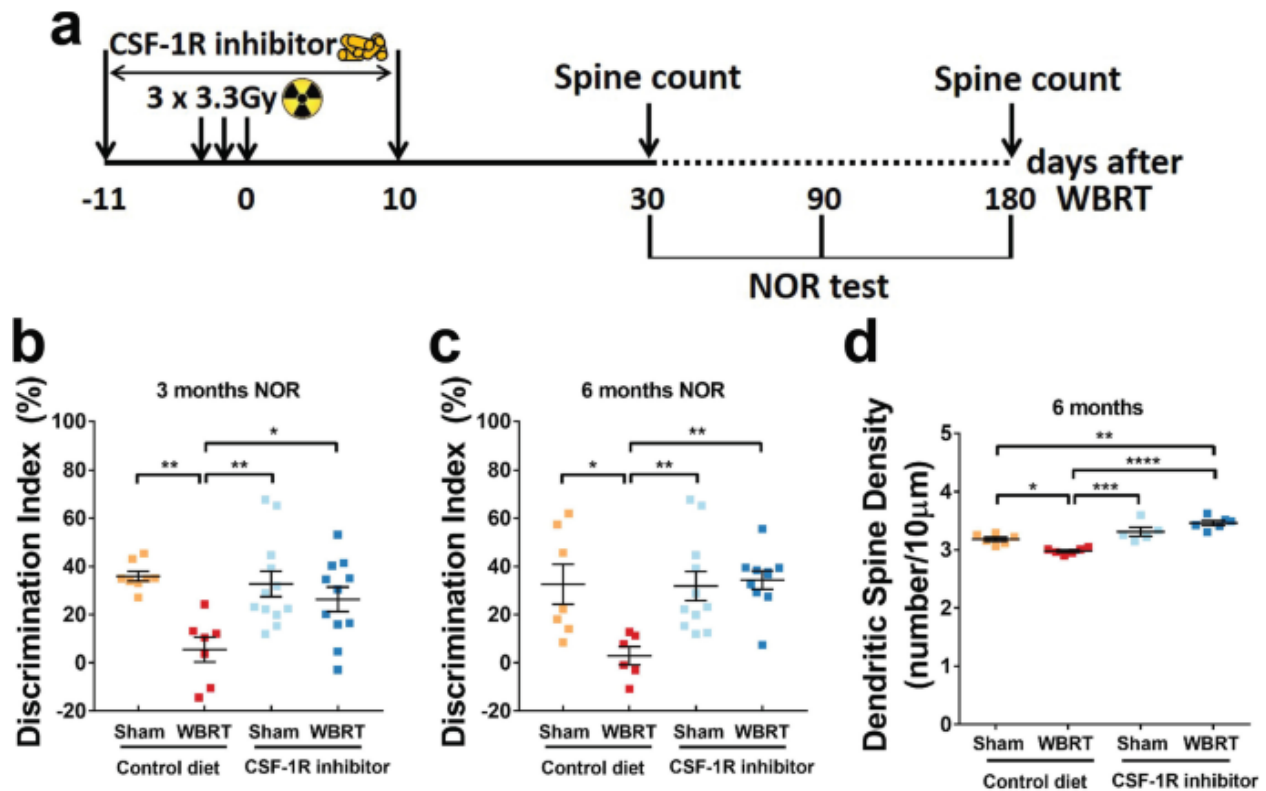
Figure 5. BEMs provide long-term protection against WBRT-induced dendritic spine and memory loss.

(**A**) Schematic of experimental design for long-term memory and dendritic spine density analyses. (**B**) and (**C**) dot plots to show NOR test results at 3 and 6 months after WBRT, respectively. $N = 6–12$. (**D**) Dendritic spine counts of hippocampal granule neurons at 6 months after WBRT, $N = 5–6$. Statistical analyses were performed using two-way ANOVA with Tukey's post hoc multiple comparisons test (**B**–**D**). $*p < 0.05$, $**p < 0.01$, $***p < 0.001$, $****p < 0.0001$.
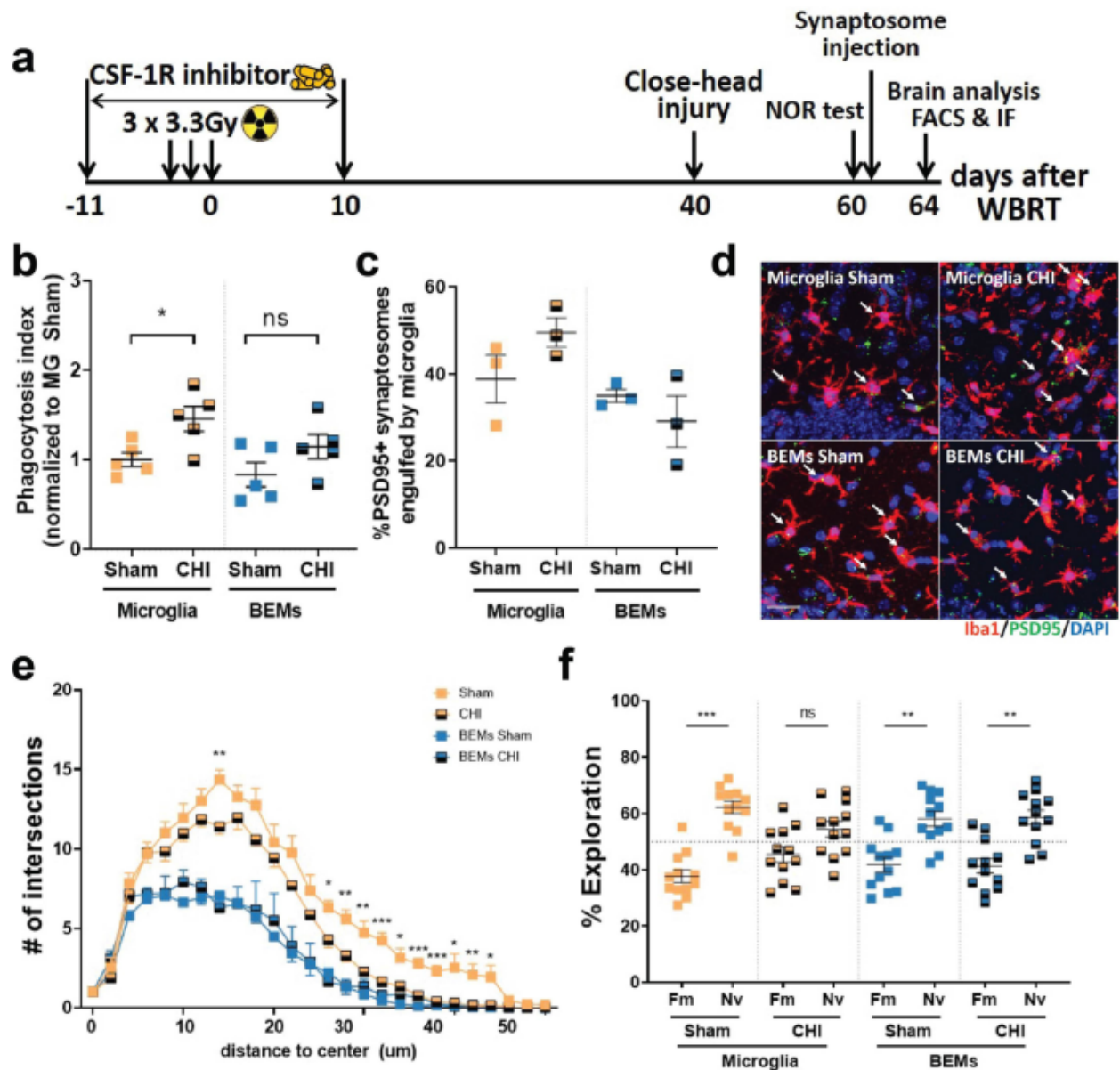
Figure 6. BEMs protects against concussive injury-induced memory deficits.

(**A**) Schematic of experimental design for concussive injury, cognitive test and following analyses. (**B**) Dot plot to show the result of in vivo phagocytosis assay by FACS after injection of pre-stained synaptosomes, each dot represents value from an individual mouse, $n = 4$–5. (**C**) Dot plot showing result of in vivo phagocytosis assay by IF imaging and quantification, each dot represents mean counts from an individual mouse, $n = 3$. (**D**) Representative images showing microglia and BEMs (arrows) phagocytosing injected synaptosomes (green dots). (**E**) Sholl analysis result showing numbers of intersections at different distances to the cell center, $n = 5$–6. (**F**) Dot plot showing NOR test result, each dot represent the performance of an individual mouse, $n = 12$. Statistical analyses were performed using two-way ANOVA with Tukey's multiple comparisons test (**B** and **C**) for each distance point (**E**) or unpaired t-test (**F**). *$p < 0.05$, **$p < 0.01$, ***$p < 0.001$.
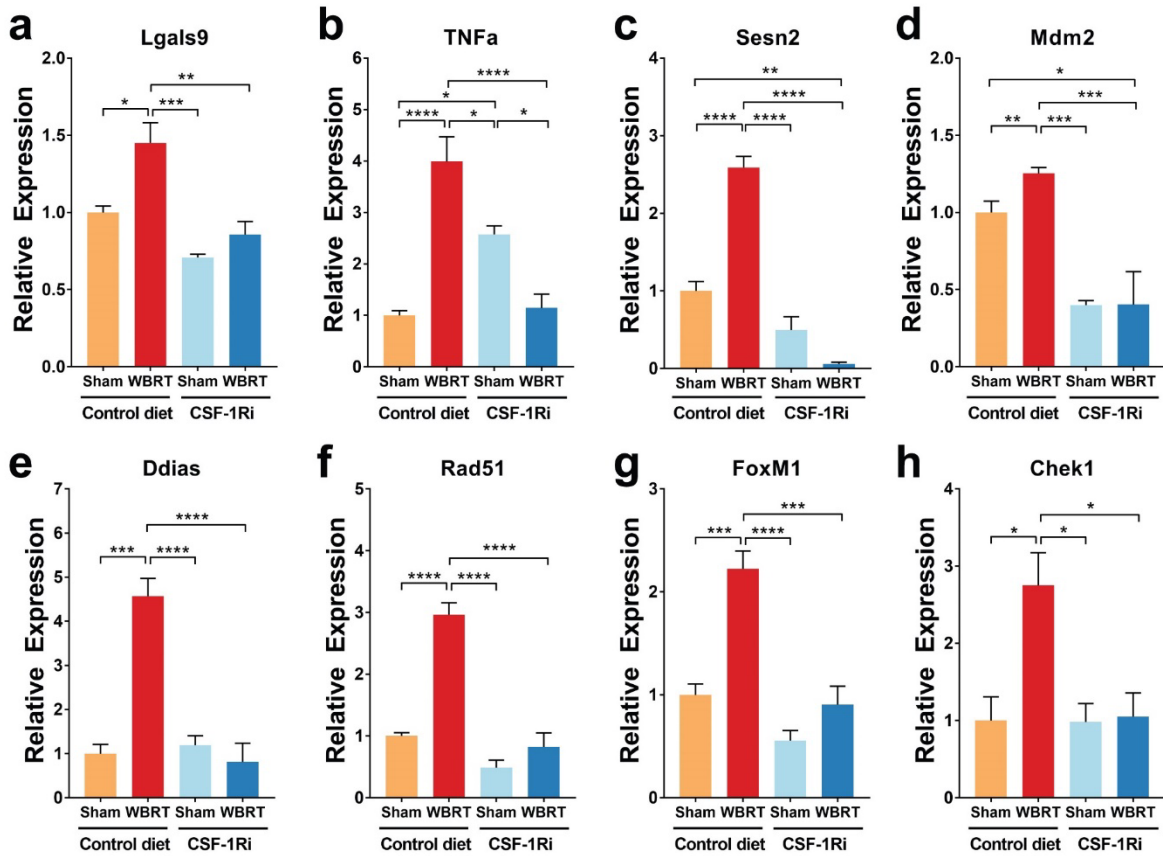
Supplemental Figure 1. qPCR validation of radiation-induced genes.

qPCR validation of radiation-induced genes. Genes from highly enriched GOBP terms were selected to validate RNAseq results. (**A**) and (**B**), Toll-like receptor 3 signaling pathway: Lgals9 and TNFa. (**B**) and (**C**), Regulation of response to reactive oxygen spieces: TNFa and Sesn2. (**D-E**), Cellular response to ionizing radiation: Mdm2, Ddias and Rad 51. (**F-H**), Regulation of double-strand break repair: Rad51, Foxm1 and Chek1. Statistical analyses were performed using two-way ANOVA with Tukey's multiple comparisons test. *p<0.05, **p<0.01, ***p<0.001, ****p<0.0001. N = 4 – 6. The experiment was repeated twice with similar results.
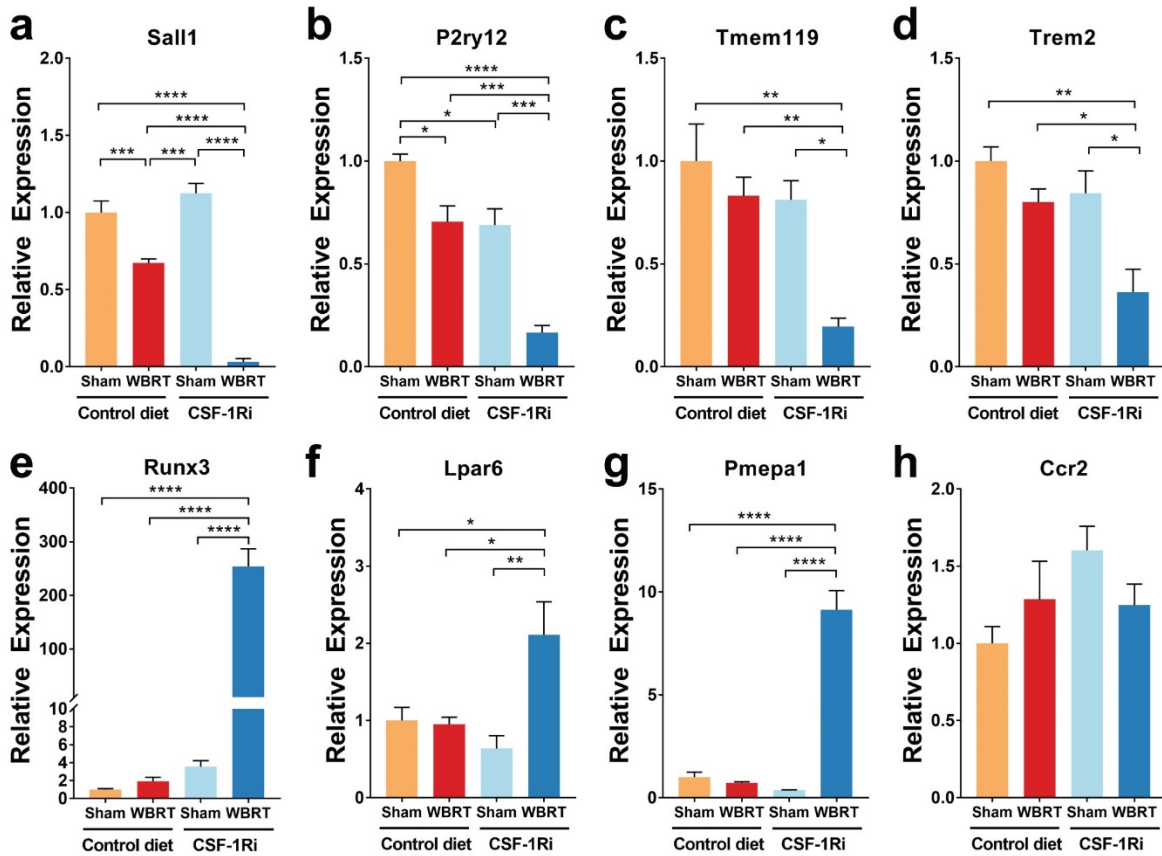
Supplemental Figure 2. qPCR validation of microglia- and monocyte-specific genes.

Selected genes that are known to highly express in microglia or monocytes were used to validate RNAseq results. (**A – D**) microglia signature genes *Sall1*, *P2ry12*, *Tmem119* and *Trem2* have lower expression levels in monocyte derived BEMs (CSF-1Ri + WBRT) compared to naïve microglia (control diet sham), irradiated microglia (control diet + WBRT) and repopulated microglia (CSF-1Ri sham). (**E – F**) monocyte signature genes *Runx3*, *Lpar6* and *Pmepa1* have higher expression levels in BEMs compared to other groups. Statistical analyses were performed using two-way ANOVA with Tukey's multiple comparisons test. *p<0.05, **p<0.01, ***p<0.001, ****p<0.0001. N = 4 – 6. The qPCR experiments were performed in duplicates with similar results. Figures shown here are representative results from one experiment.
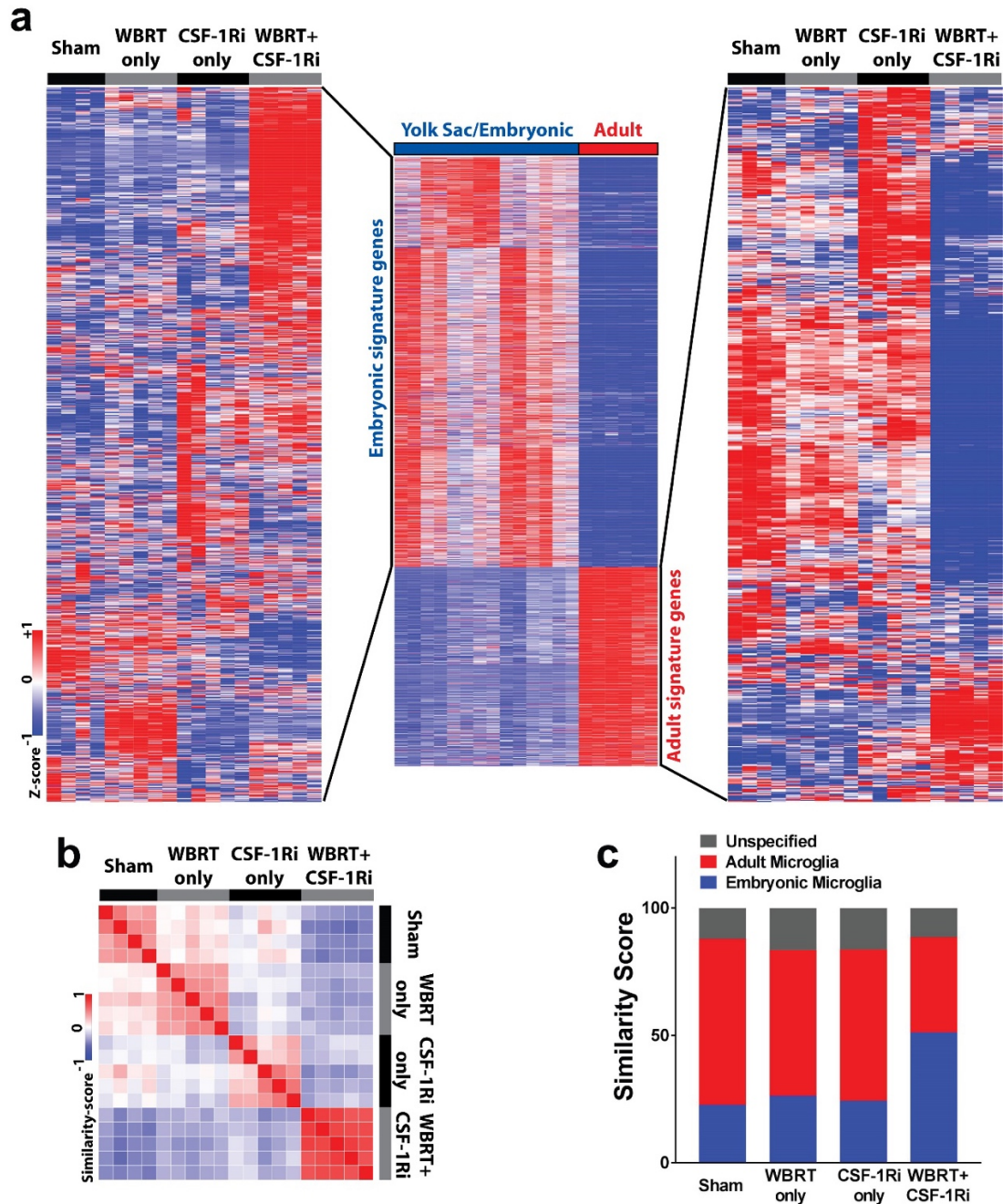
Supplemental Figure 3. Monocyte-derived BEMs after WBRT have embryonic microglia signatures.

(**A**) hierarchically clustered heatmaps to compare embryonic and adult microglia signatures across samples. Embryonic and adult signature genes were defined based on published dataset by Matchonitch and Winter et al. (Gene list and expression data in Additional file 4: Table S3). (**B**) Similarity matrix comparisons using defined embryonic and adult signature genes. (**C**) bar graph showing similarity scores to compare relative numbers of genes (shown as percentage of the defined list) that express in the same trends as embryonic or adult microglia in the Matchovitch and Winter dataset.
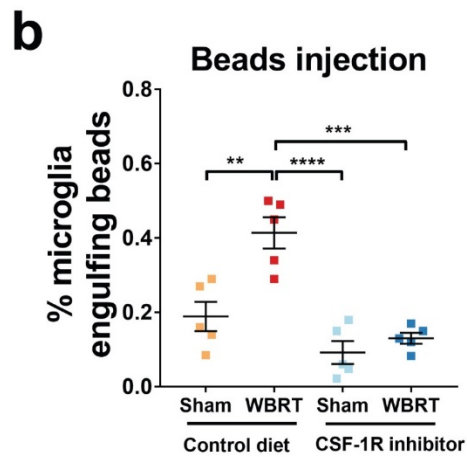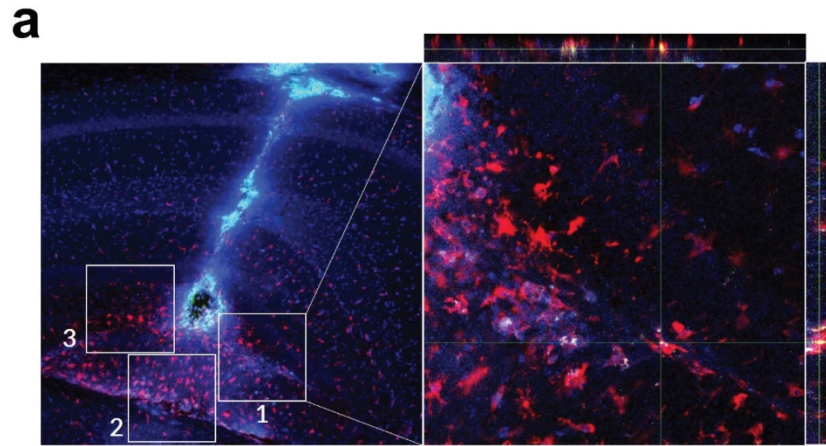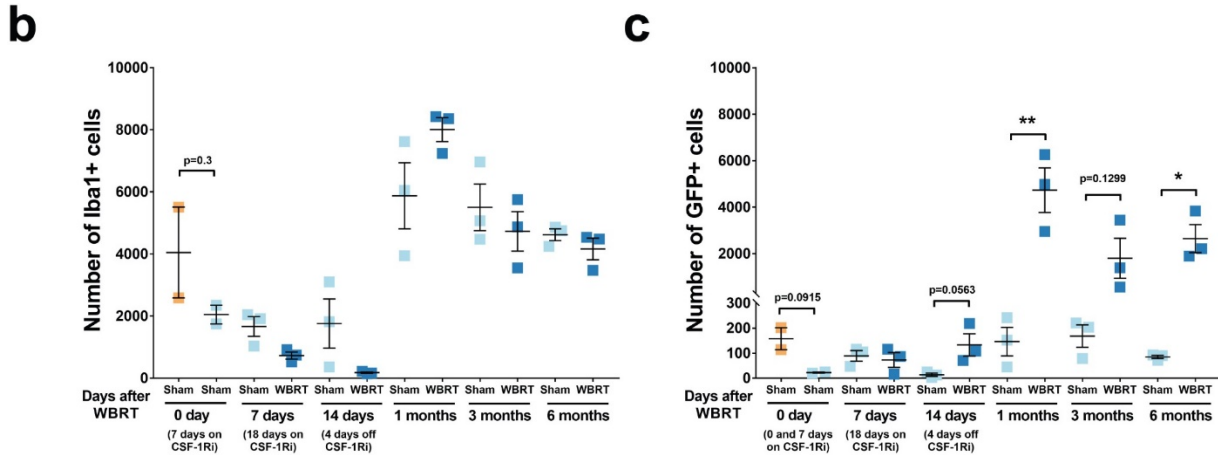
Supplemental Figure 4. Representative images of count window from phagocytosis assay by IF and result of in vivo beads phagocytosis assay by FACS.

(**A**) representative images showing injection track of pre-stained synaptosomes and count windows. (**B**) dot plot results of in vivo phagocytosis assay by FACS using fluorescent labeled beads. Statistical analyses were performed using two-way ANOVA with Tukey's multiple comparisons test. **$p<0.01$, ***$p<0.001$, ****$p<0.0001$. N = 5.
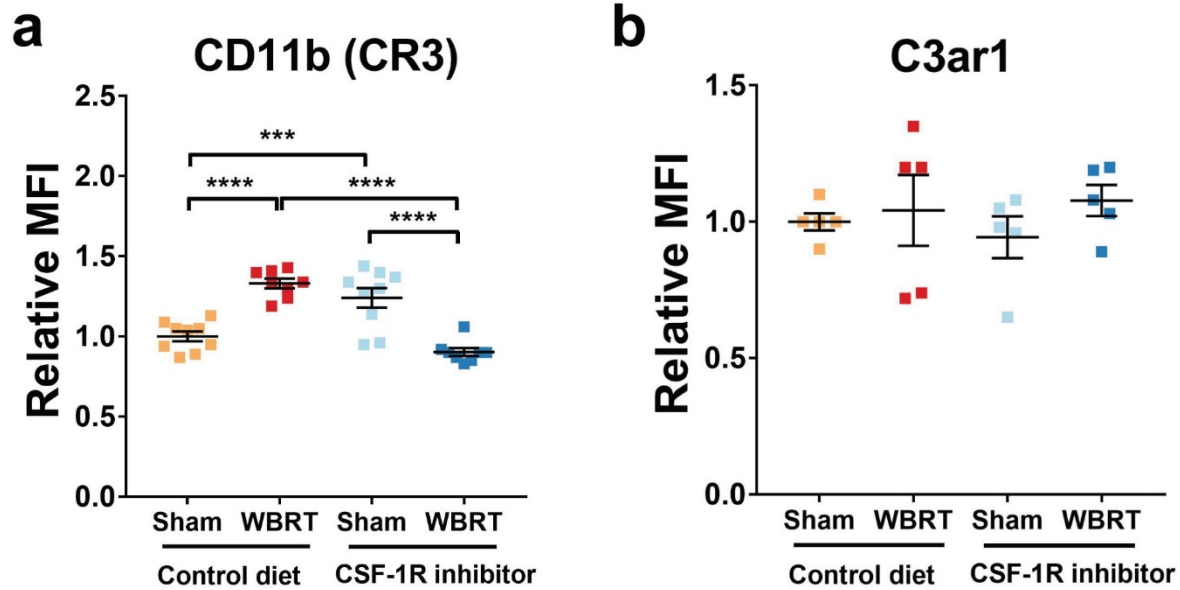
**Supplemental Figure 5. Complement receptors CR3 and C3ar1 levels in microglia and BEMs.**

(**A**) dot plot of relative MFI of complement receptor CR3 (CD11b). (**B**) dot plot of relative MFI of complement receptor C3ar1. Statistical analyses were performed using two-way ANOVA with Tukey's multiple comparisons test. ***p<0.001, ****p<0.0001. N = 8 – 9 (a), N = 5 (b).
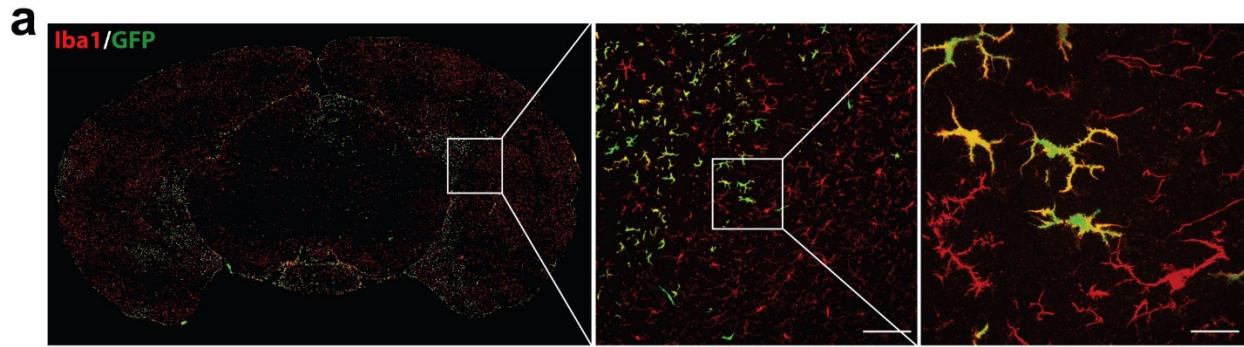
Supplemental Figure 6. Quantification of microglia and BEMs in brains from bone marrow chimeras.

(**A**) representative image of coronal section of whole brains from bone marrow chimeras. Scale bars = 100 μm (middle) and 20 μm (right). (**B**) dot plot of quantification results of Iba1 positive cells, each dot represents number of cells stained positive for Iba1 from a coronal whole brain section of an individual mouse. (**C**) dot plot of quantification results of GFP positive cells, each dot represents number of GFP positive cells from a coronal whole brain section of an individual mouse. Statistical analyses were performed using two-way ANOVA with Tukey's multiple comparisons test. *p<0.05, **p<0.01. N = 2 (0 day sham on control diet) 3 (all other groups).
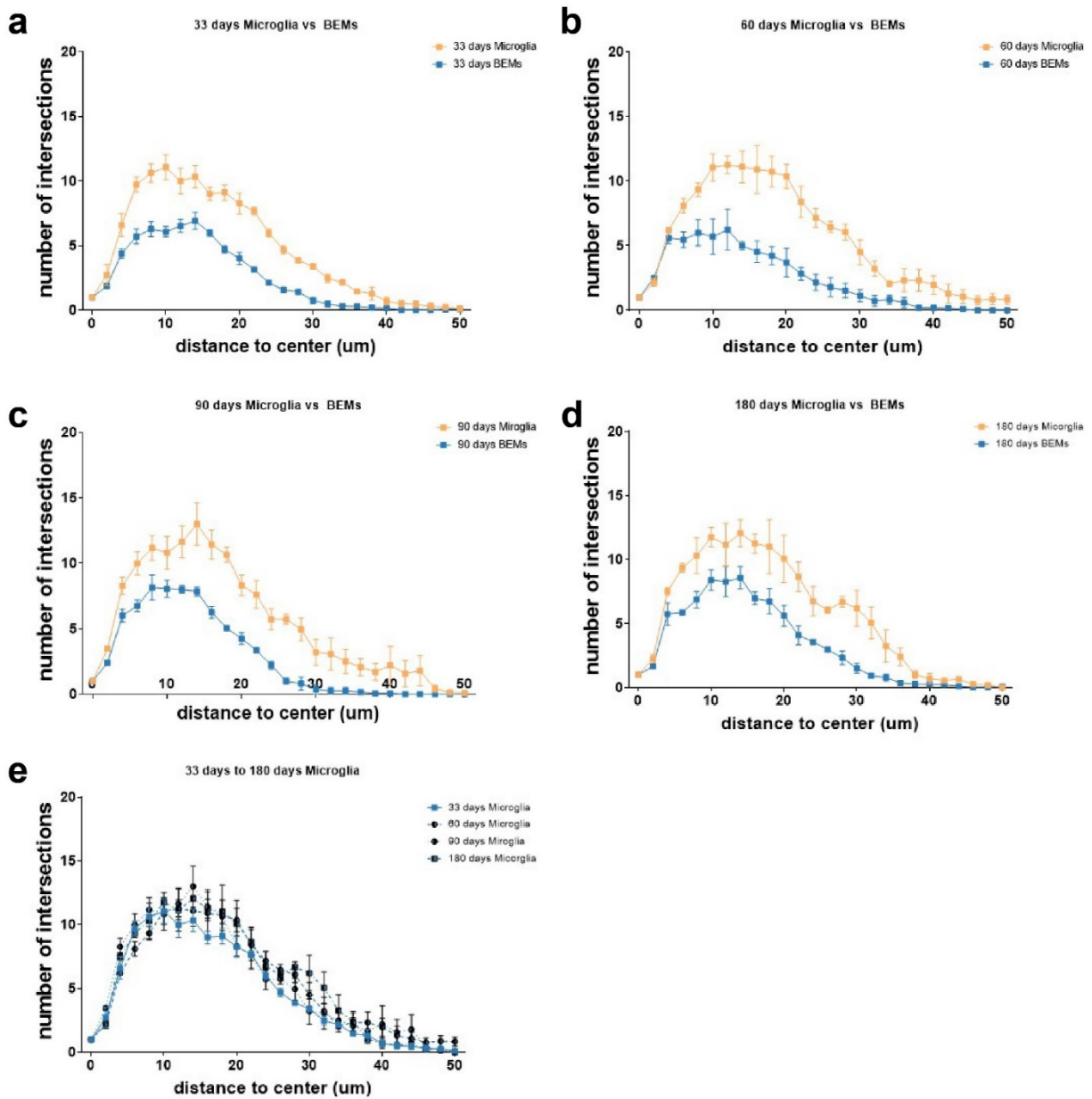
Supplemental Figure 7. Sholl analysis results of microglia vs BEMs over time.

(**A-D**) comparison of Sholl analyses results between microglia and BEMs at 33, 60, 90 and 180 days after WBRT. (**E**) Sholl analyses results of microglia at 33, 60, 90 and 180 days after WBRT. Statistics were performed using unpaired t-test at each distance point. n = 5 – 6.

References

1. Alliot, F., I. Godin, and B. Pessac, *Microglia derive from progenitors, originating from the yolk sac, and which proliferate in the brain.* Developmental Brain Research, 1999. **117**(2): p. 145-152.

2. Ginhoux, F., et al., *Fate Mapping Analysis Reveals That Adult Microglia Derive from Primitive Macrophages.* Science, 2010. **330**(6005): p. 841.

3. Ajami, B., et al., *Local self-renewal can sustain CNS microglia maintenance and function throughout adult life.* Nature Neuroscience, 2007. **10**: p. 1538.

4. Prinz, M., et al., *Heterogeneity of CNS myeloid cells and their roles in neurodegeneration.* Nat Neurosci, 2011. **14**(10): p. 1227-35.

5. Saijo, K. and C.K. Glass, *Microglial cell origin and phenotypes in health and disease.* Nat Rev Immunol, 2011. **11**(11): p. 775-87.

6. Hong, S., L. Dissing-Olesen, and B. Stevens, *New insights on the role of microglia in synaptic pruning in health and disease.* Curr Opin Neurobiol, 2015. **36**: p. 128-134.

7. Hong, S. and B. Stevens, *Microglia: Phagocytosing to Clear, Sculpt, and Eliminate.* Developmental Cell, 2016. **38**(2): p. 126-128.

8. Elmore, M.R., et al., *Colony-stimulating factor 1 receptor signaling is necessary for microglia viability, unmasking a microglia progenitor cell in the adult brain.* Neuron, 2014. **82**(2): p. 380-97.

9. Elmore, M.R., et al., *Characterizing newly repopulated microglia in the adult mouse: impacts on animal behavior, cell morphology, and neuroinflammation.* PLoS One, 2015. **10**(4): p. e0122912.

10.   Dagher, N.N., et al., *Colony-stimulating factor 1 receptor inhibition prevents microglial plaque association and improves cognition in 3xTg-AD mice.* J Neuroinflammation, 2015. **12**(1): p. 139.

11.   Spangenberg, E.E., et al., *Eliminating microglia in Alzheimer's mice prevents neuronal loss without modulating amyloid-β pathology.* Brain, 2016.

12.   Acharya, M.M., et al., *Elimination of microglia improves cognitive function following cranial irradiation.* Sci Rep, 2016. **6**: p. 31545.

13.   Feng, X., et al., *Colony-stimulating factor 1 receptor blockade prevents fractionated whole-brain irradiation-induced memory deficits.* J Neuroinflammation, 2016. **13**(1): p. 215.

14.   Feng, X., et al., *Rescue of cognitive function following fractionated brain irradiation in a novel preclinical glioma model.* eLife, 2018. **7**: p. e38865.

15.   Krukowski, K., et al., *Temporary microglia-depletion after cosmic radiation modifies phagocytic activity and prevents cognitive deficits.* Sci Rep, 2018. **8**(1): p. 7857.

16.   Rapp, S.R., et al., *Donepezil for Irradiated Brain Tumor Survivors: A Phase III Randomized Placebo-Controlled Clinical Trial.* Journal of Clinical Oncology, 2015. **33**(15): p. 1653-1659.

17.   Stupp, R., et al., *Radiotherapy plus Concomitant and Adjuvant Temozolomide for Glioblastoma.* New England Journal of Medicine, 2005. **352**(10): p. 987-996.

18.   Greene-Schloesser, D. and M.E. Robbins, *Radiation-induced cognitive impairment--from bench to bedside.* Neuro Oncol, 2012. **14 Suppl 4**: p. iv37-44.

19. Shinohara, C., et al., *Apoptosis in the Subependyma of Young Adult Rats after Single and Fractionated Doses of X-Rays.* Cancer Research, 1997. **57**(13): p. 2694-2702.

20. Morganti, J.M., et al., *Cranial Irradiation Alters the Brain's Microenvironment and Permits CCR2+ Macrophage Infiltration.* PLoS ONE, 2014. **9**(4): p. e93650.

21. Warrington, J.P., et al., *Whole Brain Radiation-Induced Vascular Cognitive Impairment: Mechanisms and Implications.* Journal of Vascular Research, 2013. **50**(6): p. 445-457.

22. Hua, K., et al., *Regionally distinct responses of microglia and glial progenitor cells to whole brain irradiation in adult and aging rats.* PLoS One, 2012. **7**(12): p. e52728.

23. Chiang, C.S., W.H. McBride, and H.R. Withers, *Radiation-induced astrocytic and microglial responses in mouse brain.* Radiotherapy and Oncology, 1993. **29**(1): p. 60-68.

24. Mizumatsu, S., et al., *Extreme Sensitivity of Adult Neurogenesis to Low Doses of X-Irradiation.* Cancer Research, 2003. **63**(14): p. 4021-4027.

25. Monje, M.L., et al., *Impaired human hippocampal neurogenesis after treatment for central nervous system malignancies.* Annals of Neurology, 2007. **62**(5): p. 515-520.

26. Fein, J.A., et al., *Co-localization of amyloid beta and tau pathology in Alzheimer's disease synaptosomes.* Am J Pathol, 2008. **172**(6): p. 1683-92.

27. Prieto, G.A., et al., *Synapse-specific IL-1 receptor subunit reconfiguration augments vulnerability to IL-1β in the aged hippocampus.* Proceedings of the National Academy of Sciences, 2015. **112**(36): p. E5078.

28. Jung, S., et al., *Analysis of Fractalkine Receptor CX<sub>3</sub>CR1 Function by Targeted Deletion and Green Fluorescent Protein Reporter Gene Insertion.* Molecular and Cellular Biology, 2000. **20**(11): p. 4106.

29. Saederup, N., et al., *Selective Chemokine Receptor Usage by Central Nervous System Myeloid Cells in CCR2-Red Fluorescent Protein Knock-In Mice.* PLoS ONE, 2010. **5**(10): p. e13693.

30. Mildner, A., et al., *Microglia in the adult brain arise from Ly-6ChiCCR2+ monocytes only under defined host conditions.* Nat Neurosci, 2007. **10**(12): p. 1544-1553.

31. Priller, J., et al., *Targeting gene-modified hematopoietic cells to the central nervous system: Use of green fluorescent protein uncovers microglial engraftment.* Nature Medicine, 2001. **7**(12): p. 1356-1361.

32. Lavin, Y., et al., *Tissue-resident macrophage enhancer landscapes are shaped by the local microenvironment.* Cell, 2014. **159**(6): p. 1312-26.

33. Cronk, J.C., et al., *Peripherally derived macrophages can engraft the brain independent of irradiation and maintain an identity distinct from microglia.* J Exp Med, 2018. **215**(6): p. 1627-1647.

34. Matcovitch-Natan, O., et al., *Microglia development follows a stepwise program to regulate brain homeostasis.* Science, 2016. **353**(6301): p. aad8670.

35.   Hong, S., et al., *Complement and microglia mediate early synapse loss in Alzheimer mouse models.* Science, 2016.

36.   Stevens, B., et al., *The classical complement cascade mediates CNS synapse elimination.* Cell, 2007. **131**(6): p. 1164-78.

37.   Vainchtein, I.D., et al., *Astrocyte-derived interleukin-33 promotes microglial synapse engulfment and neural circuit development.* Science, 2018. **359**(6381): p. 1269.

38.   Schafer, Dorothy P., et al., *Microglia Sculpt Postnatal Neural Circuits in an Activity and Complement-Dependent Manner.* Neuron, 2012. **74**(4): p. 691-705.

39.   Vasek, M.J., et al., *A complement-microglial axis drives synapse loss during virus-induced memory impairment.* Nature, 2016. **534**(7608): p. 538-43.

40.   Norris, G.T., et al., *Neuronal integrity and complement control synaptic material clearance by microglia after CNS injury.* J Exp Med, 2018.

41.   Krukowski, K., et al., *Traumatic Brain Injury in Aged Mice Induces Chronic Microglia Activation, Synapse Loss, and Complement-Dependent Memory Deficits.* International Journal of Molecular Sciences, 2018. **19**(12).

42.   Shi, Q., et al., *Complement C3-Deficient Mice Fail to Display Age-Related Hippocampal Decline.* J Neurosci, 2015. **35**(38): p. 13029-42.

43.   Tay, T.L., et al., *A new fate mapping system reveals context-dependent random or clonal expansion of microglia.* Nature Neuroscience, 2017. **20**: p. 793.

44.   Huang, Y., et al., *Repopulated microglia are solely derived from the proliferation of residual microglia after acute depletion.* Nat Neurosci, 2018. **21**(4): p. 530-540.

45.   Ajami, B., et al., *Infiltrating monocytes trigger EAE progression, but do not contribute to the resident microglia pool.* Nat Neurosci, 2011. **14**(9): p. 1142-1149.

46.   Yamasaki, R., et al., *Differential roles of microglia and monocytes in the inflamed central nervous system.* The Journal of Experimental Medicine, 2014. **211**(8): p. 1533-1549.

47.   Chen, H.-R., et al., *Fate mapping via CCR2-CreER mice reveals monocyte-to-microglia transition in development and neonatal stroke.* Science Advances, 2020. **6**(35): p. eabb2119.

48.   Chou, A., et al., *Inhibition of the integrated stress response reverses cognitive deficits after traumatic brain injury.* Proceedings of the National Academy of Sciences, 2017. **114**(31): p. E6420.

49.   Krukowski, K., et al., *Integrated Stress Response Inhibitor Reverses Sex-Dependent Behavioral and Cell-Specific Deficits after Mild Repetitive Head Trauma.* Journal of Neurotrauma, 2019. **37**(11): p. 1370-1380.

50.   Wang, C., et al., *Microglia mediate forgetting via complement-dependent synaptic elimination.* Science, 2020. **367**(6478): p. 688.

51.   *CSF-1R inhibitor DCC-3014.* NCI drug directory, 2020.

52.   Denny, W.A. and J.U. Flanagan, *Small-molecule CSF1R kinase inhibitors; review of patents 2015-present.* Expert Opin Ther Pat, 2021. **31**(2): p. 107-117.

53.   Mi, H., et al., *PANTHER version 14: more genomes, a new PANTHER GO-slim and improvements in enrichment analysis tools.* Nucleic Acids Res, 2019. **47**(D1): p. D419-D426.

54.   Ferreira, T.A. and A.V. Blackman, *Neuronal morphometry directly from bitmap images.* 2014. **11**(10): p. 982-4.

55.   Schindelin, J., et al., *Fiji: an open-source platform for biological-image analysis.* Nature Methods, 2012. **9**(7): p. 676-682.

Publishing Agreement

It is the policy of the University to encourage open access and broad distribution of all theses, dissertations, and manuscripts. The Graduate Division will facilitate the distribution of UCSF theses, dissertations, and manuscripts to the UCSF Library for open access and distribution. UCSF will make such theses, dissertations, and manuscripts accessible to the public and will take reasonable steps to preserve these works in perpetuity.

I hereby grant the non-exclusive, perpetual right to The Regents of the University of California to reproduce, publicly display, distribute, preserve, and publish copies of my thesis, dissertation, or manuscript in any form or media, now existing or later derived, including access online for teaching, research, and public service purposes.

DocuSigned by:

Elma Stephanie Frias

—1234F517F0114FE...   Author Signature

12/14/2021

Date

212